# CALIBRATION AND INTERPRETATION OF A 2.3 GHZ CONTINUUM SURVEY

Thesis

Submitted in Fulfilment of the

Requirement for the Degree of

MASTER OF SCIENCE

of Rhodes University

South Africa

by

ANDREW GREYBE

April 1984

"The old dream of wireless communication through space has now been realized in an entirely different manner than many had expected. The cosmic shortwaves bring us neither the stockmarket nor jazz from distant worlds. With soft noises they rather tell the physicist of the endless love play between electrons and protons."

A.UNSOLD (1946)

Table of contents


| | | |
|---|---|---|
| Acknowledgements | | |
| Abstract | | |
| Chapter 1 | Introduction | 1.1 |
| Chapter 2 | Mapping the Southern Sky at 2.3 GHz | |
| 2.1 | Introduction | 2.1 |
| 2.2 | The telescope | 2.1 |
| 2.2.1 | The telescope beam pattern | 2.2 |
| 2.2.2 | $T_a$ versus $T_b$ | 2.6 |
| 2.3 | The receivers | 2.9 |
| 2.3.1 | The radiometer | 2.10 |
| 2.3.2 | The maser | 2.11 |
| 2.3.3 | The gasfet | 2.11 |
| 2.4 | Observing technique for survey maps | 2.13 |
| 2.5 | Processing the data | 2.14 |
| 2.5(i) | Binning the data | 2.14 |
| 2.5(ii) | Removing a rough background | 2.15 |
| 2.5(iii) | Removing drift | 2.16 |
| 2.5(iv) | Subtracting the final background | 2.16 |
| 2.5(v) | Combining the rasters | 2.17 |
| 2.6 | Discussion of the Rhodes mapping method and proposed improvements | 2.17 |
| Chapter 3 | A graphical presentation of the Southern Sky at 2.3 GHz | |
| 3.1 | Introduction | 3.1 |
| 3.2 | Observations | 3.1 |
| | A14D63 | 3.2 |

| | | |
|---|---|---|
| | A04D80 | 3.4 |
| | A12D26 | 3.6 |
| 3.3 | Data enhancement and presentation | 3.7 |
| 3.3.1 | Black and White displays | 3.9 |
| 3.3.2 | Colour graphics | 3.12 |
| 3.3.3 | Image enhancement | 3.14 |
| Chapter 4 | Calibrating the Rhodes 2.3 GHz Survey | |
| 4.1 | Introduction | 4.1 |
| 4.2 | Absolutely calibrating a radio survey | 4.2 |
| 4.3 | Calibrating the Rhodes 2.3 Ghz Survey | 4.8 |
| 4.4 | "long scan" mapping technique | 4.13 |
| 4.5 | Reducing the "long scans" | 4.16 |
| 4.5.1 | Preliminary analysis programs | 4.16 |
| 4.5.2 | "long scans" reduction programs | 4.18 |
| 4.6 | "long scans" observations | 4.23 |
| 4.7 | Future work and improvements for the "long scans" technique | 4.25 |
| 4.8 | Conclusion | 4.28 |
| Chapter 5 | Intermediate latitude Southern Hemisphere continuum radiation at 2.3 GHz | |
| 5.1 | Introduction | 5.1 |
| 5.2 | Prominent galactic features | 5.3 |
| region A | HII region surrounding Zeta Ophiuchi | 5.3 |
| region B | Sancisi's expanding ring ? | 5.12 |
| region C | Upper Scorpius | 5.14 |
| region D | Radio spur in the direction of the galactic centre | 5.16 |
| region E | Emission in the direction of the Upper | |

| | | |
|---|---|---|
| | Centaurus-Lupus association | 5.19 |
| region F | SCO-CEN bubble | 5.21 |
| Chapter 6 | Low latitude Southern Hemisphere continuum radiation at 2.3 GHz | |
| 6.1 | Introduction | 6.1 |
| 6.2 | The galactic plane at 2.3 GHz | 6.1 |
| 6.3 | The radio continuum disk at 2.3 GHz | 6.2 |
| 6.4 | Conclusion | 6.6 |
| CONCLUSION | | |
| References | | |
| Appendix 1 | Atlas of contour maps for the regions<br>(i) 5HR to 14HR45M and $-80^{\circ}$ to $-61^{\circ}$<br>(ii) 13HR to 0HR45M and $-25^{\circ}$ to $-7^{\circ}$ | |
| Appendix 2 | Atlas of contour maps for the region<br>$\|b\| < 10^{\circ}$ and $30^{\circ} > l > 303^{\circ}$ | |
| Appendix 3 | Table of contour labels | |

## ACKNOWLEDGEMENTS

Before presenting the thesis I would like to thank the following people for their willingness to help me.

Firstly to my supervisor Gerhard de Jager for his criticism and unfailing assistance over the last two years. Without him this thesis would definitely not have reached this point.

Secondly to my other supervisor Eddie Baart for his encouragement and warm friendship over the same period.

Thirdly to George Nicolson for allowing me to pick his brains and use his telescope. This also means to his staff for maintaining the telescope in a usable state, with a special word of thanks to Joe for modifying the telescope so that I could observe the South Pole.

I would like to thank the South African CSIR for financing me during the last two years and previously to that. I would also like to thank Rhodes University's Department of Physics and Electronics for providing me with a base where I could work.

Last but by no means least I would like to thank all my friends who have kept me happy over the last two years and whom I will always remember. This includes my parents whom I don't know how to thank enough because they have always been willing to help me.

ANDY GREYBE

## ABSTRACT

This thesis continues the Rhodes 2.3 GHz Survey of the Southern Sky. It consists of two parts : a data processing part and an astronomical analysis part. In the data processing part the data for the regions 4HR to 15HR , $-80^{\circ}$ to $-61^{\circ}$ and 12HR to 23HR , $-27^{\circ}$ to $-7^{\circ}$ are presented in contour map format. A beam pattern of the Hartebeesthoek telescope at 13 cm is constructed from drift scans of the radio source TAU A. This is used to investigate the data filtering techniques applied to the Rhodes Survey. It is proposed that a set of widely spaced scans which have been referred to the South Celestial Pole can provide a single calibrated baselevel for the Rhodes Survey. The observing technique and the necessary reduction programs to create a coarse grid of antenna temperatures of the Southern Sky using these observation are developed. Preliminary results for this technique are presented as a map of the region 18HR to 6HR , $-90^{\circ}$ to $30^{\circ}$ with a $5^{\circ}$x$5^{\circ}$ resolution.

On the astronomical side two studies are undertaken. The region 13HR to 23HR, $-61^{\circ}$ to $-7^{\circ}$ is searched for large extended areas of emission. 7 features occurring at intermediate galactic latitudes are found. They are interpreted as follows : one of them is the classical HII region surrounding the star Zeta Ophiuchi $(l'',b'')=(6.7^{\circ},22.4^{\circ})$, and the rest are combinations of thermal and nonthermal emission from galactic features. The galactic equator profile for $24^{\circ} > l > -58^{\circ}$ is studied. It is dominated by a plateau of emission for $l < -26^{\circ}$. This is interpreted as a combination of thermal and nonthermal radiation emitted by a ring of gas symmetric about the galactic centre with a radius of 4 - 6 kpc.

# CHAPTER 1

## INTRODUCTION

Radio studies of the galaxy have assisted in unravelling galactic structure in amazing ways ever since Karl Jansky (1932) detected short wave hiss from the direction of the galactic centre. Today the radio spectrum is used extensively in line and continuum measurements to probe the radio sky (Downes (1982)). The limelight in radio astronomy in recent years has been on higher resolution studies. But this increased resolution has not always meant a corresponding increase in the number of new exciting objects discovered. In fact the VLA in Socorro, New Mexico which has arc second resolution and has been operating for 2 years has found no new objects. It has only increased our knowledge of known objects. The point about this is that radio astronomy research is being wooed by the super-high resolution possible with radio interferometry and is neglecting the fact that very little is understood about the absolute brightness distribution of the radio sky.

This thesis is a continuation of a 5 year old project which aims to map the sky for $\delta < 30^o$ at 2.3 GHz with a resolution of 20 minutes of arc. This represents the highest resolution large sky survey to date. Existing all sky surveys are the 150 MHz survey by Landecker and Wielebinski (1970) with a resolution of $3.5^o$ and the 408 MHz survey by Haslam et al (1982) with a resolution of $0.85^o$. Uncompleted but underway at the moment is the 1420 MHz survey by Reich (1982) with a resolution of $0.6^o$. Reich plans to extend this survey to the Southern Sky in the future using a 30m telescope in Argentine. The 1420 MHz survey is supposed to extend the existing radio sky database, at present only up to 408 MHz into the thermal radiation region. But at 1420 MHz the nonthermal component of the galaxy is still strongly visible (eg.

(eg. the central disk of the galaxy and the loop structures (Reich (1982)). Therefore the higher the frequency at which we observe the greater will be the chances of separating the two components i.e. thermal and nonthermal. This is the purpose of the Rhodes survey - to extend the all sky observations into the thermally dominated range of the radio spectrum. These observations will, together with the existing surveys permit a better determination of the radio spectrum of the galaxy.

The work presented in the following chapters has three aims. These are to continue the Rhodes Survey of the Southern Sky, to develop a technique which will provide a single baselevel for the Rhodes Survey and to interpret the existing data astronomically. These were achieved as follows.

The regions 13HR to 23HR , $-27^{0}$ to $-7^{0}$ and 4HR to 15 HR , $-80^{0}$ to $-61^{0}$ were mapped and are presented as an appendix to this thesis. The method of mapping is discussed and reviewed and data filtering techniques applied to the data are investigated in chapters 2 and 3 respectively.

When work was commenced on this thesis in 1982 the Rhodes Survey had developed to a stage where it could produce maps of large areas of the sky. These maps are typically 12 hours of right ascension and $19^{0}$ or $39^{0}$ declination. The problem facing the survey group at that stage was to design a technique which would combine these smaller maps into a single southern sky survey. This thesis has set about tackling that problem. The problem has been fully investigated and described in chapter 4. A solution which involves compiling a coarse grid of absolutely calibrated brightness temperatures is proposed. The observing technique and the reduction process were developed and are described in chapter 4. Preliminary results using a minimum number of observations for this coarse grid are obtained and presented. The technique is shown to produce good preliminary results but has not been finally implemented.

A start is made at interpreting the already completed parts of the survey. In chapters 5 and 6 the region 13HR to 23HR , $-61^{o}$ to $-7^{o}$ is analysed. The analysis is split into intermediate galactic latitude features, $|b| > 10^{o}$, and low galactic latitude features, $|b| < 10^{o}$. The analysis shows that there is a class of objects - large (> 10 square degrees) extended areas of enhanced emission, which have not been previously observed, except by the Rhodes group themselves (Baart et al (1981)). These objects trace out known large HI features. In this class of objects evidence for the following features was found - the thermal part of Sancisi's source (1974), the SCO-CEN bubble (Weaver (1978)) and the Gould belt of gas. The usual nonthermal spurs are evident with a prominent one rising out of the centre of the galaxy being extensively studied. Finally in chapter 6 the shape of the galactic equator profile for the region $30^{o} > l > -57^{o}$ is studied.

# CHAPTER 2

# MAPPING THE SOUTHERN SKY AT 2.3 GHz

## 2.1 INTRODUCTION

The maps that will be presented and discussed in this thesis were observed with one telescope - the Hartebeesthoek telescope. They were produced by using the telescope in a fast scanning mode to track fixed right ascensions. The method of reducing these scans was developed by the Rhodes group and has been described by P Mountfort (1982). The way in which these maps were produced is very relevant to the way in which they will be joined together and calibrated in chapter 4. For this reason and because a description of this method is not readily available this chapter will describe how the maps were produced.

The layout of the chapter is as follows - first the telescope and receiving equipment are discussed. This includes a description of an observation of the telescope beam pattern, the receivers used and how to relate antenna temperature to brightness temperature for this telescope. This allows us to compare the results obtained in this survey with those of other observers. Then there is a fairly detailed description of the data processing involved in producing the maps. This covers drift and background removal and how the individual observations are combined. Finally there is a discussion of this method of large sky surveying, improvements to it and how it compares to other methods of large sky surveying.

## 2.2 THE TELESCOPE

The telescope is situated about 40 miles north west of the city of Johannesburg, at a latitude of $-26^{\circ}$. It was commisioned by NASA and built by JPL (Jet Propulsion Laboratories, USA) as part of a deep space communications network. It was initially known as the Deep Space Instrumentation Facility (DSIF) 51, now it is known as the Radio Astronomy Observatory (RAO) of the National Institute of Telecommunications Research (NITR) of the South African Council for Scientific and Industrial Research (SACSIR) or simply RAO. It is a standard DSIF design. This means it has a 26m parabolic reflector, a hyperbolic subreflector and a Cassegrain cone at the focus, in which the feeds are housed. The telescope is polar mounted. The declination axis range is limited , by the telescope structure, to -90 degrees and +45 degrees declination (see chapter four for more about this, these limits were not always like this). The feed at 13 cm is a horn feed which responds to linear polarization only. The polarization axis is aligned East-West. The half power beamwidth at 2.295 GHz (13cm) is 20 minutes of arc i.e. $1/3^{o}$. This is suitable for large area mapping because the scan spacing can be quite large then, a maximum of $0.143^{o}$ if we want to avoid aliasing in the spatial frequency domain.

### 2.2.1 The telescope beam pattern

A very important parameter of the telescope is the beam pattern. This is because what we are trying to do with all our observations is not only correct them for the radiation losses introduced by the antenna but ideally we would like to find the principal solution to

eq.2.1 $$T_a = A_e / \lambda^2 \; T_b * P_n$$

where $*$ = the sign for convolution

$T_a$ = antenna temperature distribution

$A_e$ = effective aperture of telescope in $m^2$

$k$ = Boltzmann's constant

$T_b$ = brightness temperature

$P_n$ = antenna power pattern, normalised so that the peak is 1

The principal solution to this equation is

$$T_b = FT^{-1}(2k/A_e\ FT(T_a)/FT(P_n))$$

where $FT(f)$ = signifies the Fourier transform of f

$FT^{-1}(f)$ = signifies the inverse Fourier transform of f

In reality though we do not usually find the principal solution. Instead we deal with the flux of a source, or when we want to consider individual points on a map we remember that we are looking at the full beam brightness at that point. The principle solution does exist and can be found but is rarely ever computed because of the errors on the higher spatial frequency values. Even though we do not solve this equation we need to know the spatial frequency cutoff of the beam pattern and, for a qualitative evaluation of the observations, we need to know what it looks like. At the time these maps were being surveyed there did not exist a beam pattern with a high dynamic range for the 13 cm feed. A beam pattern with a high dynamic range has been recently observed by the RAO staff. These data were used to construct a beam pattern on the same grid spacing as the survey maps. In the following section the method of observing and the resulting beam will be described.

If we consider eq.2.1 we will see that if $T_b$ is a point source i.e. it has dimensions small compared to the main lobe of the beam, it can be represented by a delta function, so

eq.2.2 $$T_a = A_e/\lambda^2 \delta_b * P_n$$

where

$\delta_b$ = zero everywhere except where the source is there it can be represented by a spike which has an area equal to the brightness temperature of the source

The convolution of a function with a delta function is the function itself (Bracewell(1965), ch 5) reproduced at the position of the delta function. In our case the function which is reproduced is the beam pattern. This offers us an easy way of obtaining the beam pattern - if we observe a point source then the resulting map will be a beam pattern. In choosing a point source care was taken to find one with a high peak temperature,in this way we could reveal many of the faint sidelobes of the beam. The source chosen was Taurus A which has a flux of 795 +- 1 Jy at 2.272 GHz (Baars, 1973).

The map of Tau A was constructed out of drift scans done by Mike Gaylard (RAO staff, private correspondence). These were obtained in the following manner : the telescope was driven to right ascension $80.4^{\circ}_{1950}$ for a chosen declination, parked there and then, while the sky drifted through the radiometer was sampled every $0.0357^{\circ}$. When right ascension $85.4^{\circ}_{1950}$ had passed the telescope was driven to the next declination. Drift scans were conducted in this manner for a number of declinations. These were chosen for the beam centre, the half maximum, first null, first side lobe and then successively further out until the source wasn't visible any more. These were (1950) : $22.202^{\circ}$, $22.002^{\circ}$, $21.982^{\circ}$, $21.812^{\circ}$, $21.592^{\circ}$, $21.422^{\circ}$, $21.233^{\circ}$, $21.046^{\circ}$, $20.860^{\circ}$, $20.531^{\circ}$, $20.257^{\circ}$ and $20.058^{\circ}$. The recorded samples were then listed on a teletypewriter and fed into the Cyber at Rhodes. The only correction made to the data was the removal of a linear drift. This was estimated from the plot of each scan, but because auto scaling is applied to these plots the estimated drifts on the scans through the centre of source were not too accurate. This resulted in a bad scanning effect occurring on the line of constant declination just off the centre of the main beam. It is most noticeable in the contour plot of the beam pattern (fig.2.1) as an elongation between the 2nd and 3rd sidelobes at $22^{\circ}$ declination. In order to compare this beam pattern with the survey maps we interpolated these scans onto a $0.1^{\circ}$ by $0.1^{\circ}$ grid spacing. In the declination direction this was achieved by fitting cubic splines across declination for all corresponding right ascension bins and evaluating them every $0.1^{o}$. In right ascension this was achieved by a sinc interpolation, the first null of the sinc was at $0.1^{o}$ and only 140 terms on either side of the sinc peak were included. Note that Tau A has coordinates (1950) right ascension $82.880^{o}$ and declination $21.982^{o}$. Which means only half the beam was observed. If we assume the beam is symmetrical about the declination axis, we can fold the data about $21.982^{o}{}_{1950}$ declination and then we will have a beam pattern. Contour maps of the beam and its Fourier transform are presented in figures 2.1 and 2.2. Although this is not an excellent beam it can provide us with a lot of information.

We can use these observations to find a lower limit for the beam solid angle. If we evaluate equation 2.3 we would arrive at a lower limit for the antenna beam solid angle, $\Omega_A$. Note it is only a lower limit because the forward lobes have not been included

eq.2.3 $$\Omega_A = 1/T_p \int_{source} T_a \, d\Omega$$

where $T_p$ = the peak temperature

$T_a$ = the antenna temperature on the map

This was achieved by summing all the values above 0mK, times $d\Omega = 0.01\cos\delta$ square degrees, and dividing the total by the peak temperature, 96.4 K. The value found is quoted below :

$$\Omega_A = 4.158\times10^{-5} \text{ steradians}$$

In appearance (fig.2.1) the beam seems to be quite symmetrical in the right ascension direction which justifies the assumption involved in folding it about the declination axis. What was not seen in previous beam observations are the faint fourth sidelobes, this is due to the high dynamic range of the map. What is also interesting is the set of sidelobes running diagonally from the main lobe. These are most visible in the second and third ring of sidelobes. They occur on both sides and are therefore real. If we did a

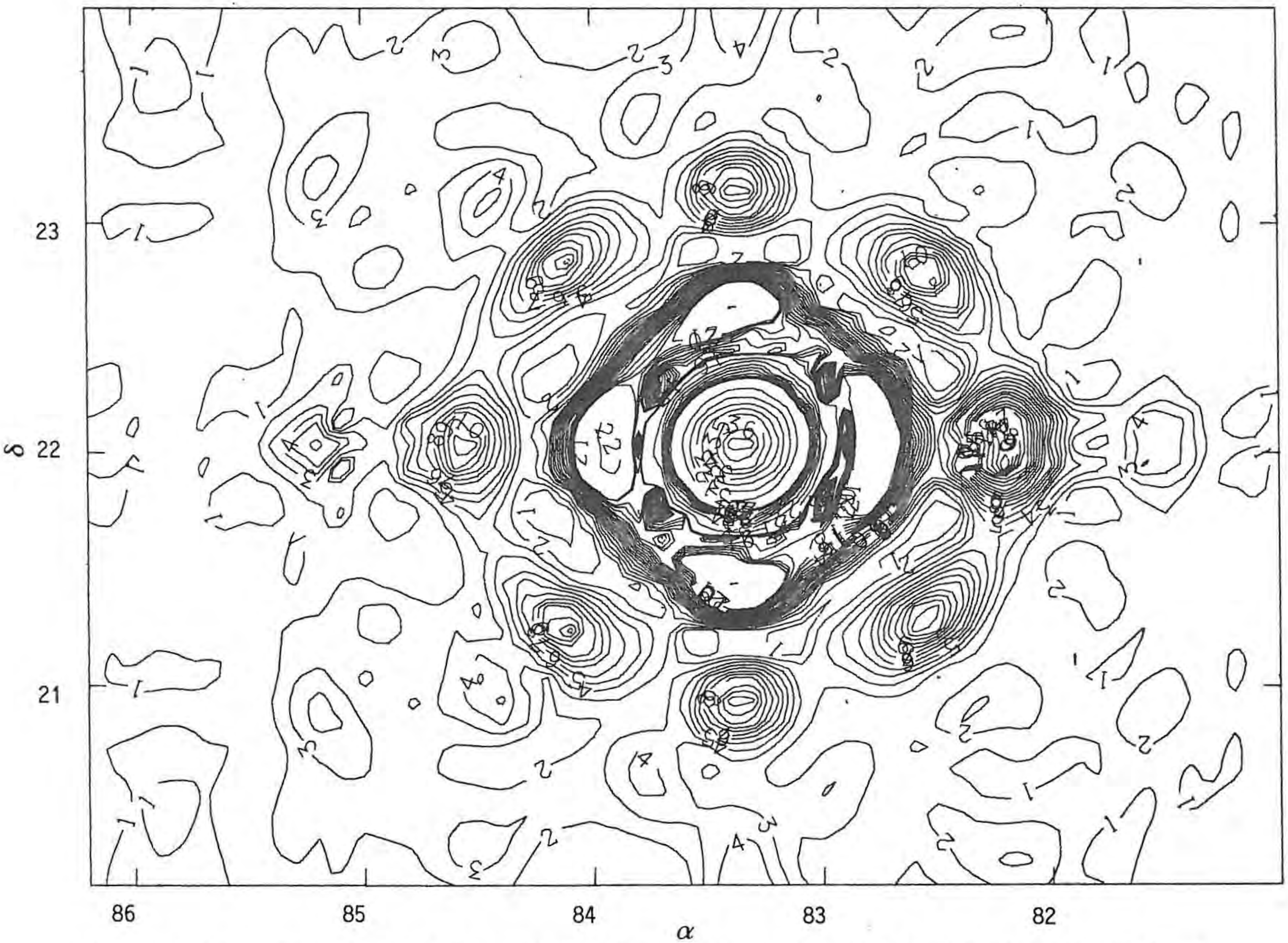


fig. 2.1 raw beam pattern for 13 cm at Hartebeesthoek, constructed from drift scans of Tau A, contour labels listed in appendix 3.

2.5b

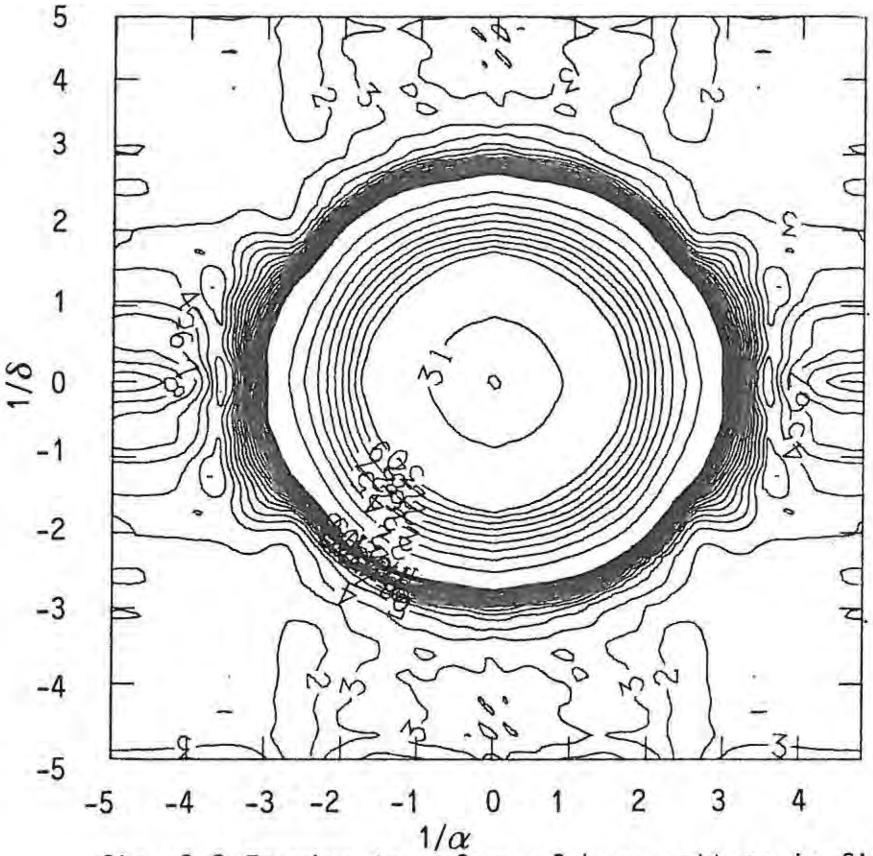


fig. 2.2 Fourier transform of beam pattern in fig. 2.1, contour labels listed in appendix 3.

transform of the aperture illumination function we would see these. Note the plot transform (fig.2.2) of the beam is slightly elliptical. This is because the program which plots the transform has compressed the whole right ascension axes by sec$\delta$, where $\delta$ is the lowest declination on the map ($\sim 24^0$) Note that the beam should cutoff at 3.5 reciprocal degrees. This is because the beam solid angle is equal to $\lambda^2/A$ (Kraus(1966), p 157) which is $200^{-2}$ radians$^2$ at 13 cm for a 26m dish. This means in a single dimension it should cutoff at 200 reciprocal radians or 3.5 reciprocal degrees. But we see it has high frequency noise outside this cutoff. This is typical of the survey maps too and we will leave this noise in for now and then in the next chapter show how this can be removed by various enhancement techniques.

### 2.2.2 $T_a$ versus $T_b$

What we want to measure with this antenna is the brightness distribution of the sky. Brightness B is defined in watts.m$^{-2}$.cps$^{-1}$.rad$^{-2}$. That means it describes the power received per unit collecting area per unit bandwidth per unit steradian of source. What is measured by the antenna though is antenna temperature. This is related theoretically to the power received by the antenna as follows

eq.2.4 $$w = kT_a$$

$w$ = power per unit bandwidth in watts.Hz$^{-1}$

$k$ = Boltzmann's constant , $1.38 \times 10^{-23}$ watts.s.K$^{-1}$

In practice the relation between power and antenna temperature is determined by firing a noise tube in the front end of the telescope. The noise tube has been previously calibrated and has a known equivalent noise temperature. In this way the conversion factor for receiver units to kelvin , $T_a$, is obtained. Therefore antenna temperature is the equivalent temperature of a thermal source. This is very convenient because when we discuss the brightness of the sky we discuss it in terms of the equivalent brightness a thermal source would emit. A perfect thermal source is known as a blackbody. This is because it is a perfect absorber, and by the reciprocity theorem also a perfect emitter. The brightness distribution of such a source can be described by Planck's function (Kraus(1966),p 85)

eq.2.5 $$B(\alpha,\delta,\nu) = \frac{2h\nu^3}{c^2}\,\frac{1}{e^{h\nu/kT_b(\alpha,\delta)}-1}$$

For a fixed frequency $\nu$ we can describe brightness in terms of brightness temperature only. This temperature, $T_b$, is the temperature at which a blackbody would have to be to produce the equivalent brightness. This can be further simplified if we consider that at radio frequencies $h\nu/kT \ll 1$ (cf. $h\nu/kT \sim 0.00048$ for 1GHz and 100K). Therefore at radio frequencies we commonly use the Rayleigh-Jeans approximation for Planck's law

eq.2.6 $$B(\alpha,\delta,\nu) = 2\nu^2 T_b(\alpha,\delta)k/\,c^2$$

The above relation allows us to get back from $T_b$ to brightness once we have related $T_a$ to $T_b$.

To relate the full beam brightness to antenna temperature we will follow the approach of Findlay (1966). We can think of the antenna as an idealized antenna with radiation losses. For the full beam brightness case we can consider the antenna to be in an enclosure which is maintained at a brightness temperature of $T_b$. Then

eq.2.7 $$T_a = \eta_R/\Omega_A \int_{4\pi} T_b(\alpha,\delta) f(\alpha,\delta)\, d\Omega$$

where $\eta_R$ = is the radiation efficiency of the telescope and will include the effects of imperfections in the surface of the telescope dish

$\Omega_A$ = is the antenna beam solid angle

$f(\alpha,\delta)$ = is the antenna power pattern normalised so that the peak is 1

This integral can be separated into contributions from within and outside the main lobe of the antenna eq.2.8 $$T_a = \eta_R/\Omega_A\int_{\text{main lobe}} T_b(\alpha,\delta)f(\alpha,\delta)d\Omega + \eta_R/\Omega_A\int_{\text{side lobes}} T_b(\alpha,\delta)f(\alpha,\delta)d\Omega$$

This form of expressing the $T_a$ will be utilised in the following section. The sidelobes detect the ground radiation and backlobe contribution. We shall refer to the integral over the side lobe region, the second term in eq.2.8, as $I_{stray}$ from now on. It has the same units as $T_a$.

If we consider a source, large enough to fill the main lobe, passing through the beam, then

eq.2.9 $$T_a = \eta_R(T_b)_{ml}/\Omega_A\int_{\text{main lobe}} f(\alpha,\delta)d\Omega + I_{stray}$$

where $(T_b)_{ml}$ = average brightness temperature over the main lobe

We can now define $\eta_R/\Omega_A\int_{\text{main lobe}} f(\alpha,\delta)d\Omega$ as the main beam efficiency, $\eta_B$. Then if we consider a source moving through the main beam of the antenna and assume $I_{stray}$ does not change, the change in $T_a$ from the no source region to the source region is

eq.2.10 $$T_a = \eta_B(T_b)_{ml}$$

Therefore the factor we want, to relate antenna temperature to main beam brightness (or vice versa) is $\eta_B$.

If we model the beam shape by a two dimensional gaussian in rectangular coordinates (x and y) of the following form (Findlay (1966))

eq.2.11 $$F = \exp\{-x^2/(0.6\xi_E)^2 - y^2/(0.6\xi_H)^2\}$$

where $\xi_E$ = is the HPBW in the E plane of polarization

and $\xi_H$ = is the HPBW in the H plane (orthogonal to the E plane)

then the integral of the main beam solid angle is (Findlay (1966))

eq.2.12 $$\int_{\text{main lobe}} f(\alpha,\delta)d\Omega = 1.133\xi_E\xi_H$$

The effective area of the antenna (which takes the radiation efficiency into account) $A_e$ can be derived from observations of a calibrated small diameter source using the following equation

eq.2.13 $$A_e = 2k\,T_a/\text{flux of source}$$

and since $A_e = \eta_R\lambda^2/\Omega_A$ we get

eq.2.14 $$\eta_B = 1.133\xi_E\xi_H A_e/\lambda^2$$

$A_e$ can be derived from observing the antenna temperature increase for a source of known flux density. Jonas (1982) found for Pictor A (which has $S_{2.3GHz}$=41.8 Jy) an antenna temperature increase of 4.77K. From this

$$A_e = 315\ m^2$$

Assuming a gaussian beam shape we also have, from the above beam pattern

$$\xi_E=\xi_H=0.333^\circ = 20 \text{ minutes of arc}$$

from which

$$\eta_B = 1.133/0.13^2 \times 1/3^2 \times 315 \times (\pi/180)^2$$
$$= 0.71$$

The $\pi/180$ term is to convert from degrees to radians. This yields a main beam brightness conversion factor for the survey maps for antenna to brightness temperature of

$$T_b = 1.41\ T_a.$$

## 2.3 THE RECEIVERS

The data presented in this thesis were observed with two receivers. This occurred because the observations were done in four distinct periods. They were June 1981, December 1981, June 1982 and May 1983. During the first three periods a travelling wave ruby maser was operating at 13 cm at Hartebeesthoek. This was used to observe the survey maps. For the fourth period the maser 'died' and the long scans (presented in chapter 4) were observed with a GaAsFET (gasfet for short) receiver.

The same radiometer was used with both receivers. In the following section the radiometer will be described and then the sensitivity of each of the two receivers discussed.

## 2.3.1 The radiometer

The radiometer is of the noise adding type and has been fully described by Nicolson (1970a,1970b). What follows is a simplified description of its operation, derived from Nicolson (1970a).

A block diagram of the radiometer appears in figure 2.3. The radiometer works in the following way - noise is modulated onto the receiver input at a frequency of 525 Hz. This is synchronously detected to yield an output voltage $V_2$, which is only proportional to $gkT_nB$ (where g is the gain, k is Boltzmann's constant, $T_n$ is the noise temperature of the modulated noise and B is the bandwidth of the IF amplifier). Because $T_n$ is constant $V_2$ is proportional to g. The square law detector voltage $V_1$, detected over a period $t > 2$ ms is proportional to $gkB(T_s + T_n/2)$. Where $T_s$ is the system noise temperature. Balancing $V_2$ against $V_1$ we get an output $V_0$ which is proportional to only the system noise temperature. Although the output $V_0$ can be made independent of g and B we do not want to have to continually calibrate the system. Therefore we balance $V_2$ against a reference signal $V_r$ to obtain a $V_{agc}$. This is used to control the gain of the IF amplifier. As long as the variations in g are not big, $V_{agc}$ will keep the system gain constant and eliminate the need to continually calibrate the system.

As far as the sensitivity and stability of the radiometer are concerned we have the following two theoretical results. The output noise fluctuation referred to the input is

eq.2.15 $$\Delta T_{s\ rms} = 2T_s(1 + T_s/T_n)/(2Bt)^{1/2}$$

Spurious changes in $T_s$ and $T_n$ cause instabilities in the output given by (Nicolson (1970b))

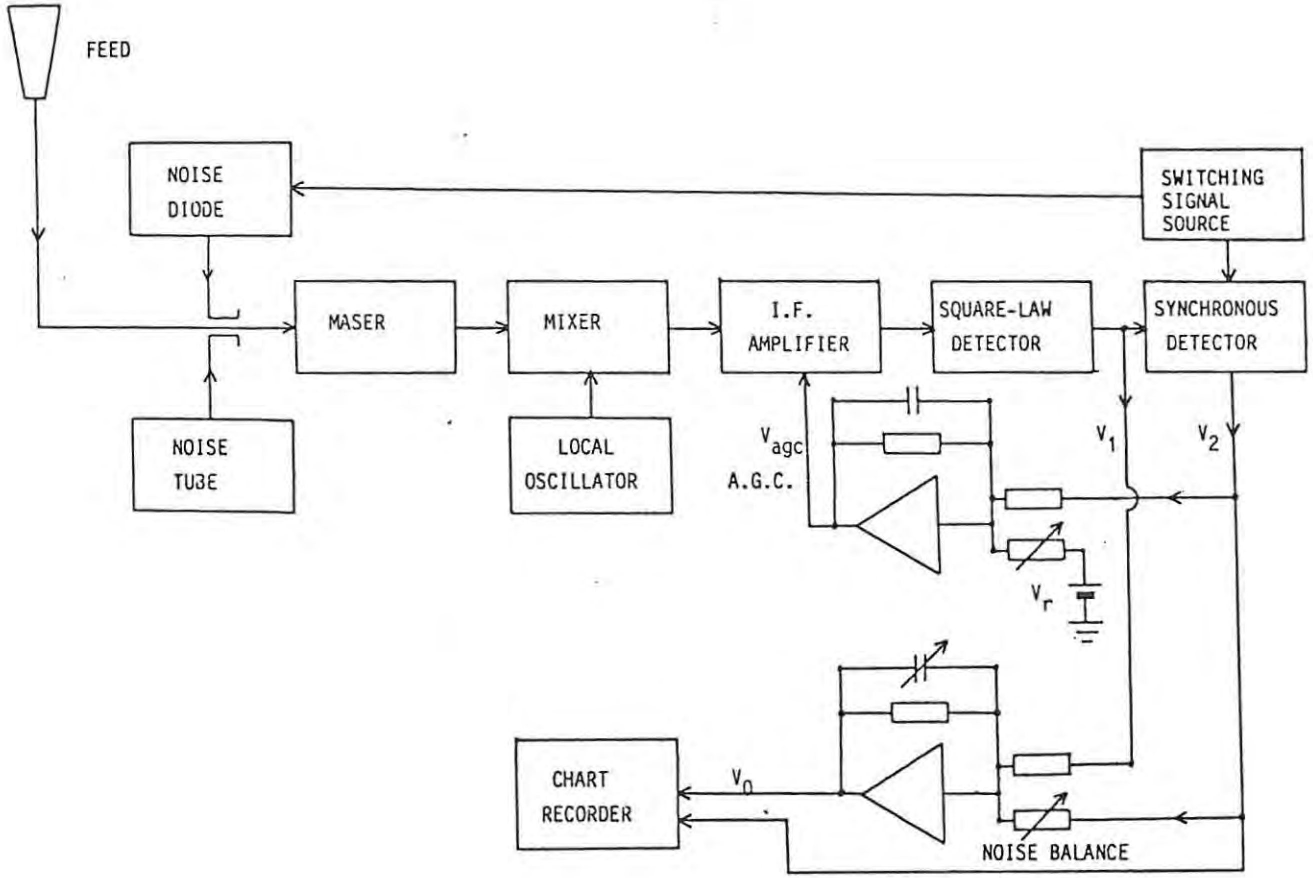


fig. 2.3 block diagram of radiometer

eq.2.16 $$\Delta T_{stab.} = T_s(\Delta T_s/T_s + \Delta T_n/T_n)$$

$\Delta T_{stab}$ = spurious changes in the output of the radiometer

$\Delta T_n$ is very small and has been shown (Nicolson(1970b)) to introduce no noticeable changes in the gain stability. Changes in $T_s$ will now be discussed.

## 2.3.2 The maser

A travelling wave ruby maser was used. It is ideal for the above radiometer because its $\Delta T_s$ over time scales of the order of 10 secs is less than 0.006 K. Drift in $T_s$ over a night's observing amounted to less than 0.1 K per hour. This was estimated from the AGC voltage displayed by the chart recorder. This type of slow drift was removed during the data analysis.

The maser system noise temperature as measured by MJ Gaylard (RAO staff) is

$$T_s = 32 \text{ K also } T_s/T_n = 0.67$$

which yields a $\Delta T_{s\ rms}$ of

$$\Delta T_{s\ rms} = 2^{1/2}\ 32\ (1 + 0.67\ )\ /\ (20\times10^6\times0.1)^{1/2}$$

for B = 20 MHz and t = 0.1 sec (the integration time per sample for the survey)

$$\Delta T_{s\ rms} = 53 \text{ mK}$$

The noise measured for the maser is

$$\text{meas}\Delta T_{s\ rms} = 62 \text{ mK} +- 11 \text{ mK}$$

Which compares favourably.

## 2.3.3 The gasfet

The gasfet has a higher operating temperature and higher coupling attenuation than the maser. Consequently it has a higher system temperature. A noise tube of 3.85 K was used to calibrate the system temperature. The system temperature was measured in the following manner - the telescope was parked at zenith and its system temperature measured in millivolts. The noise tube was fired and a conversion factor for millivolts to kelvin obtained.

This factor was then used to convert the system temperature to kelvin, $T_a$. Drift in $T_s$ for a night was estimated by referring to the south pole every 12 minutes. It was found that on a clear evening drift was a maximum of 0.75 K for the period sunset to sunrise. Note this is downward drift i.e. the system temperature became colder by this amount. On bad evenings, i.e. one with lots of cloud, drift could be as big as 2 K for a night. These drifts were also removed by the data processing. It is interesting to note that the drift with the gasfet is the same as with the maser. Which makes it seem as if 'receiver' drift is actually due to the cooling down of the telescope and its surroundings, not to changes in the receiver because we observe the same drift with two different receivers.

Using the above technique a system temperature of

131.7 K +- 1.5 K

was obtained. The theoretical $T_{s\ rms}$ on this is

169 mK +- 4 mK

Which compares reasonably with the measured rms noise of

207 mK +- 12 mK

Differences between these two values could arise from the fact that when we measured $T_{s\ rms}$ we were pointing at zenith at daytime. So that there are contributions to the antenna temperature from the sun and from the point in the sky at which we are looking. All these contributions would raise the spurious fluctuations in the measured $T_s$.

From the above results we can see that the maser is approximately four times more sensitive than the gasfet.

## 2.4 OBSERVING TECHNIQUE FOR SURVEY MAPS

The radio telescope on its own is not an imaging device, it can only be used to measure the power received from a single direction at any one time. Consequently, to make an image of the sky we need to scan the telescope across the sky and sample its output at discrete spatial intervals. This scanning motion is very similar to the way in which a raster graphics device scans across its screen to generate a picture. For this reason we have called our scans across the sky rasters. The technique of scanning the sky has been to choose a declination range and then track at a fixed right ascension over that range. Because of the earth's rotation this scanning motion will describe a diagonal line in telescope coordinates. The right ascensions of the raster scans have to be fixed so that a bad observation can be repeated or so that the same region of sky observed again on another night. Because the telescope is band limited in the spatial frequency domain we can space the scans a maximum distance apart without losing any information. The telescope cutoff is 3.5 reciprocal degrees, which means the scans must be at most $0.143^{\circ}$. To allow for non-linear processes on the data we chose a raster spacing of $0.1^{\circ}$. This means our data is oversampled or in other words we are above the aliasing limit in the spatial frequency domain. While tracking a fixed right ascension at a rate of $0.25^{\circ}\text{sec}^{-1}$ more than $0.1^{\circ}$ (the distance between scans) of sky could pass over the meridian (the sky moves at $1/240=0.0042^{\circ}\text{sec}^{-1}$).

Consider the following example : we want to map the region 0 to 12 hours right ascension and $-61^{\circ}$ to $-80^{\circ}$ declination. It will take 76 seconds to track that range of declination. In that time $0.32^{\circ}$ of right ascension will have passed overhead. So it will be impossible to track the next $0.1^{\circ}$ away right ascension scan because it will involve tracking over a different set of telescope coordinates and the atmospheric contribution will be different. Consequently the next scan will have to be on the right ascension $0.4^{o}$ away. It will be possible then, on a single night, to only observe on a $0.4^{o}$ spacing. Such a set of scans is called a raster and is identified by the right ascensions it falls on. On the next night we observe also on a $0.4^{o}$ spacing but starting on a right ascension which is not covered by the first raster. Interleaving these two sets of observations will then yield a map on a $0.2^{o}$ spacing, for example. Note that at these low declinations, because of the sec $\delta$ compression of right ascension coordinates we only need a $0.2^{o}$ spacing in right ascension to get a true spacing of $0.1^{o}$. This scanning motion is depicted in telescope coordinates in fig.2.4a. The interleaved rasters are shown in fig.2.4b. It will be noticed that a raster is made up of alternate up and down scans. A single up or down scan is referred to as a run. Note these up and down runs have to be treated separately because they will have different atmospheric contributions, having scanned through different sections of the atmosphere.

A map is approximately 12 hours of right ascension if observed in winter or 10 hours if observed in summer (because of the different night lengths). For each map we require three good observations of each raster. A good observation is one which has less than one hour of spoiled data. Data is considered spoilt if it contains rain or a satellite or thick cloud. The number of rasters per map depends on the declination range of the map. It has been found that maps which cover a declination range of $40^{o}$, and require 8 rasters, are the most economical on telescope time.

## 2.5 PROCESSING THE DATA

<u>2.5.(i) binning the data</u> - the DVM is sampled ten times a second. This means that at a scan rate of $0.25^{o}s^{-1}$ there are 4 samples per $0.1^{o}$ of declination.

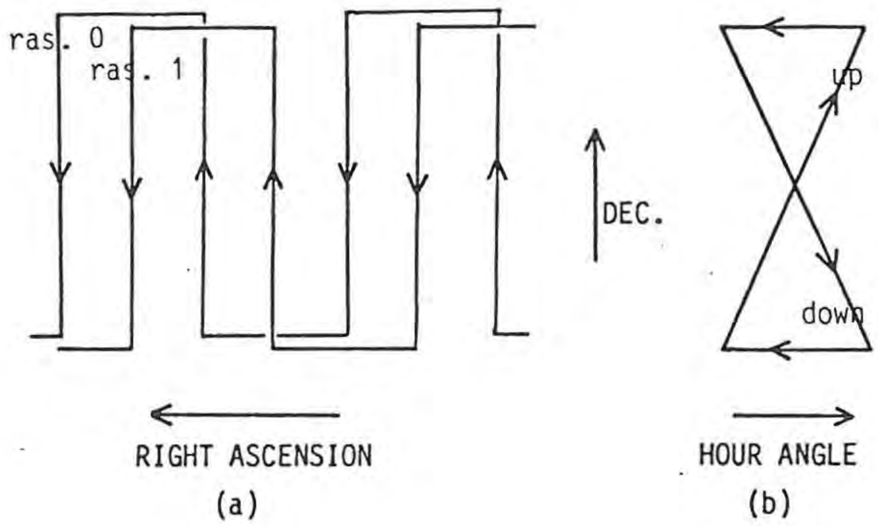


fig. 2.4 scanning path of telescope as directed by SKYMAP program in (a) equatorial coordinates and (b) telescope coordinates

Each sample, its telescope coordinates and the universal time are recorded onto tape. To make the data more manageable the data must be reduced. First a running-median-of-3 is applied to each run i.e. in the direction of changing declination. This removes spurious points which could have been recorded because of noise in the receiving and data logging equipment. The data are then averaged into bins $0.1^{\circ}$ wide in the declination direction. Another set of bins are also created at this point. These are $0.8^{\circ}$ wide in declination and $0.1^{\circ}$ wide in right ascension and contain the median for that interval. From these bins a rough background will be found. $0.8^{\circ}$ was chosen because it reduced the amount of data considerably.

2.5.(ii) removing a rough background - because the maps cross at least $20^{\circ}$ of declination there is a background slope on the data. This is due to the radiation from the atmosphere at 2.3 GHz and radiation from the ground and telescope surroundings. This has to be removed. But there is also a receiver drift on the data, this has a slope of about 1 kelvin through the night. We have to be careful that while taking these slopes out we are not weighting the data, erroneously, in a preferred direction. The way in which we get around this is to remove a rough background first and then remove drift and then remove a final background after that. It is easiest to take the background slope off first because we know that that should depend on a sec $\delta$ curve because the atmospheric contribution (which accounts for about half the background) follows this type of curve. Removing background relies on the fact that in each observation there is 'cold sky' (i.e. sky which for practical purposes has no sources). Then the lowest point along a line of constant declination will represent one point on the background. Because there is noise on the lowest point we choose the n'th lowest point instead, in our case n = 10. A low order polynomial is fitted to this background and subtracted from the small ($0.1^{\circ}$) bins. From these bins a set of drift bins (bins from which we will find drift) are created. They are the medians of $1.6^{o}$ (declination) of data. $1.6^{o}$ was chosen because with a HPBW of $0.3^{o}$ $1.6^{o}$ is the smallest a median bin must be to exclude point sources.

2.5.(iii) removing drift - by drift we mean any unwanted contributions to the map which vary in right ascension. These include things like - satellites, rain, cloud and changes in the receiver gain. The philosophy behind removing drift is: assuming there is a good observation for every right ascension of a map, we can construct a map of wide dec bins which will be made up of only good observations. The difference between individual observations and this good, constructed observation is the drift for an observation then. If we assume the drift to be linear for a run, which is reasonable seeing a run lasts at the most 5 minutes, we can take medians along lines of constant right ascension. This improves the drift SNR. Note that in constructing our good observation we run a $0.8^{o}$ wide median in the right ascension direction. This smooths this good observation, also known as the median sky because of this filtering. Medians are the closest we can come to simulating humans in an automated approach. This is because the medians return an actual observed value (the most likely one), compared to means which smooth out the errors. The flaw in this method is that we are assuming we can use the observations themselves to provide a reference level, while at the same time we are trying to find their deviation from that base level. See sec 2.6 for more discussion on this.

2.5.(iv) subtracting the final background - once this final drift has been subtracted we should rebin the small bins into background bins. But this is not being done at the moment. Final background is being found from the original backround bins which still have a drift slope on them. An improvement to the data reduction would be to make new background bins. The fitted background is a sixth order polynomial, fitted in a least squares way to the background bins.

2.5.(v) combining the rasters - the original small bins are then read in, drift and background subtracted and then binned in 0.1 square degree bins. The bins are constructed by passing a running mean, $0.1^{0}$ wide, over the rasters. Care is taken to include the effects of bad tracking by the telescope. Tracking was so bad for some maps that the beginning of most rasters occurred on the adjacent raster. This was solved by allowing a longer settling time at the start of each run.

## 2.6 DISCUSSION OF THE RHODES MAPPING METHOD AND PROPOSED IMPROVEMENTS

The above method of mapping (which we will refer to as SKYMAP from here on, after the name of the program which drives the telescope in the above described raster scanning mode and logs the data) uses a faster scan rate than any other mapping methods I have read about. Yet it does not use less time than the other methods. A point to bear in mind though is that we are trying to achieve an rms noise level of 26 mK per 0.01 square degrees. In this section we will evaluate SKYMAP, compare it with other mapping methods and discuss flaws in its philosophy. The proposed method of removing some of these flaws is to compile a set of absolute temperatures of the sky on a coarse grid. We will also comment on how this grid of absolute temperatures (which will be referred to as "long scans" from the manner in which they are observed, see chapter 4) can improve SKYMAP.

The driving philosophy behind SKYMAP is automation. The original designers wanted to have as little human intervention in the data reduction process as possible. This was most probably because at any one time the amount of data being processed is enormous. I am not in favour of this because a machine cannot (even with the help of medians!) make informed guesses as well as humans can. The ideal would be to have a large machine at one's fingertips and then process the data interactively. This way data can be discarded and chosen intelligently. That is the philosophy of the data processing part of this thesis, except that one of the very essential ingredients of such a system, an interactive graphics display, was not available while working on this thesis.

The main way in which SKYMAP differs from other mapping techniques is that the scans are not tied down to any reference level. This is also its main disadvantage, because by relying on the 'good' observations to provide a median sky we end up with an arbitrary and fluctuating zero level. This is evident as false slopes on the resulting map. There is one which always occurs in the early part of the evening and is referred to as the 'sunset effect'. This particular slope is the result of the telescope structure and surroundings cooling down after sunset during the early part of an observation, which affects the background contribution. It also means that the drift found is not the 'true' drift, i.e. deviation from the true sky brightness. It is the drift from the median sky. Consequently the data on the final maps are the means of observations with incorrect baselevels. One saving factor is that the median sky is heavily smoothed with a $0.8^{o}$ wide median. This means we haven't added any small features to the map. These slopes are on a large scale (about $15^{o}$ in right ascension and right across a map in declination). Consequently if we have a set of absolute temperatures for the sky on a coarse grid then we could find the true drift for the existing observations. If we subtract this from the existing maps we will have a set of correct maps.

For comparison let us take a look at maps which have been constructed from scans which have been referred to a fixed point in the sky, like the south or north celestial pole (eg. Haslam(1974)). Firstly these methods are more efficient. For one thing they don't waste a night's observation if some of the scans in a night are bad. Compare this to SKYMAP which, because it uses the observations themselves to find a median sky, cannot tolerate more than 1 or at most 2 hours of spoilt data in a night. Otherwise the median sky is a median of only 2 observations over this spoilt part, which would be a mean. This means that during the summer observing period, when the Transvaal experiences thunderstorms of 2 to 3 hours and then clears up again, up to 6 good hours are thrown away. It has also meant that the summer maps need many nights to complete, and in some cases (take for instance 40 degree wide maps, which need 24 nights) it is doubtful if they will ever be completed! If we found drift from an independent set of observations, which we could be sure were free of drift, then firstly we wouldn't need 3 repeats of every raster and secondly we wouldn't have to waste half-nights of good data.

Instead of going to a reference point, like one of the equatorial poles, maps have also been made by having a reference scan at each end of the region being mapped. These reference scans are in turn referred to a single point which has been previously calibrated. This is how Berkhuijsen (1971) observed the 840 MHz map. Using this method a more accurate drift than the drift SKYMAP finds can be found for each night's observation. But to correct SKYMAP using this method would be too much work for the existing SKYMAP data. SKYMAP wasn't designed with this in mind and consequently the scan endpoints, i.e. the map edges, have not been optimally chosen. Even if we did construct reference scans at all the map edges, finding backgrounds for these and removing drift would involve more work than the proposed method of "long scans". Also the long scans provide a lot more reference points for the SKYMAP maps and thereby provide a more reliable base level.

SKYMAP has its good points too. Most mapping techniques need to calibrate the system gain at least every few hours. With the self calibrating radiometer which we used we only need to calibrate at the start of a nights observation and at the end. This is borne out by an evening's long scan observation during which the system was calibrated every 10 minutes by firing the noise tube, the result (see fig.4.2) shows there to be no systematic drift in the system's gain through the night. Another good point about SKYMAP is the impulsive filtering method employed. The raw data written to tape will always have impulsive noise. This could be the result of a transient in the data communications lines or a pigeon flying through the beam, on its way to its home in the telescope girder structure! Or any other unpredictable impulse. These must obviously be removed because in the frequency domain they have an infinite power spectrum and can cause a lot of damage. Haslam (1974) uses a spike removing digital filter, but this is not sufficient because power in the low frequency wings of the impulse still creeps through. Our method of medians used in the initial binning process is easier, faster and affects the data less, but can only be used for heavily oversampled data.It must be remembered too that when SKYMAP was designed the telescope could not scan down to the south celestial pole. Consequently there was not a reference point in the sky to which scans could be referred. This explains why the described mapping method was developed and not one of the other methods which have been described chosen. Haslam et al's (1974) method would most probably have been chosen if the telescope had been able to scan to the south pole at the time the survey was started.

At 2.3 GHz we are looking at very low brightnesses. This is because the nonthermal radiation has mostly fallen off by this point and the thermal sources are not at very high temperatures. Because of these low brightnesses we are trying to achieve a low rms noise on the maps. This means repeats of observations are necessary. They improve the signal to noise ratio. But they will be of more value i.e. actually reduce the noise, if they have the right drift subtracted. The 'right drift' can be found by referring the observations to the grid of absolute temperatures. Finally the scanning effects produced by scanning at fixed right ascensions are (to my mind) more noticeable than those produced by nod scans, see the 408 MHz survey (Haslam et al (1982)). This is because nod scans have scans crossing each other diagonally and therefore they have more points in common. With the addition of "long scans" there is also going to be a grid of crossing points (a crossing point is where a long scan and a bin on a map intersect) between the long scans and the observations. This will allow the observations to be pulled more effectively onto a single baselevel and they will then combine into a more accurate survey i.e. with fewer scanning effects.

# CHAPTER 3

## A GRAPHICAL PRESENTATION OF THE SOUTHERN SKY AT 2.3 GHZ

### 3.1 INTRODUCTION

The Rhodes survey has been going on for 5 years now. In telescope time it has meant 350 days. The results have been good so far. Of a total of 43 200 square degrees 12 330 have been completed and there are preliminary results for a further 7 380 square degrees. Now that we have results we need to interpret them. But before we can interpret them we must manipulate and display them in such a way that they yield maximum information. This is of prime importance in a survey of this kind where we aim to have 3.25 million data points in the final map. This chapter will present these techniques and their results.

The layout of this chapter is (1) a description of the observations - when they were observed and by whom and notes on any special processes used to obtain the final map in each case, (2) a discussion of display techniques and a graphical presentation of the results.

### 3.2 OBSERVATIONS

The data presented in this chapter were observed as 3 separate maps. The first covers the region 12 hours to 22 hours right ascension and declination $-63^{\circ}$ to $-24^{\circ}$. It will be referred to as A14D63. The second covers the region 4h30 to 15h right ascension and $-80^{\circ}$ to $-61^{\circ}$ declination. This map will be called A04D80. Finally there is a map of the region right ascension 13 hours to 22 hours and declination $-26^{\circ}$ to $-7^{\circ}$. This is known as A12D26. We will now mention each of these in turn, discussing how they were obtained and present a greyscale of each.

A14D63

This map was observed by Justin Jonas and has been described by him (Jonas (1982)). In this section I would like to summarise his observations because they comprise half of the full data set which is discussed in chapters 5 and 6.

The observations were made over a period of 2 months, starting in June 1980. These are winter months and very good observing nights - because the sky is so clear. The declination range was $-63^{o}$ to $-24^{o}$. The right ascensions of the observations ranged from 10h30m to 24h. An hour of data is always thrown away at the start of each observation. This is because the telescope structure and its surroundings are still cooling down during this period and consequently any observations done have an extra component of emission. This is hard to eliminate from the data if there isn't a set of references scans from which to obtain a correct baselevel. In future, when we have a set of absolutely calibrated scans from which to derive drift it will not be necessary to throw this hour of data away. Therefore the final A14D63 stretches over 12h to 23h right ascension.

To cover the required range of declination 8 interleaved rasters of 3 repeats each (i.e. 24 nights) are needed. One of these repeats was bad and after many attempts at fixing it was eventually discarded. Therefore 23 nights of data were combined to make this map. What is noteworthy is that this is the last map to be observed with precession. To observe with precession means to observe the map in 1950 coordinates i.e. the map is a square grid in 1950 coordinates. The effect of precession is to make a straight line in 1950 coordinates (say a line of fixed right ascension) skew in present day coordinates (if the present day coordinates are sufficiently far away from 1950, eg 1980). This meant that a night's scans did not pass through the same telescope coordinates throughout the night, because each right ascension and declination gets skewed slightly differently in precession (i.e. differential precession across the map). Finding reliable backgrounds for up and down scans relies on all the up scans passing through the same telescope coordinates and similarly for the down scans. But the backgrounds for these precessed scans were not all the same, they were time-dependent. Thus the backgrounds found were incorrect. This meant the observations had residual offsets added to them when they were combined. These were very evident as scanning effects.

These were removed in a highly specialised and unique manner. A widely spaced ($0.1^{o}$ in right ascension and $5.5^{o}$ in declination) median sky was created from the combined rasters. This was heavily smoothed to remove the varying base levels of the combined rasters by passing a running median of $1.6^{o}$ across right ascension. Then the original observations, with drift and background removed, were compared to this median sky. Differences were found at all the points in common (7 per $0.1^{o}$ of right ascension). In the galactic plane where steep gradients and structures smaller than $1.6^{o}$ in right ascension exist none of the process described here was performed. A linear profile was fitted for each scan to the differences found and subtracted from the individual observations thereby bringing them onto a common baselevel. The end result is depicted in galactic coordinates as a grey scale in figure 3.1. Scanning effects are still visible close to the plane but all those at $|b|>10^{o}$ have disappeared. If the data are enhanced in any way so that a lower envelope is subtracted from the data, like subtraction of a plane contribution, these scanning effects become even more visible.

What has been done to the data by this process? One dreads to think! But if the observations which composed this map were good (which they are because they were observed in winter) this is a similar process to finding drift as

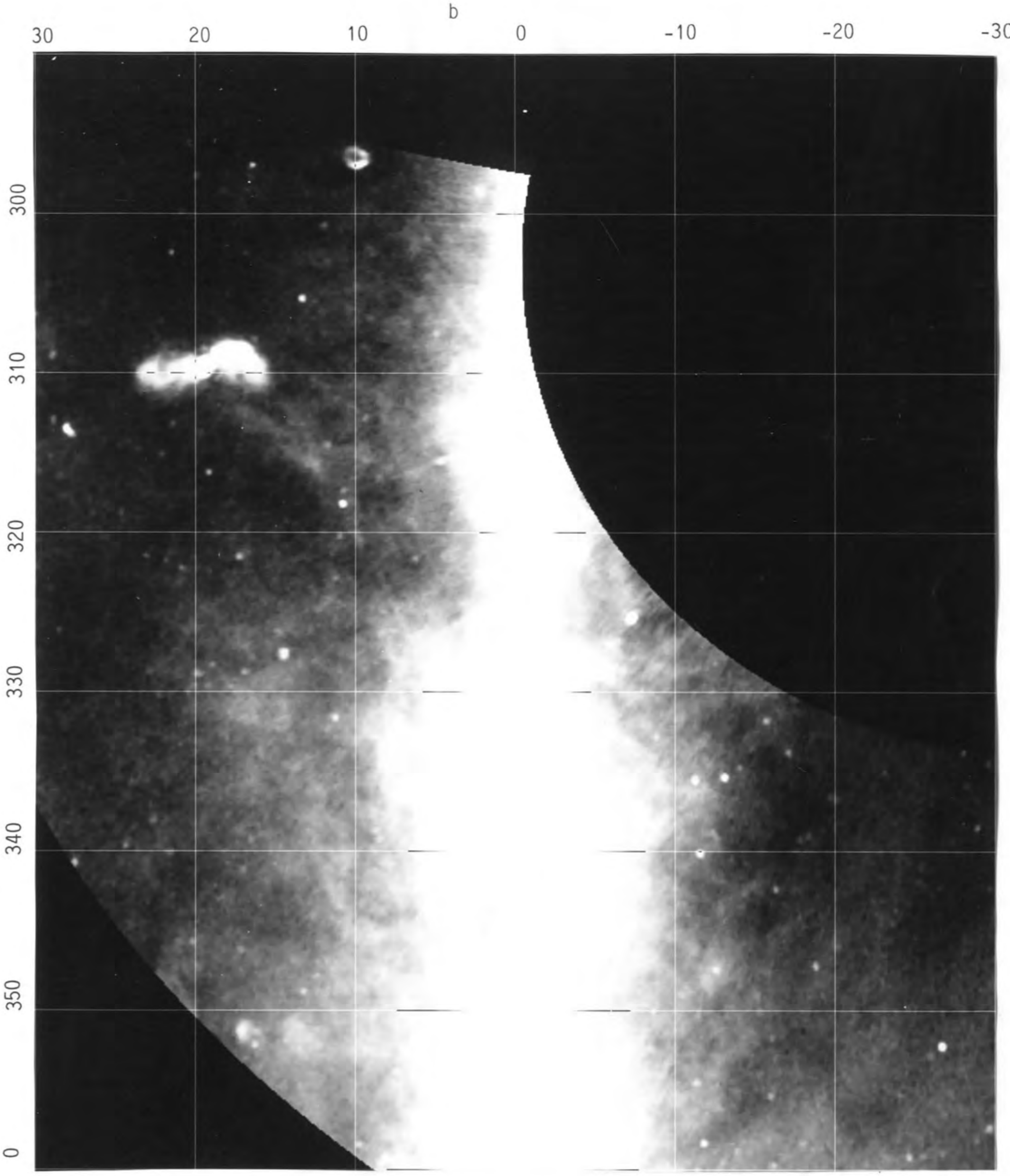


fig. 3 .1 grey scale image of the region 12HR - 23HR (RA) and -63 - -24 (DEC) in new galactic coordinates it is done in the data processing programs (cf. section 2.5(iii)). The difference being that it was done in both the declination and right ascension direction by the above process. A14D63 is an example of how much a map can be altered when drift is subtracted in both directions i.e. right ascension and declination. This must be borne in mind when we eventually come to putting the maps onto a correct baselevel. In conclusion we can say that the baselevel of A14D63 is arbitrary.

A04D80

This map covers the region 4h30m to 15h30m right ascension and $-80^{o}$ to $-61^{o}$ declination. It was observed in March of 1982. Because of the smaller declination range only 2 rasters are required for this map. Therefore with 3 repeats necessary we need 6 nights of observations. All in all 7 nights were observed. I did 5 of them and the staff at RAO did the other 2. Having 7 observations meant there were 4 repeats of one raster and 3 of the other. I tried processing the data like this but found that the median sky was heavily weighted towards lower values for the raster with 4 repeats. This was because the way in which medians were found was to take the lower one of the two middle values for an even number of points and the middle one for an odd number of points. This has since been changed so that the median of an even number of points is the mean of the middle two. At this point one observation was thrown out leaving 6. Unfortunately one of the observations of the raster with 3 repeats only had rain on it. The rain ocurred over the right ascension range $100^{o}$ to $114^{o}$. The first version of the map had a thick stripe of enhanced emission starting at 106.8 degrees right ascension. At first it was thought to be the effect of the rain. But it lies in the middle of the rain! To remove all doubt I excluded the observation with the rain completely and reprocessed the map. This time medians were found in the modified manner described above. The final map obtained using the remaining

5 observations is the one presented in figure 3.2 and in appendix 1. It still has a stripe on it. This feature will be discussed in section 5.2 with region F.

Telescope tracking for this map was very bad and the first time the observations were combined into $0.2^{o}$ bins (instead of the usual $0.1^{o}$ bins because the map lies at such a low declination) there were a lot of empty bins. This was corrected by convolving the data with a $0.3^{o}$ wide top hat in right ascension. The effect of this on the data can be estimated by looking at figure 3.4. When the data is combined in the final process (see sec. 2.5(v)) it is achieved by putting the mean of all the data which fall within $0.05^{o}$ of each bin. This is equivalent to passing a running mean of width $0.1^{o}$ over the data. In the transform domain this is the same as multiplying the transform of the data with a sinc which has its first null at 10 reciprocal degrees. Ideally the data in the transform domain consists of the transform of the brightness distribution of the sky multiplied by the transform of the antenna beam pattern (see figure 2.2). Therefore the effect of binning the data is to attenuate the high frequencies in the data slightly, and the effect of widening the bin width is to attenuate the high frequencies even more. Binning with a running mean of $0.2^{o}$ as was done for A04D80 is equivalent to multiplying in the transform domain with a sinc which has its first zero at 5 reciprocal degrees. Figure 3.4 depicts a cut through the transform of the beam and through sincs which have zeros at 10, 5, and 3.333 reciprocal degrees. From this we can estimate the degree of smoothing introduced by using different binning widths.

The background found for this map was mainly from one area in the sky - the region 8 hours to 10 hours. This is one of the coldest parts of the sky and consequently yielded good backgrounds. The fitted curves to the background


fig. 3.2 grey scale image of the region 4H30m - 15HR (RA) and -80 - -61 (DEC) in equatorial coordinates

had a maximum rms error of 10mK. The drift for each observation was smooth, containing no bumps smaller than 1hr. The drift amounted to a maximum of 250 mK for each night which shows that the observations are good. In conclusion we could say this map is accurate but could maybe do with a repeat of the one observation with the rain on it. This will improve the map over the region of enhanced emission and yield more reliable quantitative results for this region.

A12D26

This map covers the region right ascension $190^{o}$ through $0^{o}$ to $14^{o}$ and declination $-26^{o}$ to $-7^{o}$. It required 4 rasters which means 12 observations, with repeats. Observations were done by me in June 1982. This map is a very good example of how medians can remove outliers without contaminating the data too much.

This was necessary because these observations were observed with a faulty radiometer. The fault showed up in the form of lots of noise on the output. Because this fault was time dependent (it would occur for up to 10 samples and then recover) it showed up as a variation in declination. These faulty values will be referred to as dropouts. Of the 12 observations 7 had a few dropouts ( ~ 10%) and 1 had many dropouts ( ~ 33.333 %). We expect these to show up (if at all) in the final map as scanning effects because they occur along scans. These are not visible on the final map and this shows that the SKYMAP method of mapping is resistant to noise which occurs randomly over a few declination bins in a scan.

The median sky for A12D26 was compiled out of 8 of the 12 observations. 5 hours of two of the observations were thrown out because of rain. The median sky was smoothed using a wide gaussian shaped convolution filter which had a HPFW of 0.67 degrees. This was in an attempt to smooth the drift. Drift is the difference between the drift bins of each observation and the median sky. Therefore smoothing the median sky should smooth the drift. The effect was only slightly noticeable because after finding the differences a median in declination is passed over these differences. The final map was combined using a running mean 200 mdeg wide in right ascension to cater for bad tracking. See figure 3.4 and the discussion at the end of A04D80 for the effect of different binning widths on the resolution of the data. The transform of a running mean 200 mdeg wide drops to half the peak value by the time it reaches 3 reciprocal degrees. This smoothing is not unacceptable in the final map but must be quoted in the final survey.The final map of A12D26 is presented as a greyscale photograph in figure 3.3.

## 3.3 DATA ENHANCEMENT AND PRESENTATION

The maps above represent real signals which have been digitally processed. The processes by which they have been produced are fairly well defined and consequently we also know what has ocurred to the data in the Fourier transform domain. This section on enhancing the data describes various techniques and one-off methods that were developed and used in this thesis to modify the maps. There are two basic classes of modifying processes. Firstly those that change the data quantitatively. They are based on physical knowledge of the data and use this information to enhance certain features on a map. Some filtering techniques like low pass filtering are examples of this class. Secondly there are programs which affect the data quantitatively and enhance it only qualitatively. These are mainly programs which display the data. For instance when using a greyscale to display a map the program can enhance certain aspects of the data by choosing a certain set of greyscale levels. If these levels are changed the map can take on a different appearance. But the data are not changed for quantitative analysis purposes, only their qualitative appearance alters. In certain processes the

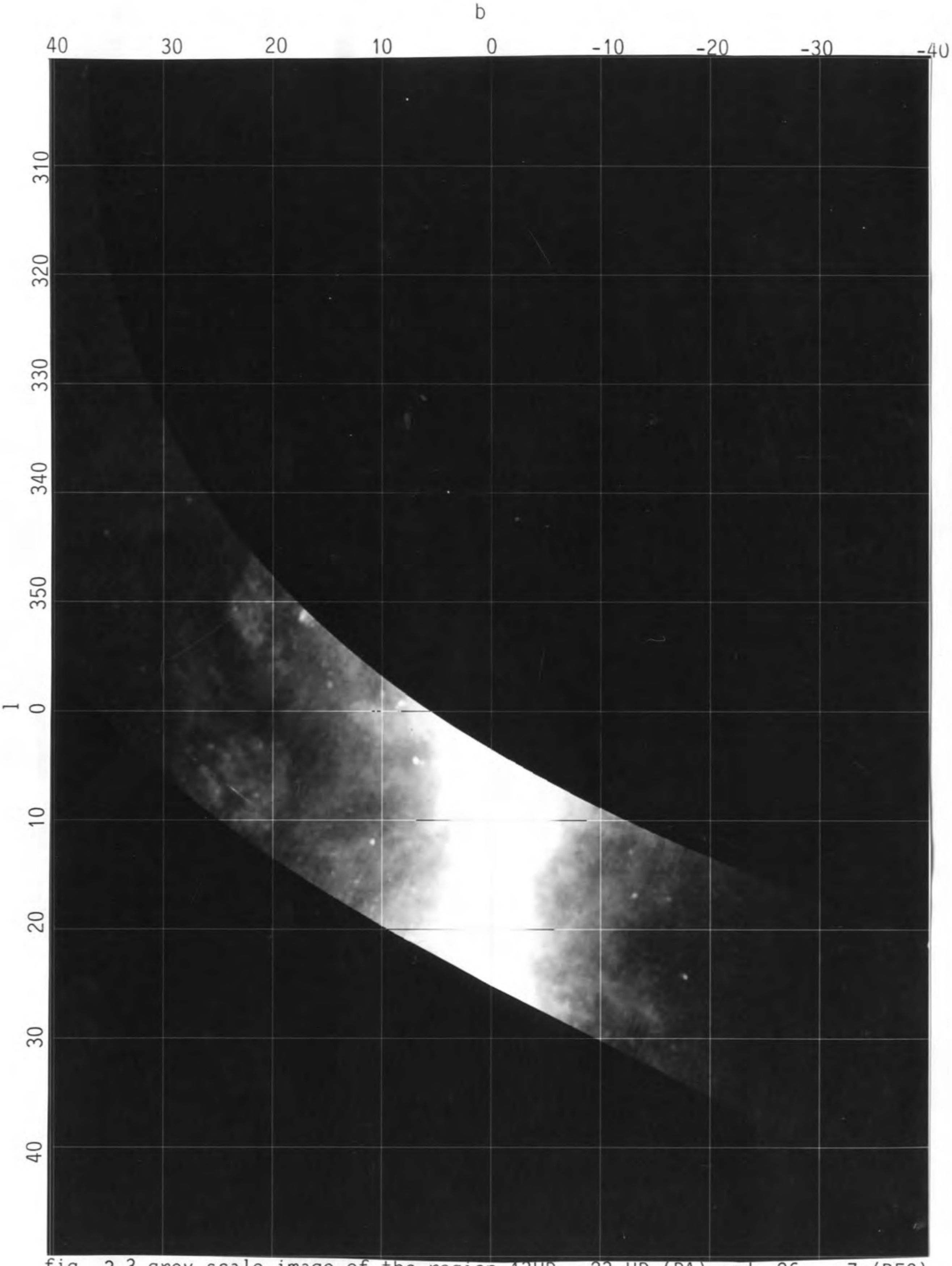


fig. 3.3 grey scale image of the region 13HR - 23 HR (RA) and -26 - -7 (DEC) in new galactic coordinates

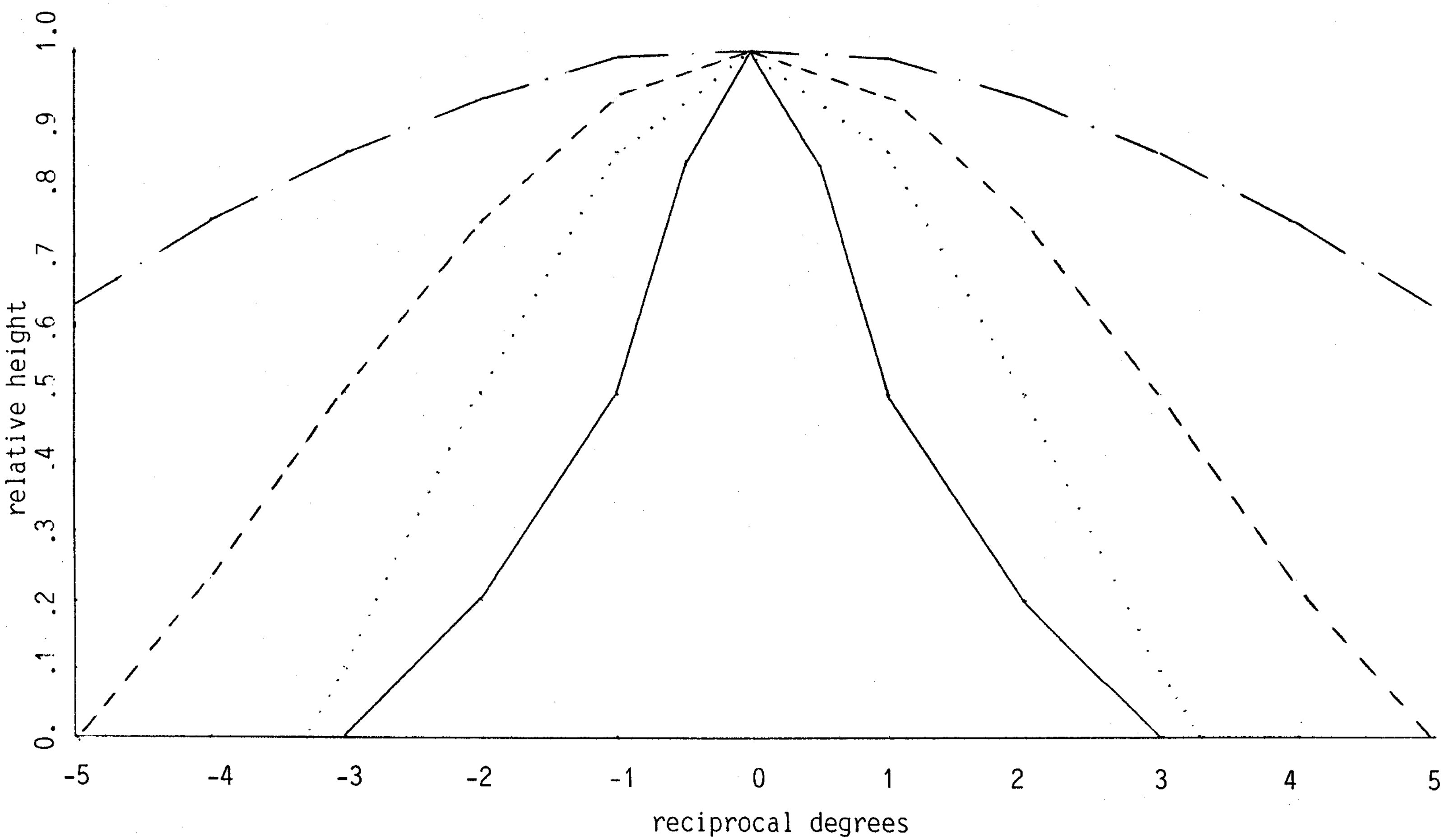


fig. 3.4 one dimensional cuts through Fourier transform of beam pattern (---) and top hats of half width 0.1° (-·-), 0.2° (---) and 0.3° (...)

data are not even affected quantitatively but only qualitatively. An example of the last is rotating the colours of a lookup table of a colour screen.

A lot of effort goes into displaying the data in suitably revealing ways - this means revealing the galaxy but not the scanning effects. Allen (1979) has discussed methods of effective data display for astronomical data and come up with the following criteria - (i) if the data consist of a modest number of beams, $10^1$-$10^3$, then contour and hide plots are sufficient. But if (ii) the data cover more than $10^3$ beam areas and/or there is a high dynamic range then grey scale and pseudo-colour are more illuminating. The images in this thesis followed the above criteria with success. For instance in the appendix, where the maps are small, they are best represented as a set of contour maps. Whereas the big joined maps, which cover vast areas, are best presented as grey scales and in pseudo-colour. One further criterion not mentioned by Allen (1979) is the use of colour when there is a small dynamic range. This is most useful for enhancing extended low brightness regions above the background, because the eye can easily distinguish small changes in colour.

A large part of the astrophysical interpreting done in chapters 5 and 6 depends on programs which displayed, manipulated, measured and joined the three data sets. This section will now describe the programs used to do this. It has been organised under three broad categories - (i) the programs which used grey scale and/or black and white (BW) displays only, (ii) the programs which used colour displays, (iii) and finally the programs which used knowledge of the data (eg. subtracting the galactic disk component) to enhance the data. Some of the techniques described in section (iii) are data processing techniques which alter the appearance of the data both in the spatial domain and the transform domain. To enable us to evaluate to what extent the data are affected these techniques have been applied to a test set of data - the beam pattern of section 2.2.1. This beam represents the antenna's response to a point source (Tau A to be specific). Studying the effects of these techniques on this beam will tell us by how much the spatial resolution of the data has been affected. Thereby we will know how the main beam brightness has changed and how point sources have been affected on the resulting maps. This applies to both the linear and non-linear techniques used.

### 3.3.1 Black and White Displays

Lacking a high resolution colour graphics display VAX VT-100 terminals, with the graphics option (the MATROX GT600 plugin board), were used instead. An interactive graphics package called IMAGE was developed for use on them. This package allows the user to interact with the data, display it, find sources coordinates and measure fluxes. Displays could be contour plots or a 2 bit plane grey scale. The grey scale option allows one to choose three cutoff levels R, G, and B. IMAGE then displays everything < R as 0, everything >= R but < G as 1, everything >= G but < B as 2 and everything >= B as 3. This is a similar process to histogram equalization and stretching. It is very useful for finding the extent of a source and for showing up a low brightness feature above the background. The flux measuring program is only effective for small diameter sources because only a single background temperature is subtracted. To measure the flux of a larger source one would want to fit a more complicated surface for the background than a plane, normal to the temperature dimension. Even with this limitation the flux measuring option is useful because the choice of the source extent is done interactively with the cursor. The source finding option has proved to be the most useful though - mainly because it is accurate and quick.

IMAGE has helped to speed up map interpretation but suffers from lack of resolution and speed. The VAX/11-730 on which it runs is very slow and can be quite frustrating at times. There are plans to put STARLINK (Disney (1982)) onto this same VAX/11-730 (the smallest in the VAX range). If this ever happens the VAX operating system, VMS, will battle to make headway. Notwithstanding this an interesting observation as regards an image processing environment can be made - having used both STARLINK at the South African Astronomical Observatory (SAAO) and IMAGE I think an equivalent system to STARLINK but using only a BW display instead of a colour one would be most suited to interpreting the data described in this thesis. Colour is of no quantitative use. We can go even further and say colour contains too much information and serves to enhance the spatial frequencies in the data which are above the spatial frequency cutoff of the data. Consequently we are actually being disinformed by colour rather than informed. The one ability of colour to enhance low brightness features can be done by histogram equalization.

Other work in BW displays involved modifications to two existing programs. One was the program which allows grey scales to be printed on an EPSON MX printer. This was modified to allow coordinates to be drawn on the image. The pictures produced by this program (which have only 25 grey levels) are only really useful for showing up gross features. This usually means very bad processing defects. The coarse grey scale used is more discriminating than contour plots which tend to smooth the features on the data. As far as assisting in the astrophysical interpretation, the grey scales produced by this program are almost useless.

The second program which was altered was the program which produces tapes for an OPTRONICS machine which makes photographic negatives. The images produced by printing these negatives are the best display medium we have.

They have a very high resolution - a pixel size of 100 microns, and their dynamic range of 256 is more than sufficient for the human eye (which can only differentiate approximately 30 levels). This program was rewritten for displaying the grey scales presented in this thesis and a routine was added which overlayed a grid on the data. This allows sources to be found on the image and generally improves its usefulness. Figures 3.1 to 3.3 illustrate what can be achieved by this method. OPTRONICS pictures are good for intermediate and high galactic latidude features because of their high dynamic range but they are not of any use in the plane of the galaxy because of saturation problems.

### 3.3.2 Colour Graphics

Colour graphics are very popular nowadays but need to be treated with caution. This section will comment on the experience obtained while working on STARLINK at SAAO and its implications for SKYMAP should it ever get installed on the Rhodes VAX.

Colour is powerful because the human eye has the ability to distinguish millions of different colours but only 30 (typically) shades of grey. But the effect of colour is devastating. It has the power, in the worst instance, to make a feature which is 1 mK above the background stand out completely. This can create features which do not exist. I agree it is useful for enhancing the edge between 2 regions but it is best ignored in the initial and intermediate stages of map interpretation. Consider the example shown in figure 3.5a and 3.5b. A comparison of a greyscale picture of the Zeta Ophiuchi nebula and a colour picture of the same shows how features can be created by colour. Once a feature has been shown, reliably, to exist on a map only then should colour be used to enhance it even more.

The colour images used in this thesis were obtained on the STARLINK image processing system. This is a graphics environment which runs under VAX VMS and has been specifically developed for astronomers. See Disney (1982) for a description of STARLINK, its history and operation. I spent three weeks working on STARLINK but I did not do any quantitative analysis on it. It was used mainly as a colour display to obtain pretty pictures.

The following are some comments on using STARLINK to display SKYMAP images. The most useful way of displaying maps it was found is to display their natural logarithm. This displays the low brightness features as well as the general outline of the high brightness regions like the plane. The big limitation of the colour displays of the SKYMAP data is the colour lookup table (LUT) used. This particular LUT saturates in black after every colour

(a)

fig. 3.5a greyscale photograph of Zeta Ophiuchi nebula

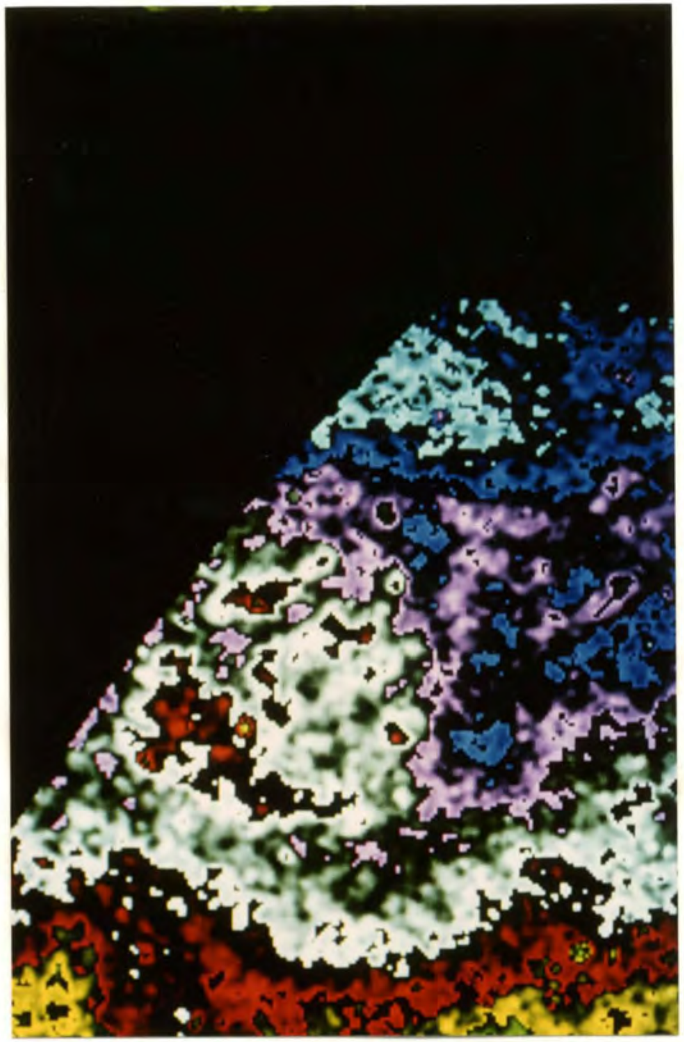

(b)

fig. 3.5b colour zoom of fig. 3.5a

has reached maximum brightness (cf. figure 3.5b). This produces horrible edge effects after the maximum of each colour. The solution to this would be to use a LUT which has the colours running continuously from one into the next. This is possible on STARLINK with the PALETTE command. A refinement on this would be to tailor the LUT so that each colour covers a range of temperatures which is astrophysically significant. The range of temperatures which is astrophysically significant will depend on the type of astrophysics being done. Some of the stochastic filtering methods were tried but they did not seem to provide uniquely meaningful results. We would have to take a closer look at the mathematics of these programs though.

Besides the programs on STARLINK which display data we have or will have to develop most of the analysis programs we need. STARLINK will not change the initial reduction process of SKYMAP maps - a high speed interactive graphics device would. But it will greatly facilitate the handling and analysis of the finished maps. This is because it provides an environment in which a suite of programs can be used on a number of different devices in a manner which is invisible to the user. This allows one to think of the data per se and what it means instead of seeing the data via a different program every time one changes terminals or computers. This latter approach mostly serves to create a disjointed view of the data.

STARLINK has not been implemented at Rhodes yet because there was not a graphics device worth doing it for.

### 3.3.3 Image enhancement

The techniques to be described here have used the knowledge of what the image represents to improve its SNR or to enhance a certain aspect of the image. The techniques have been separated into two broad categories - first the conventional filtering and transform techniques will be described. Each of these techniques will be applied to the beam pattern of section 2.2.1 so that the effects of these techniques on the data can be studied. The second category will cover techniques which are not so general and apply specifically to continuum radiation.

Running Median Filter : (we will refer to it as the 3-S filter for short) when the observations are combined into one map in the last step of the data processing they contain a lot of random noise. One of the types of noise is evident as a lot of single spikes distributed throughout the data - also known as salt-and-pepper noise. I think it is a result of combining observations with incorrect offsets - which (as discussed in section 2.6) is the result of finding drift by using medians. The running mean used to combine the observations does not smooth these out because it is too narrow in right ascension and not applied in declination. A running median filter is used to remove this noise. The filter, after Tukey (1977), works as follows : each point is replaced by the median of the 9 points centred on it. This is done by applying a running median of 3 first along bins of constant declinations and then along bins of constant right ascension. Note that this is not the same as a box median (i.e. finding the median of the 9 points simultaneously) and actually yields different results.

The effect of this is to remove spikes and leave in sources. The effects of this filter in the transform domain are unknown. De Jager (1983) maintains the effect of 2-D median filtering depends on the degree of oversampling, but this has not been shown conclusively yet. Without using analytical techniques we can observe what this 3-S filter does to the data by applying it to the beam of section 2.2. The results of applying a 3-S to the beam have been plotted in figures 3.6a (the beam) and 3.6b (its transform). What is evident in the space domain (fig. 3.6b) is that the noise has been reduced i.e. the beam is smoother than the original beam. As expected the top of the beam has been chopped off and it has a flatter top now. But what was not expected and is worth commenting on is that the round sources on the beam appear square after the 3-S. In the transform domain we find that a notch has been introduced in both dimensions at approximately 2.9 reciprocal degrees. This seems to be repeatable and dependent on the sampling rate in the space domain. Because when the original beam, for which $\Delta\alpha = .0357^{o}$, was processed with a 3-s filter, it also produced notches in the transform domain except that they were further out on the reciprocal right ascension axis. It appears that the relation between the sampling rate and the notch is almost linear. However, more work needs to be done in this region to determine the exact effect in the transform domain.

The whole idea of 3-S filtering is not very satisfactory because not only does it affect the data in the above observed manner but it also lops of the peaks of the sources. To get around having to use this median filter I tried to reduce the usual salt-and-pepper component in the data. This involved smoothing the median sky (see section 2.5) with a gaussian convolution filter of HPFW=0.67 degrees. But although this provides a smoother baselevel from which to find drift, drift is still being found for each observation with medians. The best way to remove this noise would be to find drift from an absolutely calibrated set of scans without medians. This is what chapter 4 attempts to do.

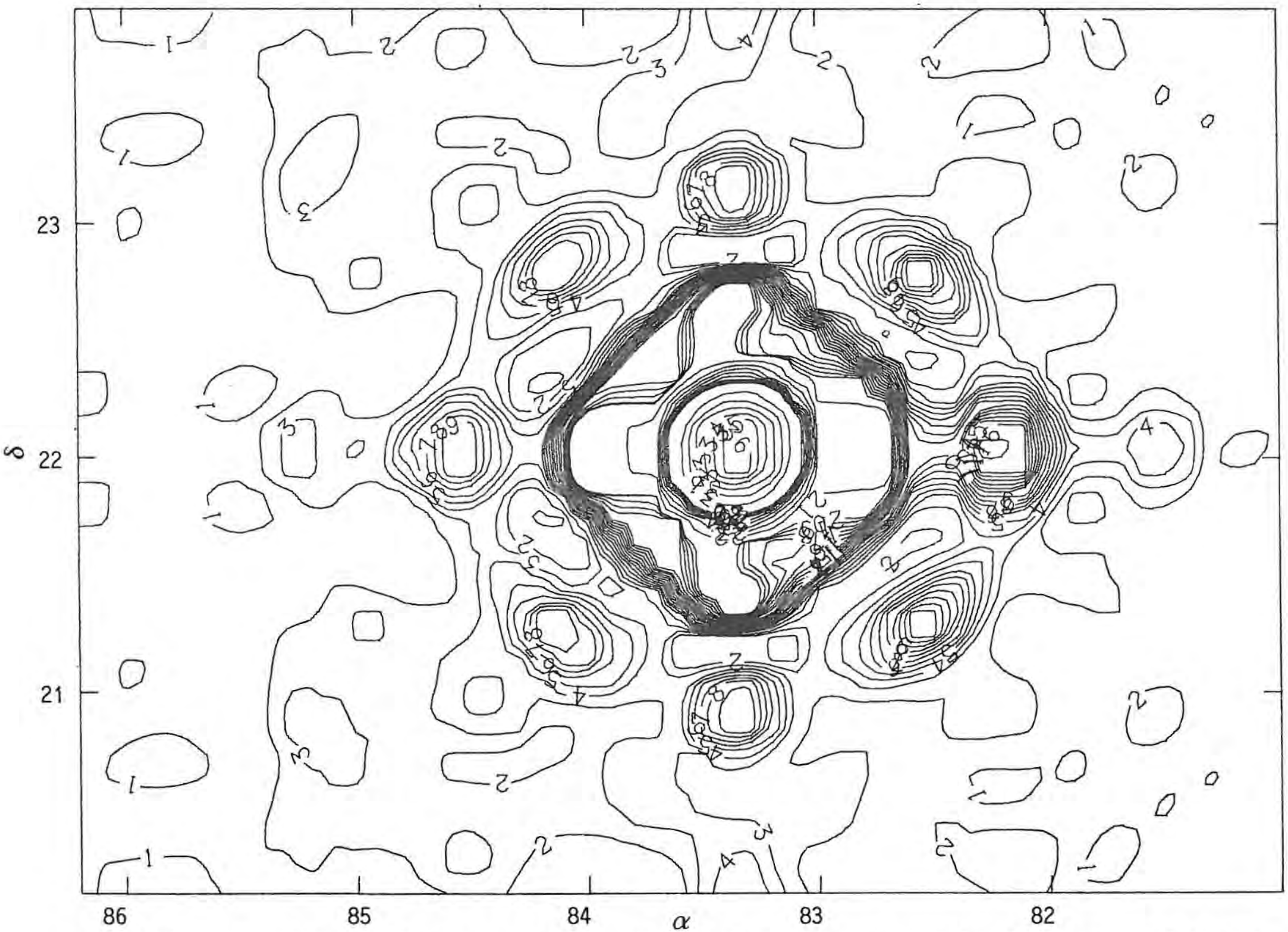


fig. 3.6a median filtered (using a running-median-of-3) beam pattern of fig 2.1, contour labels in app. 3

3.6a

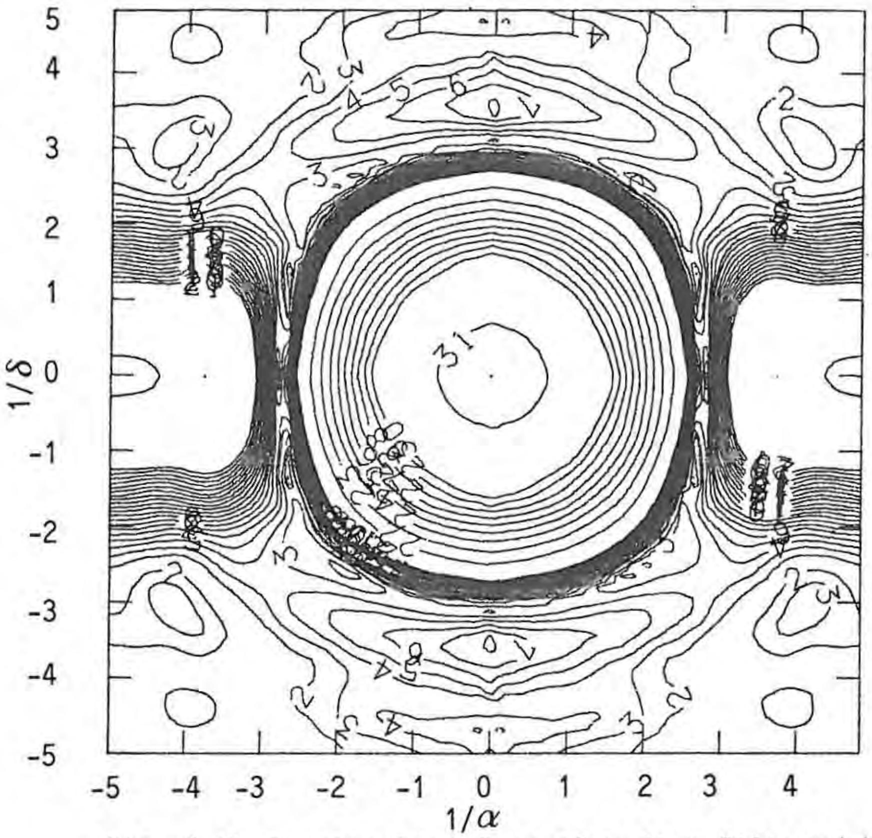


fig. 3.6b Fourier transform of median filtered beam in fig. 3.6a, contour labels in app. 3

2-D Convolution filter : after applying medians to the data initially, one of two linear filtering methods was available for limiting the noise on the maps in the spatial frequency domain. These were the convolution filter and the Fourier transform sharp cutoff filter. The convolution filter has the advantage over the Fourier filter in terms of computing because it does not require all the data to be in memory at one time (note this is not a limitation when using a computer which supports virtual memory).

The program was implemented by Jonas and has been described in Jonas (1982). It convolves the data with a 2D gaussian of halfwidth 0.2 degrees. The program takes care to widen the base of the gaussian in the right ascension direction as it moves away from the equator. The reduction in noise therefore depends on the declination of the map and decreases as follows

| declination | factor noise is reduced by |
|---|---|
| $0.0^{\circ}$ | 2.13 |
| $10.0^{\circ}$ | 2.14 |
| $20.0^{\circ}$ | 2.19 |
| $30.0^{\circ}$ | 2.28 |
| $40.0^{\circ}$ | 2.43 |
| $50.0^{\circ}$ | 2.64 |
| $60.0^{\circ}$ | 3.01 |
| $70.0^{\circ}$ | 3.63 |
| $80.0^{\circ}$ | 5.10 |
| $89.0^{\circ}$ | 16.07 |

The effect of the convolution is to broaden the beam from $0.34^{\circ}$ to $0.40^{\circ}$. This filter is useful for filtering maps in which there are sharp edges, like when sections of the plane have to filtered and they have been cutoff somewhere in the plane. The sharp cutoff Fourier filter is not much use in these cases because it rings in the space domain.

To demonstrate the effect of the convolution filter we have applied it to the beam pattern. The results are shown in figures 3.7a and 3.7b. The noise is considerably down and the sources nicely rounded (fig. 3.7a). In the transform domain the beam has been gently tapered down to zero.

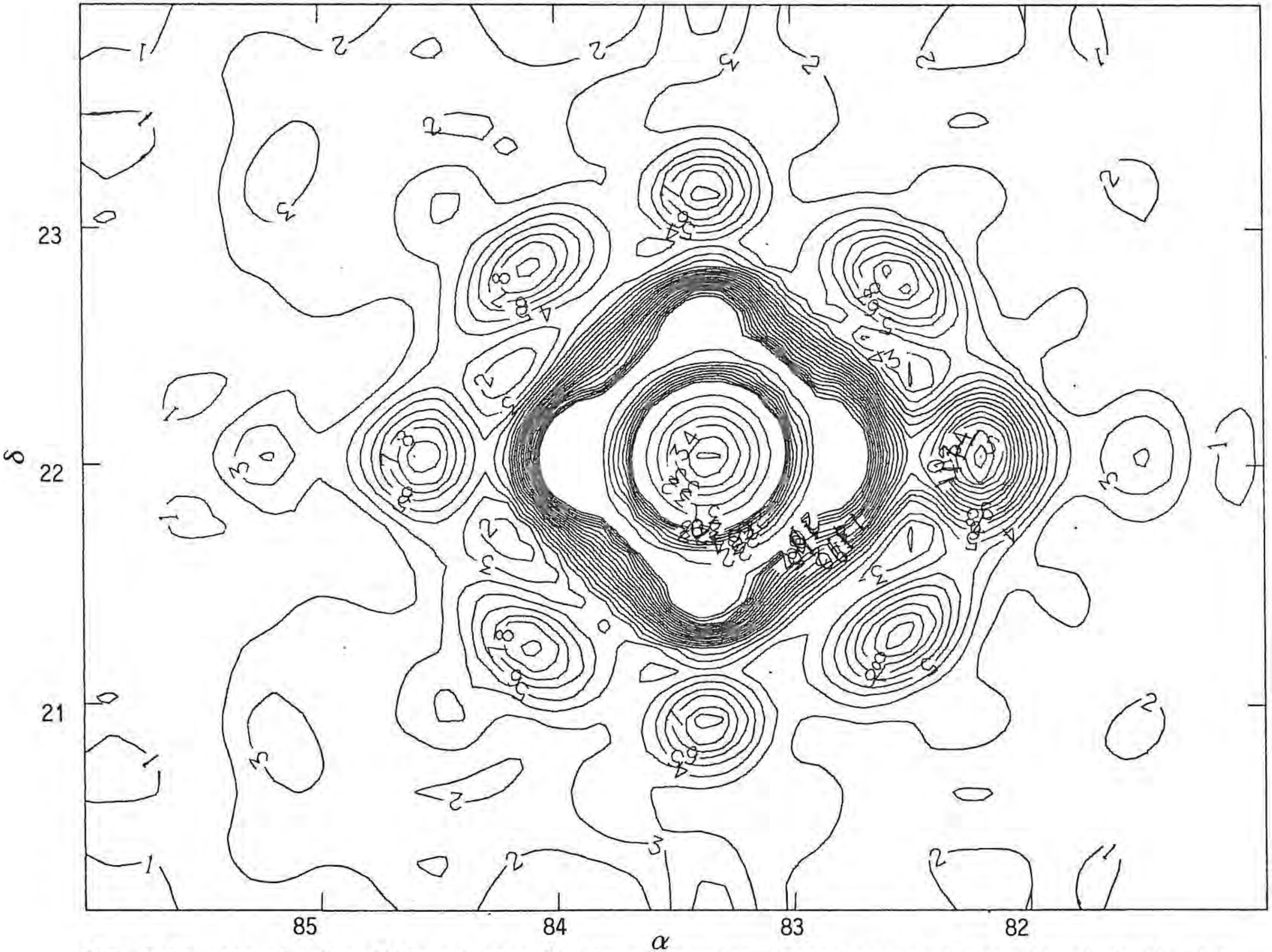


fig. 3.7a convolution filtered beam (using a gaussian shaped convolution filter) of fig 2.1 contour labels in app. 3.

3.16b

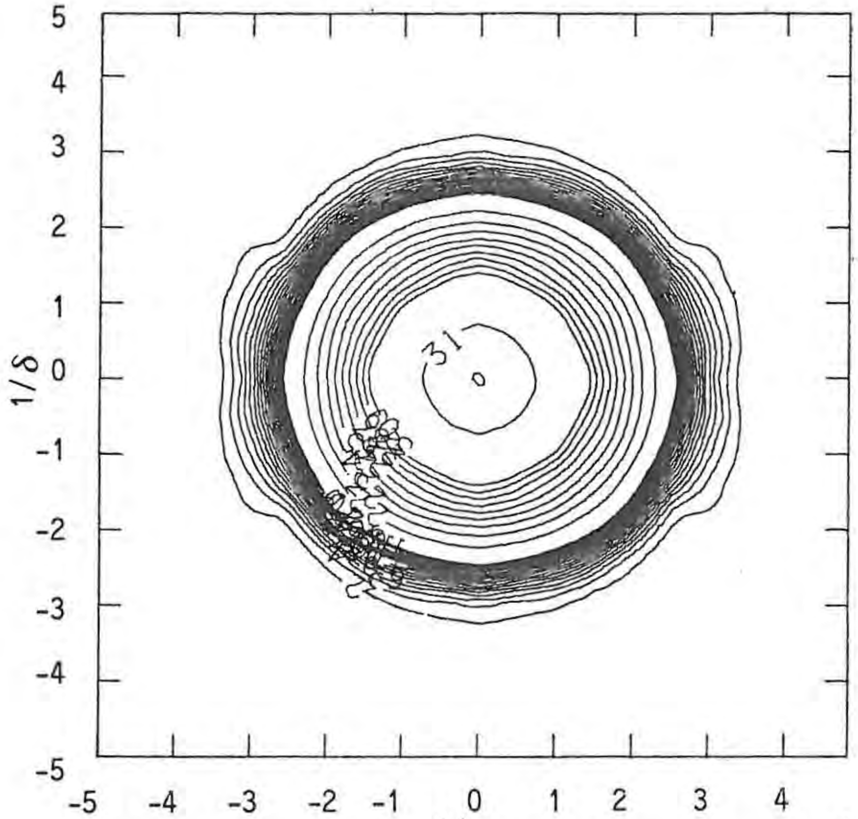


fig. 3.7b Fourier transform of convolution filtered beam of fi.g 3.7a, contour labels in app. 3

Sharp Cutoff Fourier filter : This filter is more exact than the convolution filter because it does not degrade the spatial resolution of the data. This is achieved by applying a sharp cutoff in the transform domain at the theoretical limit of the telescope spatial frequency cutoff.

The program was developed by J.Jonas and P.I.Mountfort. The Fast Fourier Transform is used to do the transform. The only limitation on the size of the map is the maximum amount of virtual memory address space on the VAX. At the moment this allows us to transform a maximum of 200 000 data points. The limitation mentioned in the previous section (ringing in the space domain) will always have to be considered. The program tries to reduce this by linearly interpolating a guard band from the first and last scan to be transformed. This guard band is then inserted into the empty rows and columns which occur in the FFT Jonas and Mountfort used because it requires $2^n$ rows and $2^n$ columns. An alternative would be to use a tapered filter like a Butterworth, exponential or a trapezoidal filter (Gonzalez and Winz (1977) ch 4). These were not used because it was decided that it was more important to retain the exact response function of the telescope in the data. A cutoff of 3.5 reciprocal degrees was used in the transform domain. See figures 3.8a and 3.8b for the Fourier filtered beam and its transform. Noise is reduced by a factor of

$$2.13(\sec\delta)^{1/2}$$

All the maps in appendix 1 were Fourier filtered.

Coordinate transforming : the maps, except for A14D63, were and will always be observed in present day coordinates. This is so that accurate backgrounds can be found (see discussion on A14D63 in section 3.2). Before they can be compared with any other maps they need to be transformed to one of the standard epochs, like 1950 or 2000. A general coordinate transform program was developed by Jonas (1982) which allowed a map to be transformed to any

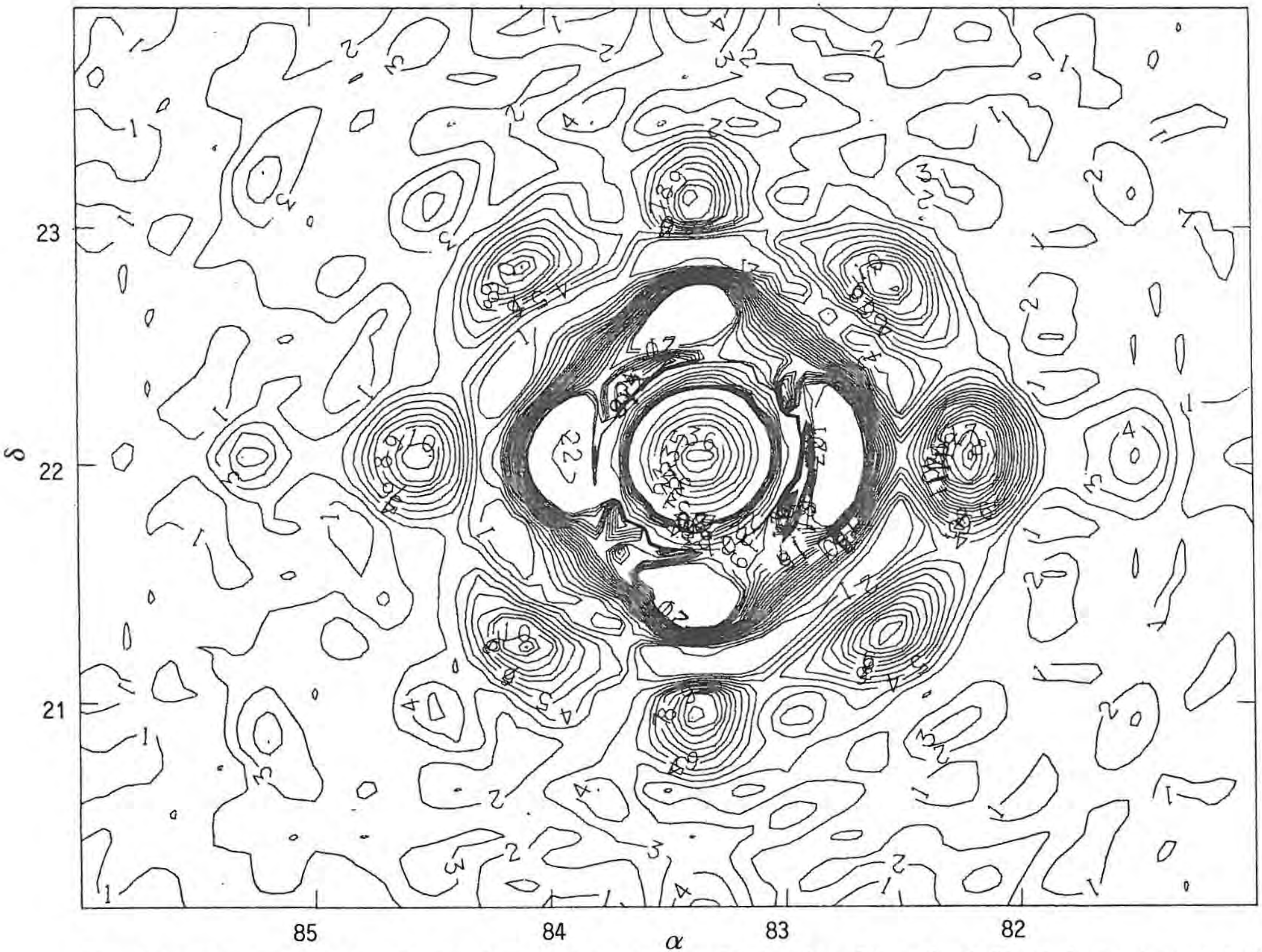


fig. 3.8a Fourier filtered beam (using a sharp cutoff Fourier filter) of fig 2.1, contour labels in app. 3.

3,17b

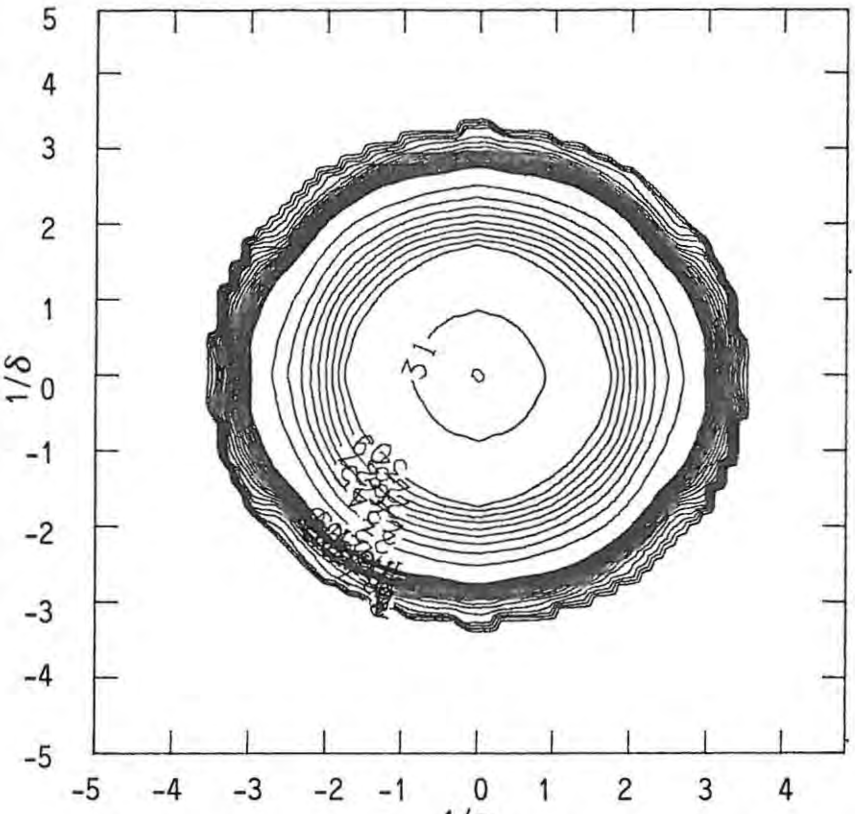


fig. 3.8b Fourier transform of Fourier filtered beam of fig. 3.8a, contour labels in app. 3

epoch and from equatorial to galactic coordinates. The interpolation is equivalent to a convolution with a cone which has a circular base on the equator and an elliptical base everywhere else. The ellipse has the form

eq.3.1 $$\frac{(\delta)^2}{(0.1)^2} + \frac{(\alpha)^2}{(0.1\sec\delta)^2} = 1$$

The affect of the coordinate transform is to degrade the resolution of the data a bit because it attenuates the high spatial frequencies a bit. In the transform domain the ellipse has a value of 0.7 at 3.5 reciprocal degrees, the telescope spatial frequency cutoff. The slight blurring of the data which is introduced is not unacceptable.

Experience was gained in using this program to precess maps in equatorial coordinates. For this we need a formula to precess the pole and origin to the desired year. The approximate formulae often used are

eq.3.2 $$\Delta\alpha = [m + n\sin\alpha\tan\delta]N$$

eq.3.3 $$\Delta\delta = [n\cos\alpha]N$$

where $m = 0.0128014^{o}\ yr^{-1}$

and $n = 0.0055685^{o}\ yr^{-1}$

and N is the number of years between the desired date and the reference date (eg. for precession from 1980 to 1950 N = -30). These formulae are only an approximation though and the error in them increases as the declination approaches the poles and at the poles $\tan\delta$ is infinite.

A program was written to perform the exact precession using the Euler angles and then rotating them. The matrix multiplication which does the rotation was obtained from Taff (1980). It is defined in the following terms -

eq.3.5 $$l(\alpha_f,\delta_f) = P(t_i,t_f) \times l(\alpha_i,\delta_i)$$

where $\alpha_i$ = right ascension in unprecessed coordinates

$\delta_i$ = declination in unprecessed coordinates

$$l(\alpha,\delta) = \begin{pmatrix} \cos\delta\cos\alpha \\ \cos\delta\sin\alpha \\ \sin\delta \end{pmatrix}$$

$$P(t_i,t_f) = \begin{pmatrix} (\cos\xi\cos\varphi\cos\theta - \sin\xi\sin\varphi) & (-\sin\xi\cos\varphi\cos\theta - \cos\xi\sin\varphi) & (-\cos\varphi\sin\theta) \\ (\cos\xi\sin\varphi\cos\theta + \sin\xi\cos\varphi) & (-\sin\xi\sin\varphi\cos\theta + \cos\xi\cos\varphi) & (-\sin\varphi\sin\theta) \\ (\cos\xi\sin\theta) & (-\sin\xi\sin\theta) & (\cos\theta) \end{pmatrix}$$

where

$$\xi = (\ (2304.253 + 1.3975t_i + 0.00006t_i^2)t_f + (0.3023 - 0.00027t_i)t_f^2 + 0.18t_f^3\ ) \ / \ 3600 \quad \text{degrees}$$

$$\varphi = (\quad + (0.7927 + 0.00066t_i)t_f^2 + 0.00032t_f^3) \ / \ 3600 \quad \text{degrees}$$

$$\theta = (\ (2004.685 - 0.8533t_i - 0.00037t_i^2)t_f - (0.4267 + 0.00037t_i)t_f^{\ 2} - 0.048t_f^3) \ / \ 3600 \quad \text{degrees}$$

fig. 3.9 matrix definitions for coordinate transform to precess equatorial coordinates from year $t_i$ to year $t_f$

$\alpha_f$ = precessed right ascension

$\delta_f$ = precessed declination

$t_i$ = unprecessed year

$t_f$ = precessed year

and $l(\alpha,\delta)$ and $P(t_i,t_f)$ are matrices defined in figure 3.9. The resulting matrix $l(\alpha_f,\delta_f)$ contains 3 terms involving $\alpha$ and $\delta$. These can be manipulated to yield $\alpha$ and $\delta$.

Using the above matrix to find the new pole and origin and Jonas's coordinate transform program it was possible to accurately precess any map to any epoch.

<u>Joining two independently observed maps</u> : because of the way in which the data processing has been done (section 2.5) SKYMAP produces a survey consisting of a series of small maps. These maps are usually 12 hours of right ascension and 19 or 39 degrees of declination. Figure 3.10 shows on an equatorial grid of the sky which sections of the southern sky have been completed and what parts of the sky they cover. To compile a southern sky survey we need to join these maps into one large map. Because the maps have been reduced using an arbitrary zero level the technique used must somehow find the true sky brightness distribution and then tie the maps to this. The "long scan" technique described in the next chapter attempts to do this. But before the observations for the long scans had been completed it was necessary to join overlapping maps to obtain preliminary results on large scale features. Because A14D63 and A12D26 are the only completed maps which overlap sufficiently to make joining them worthwhile a method was developed to join A14D63 and A12D26 and is described now.

Without knowing the true baselevel of the maps it is necessary to define one to which both maps could be referred. The way in which a baselevel has been chosen for the maps up to now has been to set the coldest part on each

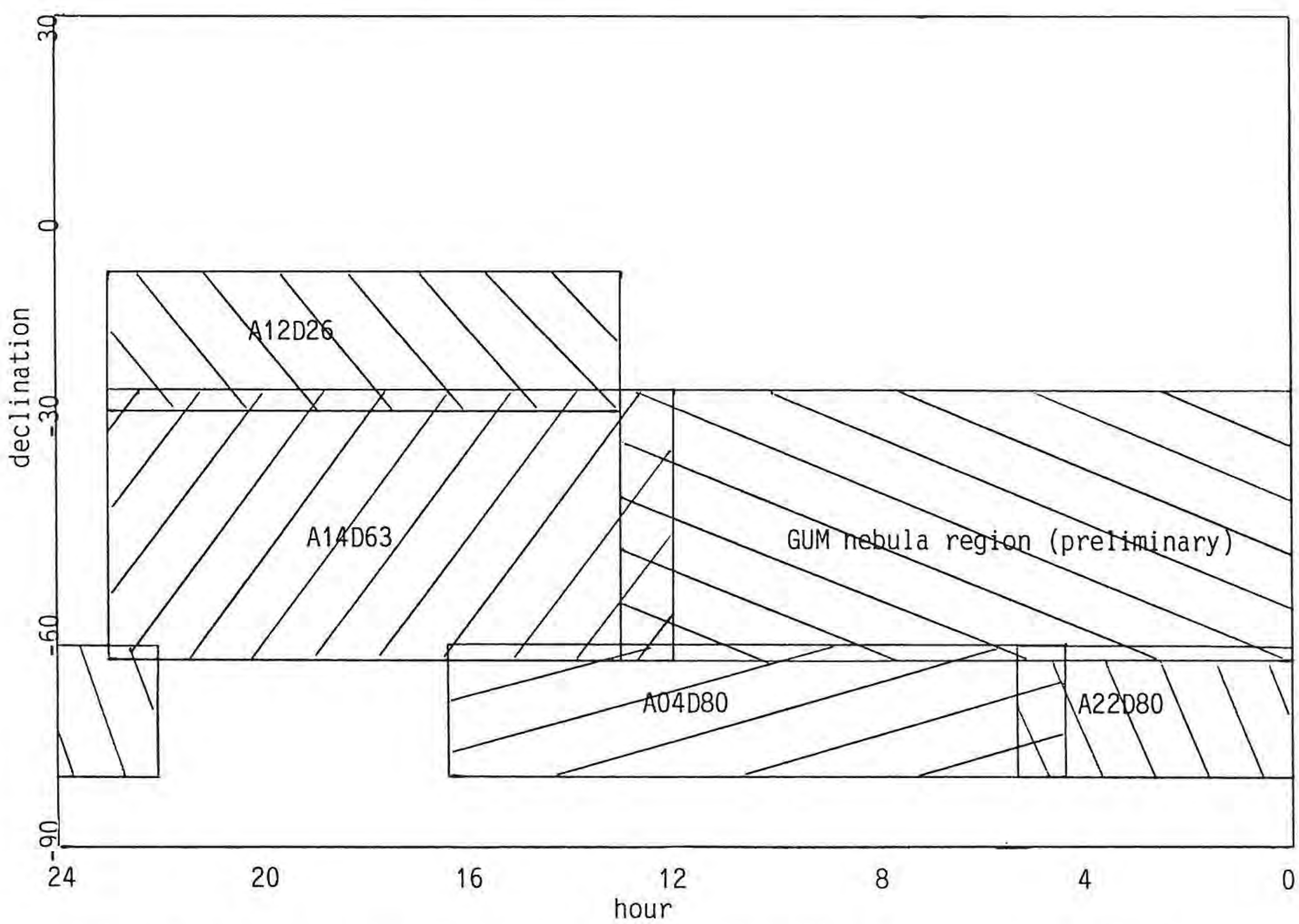


fig. 3.10 map of southern sky in equatorial coordinates showing completed (1984) parts of RHODES 2.3 GHz survey

map to zero. It was decided to do the same for the joined map and choose the zero level of A14D63 as the definitive zero level. This was because A14D63 had been forced flat after the data processing (see discussion on A14D63 in section 3.2) and consequently has a smoother appearance than A12D26. The two maps overlap by 2 degrees of declination and so the drift between the two maps can be found only as a function of right ascension. In the reality the maps deviate from the true brightness distrbution in declination and right ascension.

A14D63 was observed in 1950 coordinates and A12D26 in 1983. Therefore A12D26 had to be precessed to 1950 coordinates first. This was done as described in the last section. The difference between A14D63 and A12D26 was found for all the overlapping bins. This covered the region right ascension $190^{o}$ to $330^{o}$ and declination $-26^{o}$ to $-24^{o}$. The bins were the usual size of $0.1^{o}$ by $0.1^{o}$. It was assumed that drift was the same for all declinations therefore the median of all the differences at each constant right ascension was used. Because of the very steep gradients in the plane the differences there were of the order of 500 mK. These could not be used because if such large differences were subtracted from the bins at those right ascensions bad scanning effects would have have been created in the non-plane regions. The large differences there were as a result of the same uncertainties in the baselevels as elsewhere, except that they were larger because of the larger brightnesses in the plane. It must be noted too that Jonas in pulling A14D63 flat did not pull it flat in the plane region. It was decided to ignore the differences over this region. They were replaced by a straight line fitted between the differences at $250^{o}$ and $280^{o}$ right ascension. The differences between the maps with medians taken in declination and the plane replaced by a straight line have been drawn in figure 3.11a.

This is very noisy and has to be smoothed. One of the best ways of doing this is to fit a cubic spline. A 20 knot (the knots were chosen to be equidistant in right ascension) cubic spline was fitted in a least squares way to the curve in figure 3.11a. The result, which we will call the drift, is plotted in figure 3.11b. We can see that the drift runs from negative values at low right ascensions (corresponding to the early evening of the observations) to positive values at the higher right ascensions (early morning). This can be interpreted as radiation from the still warm telescope structure (because the sun shines on it the whole day) in the early evening which has not been removed by the data processing and a generally lower baselevel in the early morning on A12D26. It also shows up the arbitrariness of SKYMAP's baselevels. These are differences between observation of the same regions in the sky and they have a consistent drift on them of 1/2 kelvin over approximately 9 hours. What is encouraging though is that the drift is smooth (no structures smaller than $15^{o}$ right ascension). Which means the maps are still salvageable!

This smooth drift (figure 3.11b) was added to A12D26 to bring it onto the same baselevel as A14D63. The maps were then spliced together over the common declination range with a weighting function which is depicted in figure 3.11c to produce a smooth join. The resulting map is shown as an optronics photograph in figure 3.12. The join passes through the centre of the galaxy parallel to the curved boundary of the map. In the greyscale the join is not visible. It was also looked for by displaying the joined map on STARLINK using colour. By rotating the colours on the screen minute changes in baselevel show up clearly. Even this exercise did not reveal the join.

In conclusion we can say the following. It is a simple technique which strives to make the join as subtle as possible. This is achieved and we can now compare structures which lie across the join. For example the spur

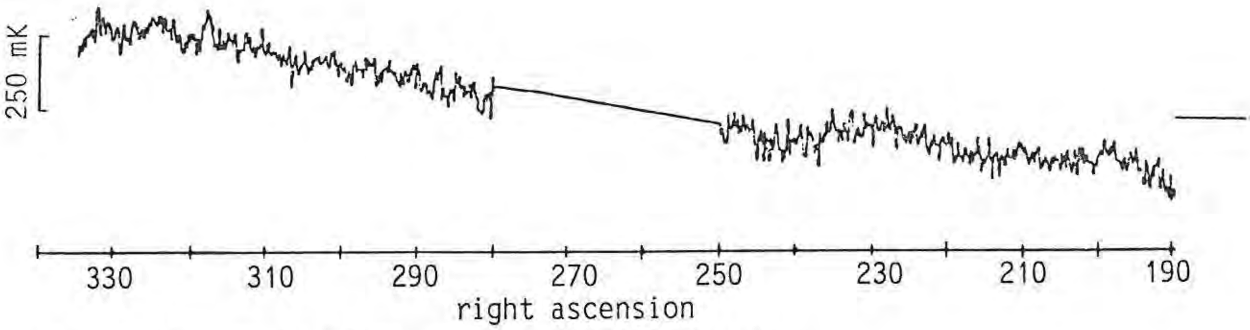


fig. 3.11a raw drift between A12D26 and A14D63

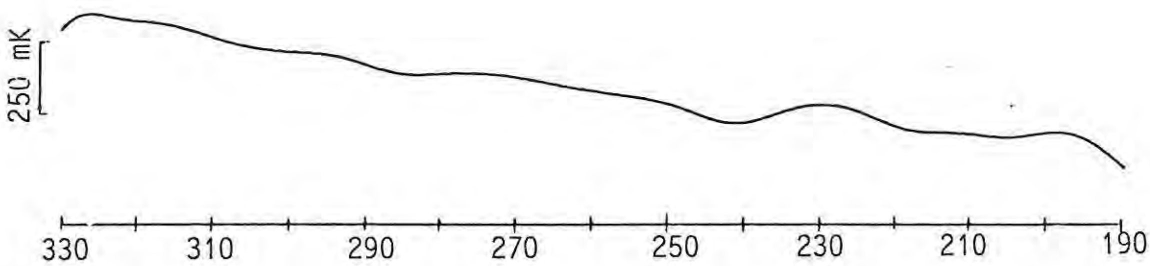


fig. 3.11b drift of fig. 3.11a fitted with cubic splines

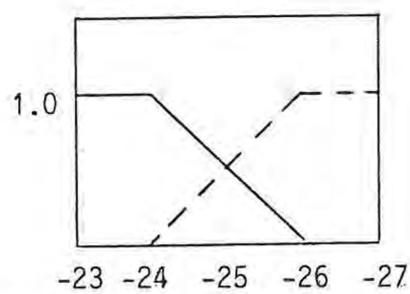


fig. 3.11c weighting functions used to splice A14D63 (---) and A12D26 (——) together

rising from the centre of the galaxy would not have been possible to discover without having joined the maps.

Subtracting the galactic disc component : if we take a look at any of the repesentations of the combined map (like the one just presented in figure 3.12) we will be struck by the strong unresolved contribution extending on either side of the plane. This is similar to the Milky Way we see overhead on a dark night. Both of these bands complete a large circle in the sky. We know that the optical Milky Way exists because the stars form a flattened disk system and we are in this disk. Therefore we view the disk edge-on as a band. The radio continuum disc component is spatially coincident with the optical one and thus, we assume, closely related. Its origin, appearance and meaning we will discuss in chapter 6. In this section we will show how we can with the assistance of a few assumptions separate this smooth component from the discrete sources on top of this contribution.

When analysing the disk component of a set of observations it is usual to only consider a cut at $b=0^{o}$ along all longitudes (eg. Price (1974)). In this case all that is done is the peaks are thrown out and the resulting curve is called the disk component. In our instance we not only want a curve through $b=0$ but a 2-D surface which can be used over the whole map. The reason for this is we want to subtract it from the map to enhance discrete low brightness features at intermediate latitudes. No assumptions were made of the type of radiation or about asymmetries in its distribution. All that was assumed was that any radiation which was symmetric about zero latitude belonged to a larger (disk) component and could be subtracted. This was refined by assuming that the base surface was monotonically decreasing towards higher latitude and smooth. By smooth was meant there are no structures smaller than $5^{O}$ longitude and $2^{O}$ latitude. A description of the method and results follows.

The data used was the joined map which was described in the previous section. It was divided into strips $5^{O}$ wide in longitude. Then for each $0.1^{O}$ latitude in each longitude strip the minimum was found. For each b the minimum of +b and -b was chosen. This resulting scan in latitude was then forced to be monotonically decreasing by running a minimum-of-20 filter over it. This was further smoothed by running a Hanning smoothing function over it. These last two processes ensured that the resulting surface had no jumps in them. The final surface which was found in the described manner is shown in figure 3.13.

The merits of using this method to find a surface which can be subtracted is that only something which is real is subtracted. The flaws in it as regards a theoretical disk component are that no assumptions are made about the longitude dependence except that there are no structures smaller than $5^{O}$. A disk component should ideally contain the nuclear bulge and be monotonically decreasing with increasing longitude from the centre of the galaxy.

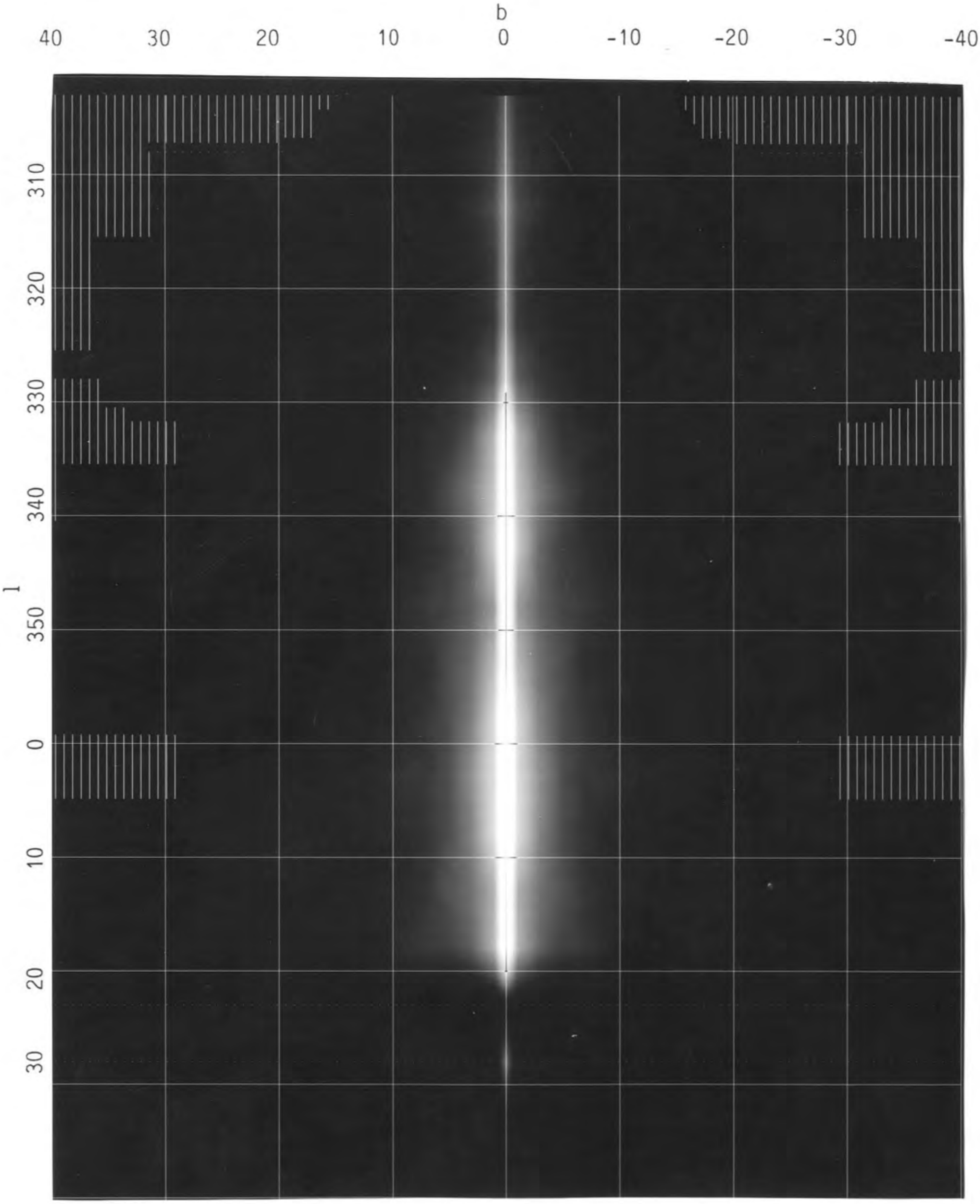


fig. 3.13 derived disk component of joined data set, fig 3.12
the horizontal lines occurring at high latitudes and l=315 outline the shape of the data set

# CHAPTER 4

## CALIBRATING THE RHODES 2.3 GHZ SOUTHERN SKY SURVEY

### 4.1 INTRODUCTION

The mapping and reduction method described in chapter 2, SKYMAP, produces a series of maps which each cover, nominally, 12 hours right ascension and 19 or 39 degrees declination. Each map is on an arbitrarily chosen baselevel, and the zero level on each map is defined as the lowest point on the map. As a result the maps are on different baselevels (cf. fig. 3.11a) and different zero levels. In order to join these maps into a single southern sky survey we need to put them on a common zero level and define the correct baselevel. If we want to compare this survey with other surveys we also need to calibrate the zero level and convert the maps of $T_a$ to maps of $T_b$. This means correcting the $T_a$ for sidelobe radiation and comparing this survey with an absolutely calibrated survey of $T_b$.

It has been proposed that to derive a consistent baselevel for all the maps a coarse grid of temperatures be constructed. These temperatures will have had drift removed from them in an independent way so that we know they are true measurements of galactic brightness in terms of $T_a$. This method has been referred to as the "long scan" method because of the way in which the grid will be observed - by $120^0$ long scans of declination.

This chapter will discuss the problems involved in calibrating the Rhodes survey, the technique of observing the long scans and how they are reduced. Finally, preliminary results from this technique will be presented and they will be discussed. The chapter will end with a discussion of improvements to the "long scan" technique and future work that remains to be done.

## 4.2 ABSOLUTE CALIBRATION OF RADIO SURVEYS

To absolutely calibrate a radio survey means to know its zero level in $T_b$ as an absolute value and to have converted from antenna temperature to brightness temperature. The telescope detects antenna temperature which is comprised of a number of contributions. We are interested only in the sky brightness and want to subtract any extra components and correct for any attenuation. Although various papers have discussed the problems of absolutely calibrating a survey - Pauliny-Toth and Shakeshaft (1961), Price (1969), Landecker and Wielebinski (1970), Price (1970), Berkhuijsen (1972), Haslam et al (1981) and Reich (1982) are some of them, we will be following our own approach here. In section 4.3 we will apply the problems involved in this procedure to the Rhodes survey particularly.

The antenna temperature measured at the terminals of the receiver consists of two components, a contribution from the telescope and noise in the receiver. The telescope term is the convolution of the beam pattern and the brightness temperature distribution over $4\pi$, that is

eq.4.1 $$T_a = G/4\pi \int_{4\pi} f(\alpha_0-\alpha, \delta_0-\delta)\, T_b(\alpha,\delta)\, d\alpha\, d\delta + T_s$$

where G = is the gain of the receiver

$f(\alpha,\delta)$ = is the beam pattern of the telescope

$T_b(\alpha,\delta)$ = is the brightness distribution surrounding the telescope

$T_s$ = is the noise contribution from the receiver

These terms can be analysed as follows -

G, the gain of the receiver can be determined by observing a calibrator source for which $T_b$ is known.

The term $f(\alpha_0-\alpha, \delta_0-\delta)\, T_b(\alpha,\delta)$ can be broken down as follows - there are two contributions, one from the main lobe of the beam and one from the sidelobes. These consist of main lobe

$T_{ML\ gal}$ : galactic and extragalactic $T_b$ attenuated by the atmosphere and convolved with the main beam

$T_{ML\ atm}$ : atmospheric emission into the main beam

side lobes

$T_{SL\ gal}$ : galactic and extragalactic $T_b$ attenuated by the atmosphere and convolved with the side lobes

$T_{SL\ atm}$ : atmospheric emission in the side lobes

$T_{SL\ grnd}$ : ground contribution and reflected ground contribution into the side lobes

In a calibrated survey we are interested only in the term $T_{ML\ gal}$. This allows us to compare surveys which have been observed with different telescopes and at various observatories. Therefore we have to devise ways to subtract out the other terms from the survey of $T_a$. We will now discuss each of the unwanted terms in detail and how to determine them.

Main lobe contribution

The galactic $T_b$ is what we want to measure. The isotropic extra galactic $T_b$ is a constant over the whole map and can be subtracted out without problems, eg. at 408 MHz it is $6^{o}$ K (Phillip et al (1981)). Atmospheric attenuation is determined by observing extinction of a source as a function of zenith angle. Atmospheric emission can be estimated from theoretical considerations of the temperature of the atmosphere and its attenuation or from observations of cold sky over the zenith angle range over which the survey was observed. If observations are conducted at a constant elevation it is often assumed the atmospheric contribution is a constant and will be corrected when the zero level is determined.

Side lobe contribution

$T_{SL\ gal}$ - estimating the galactic and extragalactic brightness radiation in the sidelobes involves the most calculation of all the terms. It can be important because the sidelobes can represent a significant fraction of the full beam solid angle. The 'catch-22' of this calculation is that we are trying to determine what the convolution of the sidelobes with the brightness distribution is, while at the same time we are trying to measure the brightness distribution. Also the full extent of the sidelobes is rarely known. One way of estimating the brightness distribution is to use another survey which has been corrected for all the extra terms or which has been observed with an antenna which has a small sidelobe contribution (eg. a horn antenna). If the survey is at another frequency it has to be scaled to the observing frequency with an appropriate spectral index (see Webster (1974) for a discussion of the spectral index). For example Berkhuijsen (1971) calibrated her 820 MHz survey with the 408 MHz survey of Seeger et al (1965). Surveys with horn antennas usually have a very coarse resolution (for example $15^{o}$). This does not affect the calculation much because $T_{SL\ gal}$ varies slowly as a function of right ascension. Therefore only a coarse grid of correcting temperatures is required - the rest can be interpolated from these. This slow variation is a result of the small contribution from each sidelobe and the extent of the sidelobes. They smooth out all but the gross variations in the galactic brightness i.e the difference between the disk and non-disk region. Sometimes when another survey is not available for this calculation, the survey itself is used to determine the contribution of the sky brightness in the sidelobes. For example Pauliny-Toth and Shakeshaft (1962) in their oft quoted 404 MHz survey did this. They superimposed their beam on their uncorrected survey and calculated the radiation in the sidelobes. This technique is sound if we assume this term varies slowly across the sky and is not sensitive to small uncertainties in the survey from which it is being derived.

$T_{SL\ atm}$ - this term is supposed to be a function of elevation but in reality it hardly varies at all with elevation. This is because the sidelobes are spread out over such a large area that there is always some contribution from every part of the sky. Therefore changing the elevation of the telescope hardly changes this term at all. Calculating this term involves a precise knowledge of the sidelobes and the attenuation of the atmosphere. Berkhuijsen (1972) performed this calculation for 820 MHz and came up with a straight line when this term was plotted against elevation angle. When calibrating a survey in $T_b$ it is usually assumed that it is a straight line and will be corrected for when the survey is put on an accurate zero level.

$T_{SL\ grnd}$ - this term includes the radiation of the ground and surrounding buildings into the spillover sidelobes and backlobes and the reflected sky radiation into these lobes. Predicting this term requires an estimate of the reflection coefficient of the ground and the temperature of the surroundings. Higgs (1967) and Berkhuijsen (1972) have done this at 820 MHz. In the Rhodes survey we will handle this term empirically, see discussion in section 4.3.

$T_S$ - is the noise temperature contributed by the losses in the line and the noise in the receiver. To measure this we need thermal noise standards or auxiliary noise sources to connect to the antenna (Stelzried (1982) chapter 11). Careful attention must be paid to the instrumentation details like matching the noise sources and the linearity of the amplifiers.

If the terms $T_{MB\ atm}$, $T_{SL\ gal}$, $T_{SL\ atm}$, $T_{SL\ grnd}$ and $T_S$ are known absolutely i.e. with respect to zero, then we can correct $T_a$ for these to obtain the equivalent antenna temperature for the galactic and extragalactic radio brightness in the main beam. The conversion factor for $T_a$ to $T_b$ is then applied to yield brightness. This factor can be determined either from measuring the parameters of the telescope (see chapter 2) or from observing a calibrated source the size of the main beam.

This methodical approach to correcting $T_a$ for all the extra terms to derive $T_{ML\ gal}$ is quite laborious though. Some observers have actually done this, eg. Pauliny-Toth and Shakeshaft (1962), Landecker and Wielebinski (1970) and Berkhuijsen (1972). As we go to higher frequencies this type of approach becomes more difficult because the extra terms remain the same but the signal ($T_{ML\ gal}$) becomes fainter, therefore any errors in the above outlined calculations cause serious errors in the final survey. An equivalent but more pragmatic approach is to be aware of all these terms but instead of calculating each one, use empirical and statistical arguments to determine these terms. For example Haslam et al (1981) at 408 MHz and Reich (1982) at 1420 MHz used the following approach to calibrate their surveys.

Observations consisted of scans which started or ended at one of the celestial poles. Because all the scans were referred to a pole, receiver drift could be accurately determined. A calibration signal was also continuously recorded so that each scan could be corrected for changes in receiver gain. Finally, because the scans cross over each other in sky coordinates they can be forced to lie on a common baselevel.

To determine brightness temperatures and a zero level a different approach was used for 408 MHz and 1420 MHz. The 408 MHz survey consisted of scans in elevation. The $T_a$'s were plotted against the corrected $T_b$'s of Pauliny-Toth and Shakeshaft (1962) at 404 MHz for each declination. It was assumed the sidelobe contribution and atmospheric contribution was the same for each declination. Therefore straight line fits to these plots yielded the zero level correction for each declination (the intercept) and the $T_a$ to $T_b$ conversion factor (the slope). Note that no correction was made for $T_{SL\ gal}$.

The scans at 1420 MHz were at a constant elevations so it was assumed the sidelobe and atmospheric contribution was constant for each scan. The zero level was determined by comparing a smoothed version of the 1420 MHz survey with absolutely calibrated measurements by other observers of certain parts of the sky. The temperature scale was checked by comparing the survey with Webster's (1974) calibrated measurements at 1407 MHz.

The above two examples bring us to the question of how to determine the zero level of a survey. The first thing is to determine the baselevel of the survey. This can be done by referring the observation to a reference point for which the drift is accurately known. Two obvious choices for this are the north and south celestial poles. Once we are sure the survey is on the true baselevel we can determine the zero level in one of the following ways. Either we can compare the survey with another absolutely calibrated survey. Usually the two surveys have different resolutions and we have to smooth them to the same resolution. Or a single point on the survey can be absolutely measured, eg. one of the poles if all the observations are made with respect to the poles. Both these methods yield a constant offset which has to be added to the whole survey.

In conclusion to this section we can say that to obtain an absolutely calibrated survey of $T_{MB\ gal}$ we have to be aware of all the extra contributions which the telescope detects. But the method we use to calibrate the survey need not be theoretical, an empirical approach is equally valid.

Drift as a result of the atmosphere changing and the telescope cooling down is removed using the median sky technique (see sec. 2.4 for a full description). This assumes that there are enough good observations in a map to create a drift-free sky (the median sky). Then drift for an observation is the difference between the observation and the median sky. It is this process which creates the arbitrary baselevel. This is because we are assuming that the observations themselves can be used to find drift on them. An illustration of these arbitrary baselevels can be got by considering fig. 3.11a. This is the difference between A12D26 and A14D63 for their common bins. It should be zero if they are on the same baselevel. Instead there are features as small as $10^{o}$ and a gradual slope of $0.5^{o}$ K over the right ascension range (9 hours).

The atmospheric and ground contribution is removed by the background removal program (sec. 2.4). This does not attempt to separate the atmospheric and ground contributions at all, even though they are of similar size (both on average $2^{o}$ K). Instead it assumes that as long as cold sky is observed at each declination somewhere along the right ascension range, the 10th lowest point along each declination will represent the background. These scans in declination are fitted by a fourth order polynomial for $19^{o}$ wide maps and a sixth order for $39^{o}$ wide maps. These fits yield a maximum rms error of 10 mK and 18 mK respectively. This shows that the atmosphere and ground contributions are smooth functions which is reasonable seeing as the atmospheric noise temperature is a sec$\delta$ function for elevation angles greater than $60^{o}$. Also the ground contribution is heavily smoothed by the large angular extent of the sidelobes. Atmospheric attenuation need not be corrected for at 2.3 GHZ because it is less than a percent (Stelzreid (1982)) at zenith.

Both drift and background found in the above manner are subtracted from the data before they are combined. Therefore the data presented in chapter 3 are of antenna temperature with the terms $T_{MB\ atm}$, $T_{SL\ atm}$ and $T_{SL\ grnd}$ subtracted and with the lowest point on each map chosen as zero.

To calibrate the Rhodes survey we need to first determine the correct baselevel of all the maps. If we assume drift is minimal over a scan then the correcting surfaces we are looking for are slowly varying functions of right ascension.

One way to derive the correct baselevel is to observe a series of widely spaced scans which have had drift removed in an independent way i.e. without referring to the scans themselves. A technique called "long scans" has been developed to do this and will be described in detail in the next section. The "long scans" consist of scans to and from the south celestial pole (SCP) over the declination range $-90^{\circ}$ to $+30^{\circ}$. Because the scans are continually referred to the SCP the correct drift can be found. The rotation of the earth provides the scanning motion in right ascension. Scanning at a rate of $0.2^{\circ}$ per sec. over the specified declination range means that each scan starts $3^{\circ}$ later than the next. A night's observation yields a pattern on the sky which is depicted in figure 4.1a. The resulting grid of temperatures is quite coarse, having a maximum spacing of $6^{\circ}$ in right ascension. The spacing in the declination direction is dependent on the sampling rate and the binning width and can be varied. A maximum of 10 samples a second are collected, so the binning width can be anything from $0.02^{\circ}$ and bigger. To improve the resolution in the right ascension direction the scans are interleaved with 5 more scans each starting a degree away from the last one. This provides a sky coverage which, in equatorial coordinates, looks like figure 4.1b. Because these scans are all at a constant hour angle ($0^{\circ}$) the atmospheric and ground contribution is the same for all the scans and can be

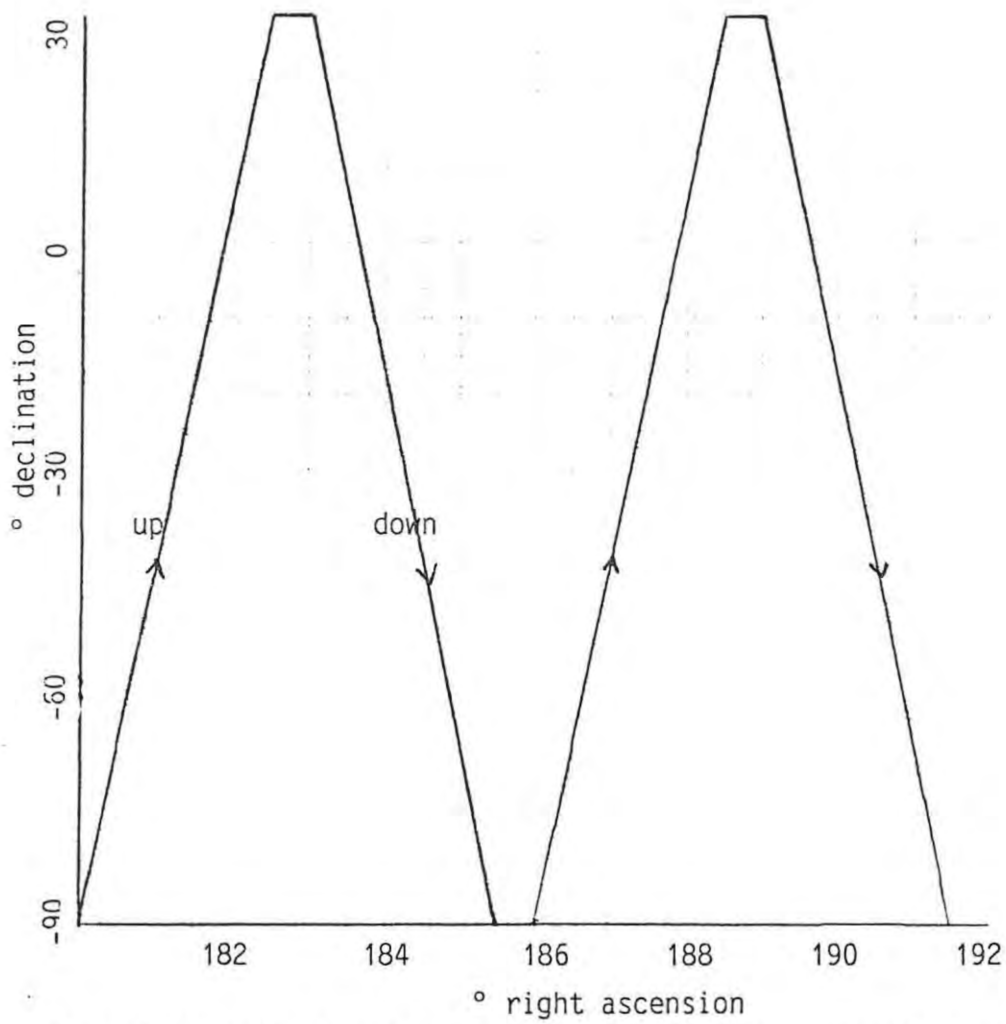


fig. 4.1a path of raster 0 of "long scans" in equatorial coordinates

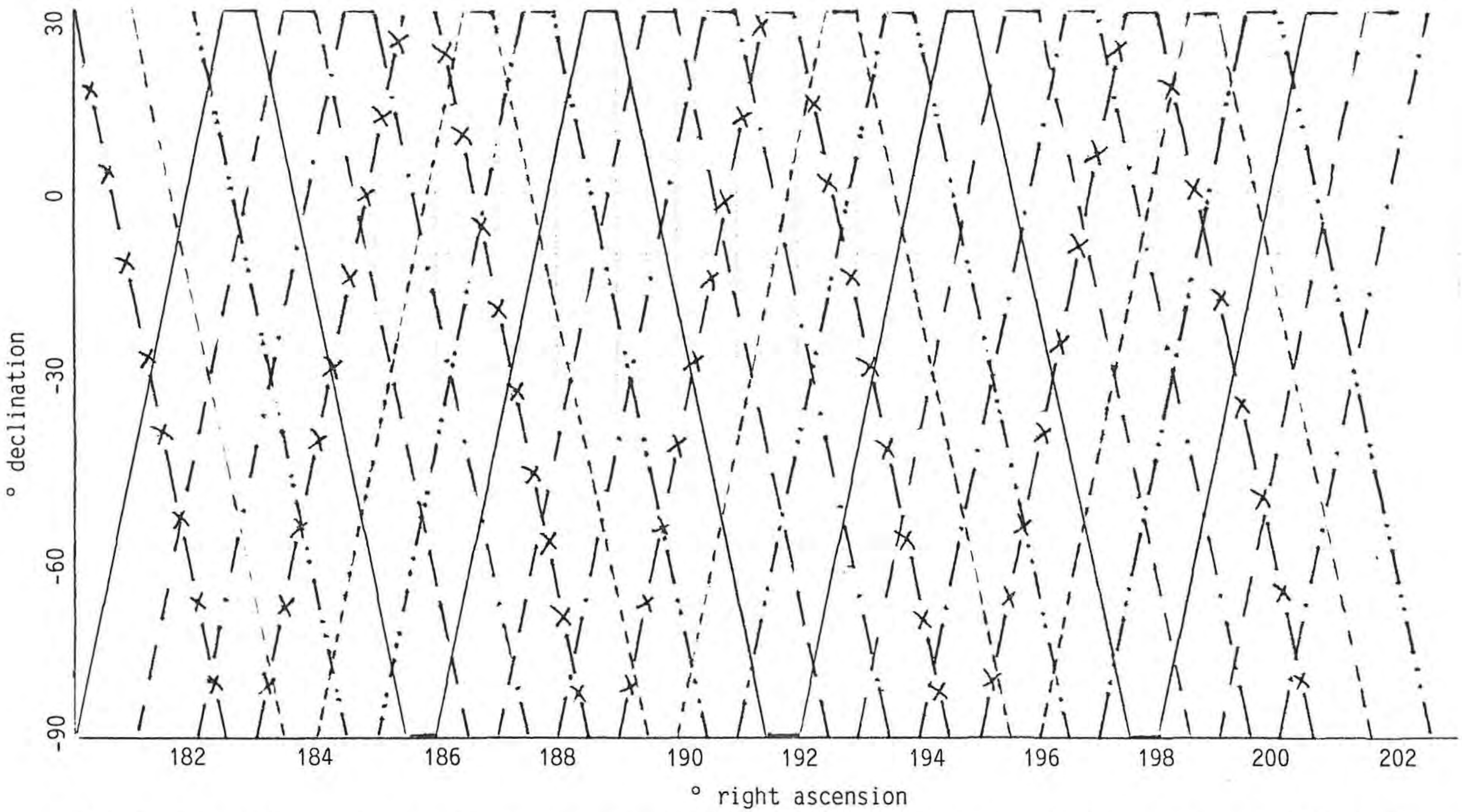


fig. 4.1b 6 rasters of "long scans" on an equatorial grid, rasters are 0(——), 1(---), 2(–.–), 3(-x-), 4(···) and 5(-··-)

removed.

What this all means is that the "long scans" can provide us with a coarse grid of the true brightness distribution of the sky in antenna temperature. These can then be used to put all the maps of the Rhodes survey on a single and correct baselevel. The Rhodes survey will then be referred to a single reference point, the SCP. The zero level can then be determined either by scaling up other surveys of the SCP (eg. Landecker and Wielebinski (1970) at 150 MHz and Price (1970) at 408 MHz) to 2.3 GHz or by measuring the temperature of the SCP with a horn antenna at 2.3 GHz. The difficulty with scaling up another survey is in choosing a spectral index. Various studies have been made of the galactic spectral index (eg. Webster (1974) and Penzias and Wilson (1966)) but these have only been of the galactic plane region. Webster derives a spectral index for the broad disk region $|b| \leq 30^{\circ}$ (northern hemisphere only) of $\beta$ = 2.80. Because the SCP occurs at $b = -27^{\circ}$ and there are no observations for $\nu$ >1 GHz of the SCP a reasonable first estimate for the SCP at 2.3 GHz can be derived with Webster's (ibid) value for $\beta$. That is, using $\beta$=2.80 and the 408 MHz absolute brightness temperature of the SCP derived by Price (1969) of 22.5 K we arrive at a 2.3 GHz absolute brightness temperature of 3.154 K.* Note this is for a 48" beam centred on the SCP. Therefore to compare the SCP temperature on the Rhodes survey and this value we will have to convolve the Rhodes survey to this resolution.A more rigorous and experimental approach is to use the Hartebeesthoek receiver to measure the absolute sky brightness at 2.3 GHz.

At this point we have discussed how to put the Rhodes survey on a single correct baselevel and how to determine the zero level. We still need to convert to brightness temperatures and decide whether to use the full beam or main beam brightnesses. The antenna temperatures which will result after using the "long scans" to correct the baselevel will be of the full beam

* A nominal value of 3K has been adopted for the constant extragalactic contribution at both 408 MHz and 2.3 GHz.

brightnesses. To convert to full beam brightness temperatures we need to have a full beam brightness conversion factor. This is almost impossible without knowing the full beam solid angle. A possibility is to compare the Rhodes Survey with another brightness temperature survey suitably scaled to 2.3 GHz. The two surveys must be converted to the same resolution. Then $T_a$ versus $T_b$ must be plotted and a straight line fitted to the resulting plot. The slope of this line will give the full beam brightness conversion factor. Unfortunately there are no absolutely calibrated surveys above 1 GHz which can be used to compare the Rhodes survey with.

What is possible though is to calibrate the "long scans" in main beam brightness temperatures and then use these to calibrate the existing maps of $T_a$.

## 4.4 "long scan" MAPPING TECHNIQUE

When the Rhodes survey was begun the Hartebeesthoek telescope was limited in declination to $-82^{o}$ in the south and $+45^{o}$ in the north. Consequently it was not possible to scan to the south celestial pole. This is the main reason for SKYMAP being developed and, as a result, for the arbitrary baselevels. "long scans" required a technique which would allow drift to be found independently. An obvious way to do this is to continuously refer to the one stationary point in the southern sky - the south celestial pole (SCP). Therefore the telescope structure needed to be altered so that it could scan to $-90^{o}$. This was easier said than done. Although the declination axis was long enough to scan to $-90^{o}$ the telescope structure was in the way. Some of the two southern leg supports had to be cut away and four large bolts had to be replaced with bolts which had smaller heads. These modifications extended the limits of the telescope to include a keyhole at declination $-83^{o}$ to $-90^{o}$ and hour angle $+18^{o}$ to $-18^{o}$. This also meant that the computer program which steers the telescope (STEER) had to be changed. But because the limits of this keyhole are so close to the physical limits of the telescope (the physical limit is now $-90.6^{o}$ declination) a special version of STEER was installed which is only used by the "long scans" observing program. This is known as STSCP (an acronym for Steer To South Celestial Pole) and has a different set of limits to STEER.

The following criteria served as guidelines for designing the "long scans" observing program :

(i) long integrations of the south pole must be performed regularly and often

(ii) the system must be calibrated regularly throughout an observation

(iii) the integration time per sample bin must be similar to that of the

Rhodes survey for the same bin width i.e. 5 seconds per degree of declination.

(iv) it must be easy to determine the correct atmospheric and ground contribution of each scan.

(v) the scans must cover the entire observable sky at Hartebeesthoek with a right ascension spacing of $1^{o}$.

The scanning technique chosen which was supposed to fulfill all these requirements has already been partially described in the previous section. We will now explain the reasons for certain decisions made. It was decided that long scans in declination at a fixed scanning rate provide the most repeatable backgrounds. This is because the telescope points more accurately in scanning mode than in tracking mode.* Scans to and from the SCP with a long integration at the end of each up and down scan provide a reliable way of finding drift. Calibrating the system by firing the noise tube at the end of each scan (north or south) provides a means of checking the system gain. Forcing rasters to scan along fixed paths in equatorial coordinates, see figure 4.1, means they are repeatable. A calibrator is observed at the start and end of each observing session to provide a means of determining the effective aperture of the telescope from which (sec. 2.2) a main beam $T_a$ to $T_b$ conversion factor for each observation can be calculated.

The program which controls the telescope in this mode is, appropriately, called NODDY (not to be confused with Haslam et al's (1982) NODDY). It is based on the original SKYMAP program SKYMP (Mountfort (1982)). That is the data is recorded and packed on tape in the same way. But the manner in which the telescope coordinates are determined and commands to STEER (the telescope driving program) are issued are totally different. These will be described now.

* Tracking involves moving the telescope along a line of fixed right ascension, whereas scanning follows a fixed hour angle.

NODDY repeats the following cycle :

while the sun is not up

(i) scan along meridian from $-90^{o}$ to $+30^{o}$ declination at $0.2^{o}.s^{-1}$, logging data to tape all the time.

(ii) stop logging. fire the noise tube at $+30^{o}$ and write away to tape and screen monitor. wait till next right ascension of this raster passes overhead.

(iii) scan along meridian from $+30^{o}$ to $-89^{o}$ at $0.2^{o}.s^{-1}$ logging data to tape all the time.

(iv) scan slowly along meridian to $-90^{o}$ at $0.05^{o}.s^{-1}$ logging data to tape all the time (this is necessary to prevent overshoot of the telescope at SCP). It also improves the reliability of the scans around the south pole by increasing the integration time.

(v) stop logging, fire noise tube and write away to tape and screen monitor.

(vi) log temperature at SCP to tape till right ascension of next raster passes overhead.

end while

The sampling rate is 1 sample per 0.13 seconds. Note this is different to the SKYMAP sampling rate of 1 sample per 0.1 seconds. This is because the DVMs at Hartebeesthoek are not reliable any more and have to be controlled with software delays. That is the program which resets and reads the DVM, LOGER, has to suspend itself for 0.13 seconds to be sure that the DVM (which is on a 0.1 second integration time) has finished. The program allows at least 30 seconds at the end of every scan for calibrating the noise tube and integrating at the SCP. With a right ascension spacing of $1^{o}$, 6 rasters are required. Which means that there is a 77 second integration of the SCP every 24 minutes and the noise tube is fired every 12 minutes.

The input parameters (observation, raster declination range and rate) are read from a disk file call MSTSRC. NODDY also automatically schedules a flux measuring program called NOD13. NOD13 is derived from Don Bramwell's (RAO staff) program TONOF. This program searches a file containing a list of calibrators to find the one closest to the meridian at the time it is scheduled. It fires the noise tube and makes sufficient measurements of the calibrator to enable a gaussian to be fitted to these and its flux measured. These measurements are (in order) the first null, half power point, peak, half power point, first null in the telescope's hour angle axis and then first null, half power point, half power point and first null along the declination axis. The final flux enables the system i.e. receiver and telescope to be calibrated every observing session. NODDY schedules NOD13 at the start and end of every observation.

## 4.5 REDUCING THE "long scans"

The data logged during an observation (one night) fills about 2/3 of a 2400 ft tape in NRZI mode i.e. 800 bpi. Therefore each tape contains about 15 Mbytes of data. Because of the limited computing resources at Hartebeesthoek the data have to be processed at Rhodes on the Cyber 170/825. To shortcircuit the long delay involved in getting the tapes to Rhodes a number of preliminary analysis programs were developed for running at RAO. These allow the observer to take a quick look at a night's observation so that it can be evaluated at the observatory. In the following section we will first describe the preliminary analysis programs which run at RAO and then discuss the programs which run at Rhodes and reduce the full set of data.

### 4.5.1 Preliminary analysis programs

These consist of three programs BINND, BACND and HIDND. They reduce the data on the tape to a manageable working set on disk. The noise tube calibrations, south pole drift and the background are plotted. The drift and background are subtracted and a hide map of the data on disk is plotted. In this way the performance of the receiver, noise tube calibrations, the quality of the data and pole drift can be checked after a night's observing. A brief description of each program and a sample of the output produced will be presented now.

BINND - averages the data into $0.1^{o}$ declination bins and writes these to disk. It also extracts the noise tube calibrations and saves them in an array. From these it produces a plot of the noise tube calibration through the night, an example of this is shown in figure 4.2. This plot should vary randomly. Any systematic effects should be queried and the validity of the observation doubted.

BACND - reads the binned output of BINND and subtracts a rough estimate of the pole drift and background i.e. atmospheric and ground contribution. The drift is estimated by subtracting the pole temperature for each scan. The background is estimated by fitting a 6th order polynomial to the 5th lowest point of each declination. This background is subtracted from the data and the resulting data written to a new file on disk. The program produces a plot of the pole temperatures with 1st, 2nd, 3rd and 4th order polynomials fitted to these. Figure 4.3 is an example of this plot. The south pole drift should be smooth (at most a 3rd order fit should be required) and drift of more than 3 kelvin should be queried. In these cases it usually means heavy cloud or rain occurred during the observation and the observation must be repeated. BACND also plots the found background i.e. 5th lowest point, as a function of declination and its fitted 6th order polynomial, see figure 4.4. The residue of the fit is plotted too, figure 4.5. The residues are quite large, +- 100mK maximum. But it was found that the shape of the residue was consistently repeated if a 6th order was fitted to the background. Therefore the background is consistently the same shape and we can use a smoothed version of itself as background. This is implemented in the analysis program at Rhodes. If the background is not the same shape as figure 4.4 it usually

4.57a

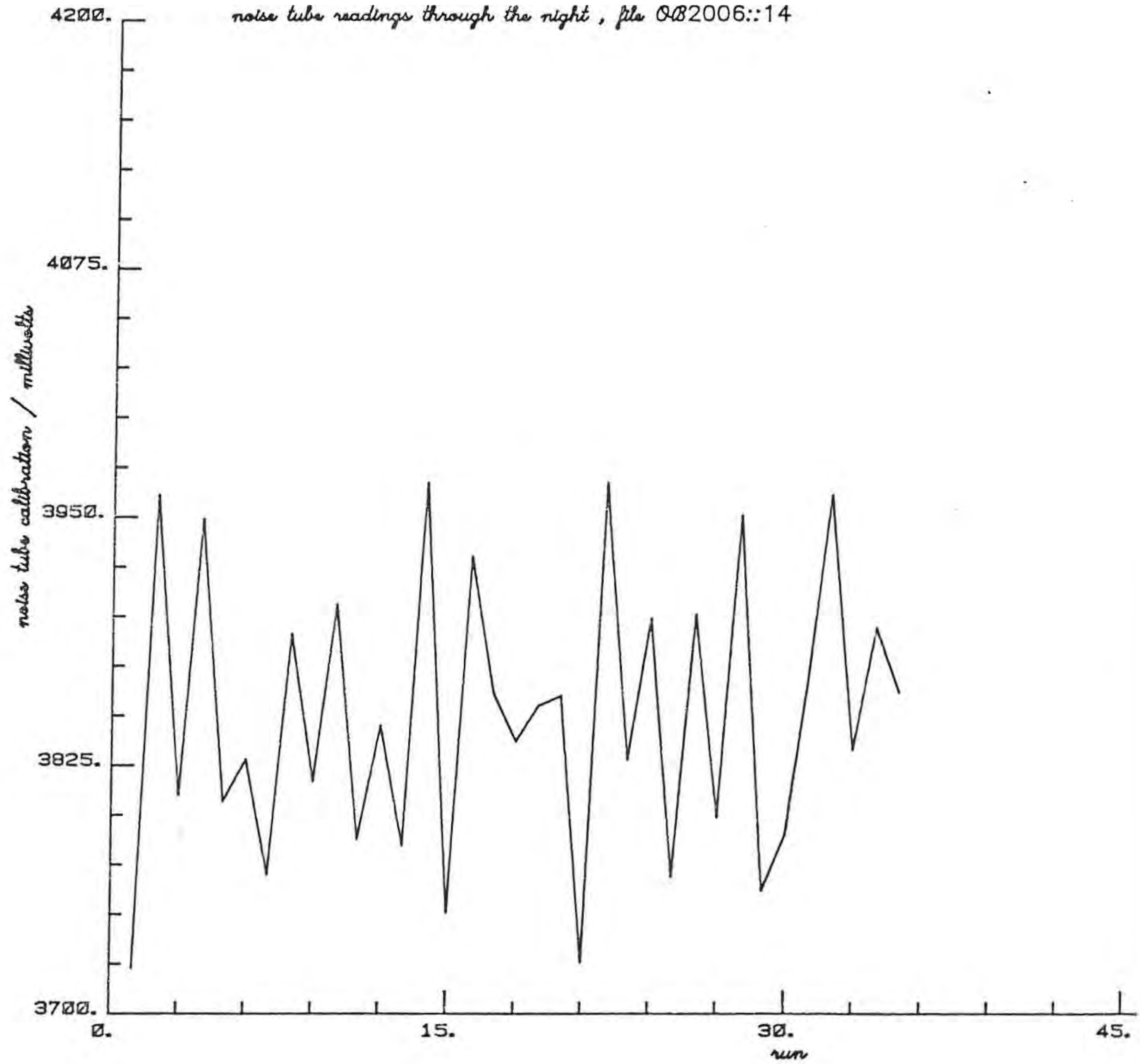


fig. 4.2 noise tube readings for observation 2006, each run is 12 minutes long
plot produced by program BINND

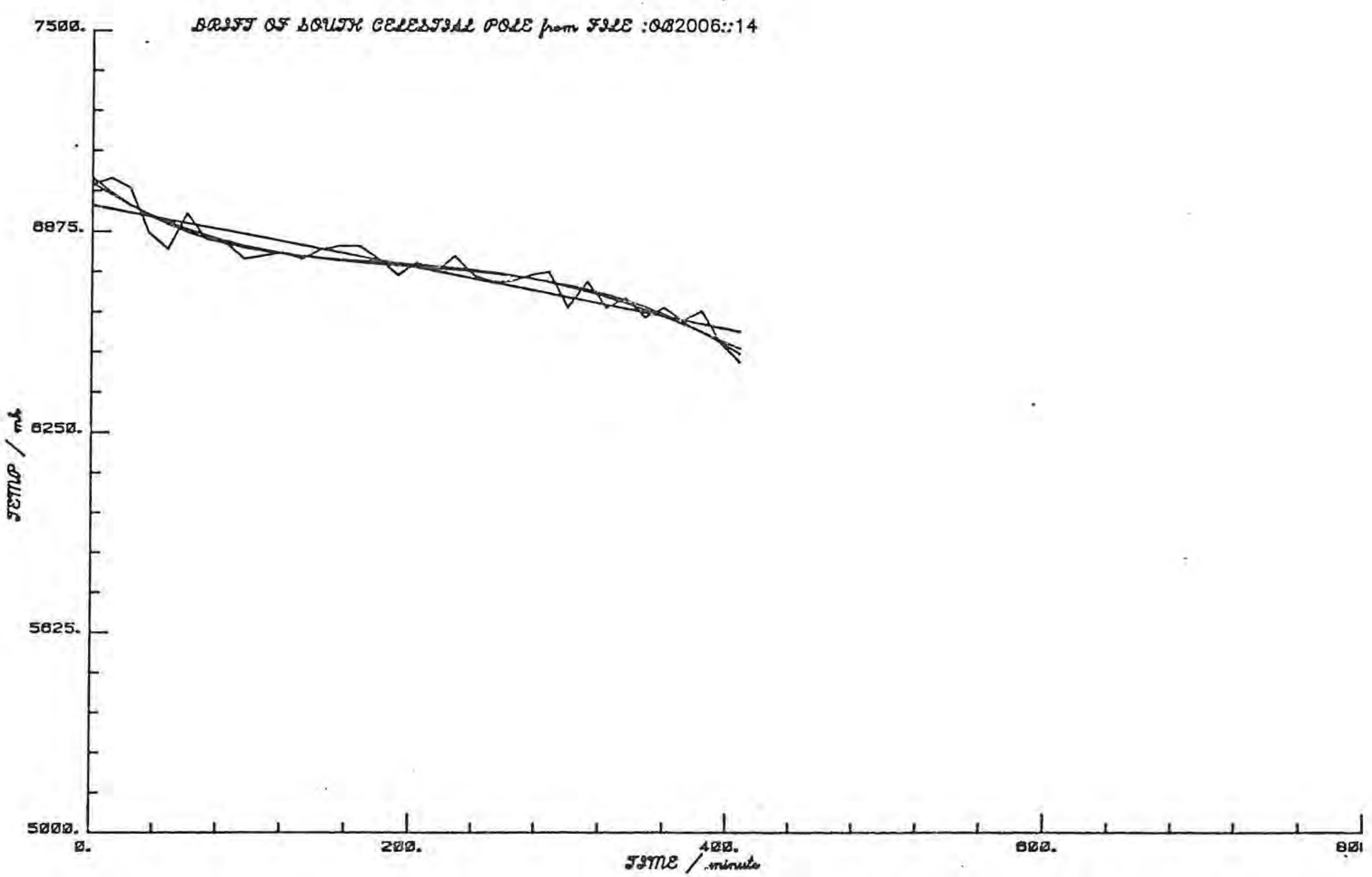


fig. 4.3 antenna temperature for south celestial pole for observation 2006. 1st, 2nd, 3rd and 4th order curves have been fitted. Plot produced by program BACND

4.17a

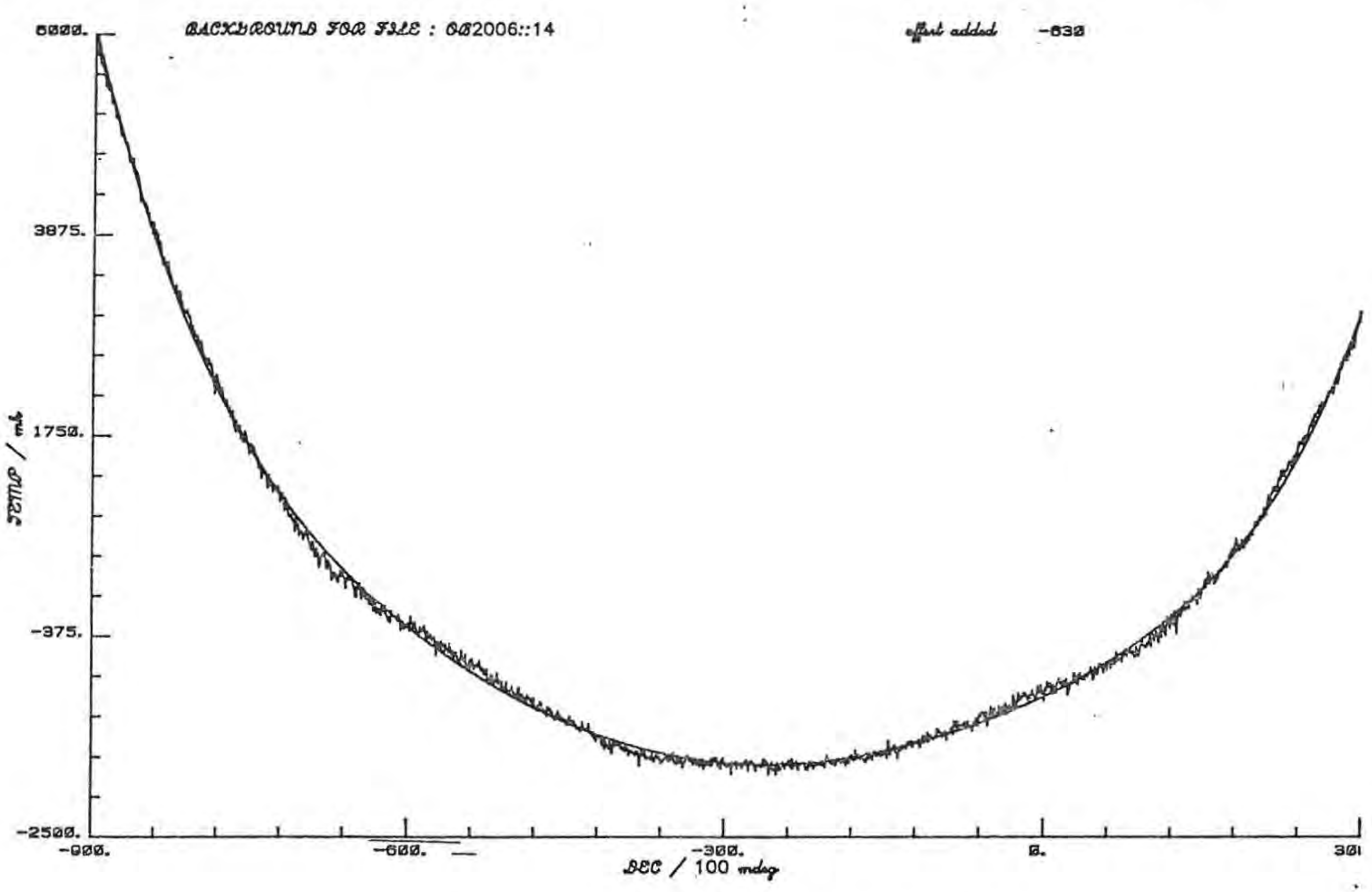


fig. 4.4 background found by program BACND. A 6th order polynomial has been fitted to it

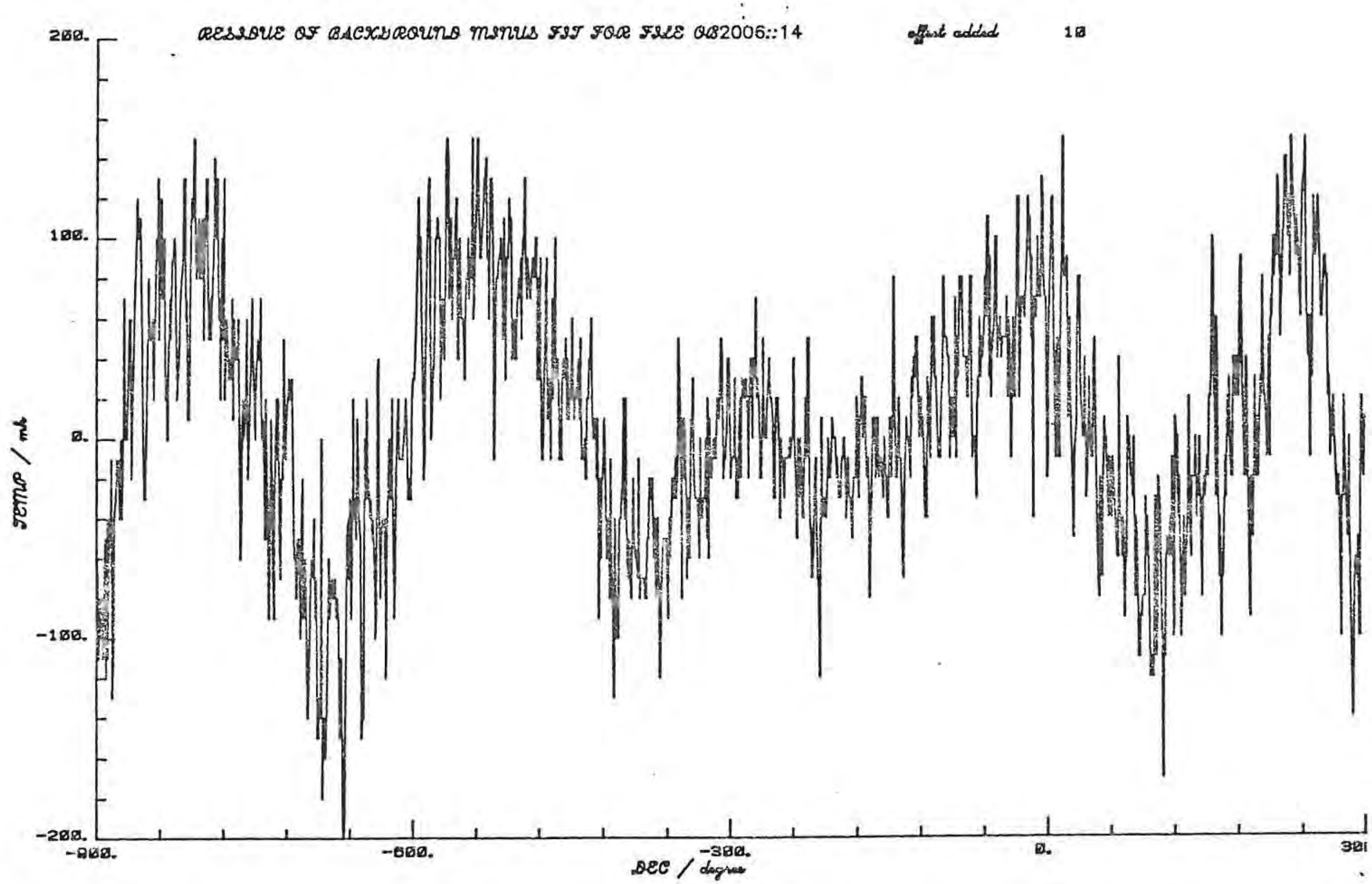


fig. 4.5 residue after subtracting 6th order fitted background from background found by program BACND (fig. 4.4)

4.17d

means that not enough scans were observed for a good background to be found and the observation can be discarded.

HIDND - plots a hide map of the NODDY data, see example in figure 4.6. A running median of 3 is applied to each scan to remove outliers which affect the baselevels of the plotted scans. The rotation of the earth i.e. changing right ascension across a scan, is ignored for a plot of a single scan - the hide program assumes each scan is at a single right ascension. The hide plots are good for showing up bad data points eg. satellite interference.

After each observation these three programs are run and the data are OK'ed or not depending on the results. If not, the observation i.e. that raster, must be repeated. It is very important to have good results for the long scans because they are being used to provide the baselevel for the Rhodes survey. Good observations are sent to Rhodes to be analysed by the following suite of programs.

4.5.2 "long scan" Reduction Programs

The magnetic tapes produced by NODDY, one per observation, are shipped to Rhodes for final analysis. This is because at Rhodes there is a Cyber 70/825 with 100 Mbytes of online disk storage space available for analysing the "long scans" data. A set of programs have been developed to remove drift and background and combine the observations. In this section we will describe these programs and what they do to the data. Preliminary observations were performed with NODDY to serve as test data for these programs and the results of running these programs on the data will be presented in section 4.6. Future work on the "long scans" technique and improvements to the programs will be discussed in section 4.7.

The "long scans" data on tape consist of blocks of 1278 ascii characters. Each block has a header followed by 40 samples. Each sample represents a 0.1 second integration of the DVM and is written to tape as four values - hour

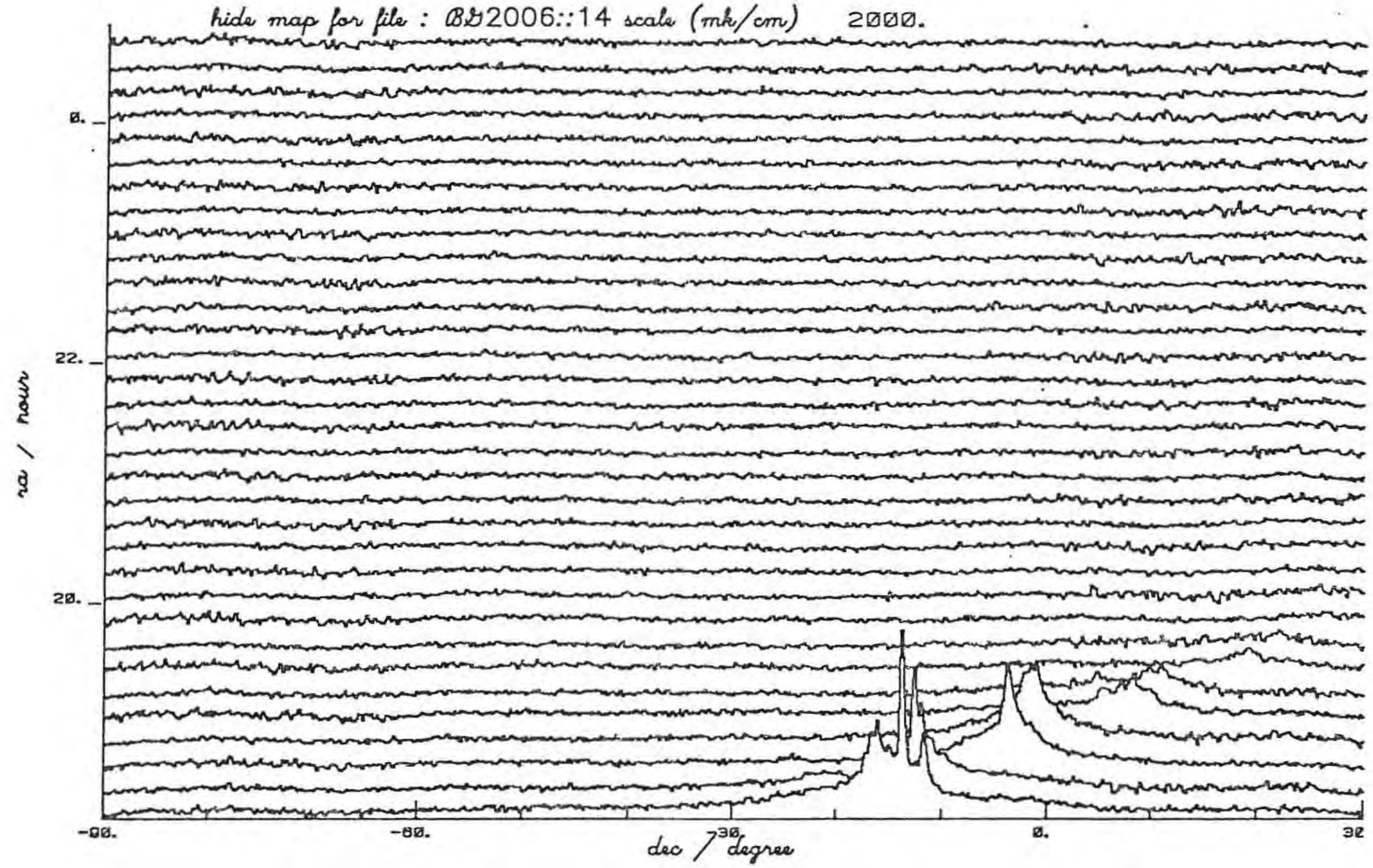


fig. 4.6 hidden line plot of observation 2006 as produced by program HIDND. The galaxy can be seen in the bottom right corner

angle, declination, universal time and DVM reading. These data ~ 12 Mbytes per observation have to be compressed. This process - called binning is performed by a program called BINNOD. To find drift and background there are two programs, MPOLDRF and MFNDBKG respectively. The output of these programs is used as input to a program, MFBIN, which subtracts the drift and background and creates bins $1^o$ wide in declination. These bins are more manageable than the original $0.1^o$ wide bins. They can then be further manipulated or be used to create a coarse grid of the sky (program CRMSKY). A description of the output and philosophy of each program will follow now.

BINNOD : scales (using the DVM units to $T_a$ scaling factor measured by firing the noise tube) and bins the data in $0.1^o$ wide declination bins, using present day declination coordinates to determine which bin a sample falls in. At the same time that a temperature bin is created three other bins, in separate files, are created, containing the mean 1950 right ascension for all the samples in each bin, and the mean 1950 declination and a file containing the number of 0.1 second samples in each bin. These bins are written away as 1 scan per record i.e. 1201 bins per record. Also created is a bin containing the present day right ascension, temperature and number of samples for the pole integration for each scan. The noise tube calibration is extracted for each scan (it is stored as the last sample of each scan by NODDY) and output to the screen monitor by BINNOD.

POLDRF : the first thing to do is to fit a smooth curve to the pole temperature. The reasoning behind this is that because the pole temperature represents a constant point in the sky and it has little noise (because of the long integrations on it) any variations in this can be regarded as drift. Therefore a smooth fit to the pole temperature can be used as a first estimate to the drift for each scan.

Because only every other scan (down scans) has a long integration on the pole this program does not just fit a smooth curve to the pole temperatures but treats them as follows. The maximum number of samples for the sum of two adjacent up and down scans is found. Then each pair of adjacent up and down scans is combined using the (no. of samples / max. no. of combined samples) as the weight for each. The mean of their present day right ascensions is used as the independent variable, and a fourth order curve is fitted to these combined pole temperatures. The fitted temperatures are written away as drift. Some examples of this fit are depicted in figure 4.7. This is only the first estimate to the drift because an improved estimate can be derived by comparing each observation with repeat observation and with other observations at their crossing points. From these comparisons a linear drift can be found for each scan instead of just a single drift value for each scan. This improvement will be discussed at the end of this chapter.

MFNDBKG : because "long scans" are observed by scanning $120^0$ of declination the atmospheric and ground contribution varies considerably over a scan. From the backgrounds found by BACND (see sec. 4.5.1) it is evident that the background is consistently the same shape. Therefore is was decided to carry on finding backgrounds in the same way except instead of finding the 5th lowest point for each declination find the 10th lowest point. Also because of the large errors resulting from a 6th order polynomial fit (up to 100 mK) a smoothed version of the found background is used. Because the observations have drift on them, which will weight the background towards the scans with the most negative drift, this drift must be removed before finding backgrounds. This is done by subtracting the fitted pole temperatures of MPOLDRF for each scan. Then MFNDBKG finds the 10th lowest point for each $0.1^0$ declination for up and down scans separately and for each observation.

4,20a

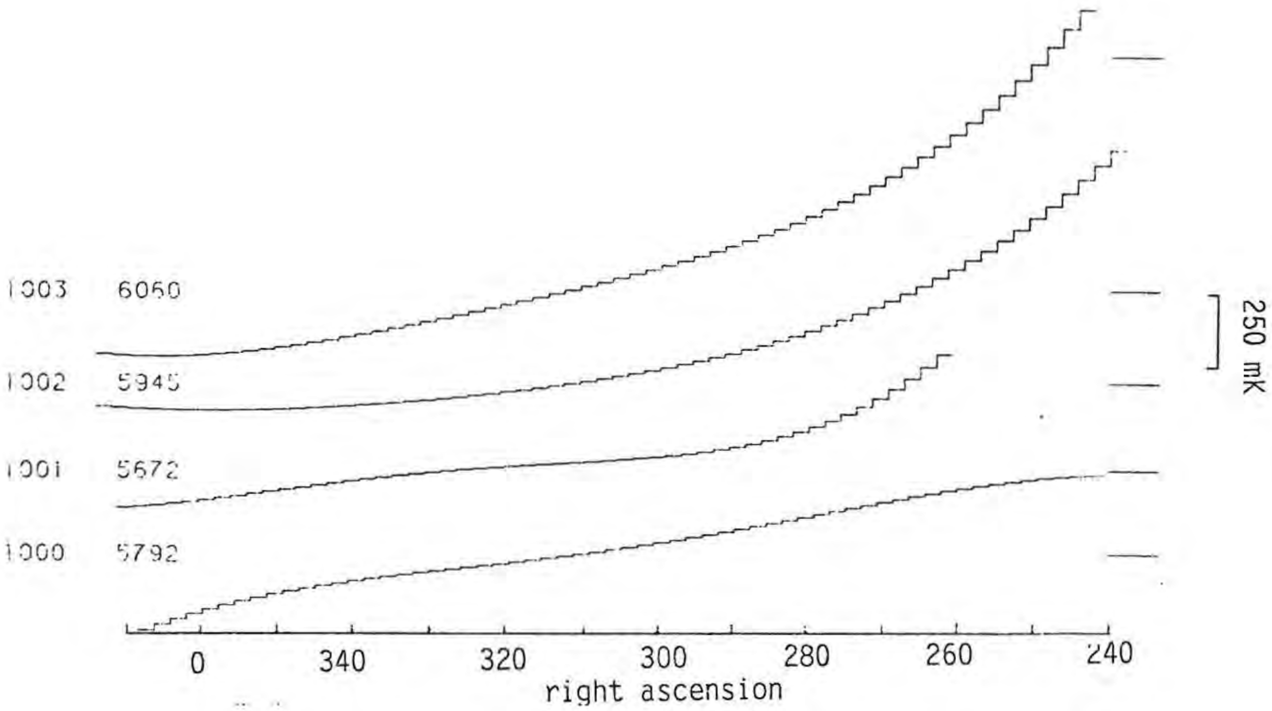


fig.4.7 fitted 4th order curves to pole temperatures for observations 1000-1003. Median temperature for each scan is second value (in mK) from left

The up and down scans are treated separately for caution's sake. Because although they are both only functions of declination, different scanning characteristics which are direction dependent would result in slightly different tracking paths for up and down scans and therefore different backgrounds. Because we are not sure yet that this is not the case, background is found separately for up and down scans. The 10th lowest point is smoothed by fitting a 20 knot (with knots equidistantly spaced) cubic spline in a least squares sense. An example of the resulting backgrounds using the test observations is depicted in figure 4.8. Notice how up and down scans do seem different. The maximum rms error per $0.1^{o}$ bin for the cubic spline fitis 90 mK.These backgrounds are written to a file for use as input to the next program, MFBIN.

MFBIN : this program creates the final large bins which can be more easily analysed and manipulated so that they can be compared with the existing Rhodes survey. Two versions of MFBIN exist, both having the same name. The one outputs data as one scan per record which is a suitable format for doing further reduction. The other version of MFBIN outputs the data as one bin per record for comparison with the Rhodes survey.

Both versions subtract the drift and background found by MPOLDRF and MFNDBKG from the small bins of data output by BINNOD. They then bin the data into $1^{o}$ wide declination bins at every integral declination, using the precessed declinations created by BINNOD. Each bin is labelled by the mean of its precessed right ascension and declination. Because the mean precessed declination of all the bins within $0.5^{o}$ of every integral declination is used to label the binned declinations the labels are not integral declinations. The bins are output differently by the two versions of MFBIN. One version outputs the data as one scan per record. Each bin in the scan is

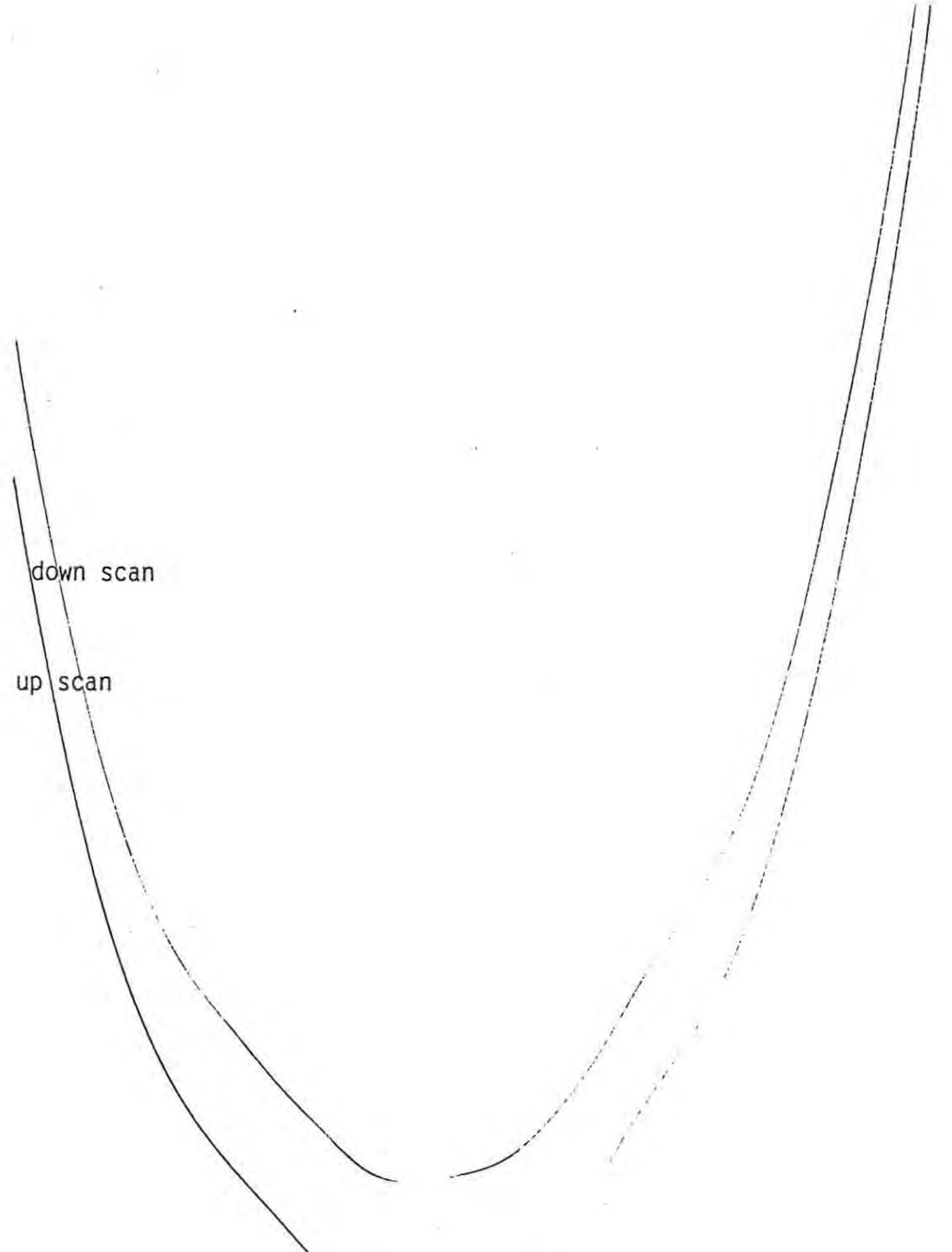


fig. 4.8 20 knot cubic spline fitted in least squares sense to background found by program MFNDBKG. Vertical scale is 250 $mK.cm^{-1}$

written as right ascension, declination and temperature. This form is suitable for further processing of the data eg. removing linear drift along the scans. The other version of MFBIN outputs one bin per record. Each record contains the right ascension, declination, number of sample and temperature for that bin. This form of output is suitable for forming a coarse map of the sky and comparing the bins with the survey maps. This is because they can be sorted in declination and right ascension order. This latter version of MFBIN was used on the test data (see next section) to produce input for a program (CRMKSY) which produced a smooth map of the sky.

## 4.6 "long scans" OBSERVATIONS

"long scans" were observed with program NODDY over the period 23 September to 14 October 1983. Although the maser receiver was not operational over this period and the gasfet was used (see section 2.2 for a description of the two receivers) it was necessary to observe "long scans" so that the technique could be developed. The observing period chosen occurs just before the summer thunderstorms at Hartebeesthoek and consequently the observations were not washed out. Some of the observations were contaminated by clouds. It was assumed that the drift cause by this cloud could be removed by the above described technique. Eleven observations were obtained. Because of problems with using software delays to read the DVMs the noise tube was not calibrated for every observation. This was subsequently sorted out and the last two observations calibrated the noise tube at the end of every scan. The observations cover the right ascension range 18 hours through 0 to 6 hours. The reducing programs were tested out using only a subset of these observations. The best repeat of each raster was used i.e. observations 1003, 2004, 2005, 2002, 2007 and 2003 in increasing raster number order respectively. The programs BINNOD, MPOLDRF, MFNDBKG and MFBIN were applied to these observations. The bins output by MFBIN were used to create a map of the southern sky on a $1^{\circ}$ by $1^{\circ}$ grid in 1950 coordinates. The program written to do this is called CRMSKY. It reads the output of MFBIN which is sorted on increasing order of declination and right ascension first. Then it creates a bin every degree which is the average of all the data within $2.5^{\circ}$ of that bin, taking into account the $\cos\delta$ compression. In other words it convolves the data with a top hat which has a base of $5^{\circ}$x$5\cos\delta^{\circ}$ binning a value every $1^{\circ}$. The output of this program had terrible scanning effects of 500 mK right across the map. On inspection it was found that observations 2005 and 2007 differed from the other observation by up to 1000 mK in places. These two observations were both observed when there was heavy cloud in the morning. Therefore they were discarded and CRMSKY was rerun using the remaining 4 observations. The result is displayed in figure 4.9. Scanning effects are still visible but they are not as bad. We will now discuss these data and see if they can be used to put the Rhodes survey on a single baselevel.

First notice the real features which occur on the data - (i) the galactic plane in the right ascension range 18 hours to 20 hours and declination $-40^{\circ}$ to $+30^{\circ}$, (ii) the Large Magellanic Cloud at 6 hours and $-67^{\circ}$, (iii) the extended source centred on 19h50m and $-69^{\circ}$, this appears on the 408 MHz survey too (Haslam (1982)), (iv) the spur extending out of the galaxy at 19h30m and $-30^{\circ}$.

The top $2.5^{\circ}$ of declination have been chopped off. This is as a result of the convolution by program CRMSKY. The worst effect on this map though is the artificial source occurring at 4h15m and $9^{\circ}$ declination. This is a very strong satellite which rose every morning during the observing period at Hartebeesthoek. It occurred on all the observations and its strength is depicted in the hide plot shown in figure 4.10. The square sources on either side in declination of the satellite at 5h30m are also due to the satellite. The satellite is responsible for the stripe occurring across the data at $10^{\circ}$ declination and $15^{\circ}$ wide. This is because the satellite must have caused negative spikes in the data and resulted in bad backgrounds being found over that declination range. Also noticeable on the data is a downward drift across left to right of approximately $1^{\circ}$ kelvin. It is difficult to ascribe this to a single cause. It could be the combined affect of going to a colder part of the sky and scanning effects resulting from using only 4 noisy observations or it could be a result of the data processing. It will not be possible to decide until we have better data available.

4.24a

fig. 4.9 the combined "long scan" data on a 1°x1° grid, convolved with a 5°x5° top hat, contours are labelled in order 300,350,400,450,500,550,600,700,800,900,1000, 1200,1400,1600,1800,2000,2500,3000,3500,4000,4500,5000,6000,..,10000

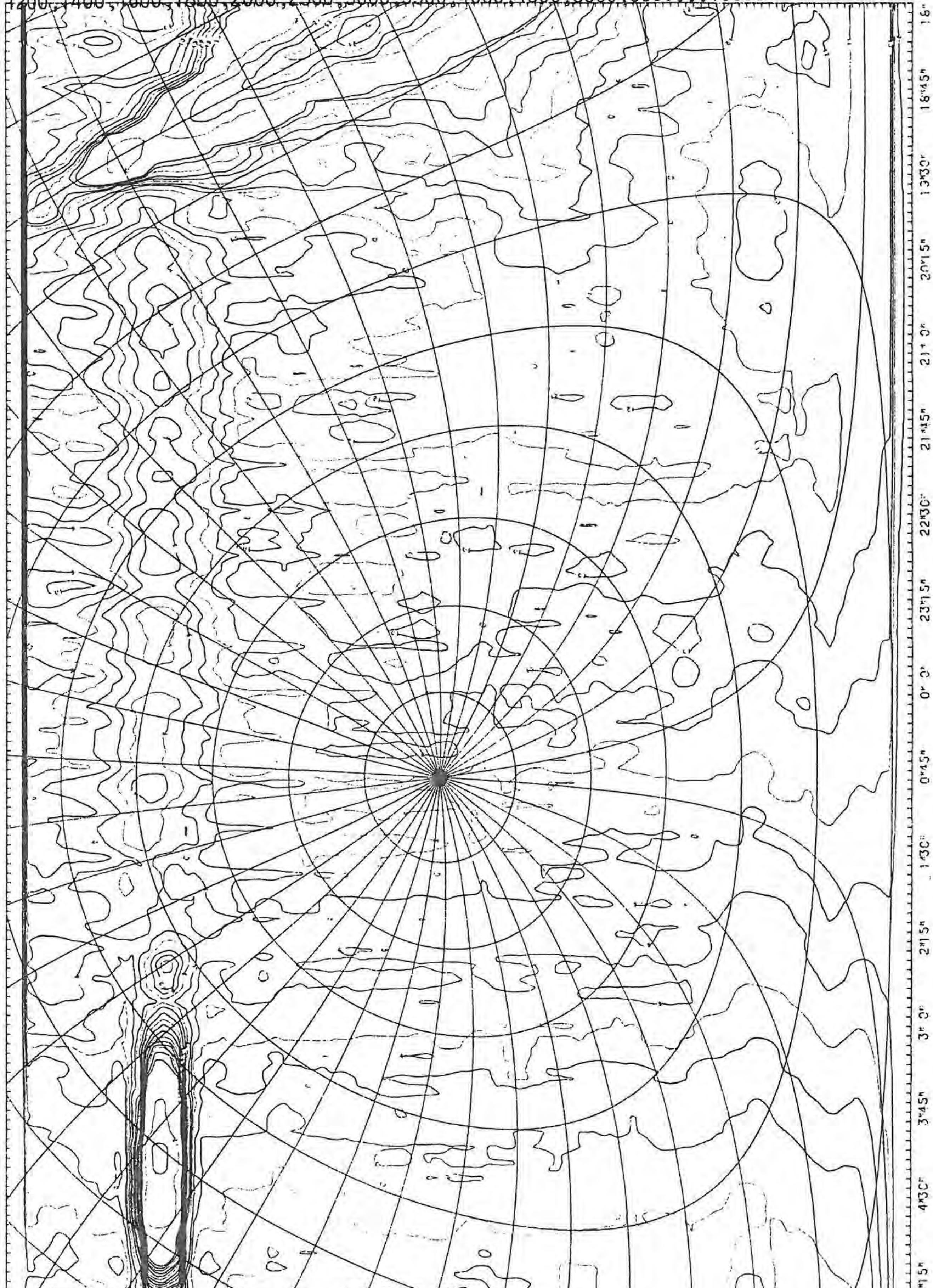

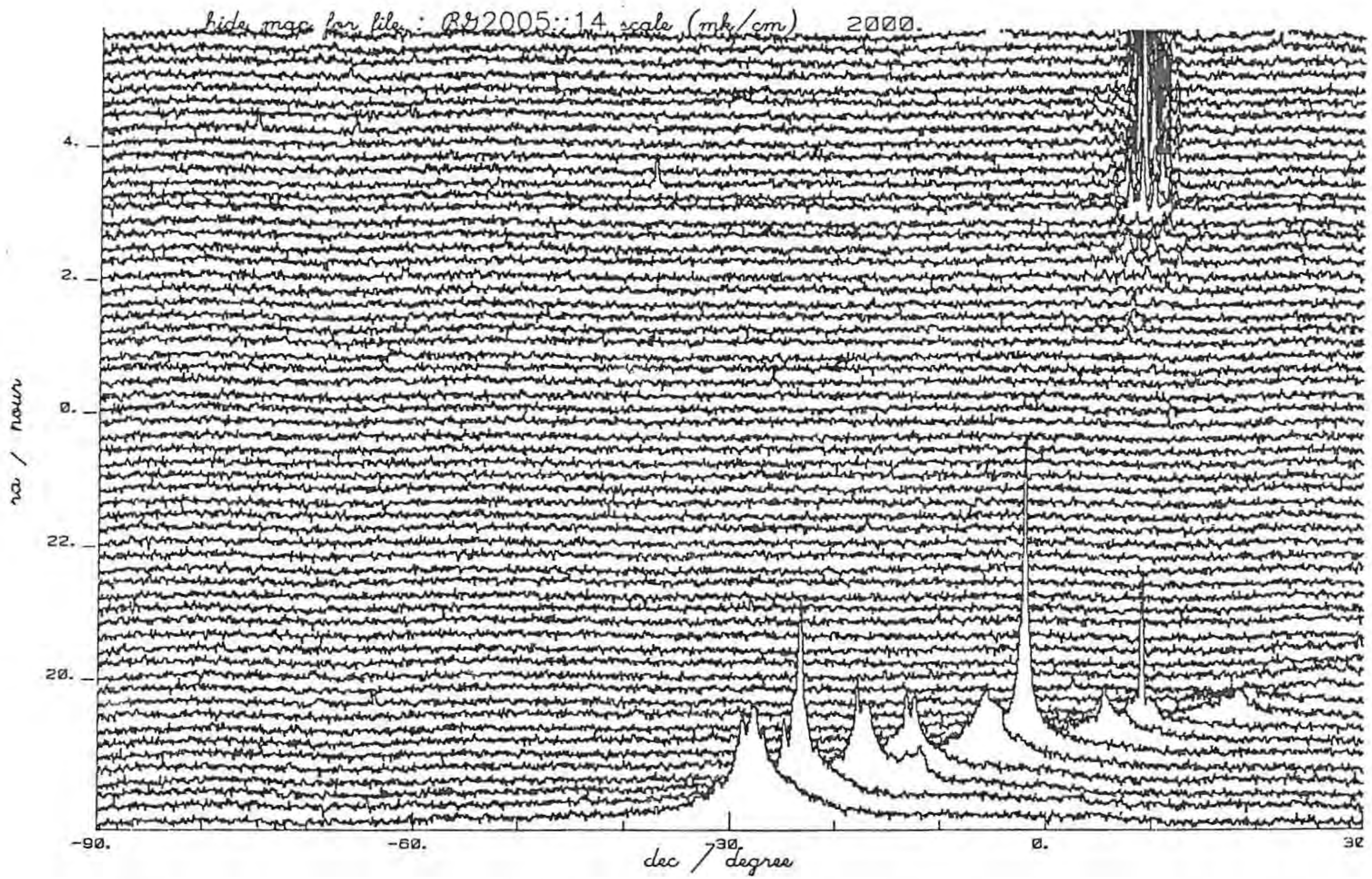


fig. 4.10 hidden line plot of observation 2005 produced by program HIDND. Depicts satellite interference in top right hand corner at dec = 10°

4,24b

What is evident though is that these data are not good enough to pull the Rhodes survey flat. They are too noisy - partly because the gasfet was used and partly because only 4 observations were used. Secondly the satellite has also made them unusable over the positive declination range.

What they do immediately reveal is that repeats of rasters are necessary, a better receiver is needed and that it is not enough to combine the observations without referring them to each other.

## 4.7 FUTURE WORK AND IMPROVEMENTS FOR THE "long scan" TECHNIQUE

Besides the fact that the "long scans" need to be observed with a better receiver and repeats of each raster need to be observed there remains other work to be done on the "long scan" technique. In this section we will discuss some of the things which need to be done and briefly outline how they could be done.

Firstly the calibrator observed at the start and end of every observation by program NOD13 needs to be utilised. This can be done either by calculating the effective aperture as outlined in section 2.2 from which a main beam $T_a$ to $T_b$ conversion factor can be obtained. Alternatively antenna temperatures can be determined for the calibrators and then the ratio of the observed to calibrated antenna temperature for each night can be used to scale up the data for that night. Whichever method is implemented the fluxes which are used for each calibrator should be referred to a single well calibrated source eg. CAS A.

On the data processing side the following needs to be done. Instead of using a single drift value for each scan a value should be interpolated from the curve fitted by MPOLDRF to each bin i.e. assume smooth drift across a scan. This applies to MFNDBKG and MFBIN which both use drift. Secondly, because the scans cross over each other they can be referred to each other at their crossing points and forced to agree there. This will remove the scanning effects (see fig. 4.9 ) and make the combined data less noisy. This type of process has previously been done with a similar set of scans (Haslam (1974)). It involves finding, for each scan, all the differences between it and other scans crossing it at their crossing points. This will necessarily involve an interpolation process because the scans do not always cross exactly at their binned right ascensions and declinations. A straight line is fitted to the differences for each scan as a function of right ascension. The fitted straight lines are then used to correct each scan. Note, up scans are only crossed by down scans and vice versa. Therefore it must be done separately for both cases. This is an iterative process and needs to be repeated a few times. Haslam (1974) has found that this iteration converges faster if instead of correcting each scan by the fitted straight line a fraction (0.7) of the line is used. For this technique to be implemented the version of program MFBIN must be used which produces 1 scan per output record. It will also be easiest to use present day coordinates for labelling the bins output by MFBIN instead of using precessed coordinates.

Once the "long scans" have been meshed together in the above manner we still need the absolute brightness temperature of the pole before we can use the "long scans" data to calibrate the Rhodes Survey. For this we can either use the extrapolated value determined in section 4.3 of 3.154K or we can measure the temperature absolutely. The extrapolated value is not very accurate. Firstly because we are not sure of the spectral index and secondly because it was extrapolated from the 408 MHz measurement.

It would be more accurate and generally more useful to measure the south pole absolute temperature at 2.3 GHz using the Hartebeesthoek telescope. This is a very involved and difficult measurement to perform. Two excellent references on the topic are Price (1969) who describes this measurement at 408 MHz and Stelzried (1982) who discusses the problem more generally.

Finally we need to discuss converting the Rhodes survey to main beam brightness temperatures using the "long scans" data. A good way to do this would be to convert the "long scans" data to main beam brightness temperatures. The "long scans" data when finally reduced (eg. fig 4.9) is of full beam antenna temperatures. To convert to main beam brightness temperatures we first need to estimate the term $T_{SL\ gal}$ (section 4.2). This can be done by using the beam pattern of section 2.2.1. If we define that beam as the full beam then we can determine the extra contribution term $T_{SL\ gal}$ by convolving the sidelobes of that beam with the "long scan" data. This is similar to the method of Pauliny-Toth and Shakeshaft (1962). This correction term must be calculated for each data bin of the "long scans" data and used to correct it. The resulting "long scans" data will then be in main beam brightnesses and a main beam brightness temperature conversion factor can be used to scale it to brightness temperatures. These data can then be directly compared to the Rhodes survey maps to obtain a scale factor and zerolevel correction for each map as a function of right ascension.

## 4.8 CONCLUSION

A technique has been developed which can be used to put the Rhodes 2.3 GHz survey on a baselevel referred to a single point in the sky, the south pole, and can be used to calibrate the survey in terms of main beam brightness temperatures. The observing program has been written and tested and is working. Data processing programs have been written which allow a smooth map ($5^{o}$x$5^{o}$ resolution) of the sky to be produced. Although "long scans" observations were carried out and reduced using these programs the observations were not good enough to allow the smooth map (fig. 4.9) to be of any use in calibrating the Rhodes survey. Therefore we cannot be sure that the "long scan" technique produces a drift-free map of the sky.But it is felt that sufficient discussion has been entered upon and effects considered in this chapter for another worker (with more time at his/her disposal) to complete this technique and verify it.

# CHAPTER 5

## INTERMEDIATE LATITUDE SOUTHERN HEMISPHERE CONTINUUM RADIATION AT 2.3 GHZ

### 5.1 INTRODUCTION

Although the Rhodes survey is not completed there are sufficient preliminary results for analysis. Jonas (1982) did some groundwork on A14D63 (see chapter 3 to find out which areas the maps refer to) which consisted of identifying some areas of extended galactic brightness and all the extragalactic sources down to a minimum flux of 1/2 Jy. But he said very little about the galactic features and made no attempt to investigate the origin or type of radiation of the galactic features he found. We have almost twice the amount of data Jonas (1982) had and our task is even more monumental. It has been decided to investigate only the large features ( larger than 100 beam areas = 19 square degrees) in this thesis. Because of this size criterion they are all galactic features.

This chapter and the next will discuss the results of the data. The discussion has been divided into two parts. Firstly, features occurring at $40^{\circ} > |b| > 10^{\circ}$ will be discussed. These have been termed intermediate latitude features and mostly occur within 500 pc of the sun. They also have the advantage of not being confused with the disk emission. All features satisfying this criterion will be discussed in this chapter. Chapter 6 will discuss the appearance of the 2.3 GHz radiation in the region $|b| < 10^{\circ}$.

The data under discussion are the joined map of A14D63 and A12D26 (figure 3.12) and a single feature occurring in A04D80 (figure 3.2). Because these are intermediate latitude features and therefore unlikely to be related to the disk component of the galaxy we can subtract the disk component found in section 3.3.3 to enhance these features. The resulting data are displayed as a greyscale photograph in figure 5.1. An overlay is attached to this figure

S.1a

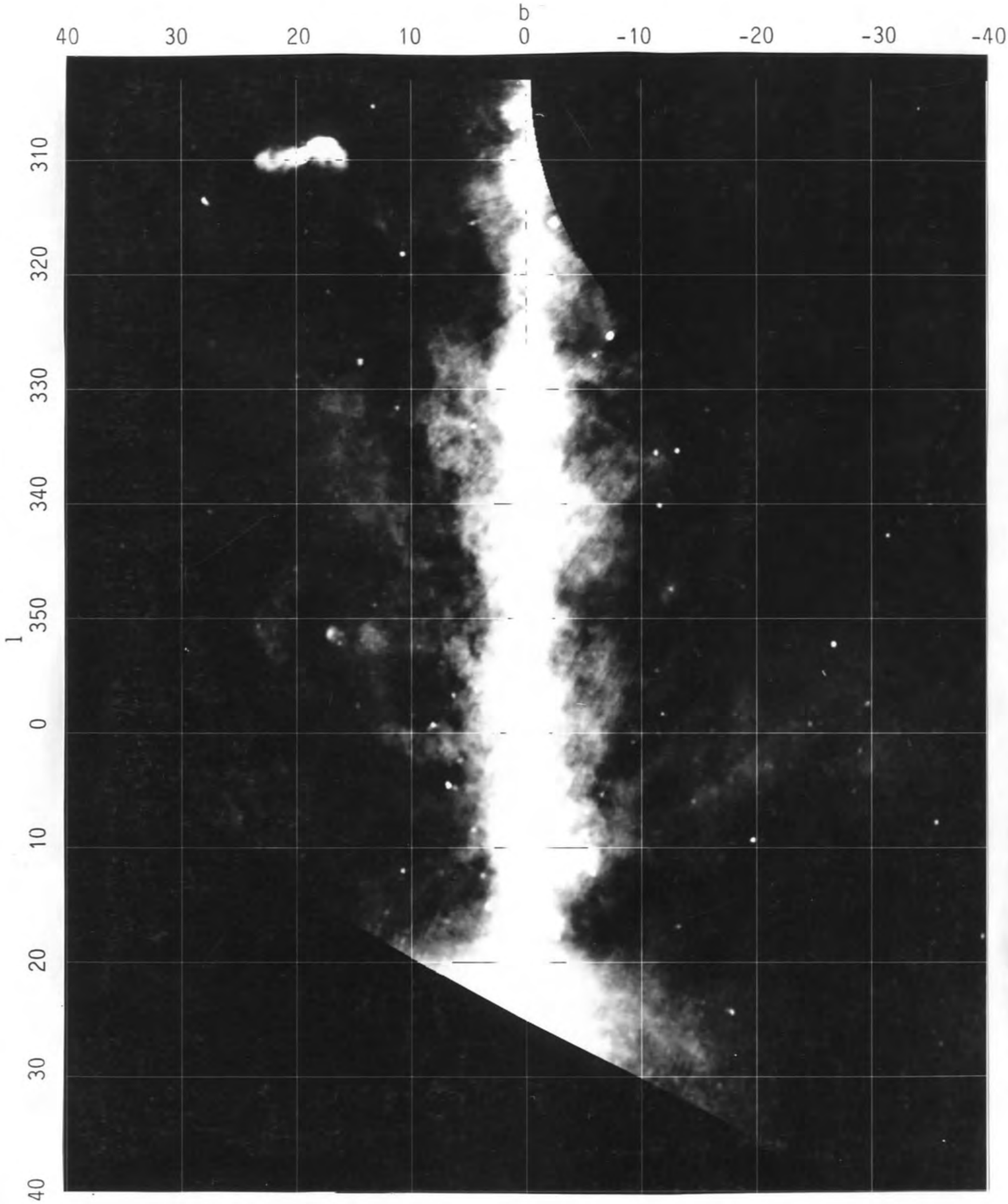


fig. 5.1 grey scale image of the region 13HR - 23HR and -61° - -7°
an underlying disk component (fig. 3.13) has been subtracted

5.1a

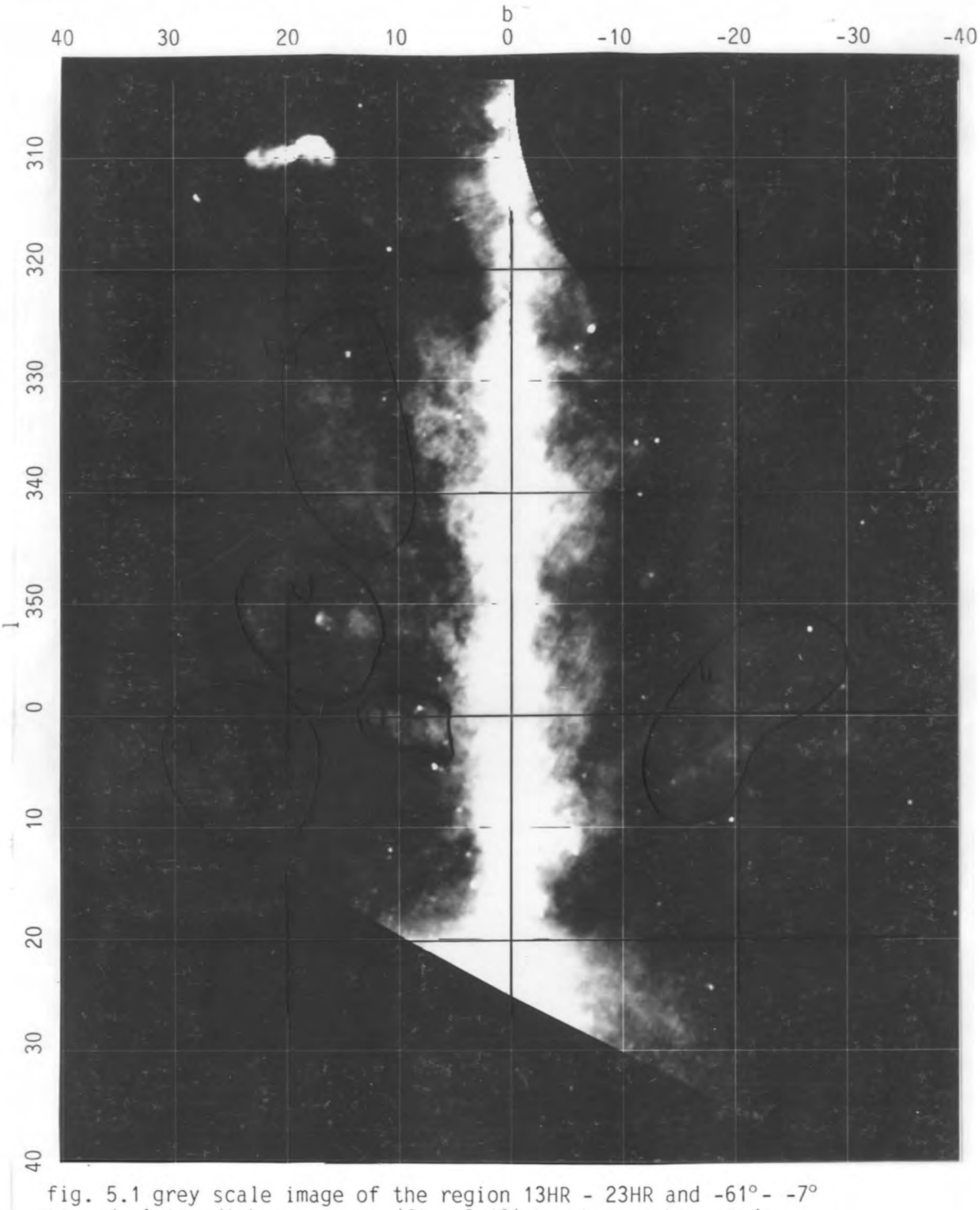


fig. 5.1 grey scale image of the region 13HR - 23HR and -61° - -7°
an underlying disk component (fig. 3.13) has been subtracted

so that the features discussed can be easily recognisable. The manner in which objects have been chosen for discussion is as follows - (i) the optronics photographs (figures 3.2 and 3.12) were studied and all patches of enhanced radio brightness (they show up as whiter than their surroundings on the greyscale photographs) which seem to form a smooth structure like an arc or loop or whatever were circled, (ii) other maps in other parts of the electromagnetic spectrum (mostly radio continuum and HI but also H$\alpha$, $\gamma$ ray and star atlases) were studied to confirm the existence of these features, (iii) if no other evidence for a feature was found then the feature is not discussed.

It will be noticed that only 7 features are discussed here compared to Jonas's (1982) 20, and he used only half the data used here. This is because these observations represent the integrated emission of all the ionized gas along the line of sight and are very confused. It is therefore impossible to derive distances for the features from these observations alone. Consequently a large number of the possible features could not be immediately related to other observations because their distance was not known.

Note that the lower envelope found in section 3.3.3 and subtracted from the data to yield figure 5.1 is not necessarily only synchroton emission. The amount of thermal and non-thermal radiation at any point will vary not only according to the spectra of the two components but also according to, among other things, the amount of gas, the magnetic field and the temperature of the gas at that point.

To assist in identifying the features to be discussed, figure 5.1 has also been displayed as a contour map, with only the low contours drawn, in figure 5.2. Because only the low contours have been drawn only the intermediate

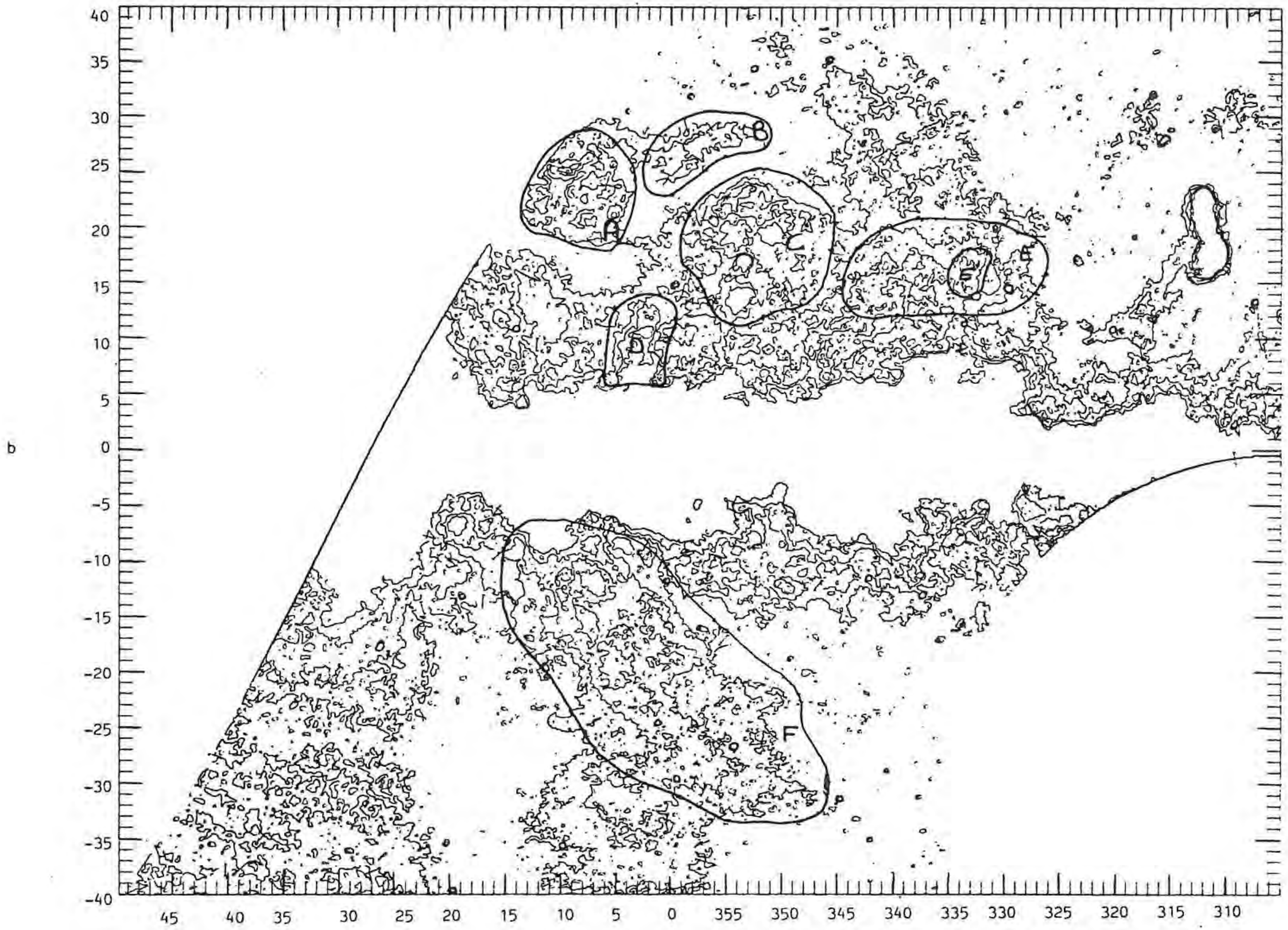


fig. 5.2 : contour plot of joined data set with galactic disk subtracted. Features to be discussed are marked. Contours are 100, 150, 200, 250 mK Ta and are numbered consecutively from 1.

latitude features are depicted. Note the radio galaxy Centaurus A at ($310^{o}$,$20^{o}$). The blank space around b=$0^{o}$ is the plane of the galaxy which all lies above 500 mK. In the ensuing discussion features will be identified and outlined both on the transparency overlaying figure 5.1 and on the large contour map of the region, figure 5.2. The features will be labelled in increasing alphabetical order and the new galactic coordinates quoted of their estimated centres. Other observations of the each feature will be mentioned and discussed if they are relevant to the radio continuum data. If there is enough information for a feature we will try to develop a consistent theory of the possible origin and nature of that feature. But it must be remembered that because of the small amount of information available at 2.3 GHz alone the main purpose of this section is to point out features which have not been observed at $\nu$ > 1 GHz before and serve as a finder chart for further higher resolution observations at 2.3 GHz and at other frequencies.

## 5.2 PROMINENT GALACTIC FEATURES

Region A: HII region surrounding Zeta Ophiuchi (l",b")=(6.7° 22.4° )

This HII region is conveniently situated out of the plane and is relatively unconfused with the disk component. Although it occurs at the edge of the mapped region there is evidence to suggest that most of the nebula in the radio region has been mapped. This is because an H$\alpha$ photograph of the nebula (Morgan et al (1955)) has an identical appearance. The nebula has been extracted from the raw data of A12D26 and Fourier filtered. A plot of the nebula with the position of the star Zeta Ophiuchi drawn appears in figure 5.3. Note the sharp cutoff following a line from ($22^{o}$,$12^{o}$) to ($6^{o}$,$30^{o}$). This represents the end of the map A12D26, i.e. declination -$7^{o}$. The shape of the nebula in H$\alpha$, as depicted in a photograph by Sivan (1974) has been

5.2a

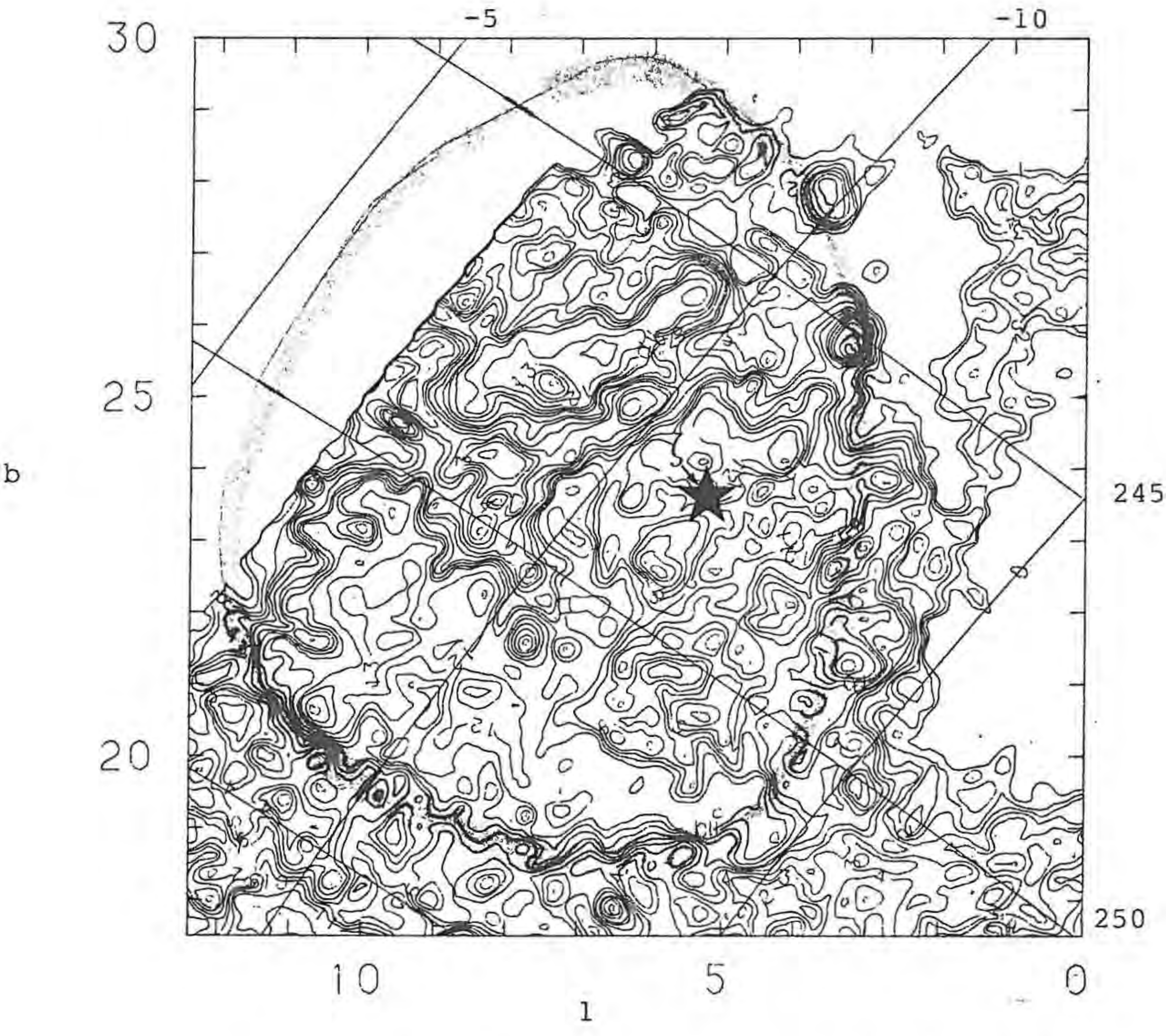


fig. 5.3 : contour map of Zeta Ophiuchi nebula Fourier filtered with a sharp cutoff at 3.5 reciprocal degrees. Contour interval is 10 mK for Ta less than 310 mK and 20 mK for Ta greater than 310 mK. The lowest contour is 200 mK
Thick line outlines shape of Hα radiation, from Sivan (1974)

superimposed on figure 5.3. From this we can see that most but not all of the nebula has been included. Because the nebula is so ideally situated and clearly defined it will serve as a case study for deriving physical parameters of an optically thin HII region at 2.3 GHz.

First we must determine the shape of the background. From figure 5.3 we can see there is a sloping background underlying region A. It has a downward slope away from the plane of the galaxy. This can be understood as emission related to the disk of the galaxy - either to the disk continuum or to foreground radiation situated in the immediate neighbourhood. Both these types of contribution would fall off in the observed manner. Whatever the case may be this contribution must be removed from the map of Zeta Ophiuchi nebula if we want it on a flat background so that we can measure its flux correctly. The background surface was obtained by plotting the lowest point along each line of constant latitude for $0^{o}<l<15^{o}$ as a function of latitude. This resulted in a fairly noisy curve with the Zeta Ophiuchi nebula evident as a lump centred on ~ $25^{o}$ latitude. A series of straight lines were estimated by eye and fitted to the lower of these points. This was subtracted from the nebula, it was assumed the background was a function of galactic latitude only and therefore the same value was subtracted for each constant latitude. The resulting nebula map (figure 5.4) has a flat background.

To derive the physical parameters of a nebula we need to make certain assumptions. If we assume a uniform electron temperature throughout the nebula and assume it is optically thin, then

eq.5.1 $$T_b = T_e \tau_c$$

where $T_b$ = brightness temperature in K

$T_e$ = electron temperature $\sim 10^4$ K

$\tau_c$ = optical depth << 1.

5.4a

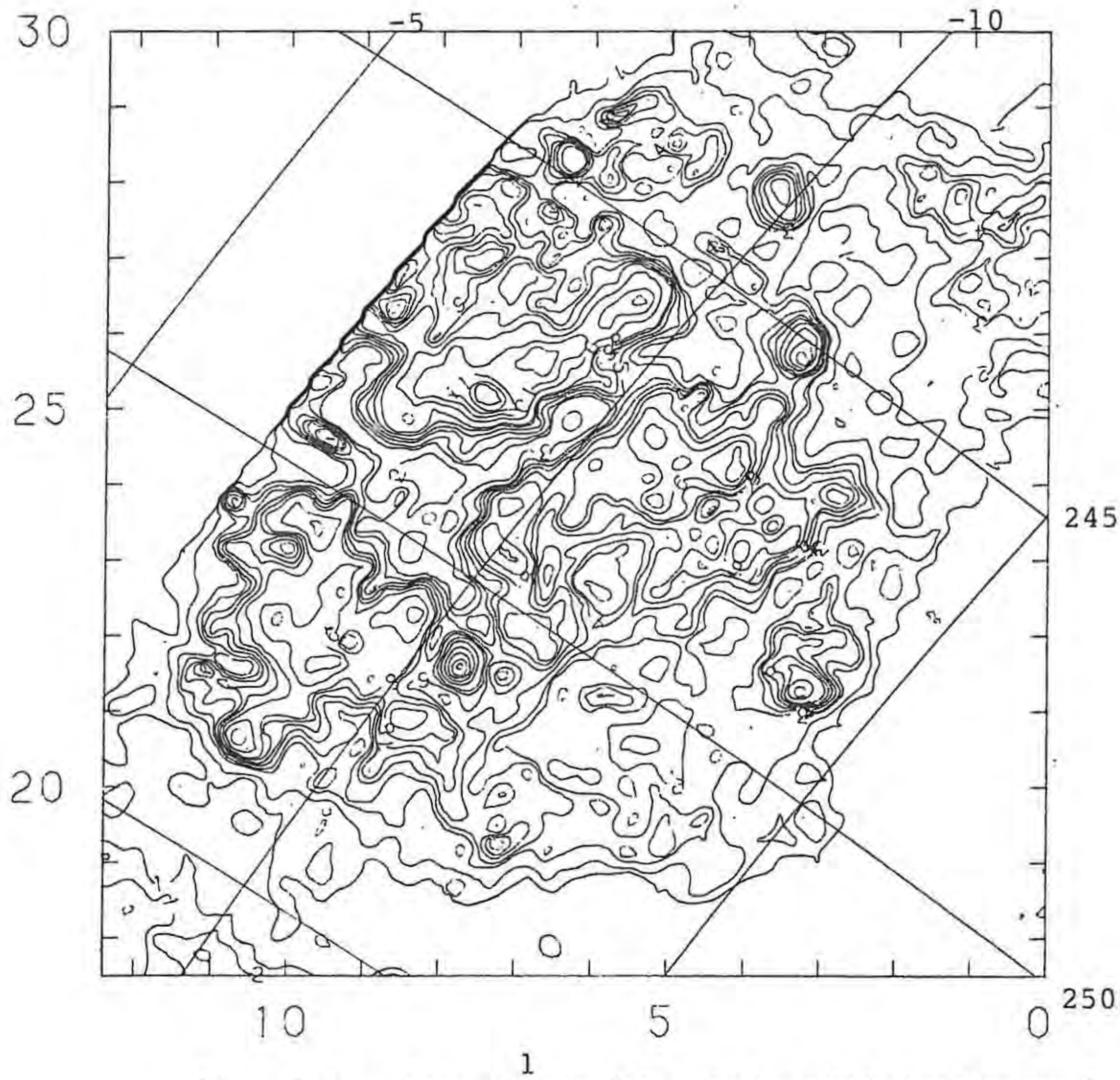


fig. 5.4 : Zeta Ophiuchi nebula with background subtracted. Contours are Ta = 100, 125, 150, 160, 170, 180, 190, 200, 220, 240, 260, 280, 300, 320 mK respectively.

$\tau_c$ for free-free emission (the case here) can be approximated by

eq.5.2 $$\tau_c = 8.235 \times 10^{-2} \times T_e^{-1.35} \times \nu^{-2.1} \times E$$

where $T_e$ in K, $10^4$ K

$\nu$ in GHz,

E = emission measure , in $pc.cm^{-6}$, is defined in eq.5.3.

eq.5.3 $$E = \int_0^{\ell} N_e^2 \, dx$$

and $N_e$ = density of electrons in $cm^{-3}$

$\ell$ = maximum path length through nebula.

Equation 5.2 is an approximation to the true $\tau_c$ which was derived by Oster (1961). A correction term $\alpha$, where

eq.5.4 $$\alpha = \tau_c(\text{Oster})/\tau_c(\text{approx}),$$

is tabulated by Mezger and Henderson (1967) but is not included here because over the range of likely $T_e$'s (7000 to 10000 $^oK$) it results in an error of less than a percent, which is minimal compared to the other errors which arise.

From the definition of flux and the above expression for $\tau_c$ we can derive the emission measure and electron density of the nebula as follows -

$$S = 2k/\lambda^2 \int T_b \, d\Omega$$

From equation 5.1

eq.5.5 $$S = 2k/\lambda^2 \int T_e \tau_c \, d\Omega$$

and from equation 5.2

$$= 2k/\lambda^2 \times 8.325 \times 10^{-2} \times T_e^{-0.35} \times \nu^{-2.1} \times E \times \int_{\text{source}} d\Omega.$$

Substituting all the parameters and converting watts to janskys we arrive at

eq.5.6 $$S = 93.123 \times E \times \int_{\text{source}} d\Omega \text{ janskys}$$

therefore

eq.5.7 $$E = S \times 1/93.123 \times 1/\int_{\text{source}} d\Omega \;\; pc.cm^{-6}.$$

In the above calculations we have assumed a cylindrical geometry in which the cylinder lies along the line of sight. Thereby, assuming too that the electron density is constant throughout, E can be assumed constant across the source and taken outside of the integration in equation 5.5

From E we can derive the electron density and mass of ionized hydrogen using the following assumption for the distribution of $N_e$. If we use equation 5.3 and a cylinder of constant $N_e$ and length (along the line of sight) of 2R.

eq.5.8 $$E = 2RN_e^2$$

where R is the radius of the nebula in parsecs

and $N_e$ is in $cm^{-3}$.

For acylindricalnebula, as we assumed above

eq.5.9 $$R = (\sin(\theta_{neb}/2)) \times D$$

where D is the distance to the nebula in parsecs

and $\theta_{neb}$ is the angle subtended by the radius of the nebula, at D.

Note $\theta_{neb}$ can be derived from $\theta_{obs}$ on the map in the following way. Because $\theta_{obs}$ has been broadened by being convolved by the telescope beam we use the following equation to get $\theta_{neb}$

eq.5.10 $$\theta_{neb} = (\theta_{obs}{}^2 - \theta_{tel}{}^2)^{1/2}$$

where $\theta_{tel}$ = half power beam width , estimated from beam pattern $= 0.333^o$.

Then from equations 5.8 and 5.9

eq.5.11 $$N_e = (E/2D\sin(\theta_{neb}/2))^{1/2}\ cm^{-3}$$

The calculations for mass and number of Lyman continuum photons can now be performed if we still assume acylindricaldistribution of $N_e$. The mass of the ionized gas in the nebula is

eq.5.11 $$M_{HII} = m_H x V x N(H)$$

where $m_H$ = mass of one hydrogen atom, $1.66 x 10^{-27}$kg

$V$ = volume of nebula

$N(H)$ = density of protons in nebula,

$= N_e$

for a nebula consisting purely of ionized hydrogen , or

$= N_e(1+N_{He}/N_H)^{-1}$

for one containing a significant fraction of $N_{He}$. From studies of the Orion nebula (Goudis (1982)) $N_{He}/N_H = 0.1$.

If we assume the number of recombinations equals the number of Lyman continuum photons, i.e. equilibrium, we can obtain $L_c$ as follows

eq.5.12 $$L_c = V\text{xno. of ions}\times N_e \times (\beta-\beta_1)$$

where $\beta-\beta_1$ = is the recombination rate to the excited levels of H minus the first level since recombination to that level yields a photon capable of ionizing an H atom and is absorbed immediately.

For a cylindrical distribution of HII and using $\beta-\beta_1$ from Goudis (1982)

eq.5.13 $$L_c = 2\pi R^3 \times N_e^2 \times 4.10\times10^{-10} T_e^{-0.8}$$
$$= 4.749\times10^{43} R^3 N_e^2$$

for $R$ in parsecs

$N_e$ in $cm^{-3}$

and $T_e = 10\ 000\ ^oK$.

We will now apply these equations to the Zeta Ophiuchi nebula and compare the results with those obtained by other means for the same region.

Because a background surface has already been subtracted from figure 5.5 all that remains to be done is to measure the flux of the nebula. Program IMAGE (see section 3.3.1) was used to measure the flux. A base level of 130 mK was used and the total flux measured for the rectangular region $(2.2^o, 18^o)$ to $(11.8^o, 30.1^o)$. The result is (1 sigma errors are quoted)

$$S_{2.3\text{ GHz zeta oph}} = 266 \pm 50\text{ Jy}$$

$$\int_{\text{zeta oph}} d\Omega = 0.0210 \pm 0.002 \text{ steradians}$$

Using the above formula for E

$$E = 136 \pm 39 \text{ pc.cm}^{-6}$$

To get $\theta_{neb}$ we use $\theta_{obs}$ equal to the geometrical mean of $\theta_1$ and $\theta_b$

$$\theta_{obs} = (10.5^o \times 10^o)^{1/2}$$

$$= 10.3^o \pm 0.5^o$$

$$\theta_{neb}/2 = 5.1^o \pm 0.25^o$$

The distance to the star is 170 pc (Sky Catalog 2000.0) , therefore

$$R = 15.0 \pm 0.75 \text{ pc}$$

$$N_e = 2.12 \pm 0.35 \text{ cm}^{-3}$$

and for a pure hydrogen nebula , i.e. $N(H) = N_e$

$$M_{HII} = 2.19 \pm 0.70 \times 10^{33} \text{ kg}$$

$$= 1101 \pm 351 \ M_\odot$$

or if $N_{He}/N_e = 0.1$

$$M_{HII} = 1001 \pm 319 \ M_\odot$$

Finally

$$L_c = 3.42 \pm 1.64 \times 10^{47} \text{ photons.}$$

Zeta Ophiuchus has been extensively studied for molecular line absorption spectra. The 2.3 GHz observations are of the HII surrounding this star. In the following discussion we will summarise the results of the previous observations of this nebula and see how they all relate to each other. We will also comment on the discrepancies between the above derived results and the results of other observers.

Herbig (1968) was the first to do a comprehensive study of Zeta Ophiuchi's interstellar line spectrum. From the densities and velocities of the 21 cm and Na I lines he deduced that most of the interstellar absorption lines arose in a large HI sheet lying between 15 pc and 50 pc from the star towards us. This deduction has been borne out by the very beautiful observations of Zeta Ophiuchus with the Copernicus satellite. These showed the absorption line velocities to lie at similar velocities to the HI. Morton (1975) has collected the Copernicus observations together. He decomposed the observed lines into 7 components/clouds. These are a Stromgren sphere at -8.0 $km.s^{-1}$ and then 6 HI clouds some distance from the star at velocities of -9.0, -12.6, -14.4, -17.5, -25.5 and -27.6 $km.s^{-1}$. These 6 HI clouds lie between 15 pc and 100 pc from the star. Morton uses optical observations by other authors of Zeta Ophiuchus to derive (i) the radius of the $H\alpha$ region = $4.3^{o}$ (from Morgan et al (1955)) which is equivalent to 15 pc at a distance of 200 pc (Lesh (1968)) (ii) $n_e$ = 5.5 $cm^{-3}$ and (iii) $EM_{H\alpha}$=910 $pc.cm^{-6}$, which can be reduced to 505 $pc.cm^{-6}$ by an interstellar absorption of $A_{\alpha} = 2.0E_{B-V}$. Morton notes in his summary that there might be considerable contribution to the HII column density from the ionized interfaces of the HI clouds. Evidence for this comes from the fact that some ions which occur in HII regions are also found in the HI clouds (eg. N II, Si III, S III and Fe III). He also derives $N_{LC} = 3.9\times10^{43}$ photons.$cm^{-3}.s^{-1}$.

Herbig (1968) obtained EM ranging from 70 to 350 $pc.cm^{-6}$ and $n_e$ = 3 $cm^{-3}$ for his interpretation of 400 MHz continuum flux. The 400 MHz observations used were those of Davis et al (1965) where the Zeta Oph nebula is their source 83. Note it is also apparent on the 408 MHz survey (Haslam et al (1982)) as the blunt edge of a spur, but not having the data we cannot predict its flux and therefore EM.

Gull and Sofia (1979) claim to have found a distorted interstellar bubble around Zeta Oph. Their evidence is an arcuate structure centred on Zeta Oph photographed in O III. It is supposed to have been blown by the stellar wind of Zeta Oph (using a mass loss rate = $2.25\times10^{-8}M_{\odot}yr^{-1}$). But if this is the case then what causes the large HII nebula, which is observed in H$\alpha$ and at 2.3 GHz, to form? It is more likely that the arcuate structure is shocked gas left over from an explosion in that region which is superimposed on Zeta Oph - for instance it is strange that if it is a stellar bubble, the arcuate structure should seem to pass through the star.

Evidence for the shocked gas theory comes from Smith et al (1978). They find that difficulties arise in interpreting CO data when it is assumed that photoionization of C and ionization of H was caused by cosmic rays. Therefore they postulated that the -14.4 $km.s^{-1}$ cloud component is a sheet of shocked gas. This means that the gas was reasonably ionized before being compressed by the UV in the interior of a SNR or a planetary nebula or by some other shocking process. This could be a stellar bubble except for the following : Herbig (1968) found the -15 $km.s^{-1}$ component in 6 stars spread out over ~ $15^{o}$ of sky, which would be too large for a stellar bubble at 170 pc. Both authors think the shocking process is due to a supernova in the SCO-CEN association, the same one which ejected Zeta Oph and gave rise to its runaway velocity.

How can we fit all these observations together to arrive at a consistent picture for the 2.3 GHz radiation of the Zeta Oph nebula?

The 2.3 GHz radiation has all the characteristics of a classical HII region : (i) Zeta Oph is at a distance of 170 pc and of type 09.5V (Sky Catalogue 2000.0) and lies in the centre of the nebula. It emits $1.202 \times 10^{48}$ Lyman continuum photons (Panagia (1973)). This is almost 3.5 times the number of photons required to produce the 2.3 GHz radiation. (ii) The 2.3 GHz brightness distribution and the H$\alpha$ photograph have the same appearance. (iii) It is more prominent at 2.3 GHz rather than at 408 MHz (Haslam et al (1982)) which means it is emitting thermal radiation.

As far as the physical parameters at 2.3 GHz are concerned in comparison to other observations the following can be said. The emission measure and consequently $N_e$ are lower than other predictions (see values quoted above). This is partly because the whole nebula has not been mapped and $S_{2.3\ GHz}$ is therefore a lower estimate. Secondly a clumping factor has not been included, this would increase $N_e$. The radius is also a lower limit because some of the radiation comes from the interfaces and therefore it is not all concentrated in a sphere of radius 15 pc. This is supported by the velocity for the H$\alpha$ of Reynolds and Ogden (1982) of -13 kms$^{-1}$, which puts it in between the first and second HI cloud.

A possible scenario for Zeta Oph could be as Smith et al (1978) suggested : Zeta Oph was ejected by a supernova explosion approximately 1.1x10$^6$ yrs ago. The remnant of this supernova is the spherical structure of filaments centred on approximately l=0$^o$ and b=24$^o$ visible in HI (Heiles (1976)). This Supernova also gave Zeta Oph its high velocity. By now Zeta Oph has moved passedthe edge of the SNR (possibly the -14.4 kms$^{-1}$ component) and has created an HII region around itself - this is what we observe in H$\alpha$ and 2.3GHz radiation.The HII regionwill be highly clumped if it is made up of shocked gas swept up by the supernova. Note this is very similar to what Blaauw said in 1961.

From the above analysis we could say that radio observations are most useful for showing the presence and shape of a nebula, but when used to derive physical parameters they must be treated with caution. Because of the assumptions of the shape of the nebula and the distribution of its $N_e$ the physical parameters derived from radio observations are only estimates of the average values and should be treated accordingly.

Finally, it would be interesting to map the shape of the HI clouds and see if they correlate with the fingers of 2.3 GHz radiation (see figure 3.5).

Region B: Sancisi's expanding ring? (l",b")=(355.4°, 27.2°)

On the grey scale photograph (figure 5.1) we see faint but distinct filamentary structure extending from the Zeta Oph nebula. It arcs slightly and eventually narrows down to a point ($350^{o}$,$29^{o}$). Beside the fact that the filaments are adjacent to the Zeta Oph nebula there is nothing else to connect them dynamically. These filaments could be intercloud HII ionized by Zeta Oph. If this is so then it could be some interstellar gas swept up by the supernova which ejected Zeta Oph. But it is more likely that these filaments are related to the HI gas in that direction.

Sancisi and van Woerden (1970) observed a neutral hydrogen feature in the Scorpius-Ophiuchus direction. It is narrow and has a filamentary streamer-like shape. It has a radial velocity of $-12\ \mathrm{kms}^{-1}{}_{LSR}$. Later on Sancisi (1974) interpreted this feature as a semispherical shell centred on ($354^{o}$,$23^{o}$) with a radius of $5^{o}$. At the distance determined for the HI (170 pc) this corresponds to a diameter of 15 pc and a mass of $3\times10^{3} M_{\odot}$. The small circle described by the above coordinates passes exactly through the inner edge of feature B. Feature B could be the thermal part of this expanding ring. According to Sancisi (1974) this ring is the result of a supernova of one of the early stars in the SCO-CEN association. Monnet (1974) also observed a ring of ionized gas (in Hα light) describing the same small circle. We need high resolution radio continuum observations of this region in order to derive a spectral index. All we can say so far is that it does follow the small circle centred on the neutral hydrogen feature surrounding the SCO OBII association. Note it could also be part of a bubble blown by the stars of the SCO OBII association, this is found around quite a few associations (see Wouterloot (1982) for more examples). An approximation for the radiation emitted by this feature was obtained by measuring the flux (assuming a base of 80 mK) for the region ($-11.0^{o}$,$23.2^{o}$) to ($0.0^{o}$,$29.7^{o}$).

The physical parameters for this feature are -

$S_{2.3\ GHz} = 78 \quad +- \ 29 \quad Jy$

$\int d\Omega = 0.0112 +- 0.0026$ steradians

$R = 12.0 +- 0.2$ pc

$E = 75.4 +- 45.5$ pc.cm$^{-6}$

$N_e = 3.14 +- 0.97$ cm$^{-3}$

$M_{HII} = 1.67 +- 0.60 \times 10^{33}$ kg
$= 836 +- 300\ M_o$

$L_c = 2.58 +- 1.73 \times 10^{47}$ photons

But these are very much upper limits because of the approximation that the filaments form a filled sphere of constant density.

Finally, if these filaments are associated with the HI ridge so that they form an expanding shell with the centre of expansion centred on the SCO OBII association then the reason for this expansion must be related to this association. This is in contradiction to the interpretation that their expansion is related to the Gould belt expansion (Olano and Poeppel (1981)).

Region C: Upper Scorpius (l",b")=(351.5° ,18.4° )

This region surrounds the SCO OBII association, the closest association to our sun. Baart et al (1980) have previously mapped this region also at 2.3 GHz and with the same telescope. These data were observed differently but yielded the same results for their extended region 1. Some of the surrounding features are different though. We agree with them that there are insufficient stars to ionize this whole region but there does not seem to be sufficient evidence to suggest a supernova in this association.

The area ($340^o$,$10^o$) to ($0^o$,$28^o$) was selected from the map of figure 3.5. A galactic plane contribution was removed in the same way as described for region A. The result after removal of this background is plotted in figure 5.5. Some of the prominent stars in the association are surrounded by nebulae and they have been marked. The flux for the region ($344.1^o$,$11.0^o$) to ($356.0^o$,$24.7^o$) was measured to be 398 +- 86 Jy compared to 496 by Baart et al (1981). This is equivalent to a lower limit of 765 +- 356 $\times 10^{45}$ photons.$s^{-1}$ which is above the predictions of $L_c$ for the stars in that region, see Baart et al (1980). Note that the flux measured here is lower than that measured by Baart et al (1980), by 98 Jy. This can be attributed to the different methods which were employed to find the disk contribution and also to the different observations used. It also means that there is not so much excess radiation as Baart et al (1980) say there is.

Baart et al (1980) conclude some of this emission could be non-thermal or produced by stars which are not visible. They then intimate that there are early B type stars in the compressed material at the edge of the association, like in the nebulae around δ, π and ω Sco and these stars are producing the 'extra' emission observed at 2.3 GHz. But note that Elias (1978) in a Far Infra Red (FIR) survey of the ρ Oph clouds (which occur in this region) found very few hidden stars in the spectral range B3 and

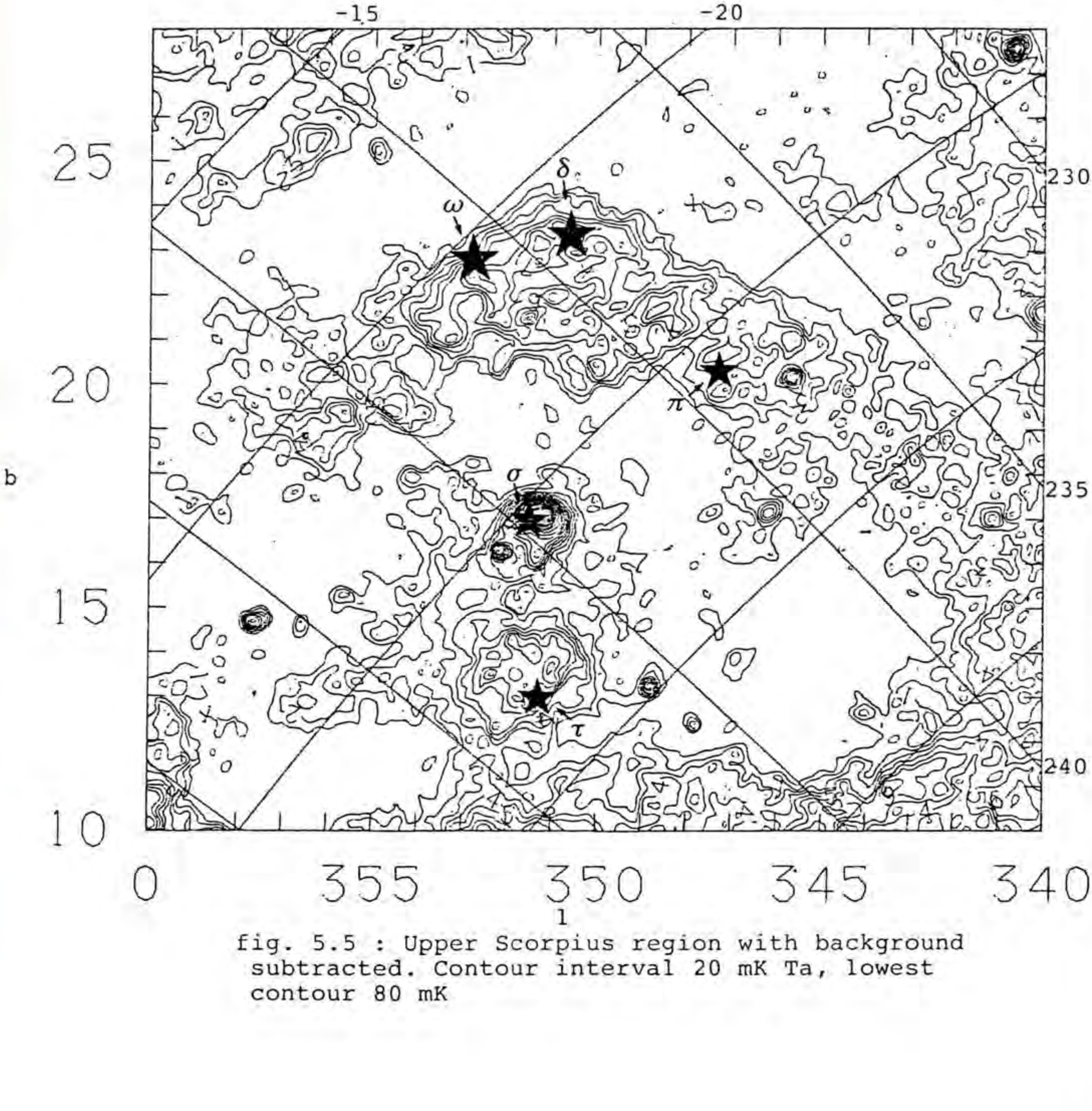

fig. 5.5 : Upper Scorpius region with background subtracted. Contour interval 20 mK Ta, lowest contour 80 mK

hotter. Baart et al (1980) then invoke Sancisi's expanding ring, the runaway velocity of Zeta Oph and the obscuration at the edge of this region C to postulate a supernova in this region.

Wouterloot (1982) mapped the molecular cloud in OH and found the following. There are two elongated streamers which start at ρ Oph and stretch over $\sim 8^0$. There is no velocity gradient over them and we are more than likely viewing them almost perpendicularly. Wouterloot concludes that the most probable origin for these streamers is that the molecular cloud was shocked by an expanding HI shell. This passed the molecular cloud drawing out these streamers in its wake. It also initiated star formation in the ρ Oph cloud. This is supported by the observations of very recent star formation (Elias (1978)). The expanding HI shell observed by Sancisi and van Woerden (1970) is supposed to be the shell which moved through the ρ Oph cloud. How does all this tie in with the excess 2.3 GHz radiation of region C and region B observed above, or are they not related at all?

I think they are. The shock which gave rise to the shape of region B and Sancisi's ring could be remnants of the same explosion which formed the SCO-CEN bubble (Weaver (1978)). They need not be at the same distance as the SCO-CEN bubble but are interior to it. Being close to the molecular cloud around ρ Oph and therefore denser they have not travelled as far as the SCO-CEN bubble. This shock initiated the SCO OBII association. Note that the X-ray source SCO-XI, at the same distance as SCO OBII, occurs in this region and has been used to explain the excess Hβ radiation in the same area (Johnson (1971)). The excess 2.3 GHz radiation could be bremsstrahlung from SCO-XI. But we still have not ruled out the possibility of there being hidden stars in this association (Baart et al (1980)). It is unlikely that the excess emission outlines the interior of an SNR. SNR interiors are at high temperatures, ($10^6$ °K) and would not radiate in the radio region. Also we find too much gas (note HI in this region in Colomb et al (1980)) still around SCO OBII for it to have been the centre of an explosion, it would have been blown outwards.

<u>Region D: Radio spur in the direction of the galactic centre (W80)</u>

<u>(l",b")=(1.3° ,9.8° )</u>

After the North Polar Spur this radio spur must be one of the most prominent and clearly defined radio spurs. It is definitely the most clearly defined radio spur in this data set. It stands out best in the grey scale photograph of figure 5.1. It is just under $5^o$ wide and starts at ($1^o$,$5^o$) curving around to ($-0.5^o$,$14^o$). This spur is visible on other large sky surveys but has rarely been commented on. It can be discerned as a faint ridge in the 150 MHz map (Landecker and Wielebinski (1970)). It was noted by Westerhout (1958) at 1420 MHz as his source 80. Berkhuisjen (1971) marks it as an internal ridge to the North Polar spur at 820 MHz. Haslam et al (1981) use it as an example of the high dynamic range on the 408 MHz all sky survey. The maps from the 408 MHz survey (Haslam et al (1982)) covering this region have been reproduced in figure 5.6. At 408 MHz we see the spur extending to higher latitudes, b ~ $24^o$, where it is narrower and has a much steeper edge than at b<$16^o$. But this higher latitude component coincides with $\delta$, $\pi$ and $\omega$ Sco and is not part of this spur. This is substantiated by figure 5.1 - there is no emission connecting the spur and this high latitude component associated with SCO OBII. What happens is that the spur stops at $14^o$ latitude and then there is a source directly above it on the 408 MHz map at ($-1.5^o$,$17^o$) which gives the spur the appearance of continuing on the contour map. This type of confusion - extended sources appearing as spurs, is a result of a lack of resolution, and ridges on radio maps should be scrutinised carefully before they are identified as spurs associated with

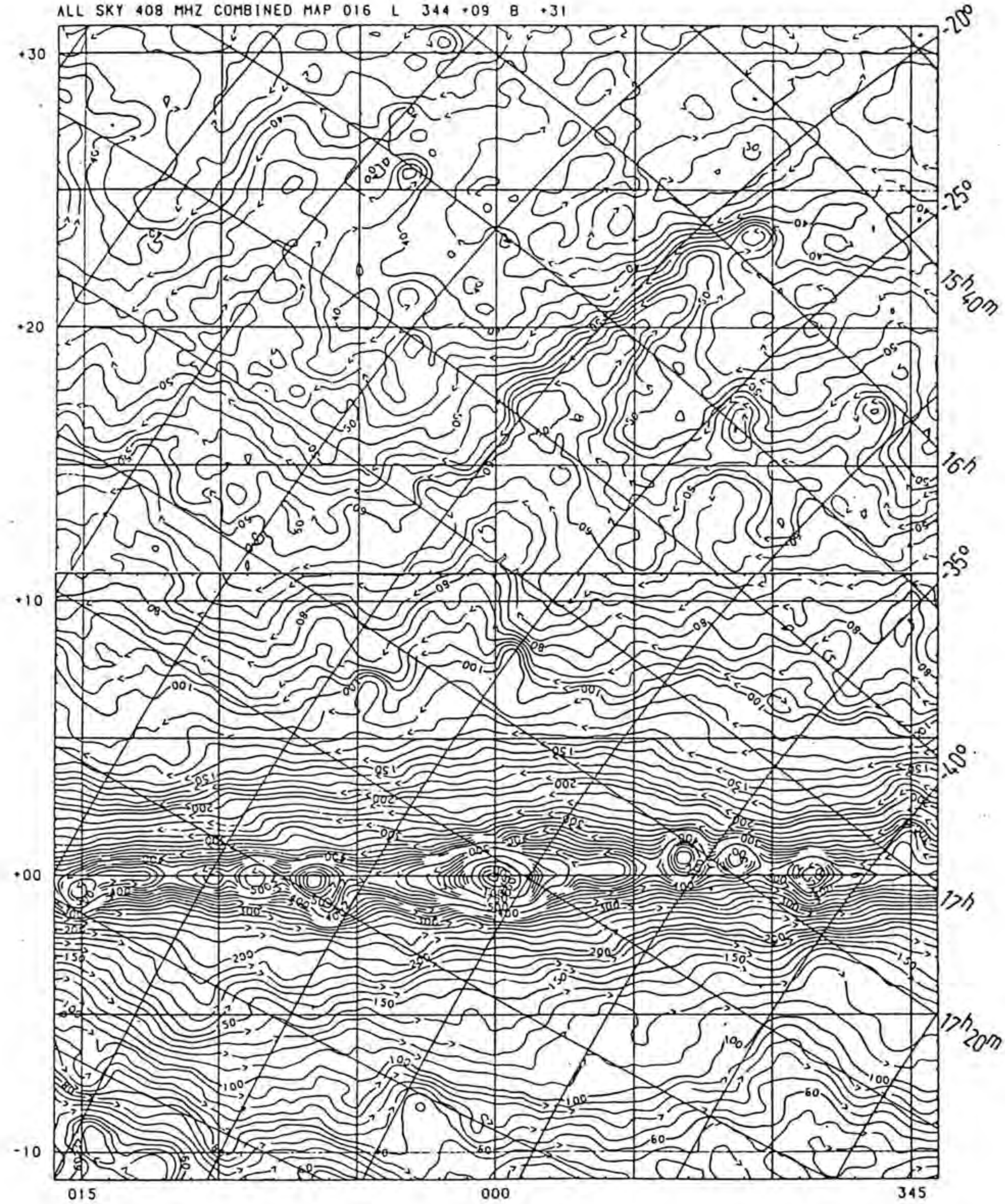


fig. 5.6 : 408 MHz map of the galactic centre. Contours labeled in Tb. Map from Haslam et al (1982), Astron. and Astroph. Suppl. Series, 47:1-143

the galactic disk. Take for example the broad spur Haslam et al (1981) identify as lying interior to the North Polar Spur, its top end is actually the Zeta Ophiuchi nebula.

Radio spurs occur often enough for them to be considered a class of astronomical object. Berkhuisjen (1971) discussed them in relation to her continuum map at 820 MHz and polarization data at the same frequency. Her conclusion that they are internal ridges to the larger loops and could be the result of successive explosions of a supernova is not well supported. Sofue (1973) has given an extensive discussion of radio spurs and their relation to the spiral structure of the galaxy. Region D represents the best example of a spur in these data and we will study it here as an example of that class. By spur we will mean a ridge of intensity (in any part of the electromagnetic spectrum) which is longer than it is wide, extending out of the plane of the galaxy. It does not extend through the plane of the galaxy and must be discernible within $b<10^{o}$. Note that according to this definition the North Polar spur remains a spur and is not a loop, as it is sometime interpreted to be.

Region D has been extracted from figure 5.1 and plotted as a contour map in figure 5.7. Because of its prominence we are able to compare it with the 408 MHz map (Haslam et al (1982)) and derive a spectral index (see equation 5.13).

eq.5.13 $$\beta_{Tb} = \log(T_{b\ 2.3\ GHz}/T_{b\ 408\ MHz}) \ / \ \log(2.3GHz/408Mhz)$$

The main difficulty with this exercise is finding $T_b$ from our map of $T_a$. The 408 MHz map is in $T_b$. So to find $T_b$ for the spur at 408 MHz all we need do is subtract a base level. This will be comprised of a sloping disk component and an unknown background. This was estimated by averaging the temperatures either side, but away from, the spur (i.e. at $l \sim 4^{o}$ and $-3^{o}$). For the 2.3

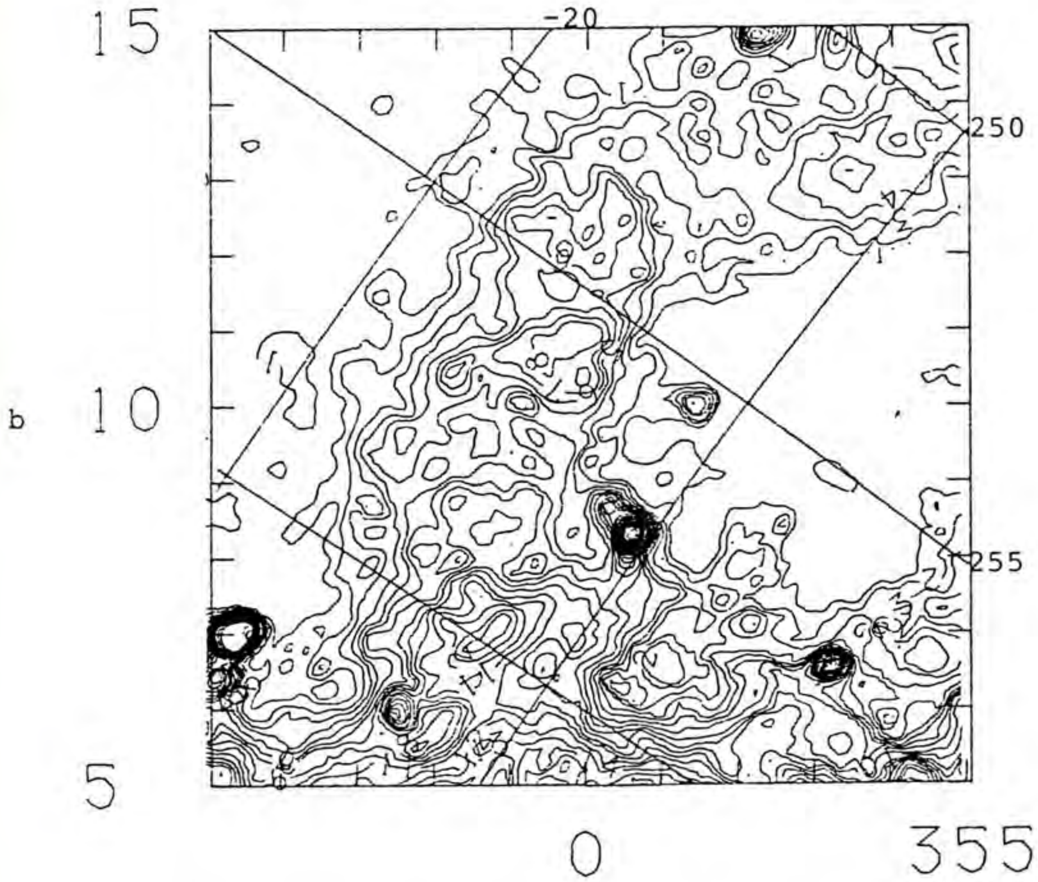


fig. 5.7 : Radio spur in the direction of the galactic centre, at 2.3 GHz. Contour interval is 20 mK Ta, lowest contour is 140 mK.

GHz map we have to convert from $T_a$ to $T_b$ and subtract a background. It was assumed all atmospheric contribution and stray radiation had already been removed or was constant and could be removed by subtracting a base level. The background at 2.3 GHz was estimated in the same way as described above for 408 MHz, except that we used the actual data for 2.3 GHz rather than estimating it off the maps. To convert from $T_a$ to $T_b$ a main beam brightness conversion of $1.41T_a$ was used. This means that we assumed the spur filled the main lobe of the antenna, which is reasonable considering its size. The resulting brightness spectral index β, defined in equation 5.13, was then calculated over the part of the spur for which it was possible to determine a background. This has been superimposed on a copy of figure 5.7 and is displayed in figure 5.8.

Estimated error in $T_{b\ 2.3\ GHz}$ is 40 mK and in $T_{b\ 408\ MHz}$ is 4 K - errors come from estimating the background and from the noise on the data. If we use these to determine an upper and lower limit to $\beta_{Tb}$ for the spur we can estimate the error in the spectral index to be +- 0.1.

The mean of the brightness temperature spectral indices in figure 5.8 is -2.6. This indicates that the spur is definitely non-thermal. From the HI survey for b >=10$^{o}$ of Colomb et al (1980) there does not seem to be any HI coincident with this spur. This supports the idea that the spur is the result of electrons spiralling in an inflated magnetic field (Sofue (1973)), rather than non-thermal emission from the shell of a supernova. A supernova remnant origin for the North Polar spur has been widely accepted as correct (Hanbury Brown, Davies and Hazard (1960)) and therefore it is assumed that all spurs are of SN origin. But this has been successively attacked by Sofue, Hamajima and Fujimoto (1974) and there is little doubt that radio spurs are not generally explained by the Supernova Remnant Hypothesis. A more likely origin is proposed in Sofue (1973). He relates the occurrence of

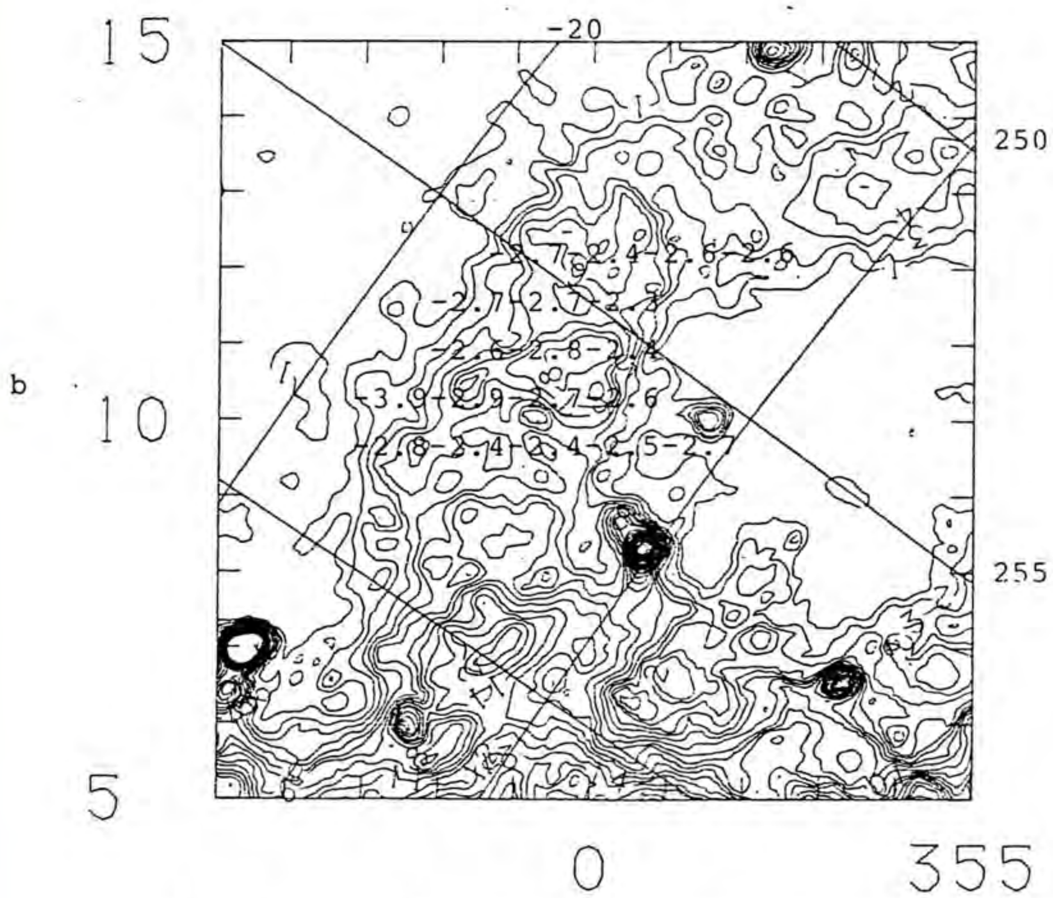


fig. 5.8 : fig. 5.7 with brightness temperature spectral indices superimposed. Spectral index derived by comparing 2.3 GHz and 408 MHz maps

radio and HI spurs with optical obscuration and the tangential viewing of the spiral arms of the galaxy. Using Parker's (1969) theory for instability of the gas in the spiral arms, a nonthermal halo is postulated for each spiral arm (see figure 5.9, from Sofue (1973)). The spurs are then the result of viewing the nonthermal halo, where it has inflated the magnetic fields, tangentially. Model calculations using this view of spiral arms yield a radio continuum distribution with most of the spurs in the correct places. If the spur discussed here does lie above a spiral arm in the direction of the galactic centre it could lie at any of the following heliocentric distances 1.3kpc, 3.7kpc or 6kpc (using the spiral pattern of Georgelin and Georgelin (1976)). The nonthermal haloes of the spiral arms have a scale height of ~ 1-2kpc. This makes the spiral arm at 6kpc, which yields a height of 850pc, the most likely distance for region D.

Region E: Emission in the direction of the Upper Centaurus-Lupus association (l",b")=(335.7° ,13° )

This region is Jonas's (1982) region L. It is very faint on the grey scale photograph but its shape is well outlined by the contour map of figure 5.2. The bright region inside this large region, which has been marked E' here, is the SNR known as the Lupus loop. It appears as a strong feature at 408 MHz (Haslam et al (1982)). Jonas has discussed it and we will not consider it further except to note Jonas identified a thermal component which he thought could be the result of thermalization of part of the remnant by the stars in the SCO-CEN association. Because of the faintness and extendedness of this region it is impossible to do any quantitative analysis of this area. Therefore in the ensuing discussion we will comment only on the appearance of the region, the stars in that region and the origin of the radiation.

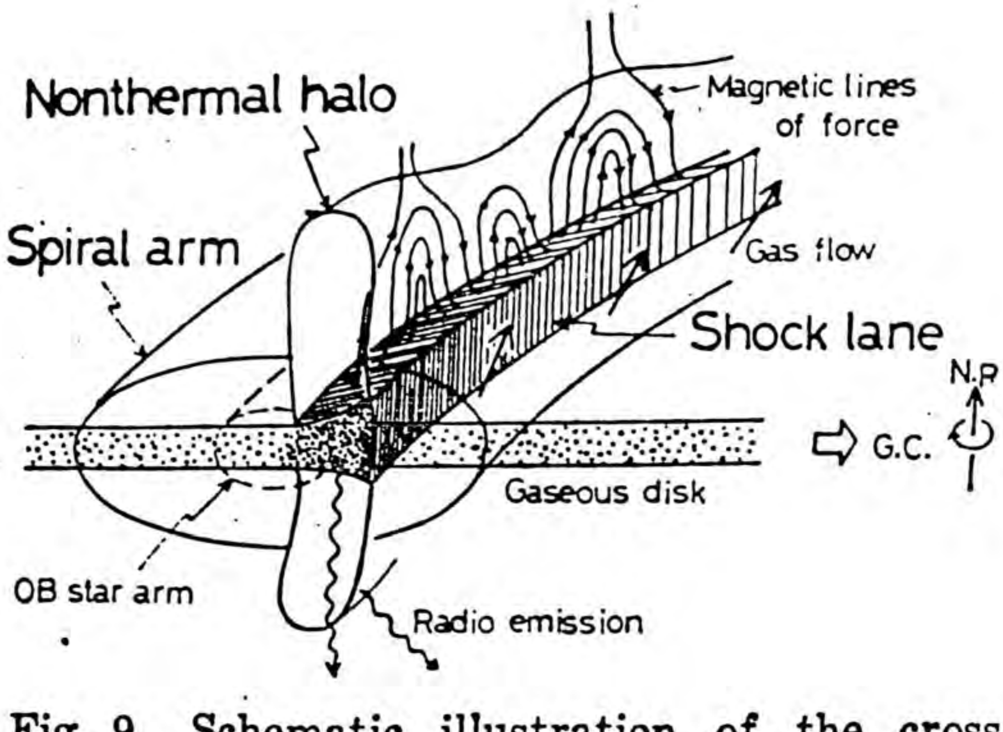


**Fig. 9. Schematic illustration of the cross section of the spiral arm accompanying a shock lane and a radio halo (nonthermal radio bank) responsible for the radio spur.**

fig 5.9 : from Sofue (1973), Publications of the Astronomical Society of Japan, 25 : 207-229

A study of the UV flux and the 408 MHz radiation of this region imply that region E is thermal. Blaauw (1964) has reviewed the O stars in the solar neighbourhood. He identifies the O stars in the direction of the fourth quadrant (in galactic coordinates) as belonging to the SCO-CEN association. He divides this association into 3 subgroups : Upper Scorpius (SCO II), Upper Centaurus-Lupus and Lower Centaurus-Crux with the following centres $(l'',b'') = (351.5^{o},20^{o})$, $(326.5^{o},17.5^{o})$ and $(302^{o},2.5^{o})$ respectively. The first two lie at a distance of 170 pc and the second at 160 pc. The Upper Centaurus-Lupus subgroup covers the region l ($312^{o}$ -- $341^{o}$) and b ($10^{o}$ -- $25^{o}$) which coincides with region E. It also has the largest projected dimension of the 3 subgroups - 80 pc. There are 17 stars in this subgroup in the spectral type range B2 to O, which is sufficient to ionize an area larger than the SCO OBII region (region C). But there are no compact (i.e. high emission measure) nebulae in this region like that around $\sigma$ Sco in region C. We conclude then that the UV photons from the OB stars in the Upper Centaurus-Lupus subgroup are ionizing the gas around them to produce the radiation which we have called region E. If this is the case then it is thermal radiation which we observe as region E. This is supported by the weak appearance this region has at 408 MHz on the large contour map of Haslam et al (1982) (ignore their source at $(330^{o},16^{o})$ which is the Lupus loop SNR).

We need to explain though why region E stops at $l \sim 326^{o}$ when the Upper Centaurus-Lupus subgroup extends across this boundary. An explanation can be found by considering the local distribution of stars, gas and dust. These can be separated into two components (see Stothers and Frogel (1974)) - the galactic plane and Gould's belt. Gould's belt lies on a great circle inclined at an angle of $20^{o}$ to the galactic plane. In the fourth quadrant it follows (Lindblad (1974)) a line going from $(294^{o},0^{o})$ to $(0^{o},18^{o})$, which passes through regions E and C.

Therefore region E represents the ionized gas of Gould's belt. This supports the idea that the Gould belt was formed from a disc of HI inclined to the plane (Colomb et al (1982)). It also means that the Upper Centaurus-Lupus stars in the range $l = 312^{o}$ to $325^{o}$ for some reason lie outside the HI disc and are not surrounded by gas. This could either be because they were formed at a different time or because they were ejected from the subgroup but this is entirely speculative and there is no evidence favouring one above the other.

Region F: SCO-CEN bubble (l",b")=(5.3° ,-1.6° )

This region is arranged in drawn out streamers along the magnetic field lines, as depicted by Mathewson (1968). Three tongues $5^{o}$ wide each can be identified on the greyscale photograph (fig. 5.1). The centre one is the brightest ( 250 mK) and extends the furthest, to ($350^{o}$,$-32^{o}$). What is very remarkable about this central tongue is its shape. It follows a tube shape from ($10^{o}$,$-10^{o}$) to ($355^{o}$,$-30^{o}$). This tube of emission is exactly along the magnetic field lines of Mathewson (1963).

If we assume region F lies on a small circle with a centre at ($315^{o}$,$20^{o}$) - estimated from a visual inspection of the curvature of the streamers of region F, we find it crosses map A04D80 at 7 hrs right ascension and $-70^{o}$ declination. But this is exactly where a patch of emission occurs on A04D80, see appendix 1. We will refer to this as region G. In equatorial coordinates it covers right ascension 7 hrs to 7h45 and declination $-80^{o}$ to $-68^{o}$.

Both feature F and G coincide with intermediate velocity HI features discussed by Cleary (1977), her features A and C respectively. Figure 5.10 (Cleary's figure 3.1) shows where features F and G lie in relation to Cleary's features A and C, the direction of the magnetic field lines is also drawn. Cleary (1977) relates these features to an expanding HI bubble centred on the SCO-CEN association. This interstellar bubble has been postulated by Weaver (1978) to have been blown by the stellar winds of the young stars in SCO-CEN. The centre of the HI filaments (Weaver (1978)) is $(331.3^{o}\pm1.3^{o}, 14.0^{o}\pm1.4^{o})$ with a radius of $85^{o}$. A small circle drawn with these parameters passes through regions F and G. Therefore we can say that these two features definitely seem related to the SCO-CEN bubble. Cleary et al (1979) also discussed this bubble in their 'Synoptic View of the Galaxy in HI', but the most thorough analysis is that of Cleary (1977) in her PhD thesis. The latter reference will be used in the ensuing discussion. She deduces the following - a low velocity bubble centred on the Sco-Cen association is being blown by the stellar winds in this association. This is the bubble postulated by Weaver (1978) and is beautifully evident in the HI survey of Colomb et al (1981). Then there is a second bubble which formed inside the Sco-Cen bubble and has now reached it and is visible as the intermediate velocity features. A shock origin is used to explain the high (i.e. intermediate) velocities of this second bubble. Parameters for this second shell, derived from HI data, are - a distance to the centre of 170+-15 pcs, a radius of 156+-4 pcs, a thickness of about 52 pcs, a density of $0.33 cm^{-3}$ and an expansion velocity of 60+-5 $kms^{-1}$. Using these values we can make the same predictions about region F. If we assume region F is purely thermal then we should be able to derive an emission measure for this feature. If we assume $n_H=n_i$ we arrive at the low emmision measure of 5.7 $cm^{-6}pc$ for the line of sight taken along the entire thickness of the bubble. A lower estimate for the area of region F is $10^{o}$ by $15^{o}$. These two values yield a flux of 24.1 Jy at 2.3 GHz. It is almost impossible to measure a flux for F because it is so extended, but we can estimate its flux by comparing it to the Zeta Ophiuchi nebula. They both have similar brightnesses on the greyscale photograph (fig. 5.1) and are of similar area. But Zeta Oph has a measured flux of 265.9 Jy (see discussion of region A). Therefore if all the above physical paramters and assumptions are correct it appears that region F is not predominantly thermal radiation. How does this fit in with what is supposed to have happened in the SCO-CEN bubble.?

Weaver (1978) and Cleary (1977) describe the following situation for the HI filaments in this region. The stars in the Sco-Cen association have sufficient power to blow a stellar bubble with a low velocity of expansion of 2 $kms^{-1}$. While this bubble has been expanding a shock, possibly a supernova, has swept through the interior of the bubble and is now interacting with it. This interaction has enhanced the emission there and the shock has produced the intermediate velocity filaments , +-50 $kms^{-1}$ (these are features A, B and C of Cleary (1977) and depicted here in fig. 5.10). The region of interaction should be visible in the continuum as a result of thermal radiation caused by UV photons from the Sco-Cen association and enhanced synchroton emission as a result of the compressed magnetic fields and increased elctron density. This is what we see as features F and G.

The second shock, which is supposed to have created the intermediate velocity features could be the supernova which caused loop I (Weaver (1978) and Cleary (1977)). But the shape of features F and G argues against this. Firstly the curvature of the features shows F to emerge from the disk at ~ $7^{o}$ longitude, as opposed to loop I which occurs at $30^{o}$ longitude. Secondly there in no evidence on other continuum maps of loop I crossing $0^{o}$ latitude. This might be a result of loop I being very close to the sun but distance estimates for loop I do not point to this.

If features F and G are part of the SCO-CEN bubble it is interesting that

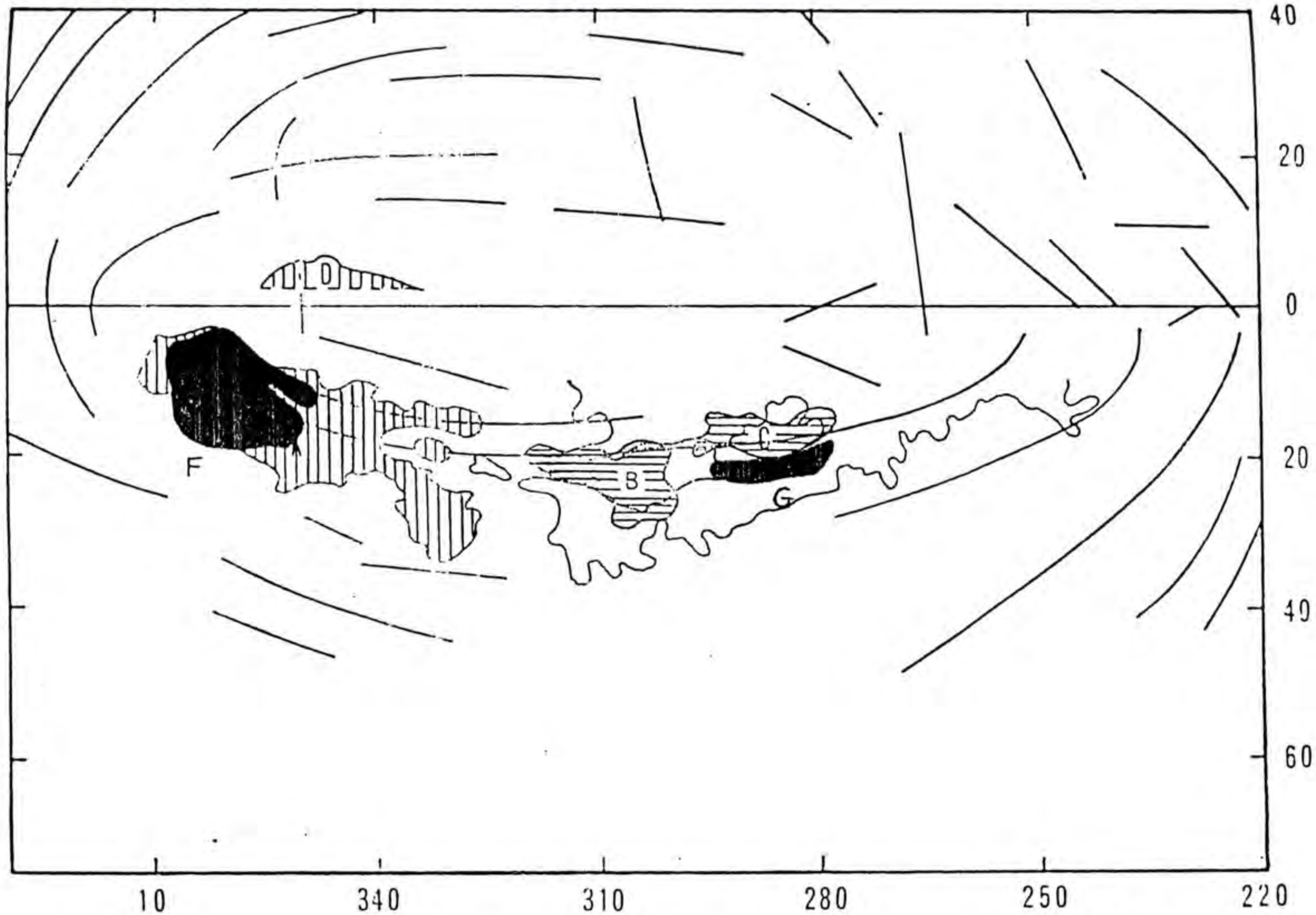


fig 5.10 : positions of features F and G superimposed on a plot of the positions of Cleary's (1977) features A, B and C (from her fig 3.1). The black lines are a schematic representation of the direction of the local magnetic field, from Mathewson (1968).

this is the first time they are observed in the continuum. If these features are nonthermal why have they not been seen at 408 MHz? These features show up at 2.3 GHz because the disk contribution falls off more rapidly with galactic latitude at this frequency than at 408 MHz. Also note that these features are actually visible at 408 MHz but no one knew what to look for previously. The contour at 7 hrs right ascension, which coincides with G, occurs at 408 MHz on the south polar plot of Haslam et al (1982). One reason why it is not so prominent at 408 MHz could be because there is a plateau of nonthermal emission extending from the LMC which hides it. Feature F also occurs at 408 MHz. If we look at Haslam et al's (1982) all sky map (on a resolution of $2^{\circ}x2^{\circ}$) we see a blunt spur passing through ($0^{\circ}$, $-30^{\circ}$) down towards ($330^{\circ}$, $-45^{\circ}$). It is largely hidden by the strong disk component. In conclusion we can say this is the first continuum map of the SCO-CEN bubble, albeit of the interaction of the low velocity windblown bubble and the intermediate velocity shockdriven bubble.

# CHAPTER 6

## LOW LATITUDE SOUTHERN HEMISPHERE CONTINUUM RADIATION AT 2.3 GHZ

### 6.1 INTRODUCTION

The galactic plane, as is the case in other parts of the electromagnetic spectrum, is the most studied part of the galaxy at radio frequencies. This is mostly because it is the most interesting part of the galaxy and because it is so bright. The latter reason makes it easier to detect than the rest of the galaxy. Because of the vast number of sources in the plane we will not analyse it in depth. Instead we will present maps of the area $|b| < 10^{o}$, $303^{o} < l < 30^{o}$ in a form that they can be compared with other plane surveys. We will also discuss the appearance of the radio disk at 2.3 GHz.

This chapter is arranged as follows : first maps of the region $|b| < 10^{o}$ from the joined data set of section 3.3.3 will be presented and compared with existing observations. Then the appearance of the radio disk for $|b|<10^{o}$ will be discussed. Special attention will be given to the relation between galactic structure and the radio disk. The chapter ends with a summary of the results and suggestions for further work to be done on these data.

### 6.2 THE GALACTIC PLANE AT 2.3 GHZ

Many radio surveys exist of the plane and consequently there is very little new work to be done on identifying sources. But we can check our results with existing plane surveys. The data for $|b| < 10^{o}$ have been presented as a series of maps of $T_a$ in appendix 2. The data for these maps have been taken from the combined map of A12D26 and A14D63. No filtering besides the coordinate transform has been applied (see sec. 3.3.3) and the resolution is therefore the resolution of the raw maps i.e. 20 minutes of arc. These data have also been compared with other surveys of various resolution. Namely Nicolson (1965) at 960 MHz with 50' arc resolution, Haynes, Caswell and Simmons (1978) at 5 GHz with 4.1' arc resolution, MacAThomas et al and references therein (1969) at 2.650 GHz with 8.2' arc resolution, Mathewson, Healey and Rome (1962) at 1440 MHz with 50' arc resolution and Altenhoff et al (1970) at 1.414, 2.695 and 5.000 GHz with 11' arc resolution. From a comparison with higher resolution surveys the 2.3 GHz plane survey has a pointing accuracy of $0.1^{o}$ and $0.1^{o}$ in l and b. The sources at 2.3 GHz have the same shape as those mapped at other frequencies. Also the ridges perpendicular to constant latitudes which are visible on other surveys eg. at 820 MHz (Berkhuijsen (1972)), especially in the galactic centre region are reproduced. It is interesting to note that even on the higher resolution maps eg. Haynes et al's (1978) 4.1' arc resolution survey, these ridges are not resolved. These ridges are most probably radio spurs emanating from the radio disk and not unresolved sources.

## 6.3 THE RADIO CONTINUUM DISK AT 2.3 GHZ

In addition to the sources in the plane of the galaxy there is a smooth component of radio continuum which does not get resolved by higher resolution surveys. This component is known as the radio continuum disk and is visible at all radio frequencies, IR frequencies (see Okuda (1981) for a review of all large IR surveys) and gamma ray observations (Mayer-Hasselwander et al (1982)). All these observations are related and can be correlated with the distribution of interstellar gas. In this section we will discuss the appearance of the 2.3 GHz radio continuum disk in the fourth quadrant. We will discuss the nature of features appearing on the profile of the galactic equator and the extent of the continuum in the latitudinal direction. The 2.3 GHz observations will be especially related to the 408 MHz data, 1440 MHz data and the gamma ray observations.

A cut through $b''=0^{\circ}$ of the raw data of the joined maps of section 3.3.3 with minimal smoothing applied (i.e. only the $0.1^{\circ}$ degree convolution of the coordinate transform program) is plotted in figure 6.1. The lower envelope which could be fitted to this profile represents the background continuum radiation. This radiation consists of diffuse thermal radiation arising in unresolved and extended HII regions and synchroton radiation emitted by cosmic ray electrons (with energy in the 1-5 GeV range) spiralling in the galactic magnetic field. Therefore we expect the 2.3 GHz radiation to be a tracer of the spiral structure of the galaxy as outlined by HII regions (Georgelin et Georgelin (1976)). Because of the steep spectrum of synchroton radiation ($\beta=-2.6$) we also expect the 2.3 GHz radiation to be a weak tracer of the cosmic rays and galactic magnetic field.

Seeing as we are considering background radiation here we need to know the brightness temperatures of the background radiation with respect to an absolute zero level if we want to make comparisons with observations at other frequencies. The profile of figure 6.1 has an arbitrary zero level and therefore we cannot make quantitative comparisons of this data with other data. The only possibility is to compare the shapes of the profiles and heights of steps in them. When interpreting the longitudinal profile there are two basic approaches - one is to postulate a galactic distribution and then compare the line of sight integrals expected from the model with observed profiles, varying the model's parameters until they agree (eg. Georgelin and Georgelin (1976) and Simonson (1976)). The other approach is to deconvolve an observed profile by unfolding the line of sight integrals so that they fit a proposed spiral structure. The latter method involves

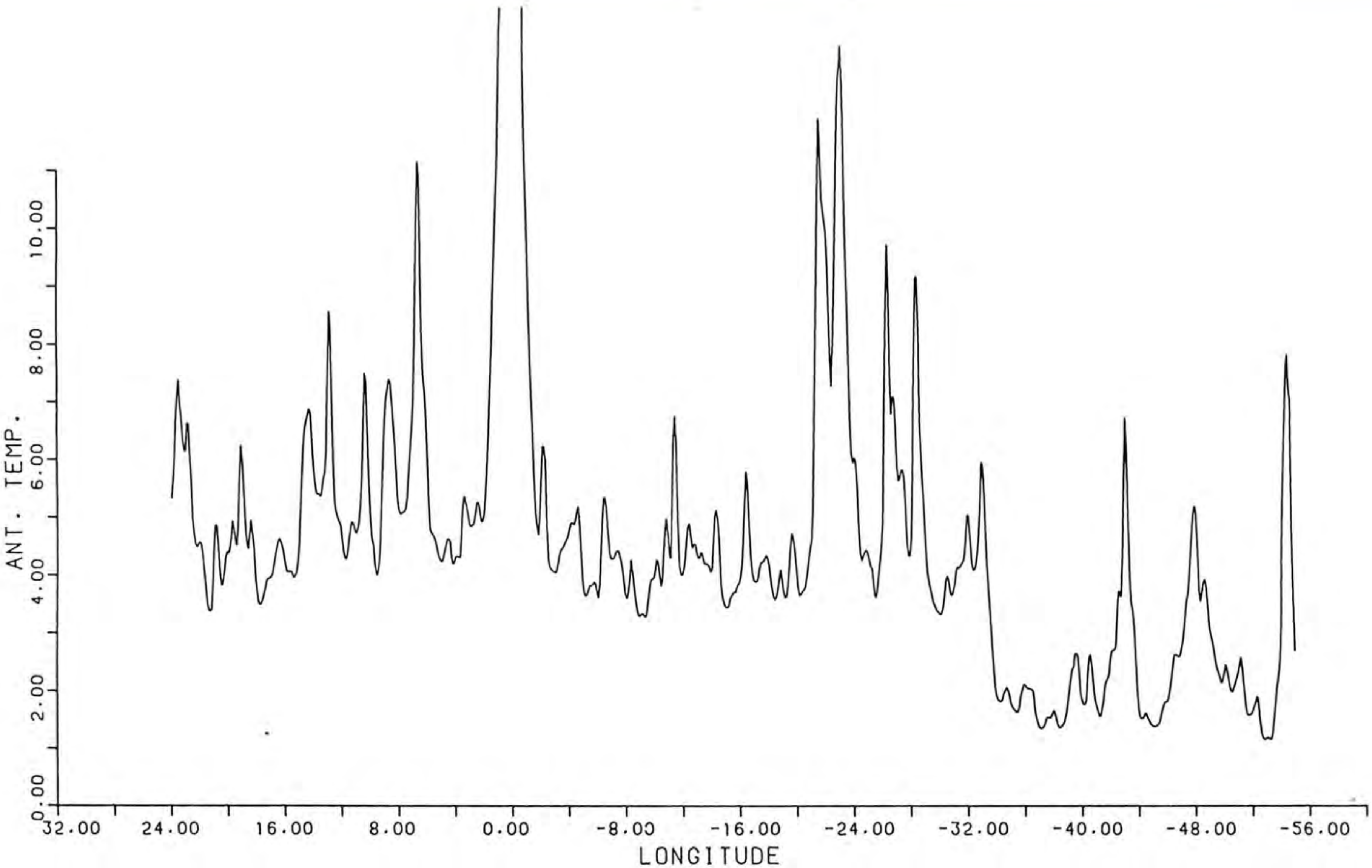


fig. 6.1 longitudinal profile for 2.3 GHz survey in appendix 2.

more stringent limits on the symmetry of galactic structure than the first. This approach has been attempted by, among others, French and Osborne (1976) at 150 MHz and 408 MHz, by Phillips et al (1981) at 408 MHz and by Kniffen and Fichtel (1981) in gamma rays. But at these frequencies the predominant radiation mechanism is nonthermal whereas at 2.3 GHz thermal radiation is predominant. This is immediately evident on comparison because the profiles actually have different shapes. For example we have displayed the 150 MHz profile used by French and Osborne (1976) in figure 6.2c. Although this has been smoothed and corrected by the profiles in figure 6.2a and b the general shape is large steps ( $1000^{o}$ K $T_b$) superimposed on an exponential disk. At 408 MHz we have a similar situation but because higher resolution surveys are available the smooth appearance disappears. For example the 408 MHz galactic equator profile by Green (1974) displayed in figure 6.3 has been obtained from a survey with a resolution of 2.86'(RA)x2.86'sec(z)(dec.). The plot in figure 6.3 is of the averages over $0.5^{o}$ l and $6^{o}$ b. For comparison we have averaged the 2.3 GHz profile over $|b| < 3$ (fig. 6.4) with the 408 MHz profile of fig. 6.3 superimposed on it. The resolution of the 2.3 GHz profile (20' arc) is comparable.

The main feature apparent at lower frequencies but not on fig. 6.1 is the sloping disk symmetric about $l=0^{o}$. This is surprising because this slope is $\sim 2^{o}$ K $T_b$ at 2.3 GHz. This could be because the baselevel error is such that it has removed this disk. Although this is possible it would be quite a coincidence if it is so. A more plausible explanation is that the thermal and nonthermal components are so shaped that the sum of the two results in the shape observed in figure 6.1. This is supported by the following : Mathewson, Healey and Rome (1962) decomposed their 1440 MHz observations into thermal and nonthermal components (fig 6.6) and from this we can see that the sum of these two components (fig 6.7) has the same shape as fig.

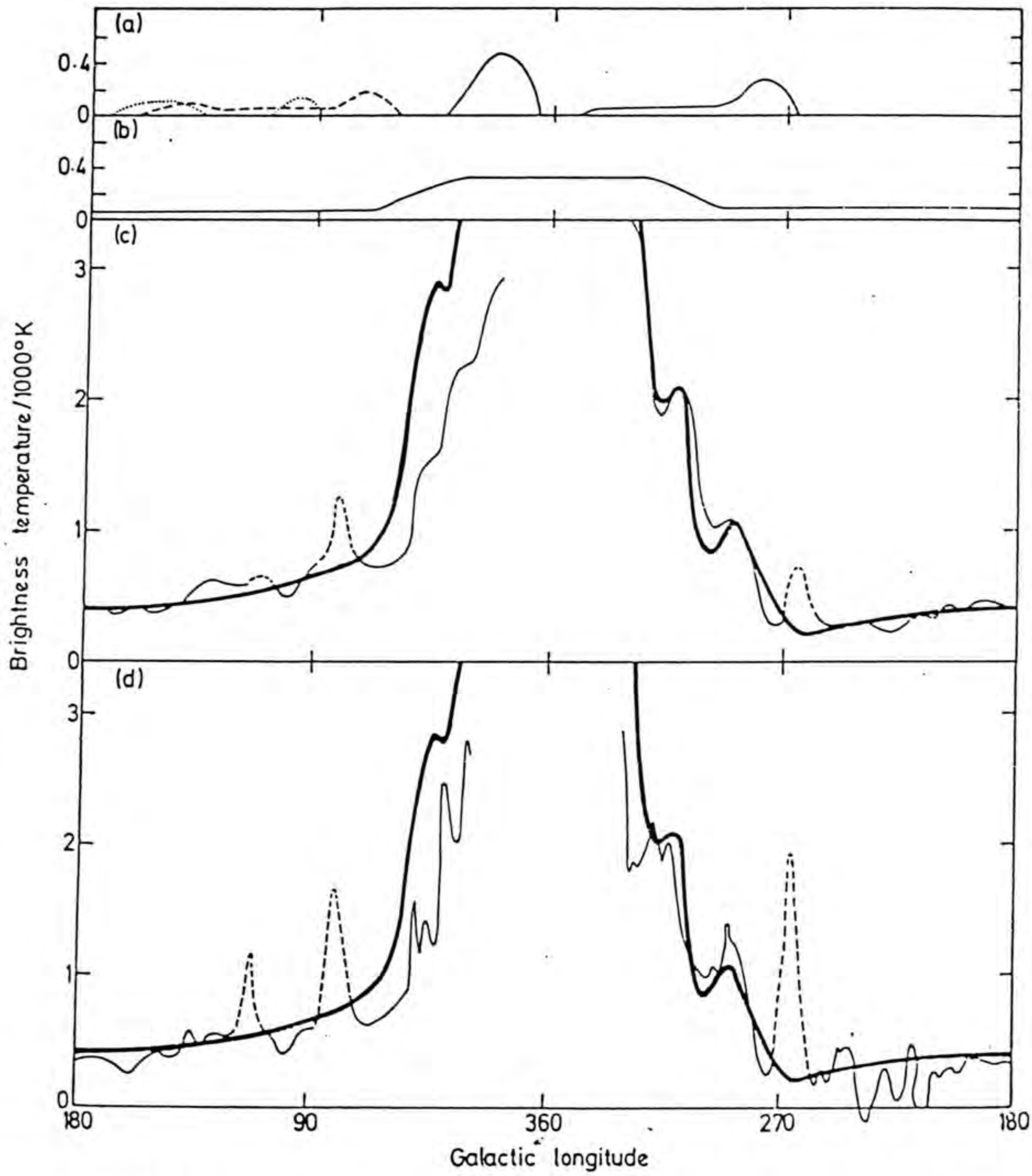


fig. 6.2 (a)contribution to observed $T_b$ at 150 MHz from galactic spurs (b) thermal emission at 150 MHz (c) thin line - observed brightness at 150 MHz after subtraction of (a) and (b), thick line is fitted model (d) thin line - 408 MHz brightness scaled to 150 MHz using a spectral index of -2.8, thick line is fitted model (from Osborne and French (1976))

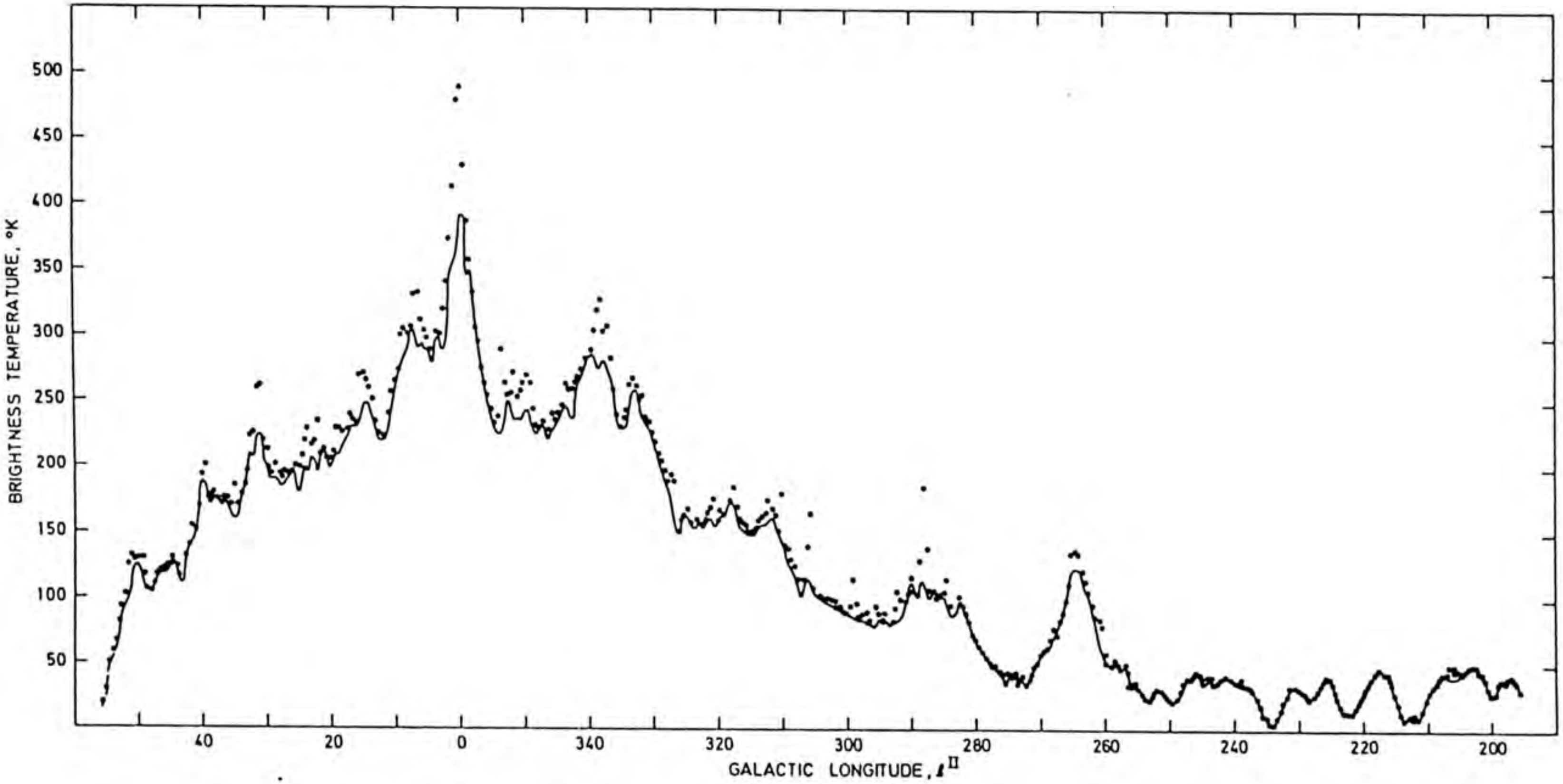


fig. 6.3 longitudinal distribution of 408 MHz survey by Green (1974), each data point is the average over (l,b)=(0.5°,6.0°), solid line represents continuum background (from Green (ibid.))

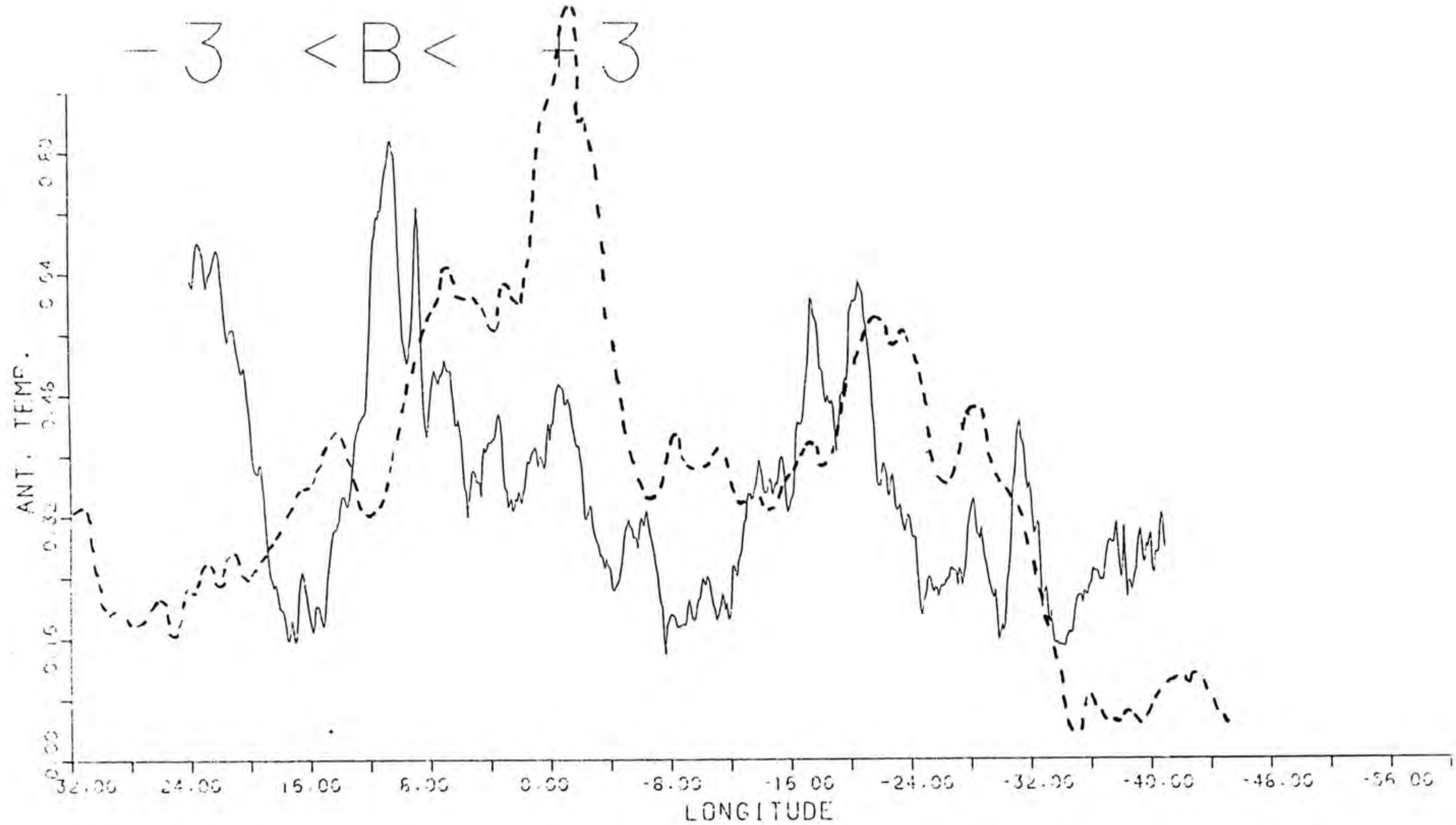


fig 6.4 solid line - longitudinal distribution for 2.3 GHz plane survey in app. 2 averaged over b 3°. dotted line - 408 MHz distribution averaged over same latitude range (fig. 6.3) on arbitrary scale.

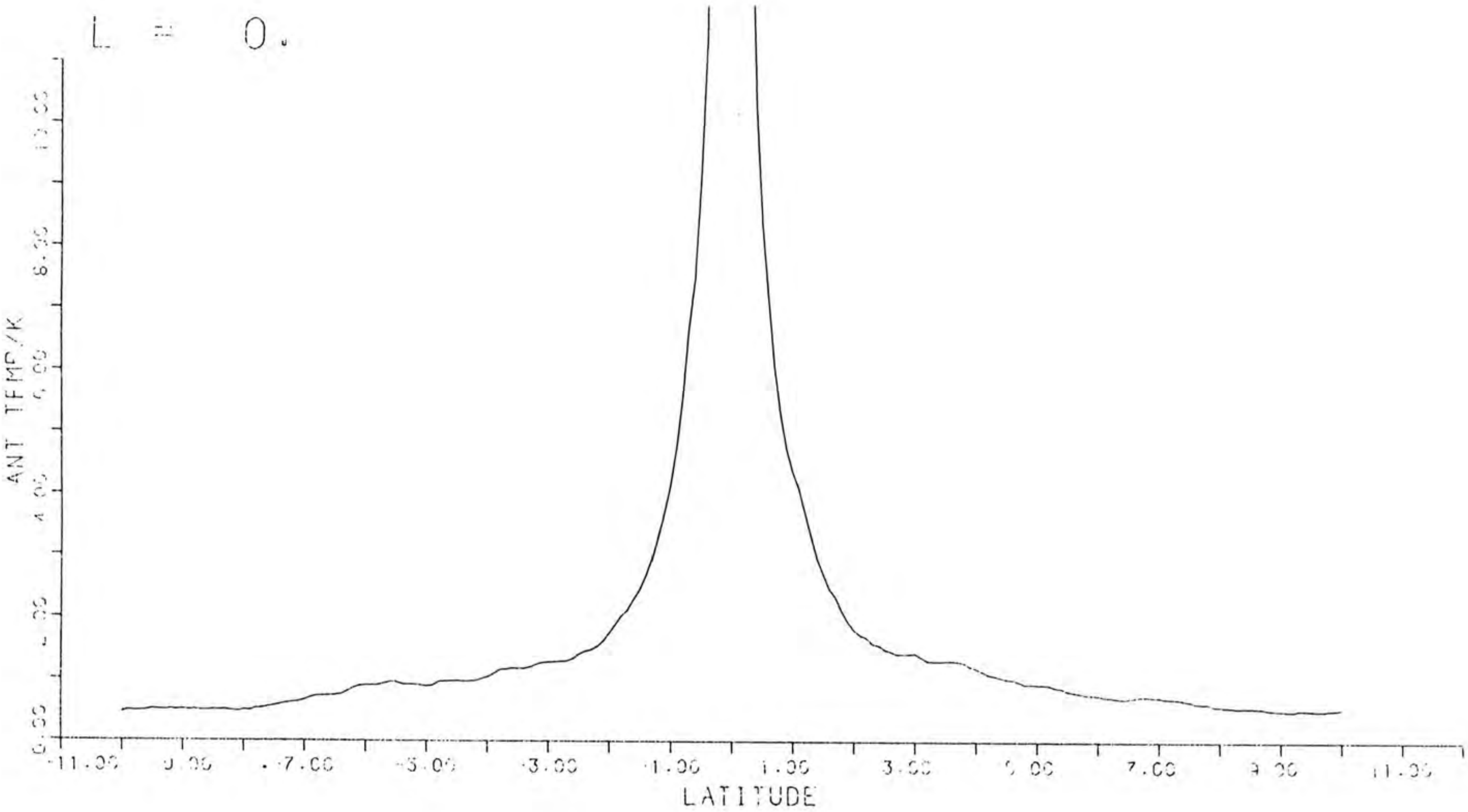


fig. 6.5 latitudinal distribution of 2.3 GHz survey in appendix 2 at l=0°

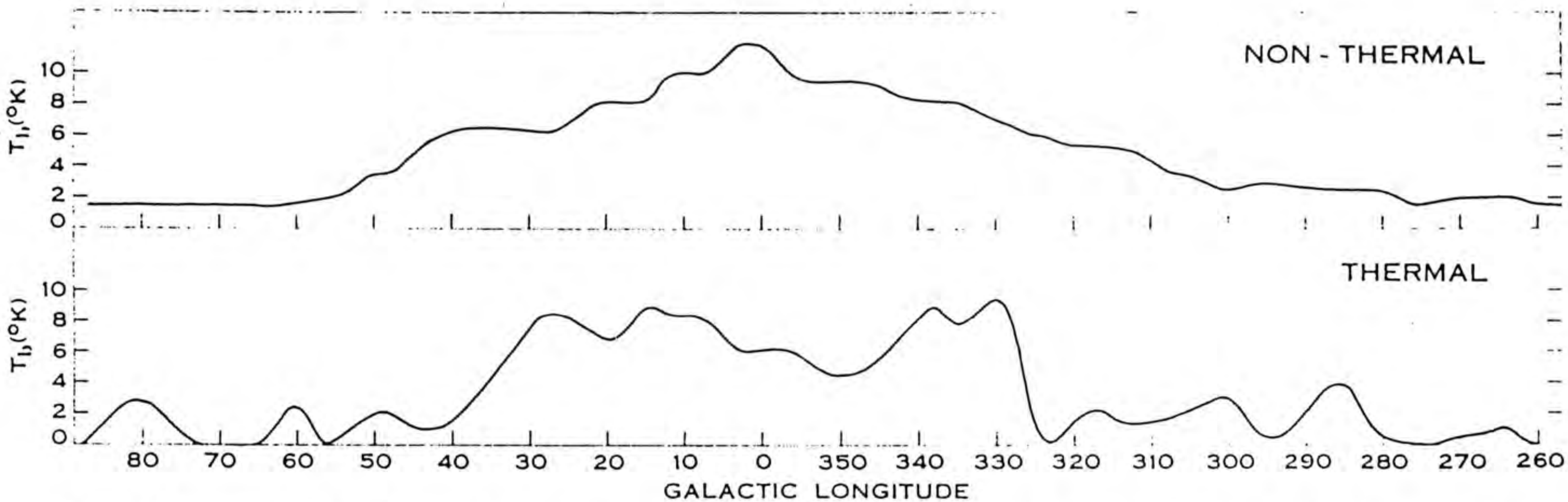


fig. 6.6 nonthermal and thermal components of galactic equator profile at 1440 MHz, from Mathewson, Healey and Rome (1962)

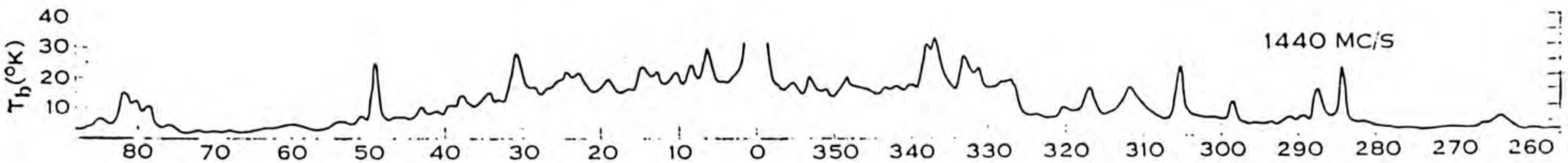


fig. 6.7 longitudinal distribution of 1440 MHz brightness, from Mathewson, Healey and Rome (1962)

6.1.

The most prominent feature in fig. 6.1 is the plateau occurring after the step at $-34^{o}$ of $2.2^{o}$ K $T_a$. This step was first observed by Westerhout (1958) at 1390 MHz. It is believed to be symmetric about b"=0 and is manifested in the first quadrant by a step at l"=$26^{o}$. Westerhout (ibid) and Komesaroff (1966) identified this plateau as a ring of gas with a radius of between 4 and 6 kpc. The step at $326^{o}$ on the 2.3 GHz profile compared to the step on the 1440 MHz profile (fig. 6.7) yields a nonthermal spectrum - $\beta$= 3.2. This result is not conclusive though because we have not separated the thermal and nonthermal components out. Notwithstanding this fact, Komesaroff (1966) identifies this plateau (using 85.5 MHz and 408 MHz results) as nonthermal. He postulates a ring of enhanced nonthermal radiation due to a ring of enhanced density gas. The HI data (ibid) show neutral gas expanding out from the centre of the galaxy and slowing down as it comes into contact with the ring of gas. This theory is also supported by the galactic equator gamma ray profile (fig. 6.8 from Mayer-Hasselwander (1983)) which also shows a plateau of enhanced emission in the range $34^{o}>l>-34^{o}$. The gamma ray profile is a tracer of the total gas content of the galaxy and therefore should trace out this plateau if it is a ring of gas of enhanced density. It is interesting too that a ring of molecular gas is observed in this region (Solomon and Sanders (1980)) and in the IR (Nishimura et al (1980)). It is possible that it is this ring of molecular gas which slows down the expanding HI. The origin of this ring must be related to the dynamics of the galactic spiral structure (note Lindblad's resonance which is supposed to cause a disc at the centre of the galaxy of radius 4 kpc (Simonson (1976)).

Finally let us consider evidence for the spiral arms. HII regions are a good

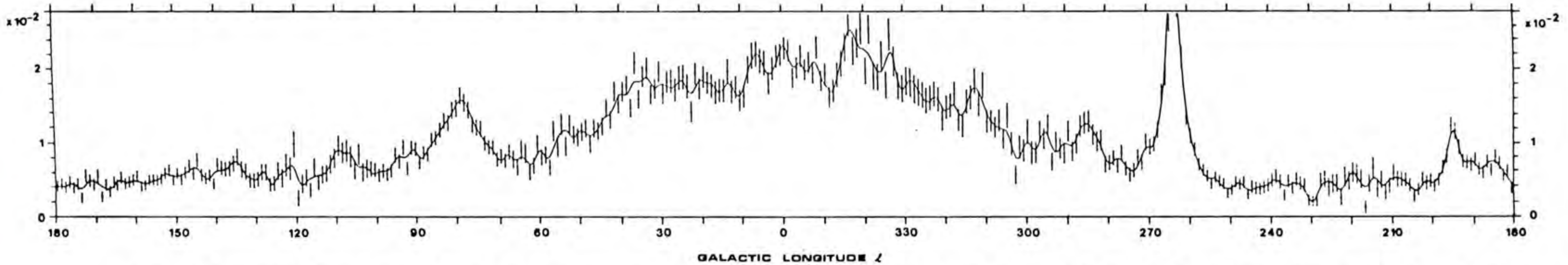


fig. 6.8 longitudinal profile of gamma ray emission as measured by the COS B satellite in the energy range 70 MeV - 5 GeV profile is averaged over 5° of latitude, the vertical axis is labelled in on-axis counts.$s^{-1}$.$sr^{-1}$, from Mayer-Hasselwander (1983)

tracer of galactic spiral structure and it is reassuring to find that the peaks in fig. 6.1 at $310^{\circ}$ and $330^{\circ}$ coincide with the peaks predicted by the spiral structure of Georgelin et Georgelin (1976).

## 6.4 CONCLUSION

Maps of the region $|b| < 10^{\circ}$ , $30^{\circ} > l > 303^{\circ}$ were presented and compared with other radio surveys of the same area. The thermal continuum radiation is predominant at this frequency and a continuum disk $2^{\circ}$ wide is visible. The profile of the galactic equator over this longitude range is dominated by a step at $l=326^{\circ}$ which was identified as predominantly nonthermal and related to a ring of enhanced nonthermal radiation concentric with the galactic centre and with a radius of 4-6 kpc (Komesaroff (1966)). Because this ring consists of gas it must be mentioned though that it will also be a region of enhanced thermal radiation - we find a concentration of HII regions 5 kpc from the centre of the galaxy (Lockman (1979)). Consequently the plateau is partly thermal too (cf. thermal component at 1440 MHz in fig. 6.6). The steps in the galactic profile due to viewing the spiral arms tangentially at $310^{\circ}$ and $330^{\circ}$ as identified by Georgelin et Georgelin (1976) are evident. They appear narrower than predicted though.

Finally it must be noted that we have only taken a cursory look at this plane survey. If the survey were calibrated in $T_b$ with respect to absolute zero we could use Westerhout's (1958) method and another plane survey to separate the thermal and nonthermal components. More quantitative work needs to be done too on evaluating the line of sight integrals expected at 2.3 GHz for the galaxy as predicted by various spiral models and then comparing them with the profile of fig. 6.1.

## CONCLUSION

This thesis had three main objectives. These were to continue the Rhodes 2.3 GHz Survey, develop a technique to put the existing survey maps on a single baselevel and interpret the already completed parts of the survey. The following paragraphs will outline to what extent these objectives were realized and what conclusions can be drawn.

The Rhodes Survey was extended to cover half the Southern Sky by mapping a further 6128 square degrees. The mapping technique used, SKYMAP, was developed prior to this thesis and was found to yield good results with the following exceptions (i) background should be found from observations which have had diurnal drift removed from them, (ii) the full set of 3 repeats for each raster are not necessary, 2 will do, (iii) the method of finding drift is not good enough and must be supplemented by a better technique. This is because it results in an arbitrary baselevel for each map.

An investigation into the data filtering techniques being used was conducted using the beam pattern of the Hartebeesthoek 13 cm system as test data. It was found that the running median filter squares round sources in the spatial domain and introduces notches in the spatial frequency domain, as well as enhancing some of the high frequencies. Therefore the practice of running a 2 pass median-of-3 filter over the data should not be continued.

As mentioned above the Rhodes Survey consists of a number of maps which are on an arbitrary baselevel and need to be put on a single baselevel. It was proposed that this can be achieved by creating a coarse grid of antenna temperatures which have had drift removed by referring them to the south celestial pole. The observing and analysis programs for this technique were developed and presented. Preliminary results were obtained and show that the programs do provide a coarse grid of antenna temperatures of the sky. The drift on these results was not estimated but it was shown that the grid does reproduce faint galactic features. The work that remains to be done on this technique is to obtain more and better observations and then compare the grid of temperatures produced from these good observations with an already calibrated survey eg. the 1420 MHz survey by Reich (1982). The question of calibrating the final survey in main beam or full beam brightness temperatures was dicussed but left open for later decision.

The following two studies were undertaken - the region 13HR to 23HR , $-61^{o}$ to $-7^{o}$ was searched for large (> 10 square degrees) extended areas of emission and secondly the shape of the galactic equator profile for the region $30^{o} > l > -60^{o}$ was studied. For the first time the classical HII region around the star Zeta Ophiuchi was mapped and analysed. A flux of 266 Jy was measured at 2.3 GHz. A lower limit for the mass and number of Lyman continuum photons was calculated to be 1101 $M_{\odot}$ and $3.42 \times 10^{47}$ photons respectively. This is in keeping with the nebula being a classical HII region. Several large (> 100 square degrees) patches of emission dominate the intermediate galactic latitudes and were related to observations at other frequencies. These were an expanding ring of gas centred on (l,b) = (354,23), the SCO OBII association, a spur in the direction of the centre of the galaxy, the Upper Centaurus-Lupus association in the Gould belt of gas and the SCO-CEN bubble. Although these regions were too extended to find an accurate flux, for an attempt was made at trying to determine the type of radiation being emitted. After consideration of observations at other frequencies it was concluded that these features are a combination of thermal and nonthermal radiation.

The galactic equator profile was found to support the results at other frequencies - nonthermal radio continuum, radio recombination line surveys, molecular cloud surveys, infra-red and gamma rays i.e. an enhanced plateau of emission for $26^{0} > l > 326^{0}$. This is interpreted as a ring of gas centred on the galactic centre with a radius between 4 and 6 kpc. The present results yield a nonthermal spectrum for the plateau.

Finally it must be noted that the Galaxy at 2.3 GHz has a filamentary appearance. This is however not the first time that this has been observed in radio continuum. The 408 MHz all sky survey also depicts this. It can be concluded that the data presented in this thesis supports the view of the Galaxy that it is a cosmic bubble bath in which violent events are a common occurrence.

## REFERENCES


ALLEN,R.J. (1979), Image Formation from Coherence Functions in Astronomy, C van Schooneveld (ed), D Reidel Publishing Co., 143 - 145.

ALTENHOFF,W.J. et al (1970), Astron. Astroph. Suppl. Ser., 1 : 319 - 355.

BAARS, (1973), IEEE AP-21, no. 4 : 461 - 474.

BAART,E.E et al (1980), Astron. Astroph., 92 : 156 - 162.

BERKHUIJSEN,E. (1971), Astron. Astroph., 14 : 359 - 386.

BERKHUIJSEN,E. (1972), Astron. Astroph. Supll. Ser., 5 : 263 - 312.

BLAAUW,A. (1961), Bull. Astr. Inst. Netherlands, 16 : 265.

BLAAUW,A. (1964), Ann. Rev. Astr. Astroph., 2 : 213 - 246.

BRACEWELL,R. (1965), The Fourier Transform and its Applications, McGraw-Hill Book Co.

CLEARY,M.N. HEILES,C. and HASLAM,C.G.T. (1979), Astr. Astroph. Suppl. Ser., 36 : 95 127.

CLEARY,M.N. (1977), PhD Thesis, Australian National University, Canberra.

COLOMB,F.R. POEPPEL,W.G.L. and HEILES,C. (1980), Astron. Astroph. Suppl. Ser., 40 : 47 - 55.

COLOMB,F.R. DUBNER,G. (1982), Astron. Astroph., 112 : 141

* DE JAGER,G. (1983), Proceedings of the first South African Symposium on Digital Image Processing, Sartori-Angus, A.G. Handley, C.C. (eds) p11.

DISNEY,M.J. WALLACE,P.T. (1982), Q. J. R. Astron. Soc., 23 : 485 - 504.

DOWNES,D. GUSTEN,R. (1982), Conference : Spring Meeting of the Astronomischen Gesellschaft, pp 207 - 232.

* DAVIS,M.M. et al (1965), Bull. Astr. Inst. Netherlands, 18 : 42

ELIAS,J.H. (1978), Ap. J., 224 : 453 - 472.

FRENCH,D.K. OSBORNE,J.L. (1976), MNRAS, 177 : 569 - 581.

FINDLAY,J.W. (1966), Ann. Rev. Astron. Astroph., 4 : 77 - 94.

GEORGELIN,Y.M. and GEORGELIN,Y.P. (1976), Astron. Astroph., 49 : 57 - 59.

GONZALEZ,R.C. WINTZ,P. (1977), Digital Image Processing, Addison-Wesley, Reading, Massachusetts.

GOUDIS,C. (1982), The Orion Complex : A case study of interstellar matter, D Reidel Publishing Co.

GREEN,A.J. (1974), Astron. Astroph. Suppl. Ser., 18 : 267 - 307.

GULL,T.R. and SOFIA,S. (1979), Ap. J, 230 : 138 - 148.

HANBURY BROWN,R. et al (1960), Observatory, 80 : 191.

HASLAM,C.G.T (1974), Astron. Astroph. Suppl. Ser., 36 : 95.

HASLAM,C.G.T. et al (1981), Astron. Astroph., 100 : 209.

HASLAM,C.G.T et al (1982), Astron. Astroph. Suppl. Ser., 47 : 1 - 143.

HAYNES,R.F. CASWELL,J.L. SIMMONS,L.W.J. (1978), Aust. J. Phys. Astron. Suppl., 45 :

HEILES,C. (1976), Ap. J. (Letters), 208 : L137.

HEILES,C. (1979), Ap. J., 229 : 533 - 544.

HERBIG,G.H. (1968), Zeitschrift fur Astrophysik, 68 : 243 - 277.

HIGGS,L.A. (1967), Bull. Astron. Inst. Neth. Suppl. Ser., 2 : 59.

HILL,E.R. (1968), Aust. J. Phys., 21 : 735 - 737.

JANSKY,K.G. (1932), Proceedings of the Institute of Radio Engineers, 20 : 1920 - 1932.

JOHNSON,J.B. (1928), Physical Review, 32 : 97.

JOHNSON,H.M. (1971), Ap. J., 164 : 67 - 76.

JONAS,J. (1982), MSc thesis, Rhodes University, South Africa.

KNIFFEN,D.A. FICHTEL,C.E. (1981), Ap. J., 250 : 389.

KOMESAROFF,M.M. (1966), Aust. J. Phys., 14 : 515.

KRAUS,J.D. (1966), Radio Astronomy, McGraw-Hill Book Company.

LANDECKER,T.L and WIELEBINSKI,R. (1970), Aust. J. Phys. Astroph. Suppl., 16 : 1 - 30.

LESH, (1968), Ap. J. Suppl., 17 : 371.

LINDBLAD,P.O. (1974), Stars and the Milky Way System, LN Mavridis (ed), Springer Verlag, Proceedings of the First European Astronomical Meeting, vol 2.

LOCKMAN,F.J. (1979), Ap. J., 232 : 761 - 781.

MACATHOMAS,B. et al (1969), Aust. J. Phys. Astron. Suppl., 11 :

MAYER-HASSELWANDER,H.A. et al (1982), Astron. Astroph., 105 : 164.

MAYER-HASSELWANDER,H.A. (1983), Space Science Reviews, 36 : 223 - 247.

MATHEWSON,D.S. (1968), Ap. J. (Letters), 153 : L47.

MATHEWSON,P.S. HEALEY,J.R. ROME,J.M. (1962), Aust. J. Phys., 15 : 354.

MEZGER,P.G. and HENDERSON,A.P. (1967), Ap. J., 147 : 471.

MONNET,G. (1974), Galactic Radio Astronomy, IAU Symposium no. 60, FJ Kerr and SC Simonson (eds), D Reidel, p249.

MORGAN,W.W. STROMGREN,B. JOHNSON,M.H. (1955), Ap. J., 121 : 611.

MORTON,D.C. (1975), Ap. J., 197 : 85 - 115.

MOUNTFORT,P. (1982), MSc thesis, Rhodes University, South Africa, unpublished.

NICOLSON,G.D. (1965), Publ. Astron. Soc. Pac., 77 : 260 - 268.

NICOLSON,G.D. (1970a), IEEE T.M.T.T., vol. 18, no. 3 : 169.

NICOLSON,G.D. (1970b), REPORT no. TEL 80, NITR, SACSIR.

NISHIMURA,T. et al (1980), Ap. J., 239 : L101 - L106.

NYQUIST,H. (1928), Physical Reviews, vol. 32, no. 1 : 110.

OKUDA,H. (1981), Infrared Astronomy, IAU Symposium no. 96, Wynn-Williams,C.G. Cruikshank,D.P (eds), D Reidel, p247.

OLANO,C.A. POEPPEL, W.G. (1981), Astron. Astroph., 95 : 316 - 320.

OSTER,L. (1961), Ap. J., 134 : 1010.

PANAGIA,N. (1973), Astron. J., 78 : 929 - 934.

PARKER,E.N. (1969), Space Science Reviews, 9 : 651 - 712.

PAULINY-TOTH,I.I.K. SHAKESHAFT,J.R. (1962), MNRAS, 124 : 61 - 77.

PENZIAS,A.A. WILSON,R.W. (1966), Ap. J., 146 : 666 - 669.

PHILLIPS,S. et al (1981), Astron. Astroph., 98 : 286 - 294.

PRICE,R.M. (1969), Aust. J. Phys., 22 : 641 - 654.

PRICE,R.M. (1970), Astron. J., 75 : 144 - 147.

PRICE.R.M. (1972), Astron. J., 77 : 845 - 848.

PRICE,R.M. (1974), Astron. Astroph., 33 : 33 - 38.

REICH,W. (1982), Astron. Astroph. Suppl. Ser., 48 : 219 - 297.

REICH,W. (1983), Naturwissenschaften, 70 : 1 - 6.

REYNOLDS,R.J. OGDEN,P.M. (1982), Astron. J., 87 : 306 - 313.

SANCISI,R. van WOERDEN,H. (1970), Astron. Astroph., 5 : 135 - 139.

SANCISI,R. (1974), Galactic Radio Astronomy, IAU Symposium 60, Kerr, F.J. and Simonson, S.C. (eds), D Reidel Publ. Co. : 115 - 128.

SEEGER,Ch.L. et al (1965), Bull. Astron. Inst. Neth., 18 : 11.

SIMONSON,C. (1976), Astron. Astroph., 46 : 261.

SIVAN,J.P. (1974), Astron. Astroph. Suppl. Ser., 16 : 163.

SMITH,A.M. et al (1978), Ap. J., 220 : 138 - 148.

SOFUE,Y. (1973), Publ. Astron. Soc. Japan, 25 : 207 - 229.

SOFUE,Y. HAMAJIMA,K. FUJIMOTO,M. (1974), Publ. Astron. Soc. Japan, 26 : 399 - 416.

SOLOMON,P.M. SANDERS,D.B. (1980), Giant Molecular Clouds in the Galaxy, Solomon,P.M. Edmunds,E.G. (eds), Pergamon Press : 41 - 63.

STELZREID,C. (1982), Noise Temperature Concepts, Measurements and

Performance, JPL Publication 82.33.

STOTHERS,R. FROGEL,J.A. (1974), Astron. J., 79 : 456 - 471.

TAFF,L.G. (1981), Computational Spherical Astronomy, John Wiley & sons.

TUKEY,J.W. (1977), Exploratory Data Analysis, Addison-Wesley Publ. Co.

UNSOLD,A. (1946), Naturwissenschaften, 33 : 37.

WEAVER,H. (1978), The Large-Scale Characteristics of the Galaxy, IAU Symposium 84, Burton, W.B. (ed), D Reidel Publ. Co. : 295 - 300.

WEBSTER,A.S. (1974), MNRAS , 166 : 355 - 371.

WESTERHOUT (1958), Bull. Astron. Soc. of the Netherlands, 14 : 215 - 263.

WOUTERLOOT,J. (1982), PhD Thesis, Leiden.

## APPENDIX 1

### Key to equatorial contour maps

Resolution (HPBW) : $0.333^{\circ}$

Beam sensitivity : 11.38 Jy/K

Noise level :

| declination | rms noise (mK) |
|---|---|
| -80 to -69 | 17 |
| -72 to -61 | 22 |
| -25 to -14 | 15 |
| -18 to -7 | 16 |

Contour label table

| contour label | $T_a$ mK | contour label | $T_a$ mK |
|---|---|---|---|
| 1 | 12 | 24 | 1000 |
| 2 | 25 | 25 | 1200 |
| 3 | 37 | 26 | 1400 |
| 4 | 50 | 27 | 1600 |
| 5 | 75 | 28 | 1800 |
| 6 | 100 | 29 | 2000 |
| 7 | 125 | 30 | 2500 |
| 8 | 150 | 31 | 3000 |
| 9 | 175 | 32 | 3500 |
| 10 | 200 | 33 | 4000 |
| 11 | 225 | 34 | 4500 |
| 12 | 250 | 35 | 5000 |
| 13 | 275 | 36 | 6000 |
| 14 | 300 | 37 | 7000 |
| 15 | 350 | 38 | 8000 |
| 16 | 400 | 39 | 9000 |
| 17 | 450 | 40 | 10000 |
| 18 | 500 | 41 | 12000 |
| 19 | 550 | 42 | 14000 |
| 20 | 600 | 43 | 20000 |
| 21 | 700 | 44 | 25000 |
| 22 | 800 | 45 | 30000 |
| 23 | 900 | | |

1 K full beam antenna temperature corresponds to 1.41 K full beam brightness temperature.The grid lines on the maps represent Galactic longitude and latitude at $5^{\circ}$ spacing.

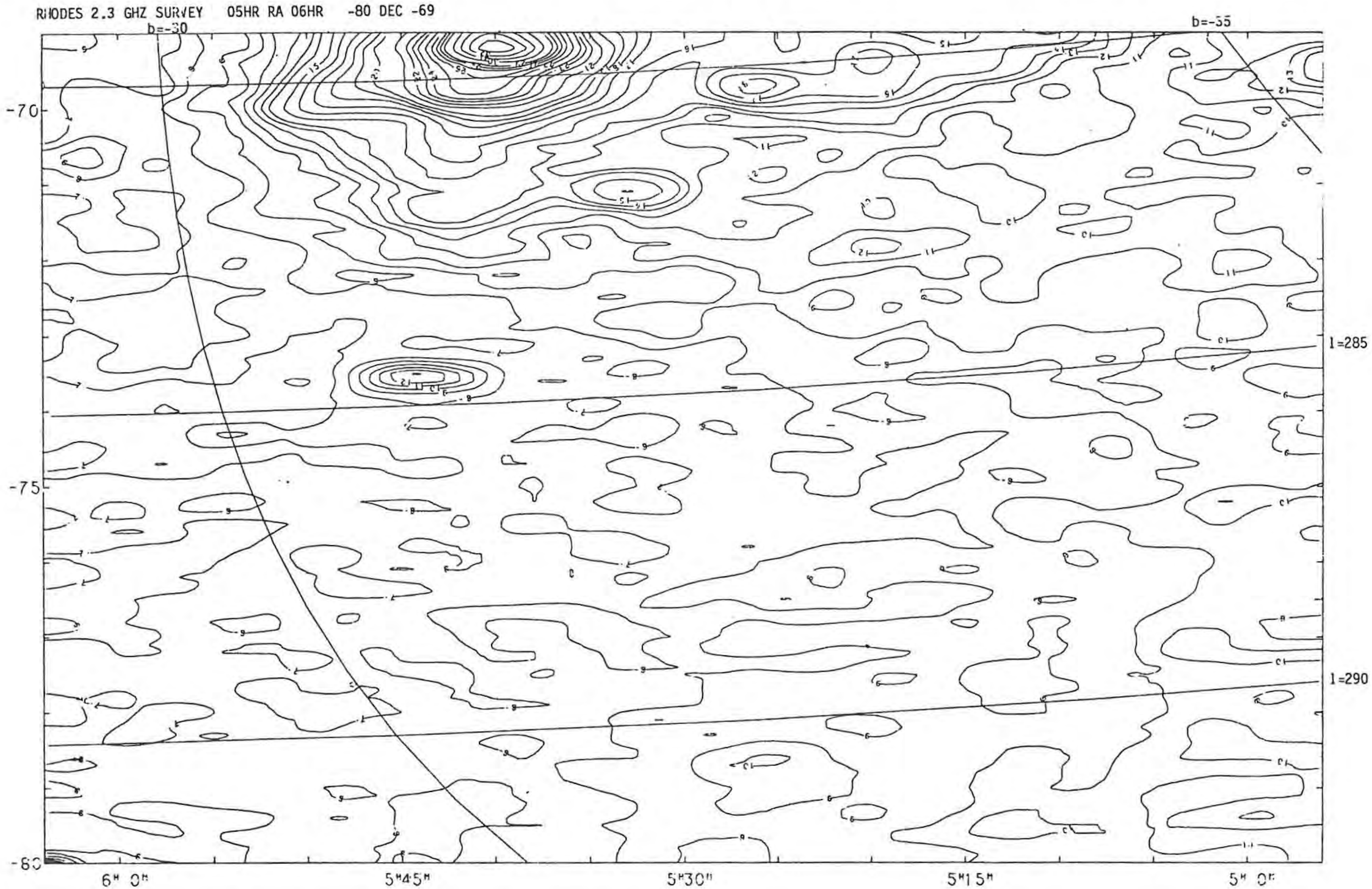
RHODES 2.3 GHZ SURVEY 05HR RA 06HR -80 DEC -69
b=-30
b=-35
1=285
1=290
-70
-75
-80
6H 0M
5H45M
5H30M
5H15M
5H 0M

RHODES 2.3 GHZ SURVEY   05HR RA 06HR  -72 DEC -61

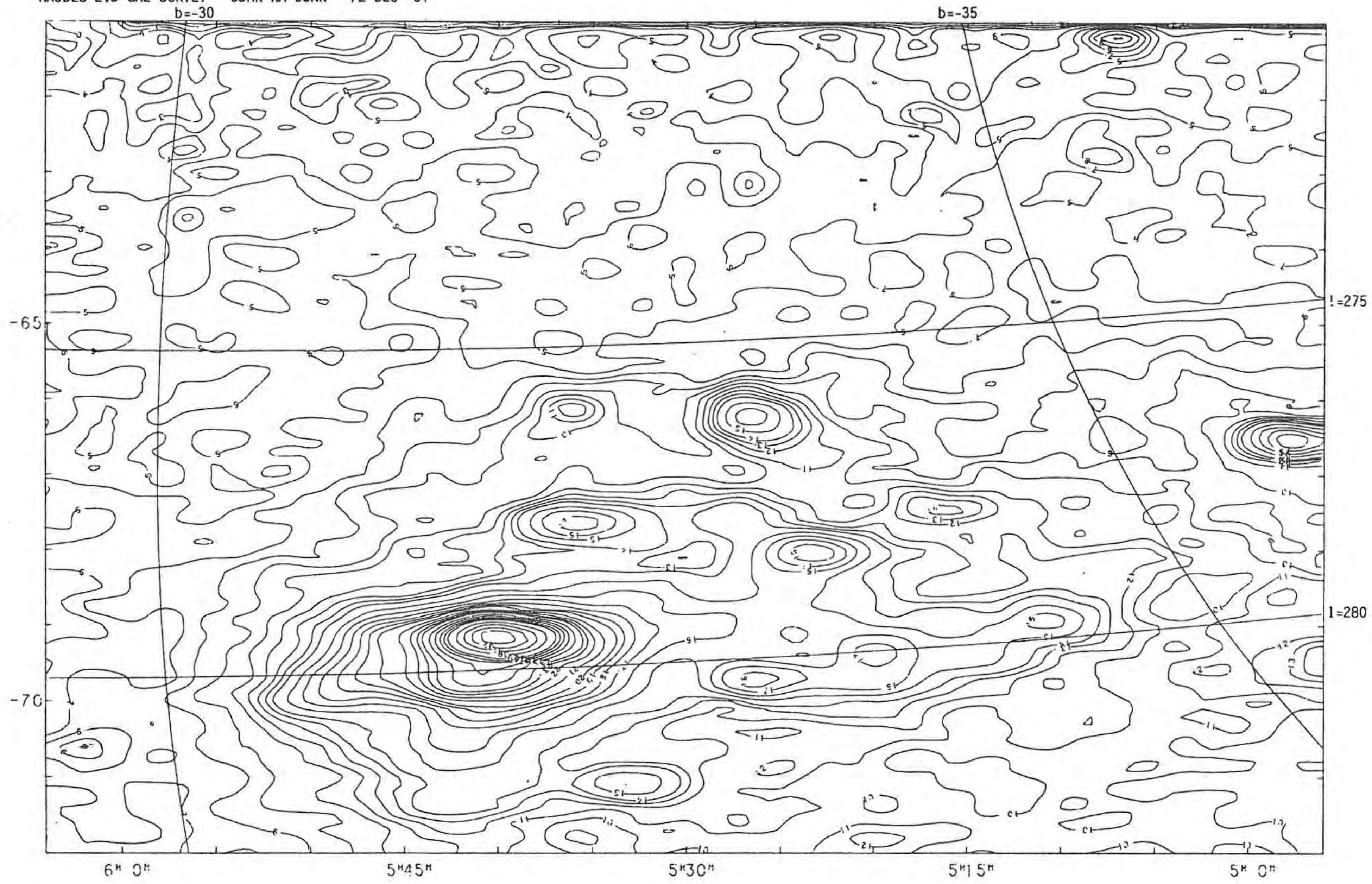

RHODES 2.3 GHZ SURVEY   06HR RA 07HR   -80 DEC -69

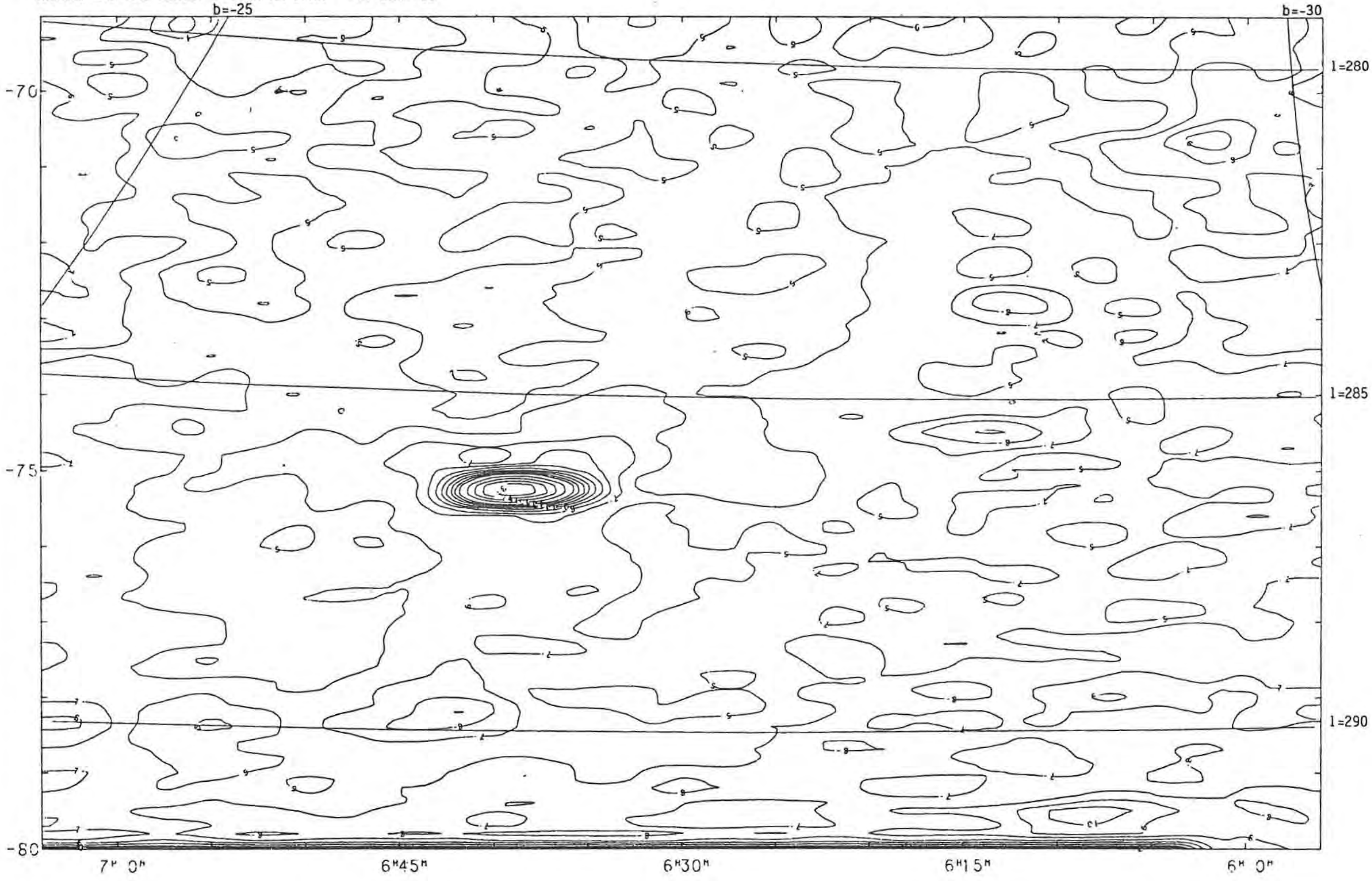

RHODES 2.3 GHZ SURVEY  07HR RA 08HR  -80 DEC -69

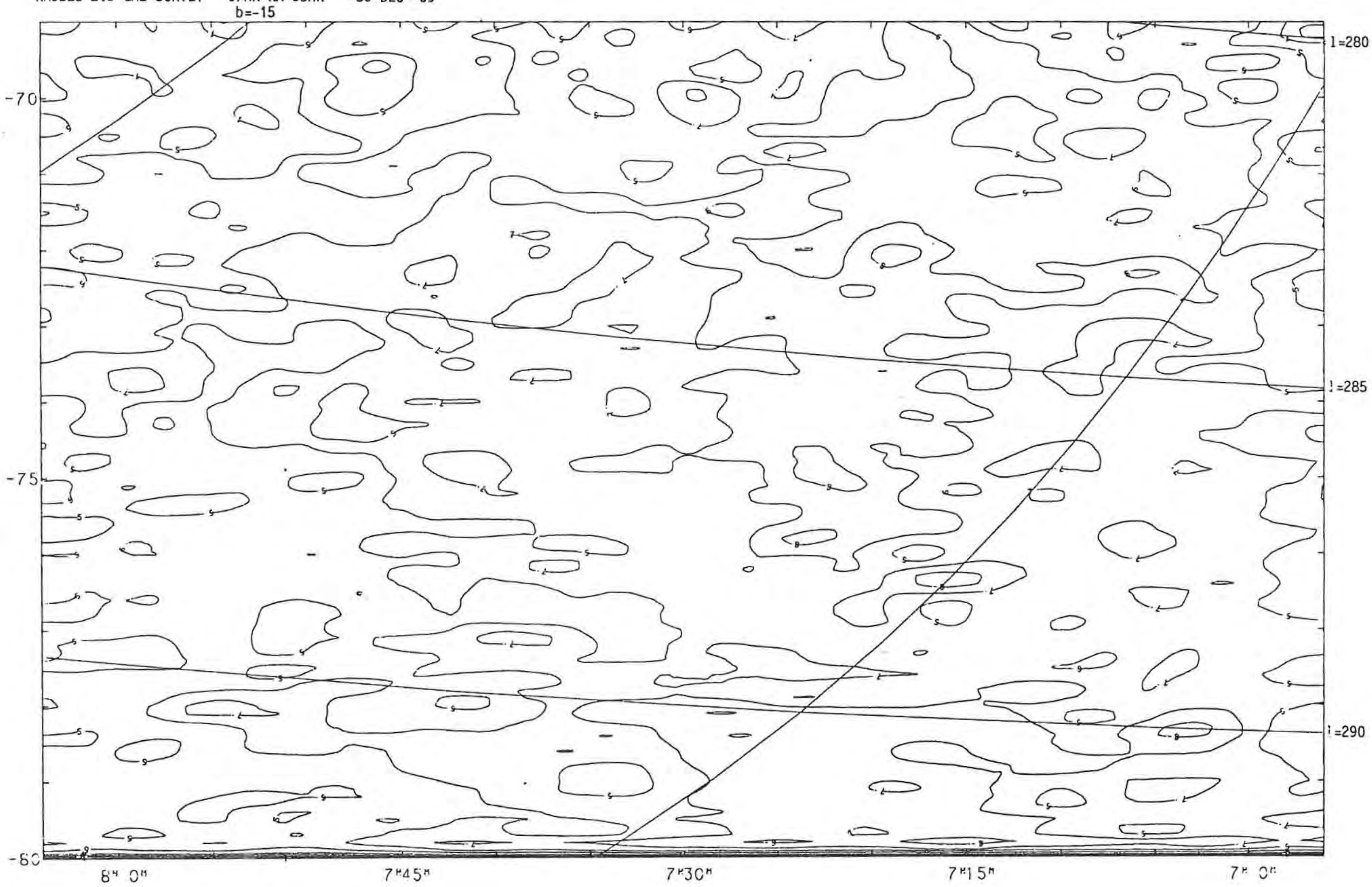

RHODES 2.3 GHZ SURVEY   06HR RA 07HR   -72 DEC -61

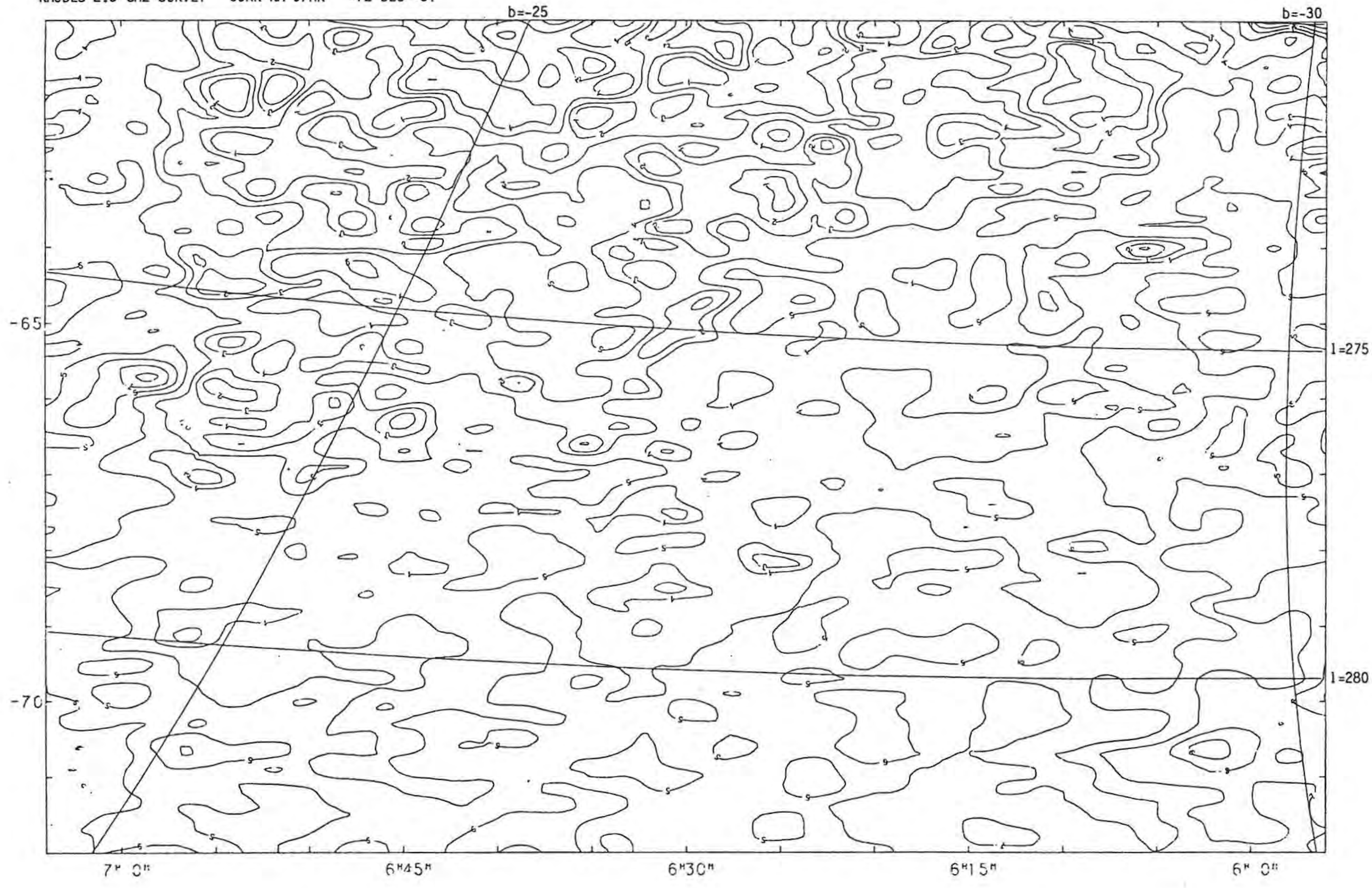

RHODES 2.3 GHZ SURVEY   07HR RA 08HR   -72 DEC -61

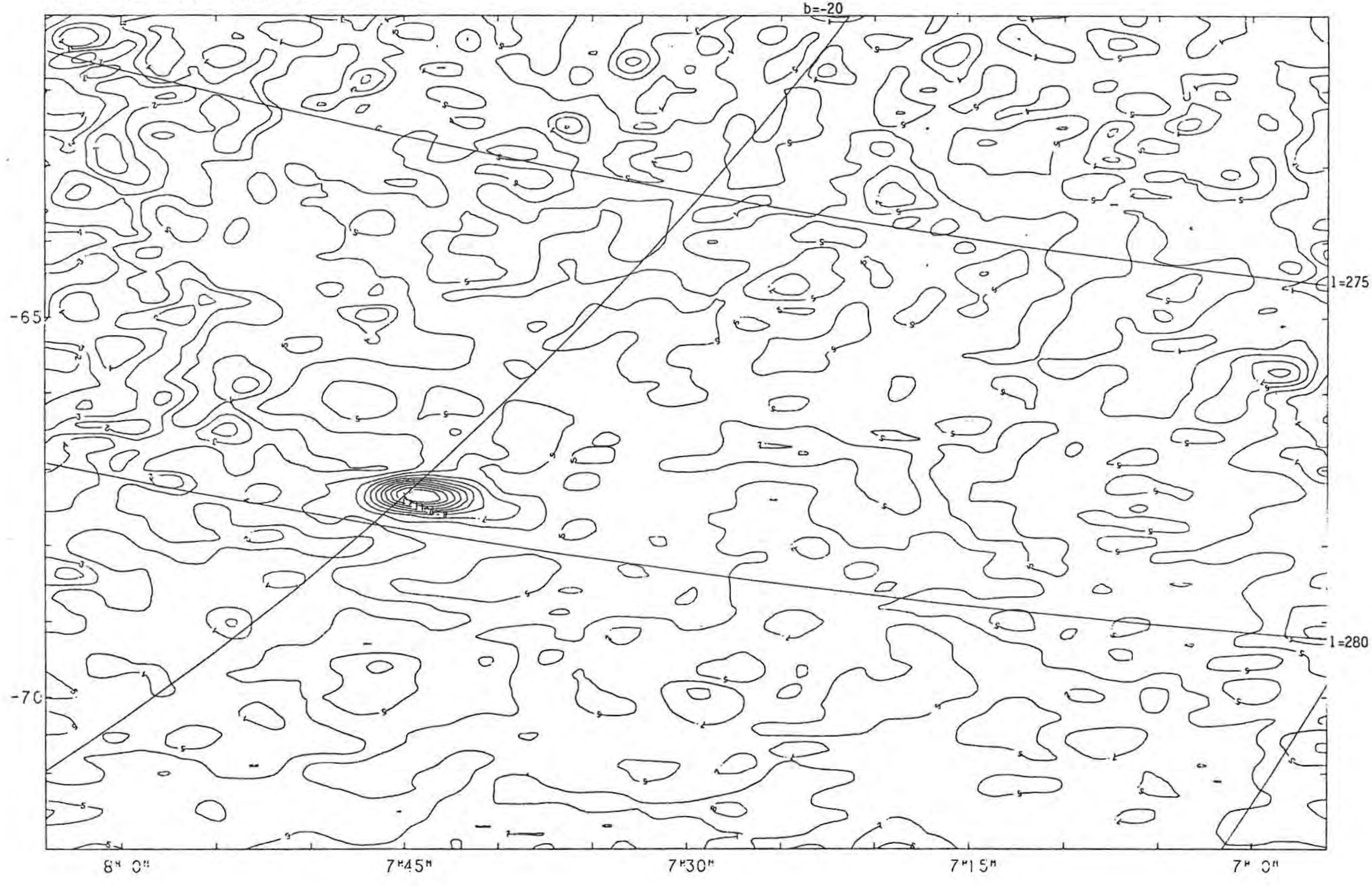

RHODES 2.3 GHZ SURVEY  08HR RA 09HR  -80 DEC -69

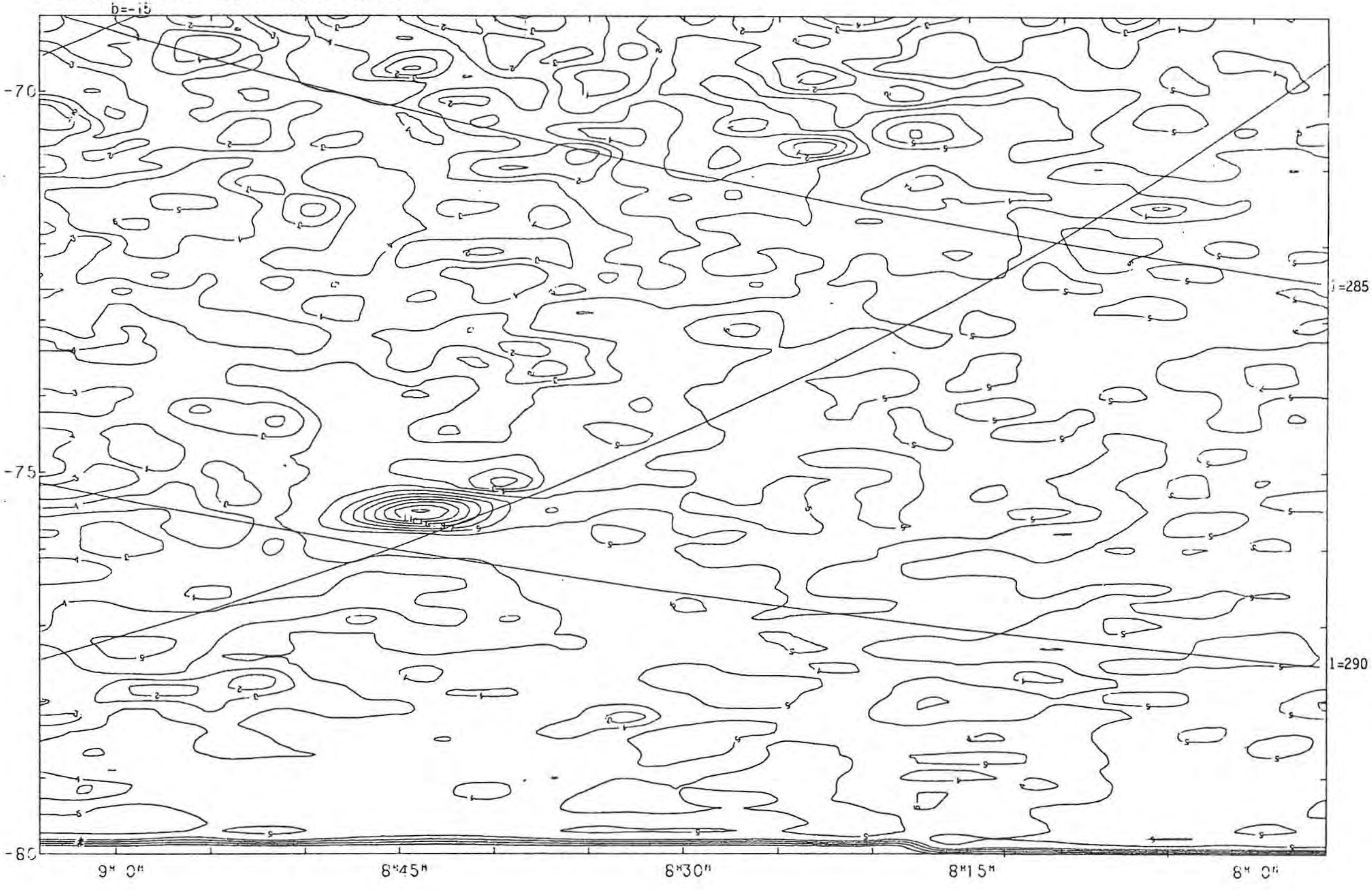

RHODES 2.3 GHZ SURVEY   08HR RA 09HR   -72 DEC -61

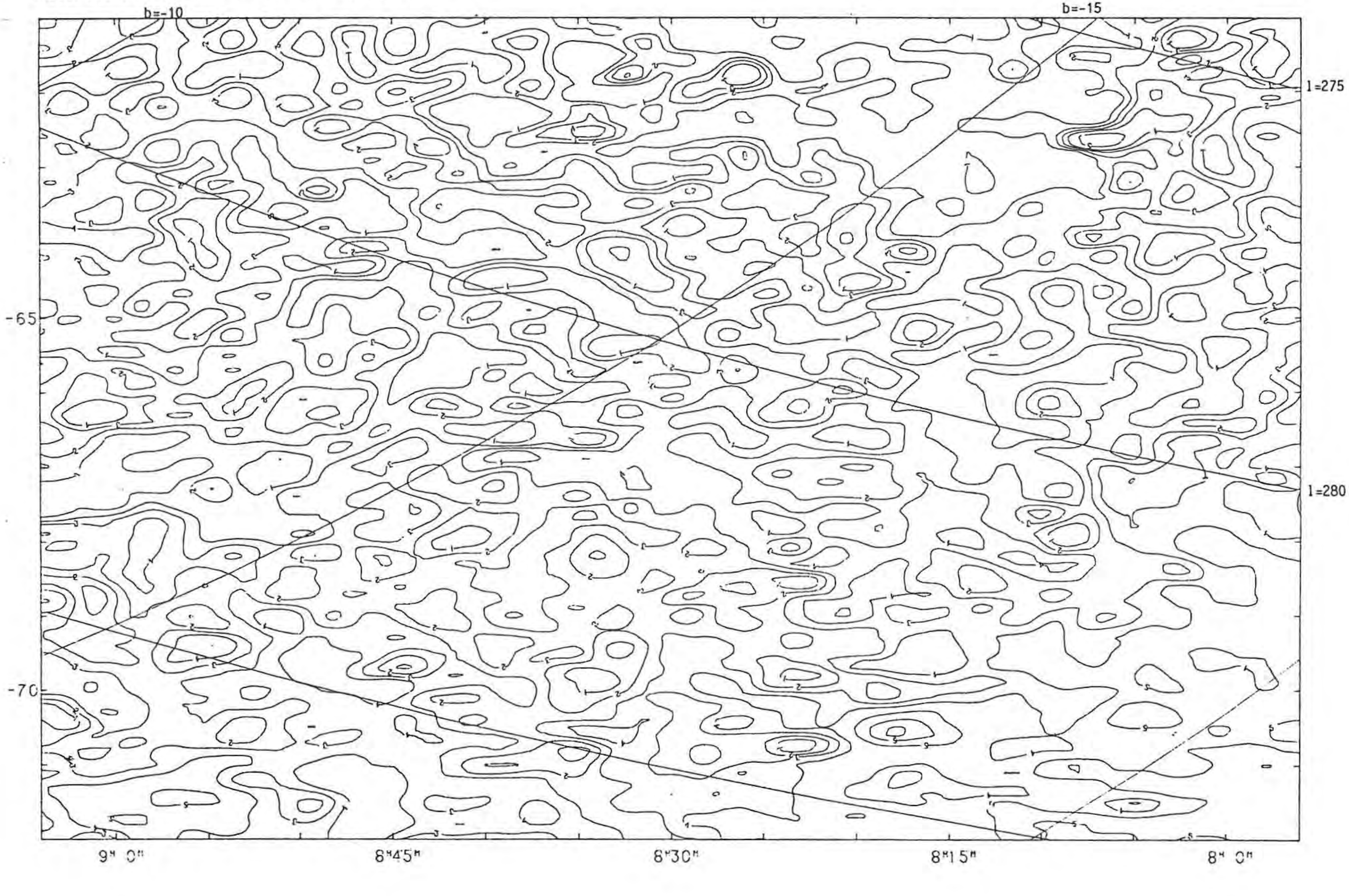

RHODES 2.3 GHZ SURVEY 09HR RA 10HR -80 DEC -69

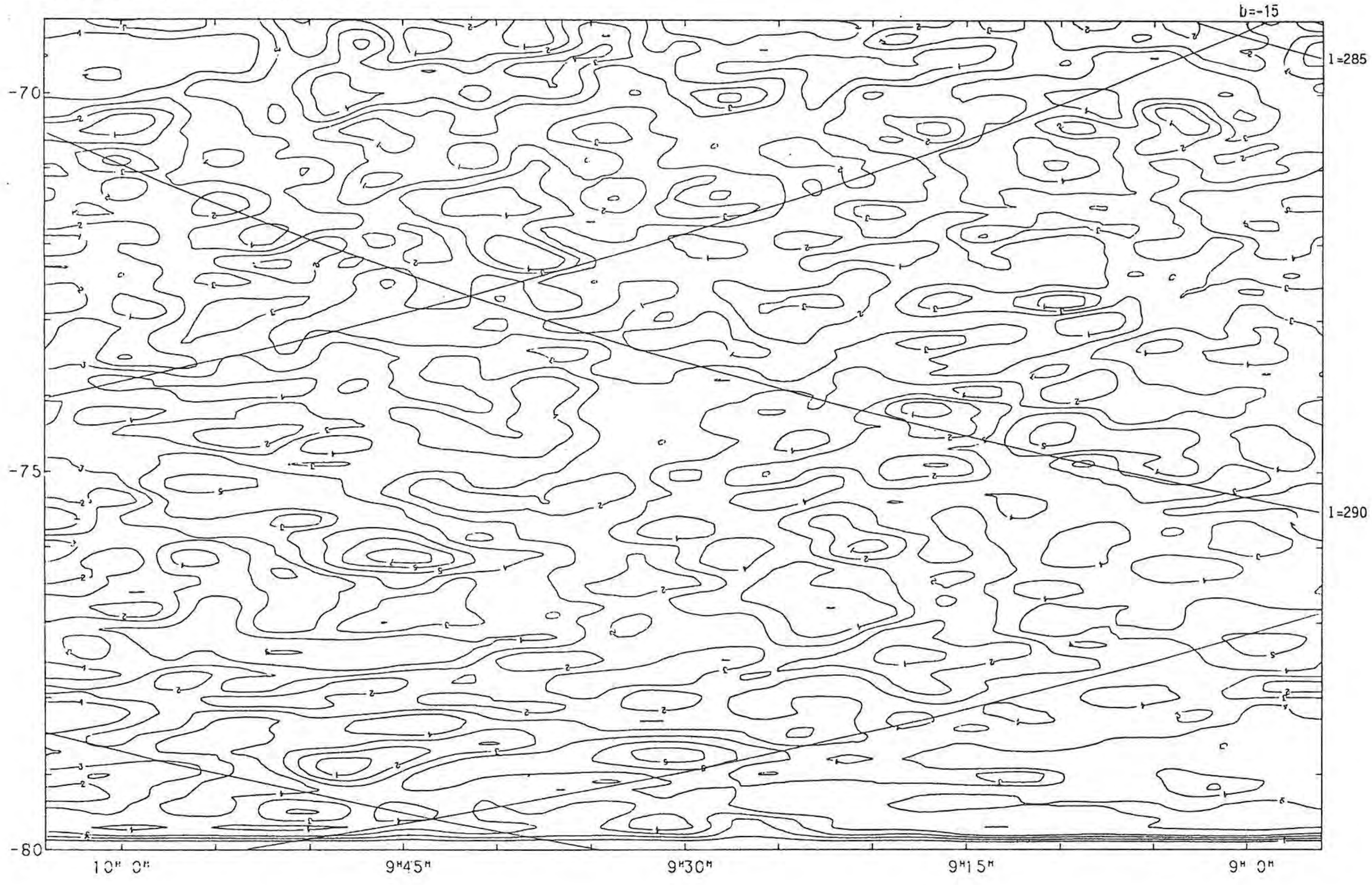

RHODES 2.3 GHZ SURVEY 09HR RA 10HR -72 DEC -61

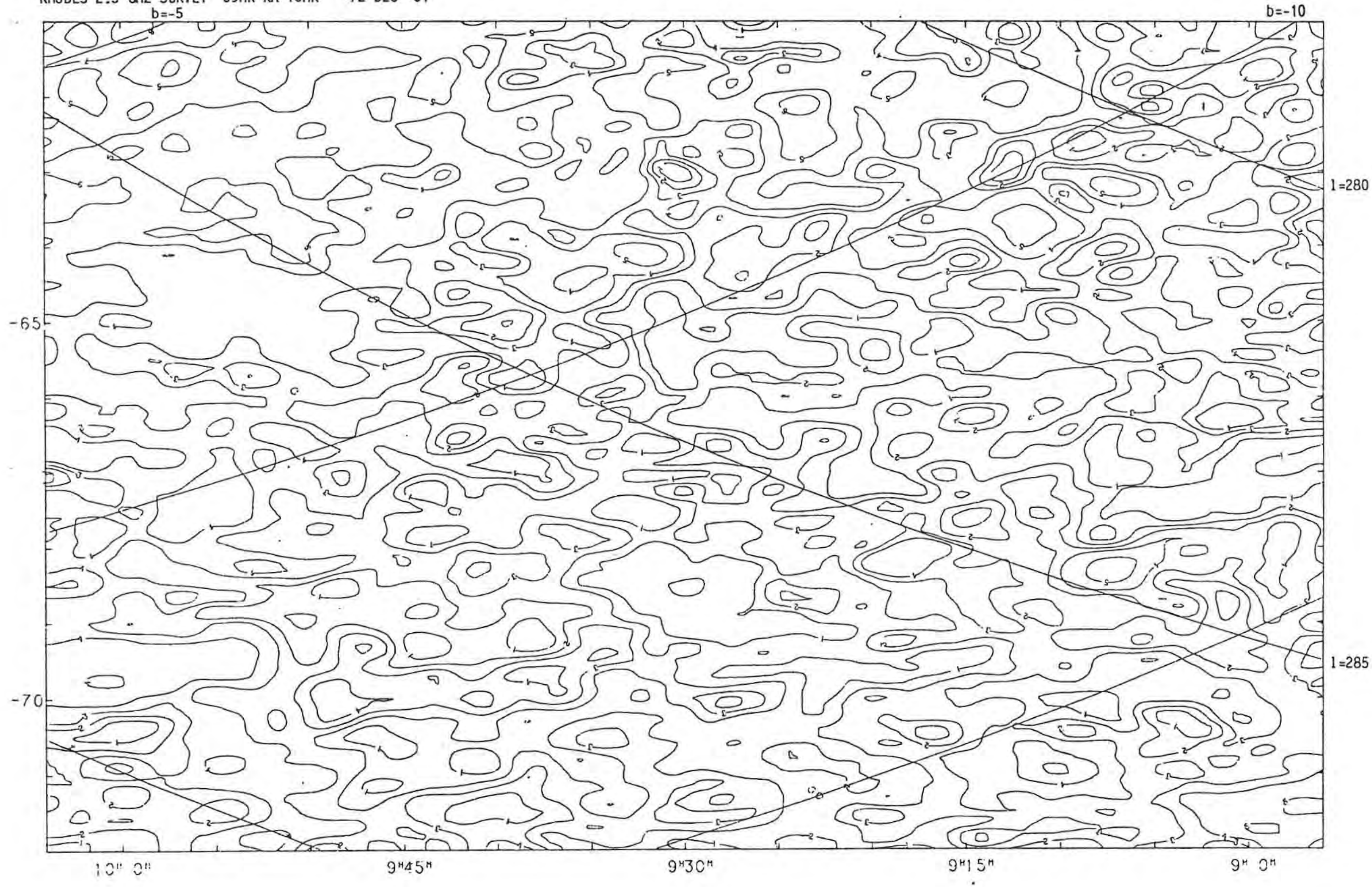

RHODES 2.3 GHZ SURVEY 10HR RA 11HR -80 DEC -69

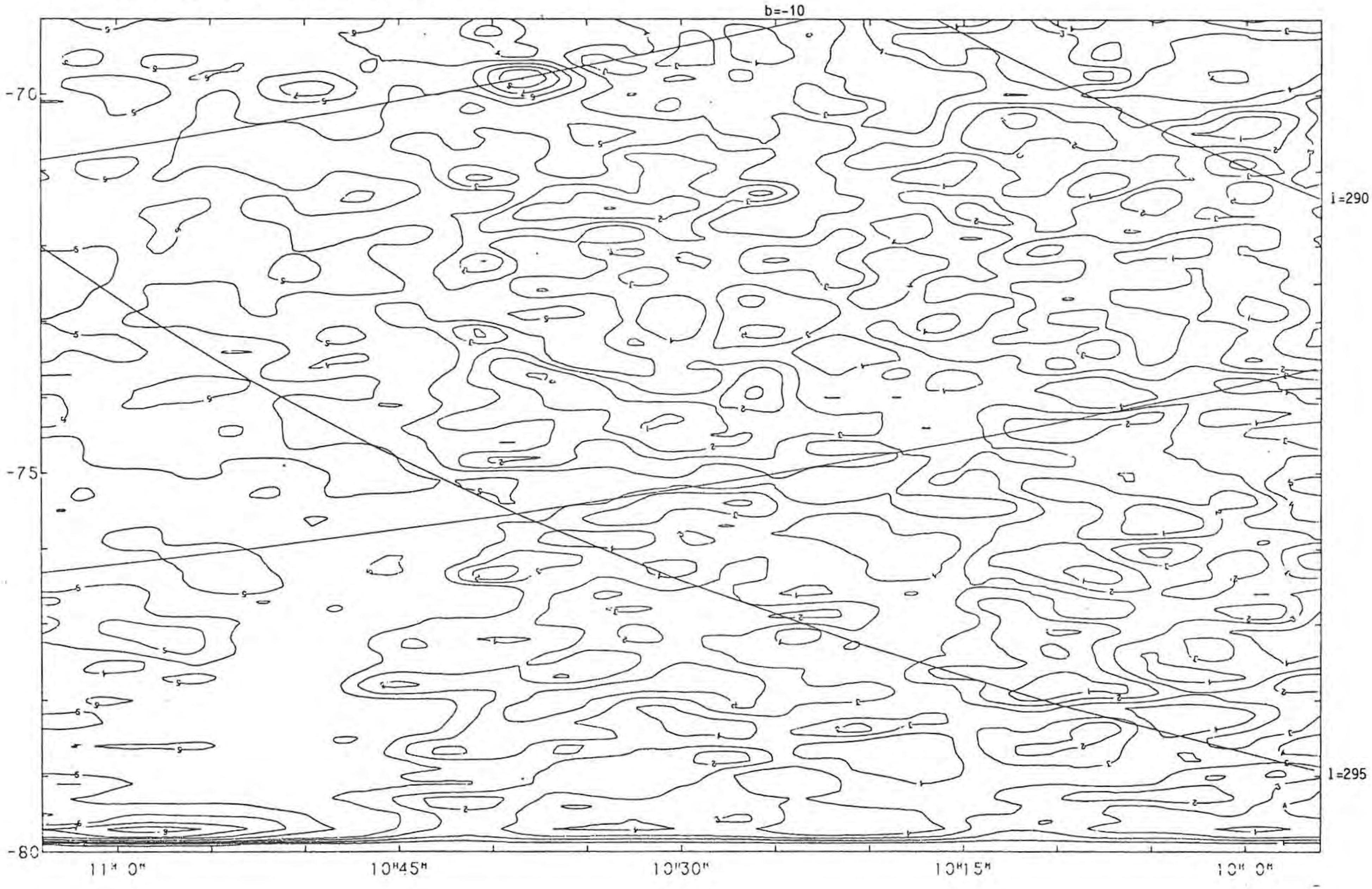

RHODES 2.3 GHZ SURVEY 10HR RA 11HR -72 DEC -61

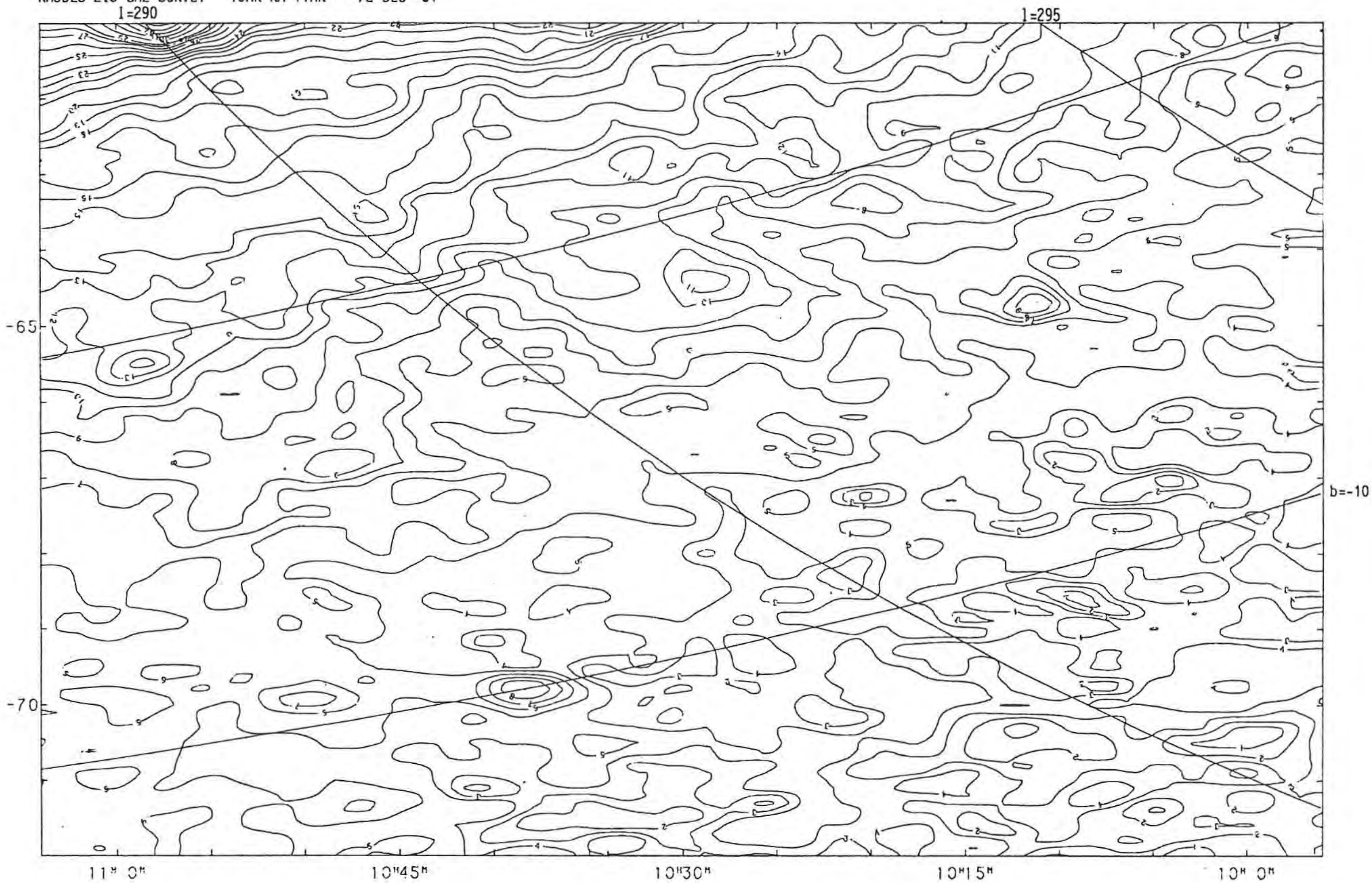

RHODES 2.3 GHZ SURVEY   11HR RA 12HR   -80 DEC -69

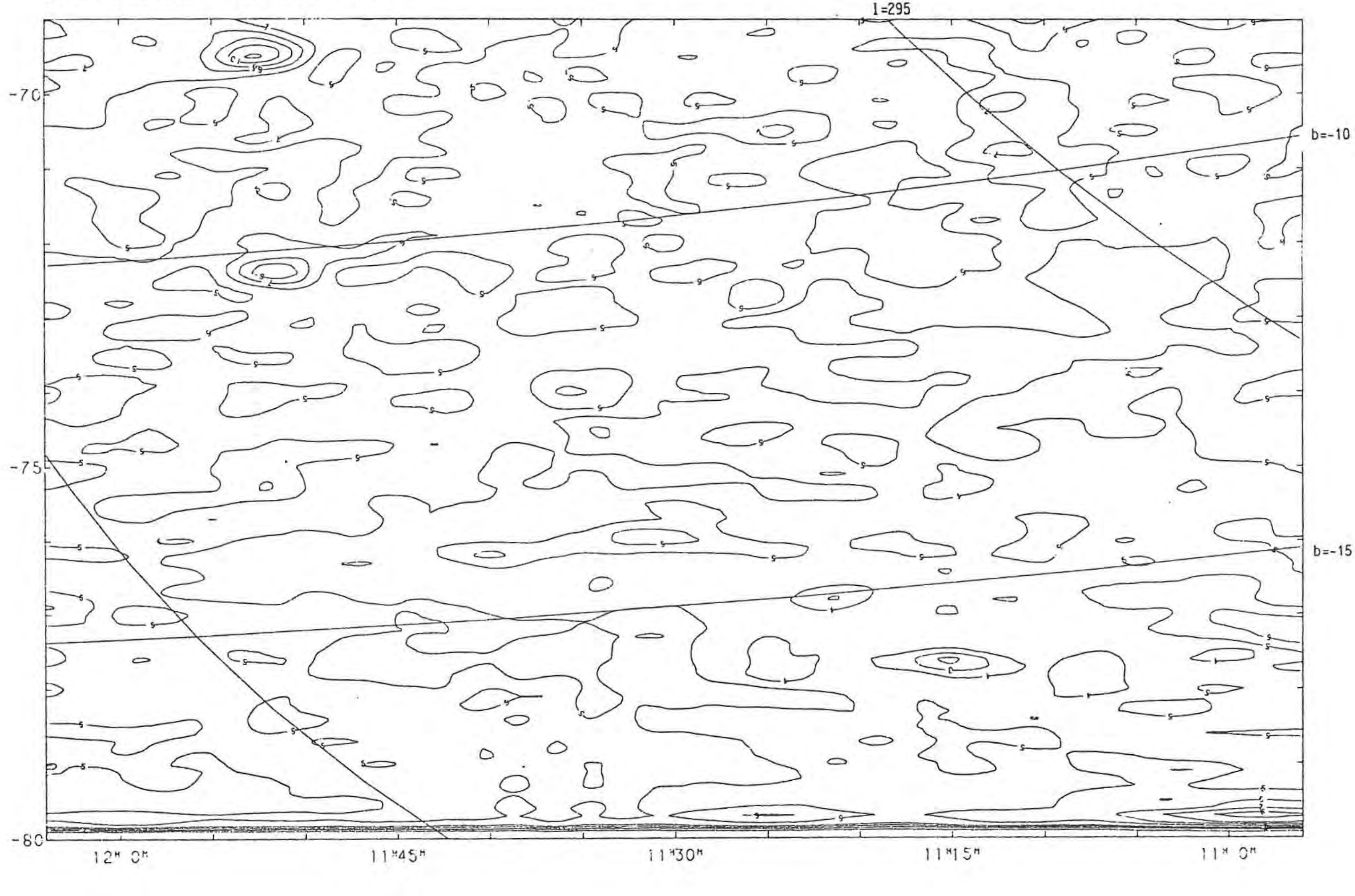

RHODES 2.3 GHZ SURVEY 11HR RA 12HR -72 DEC -61

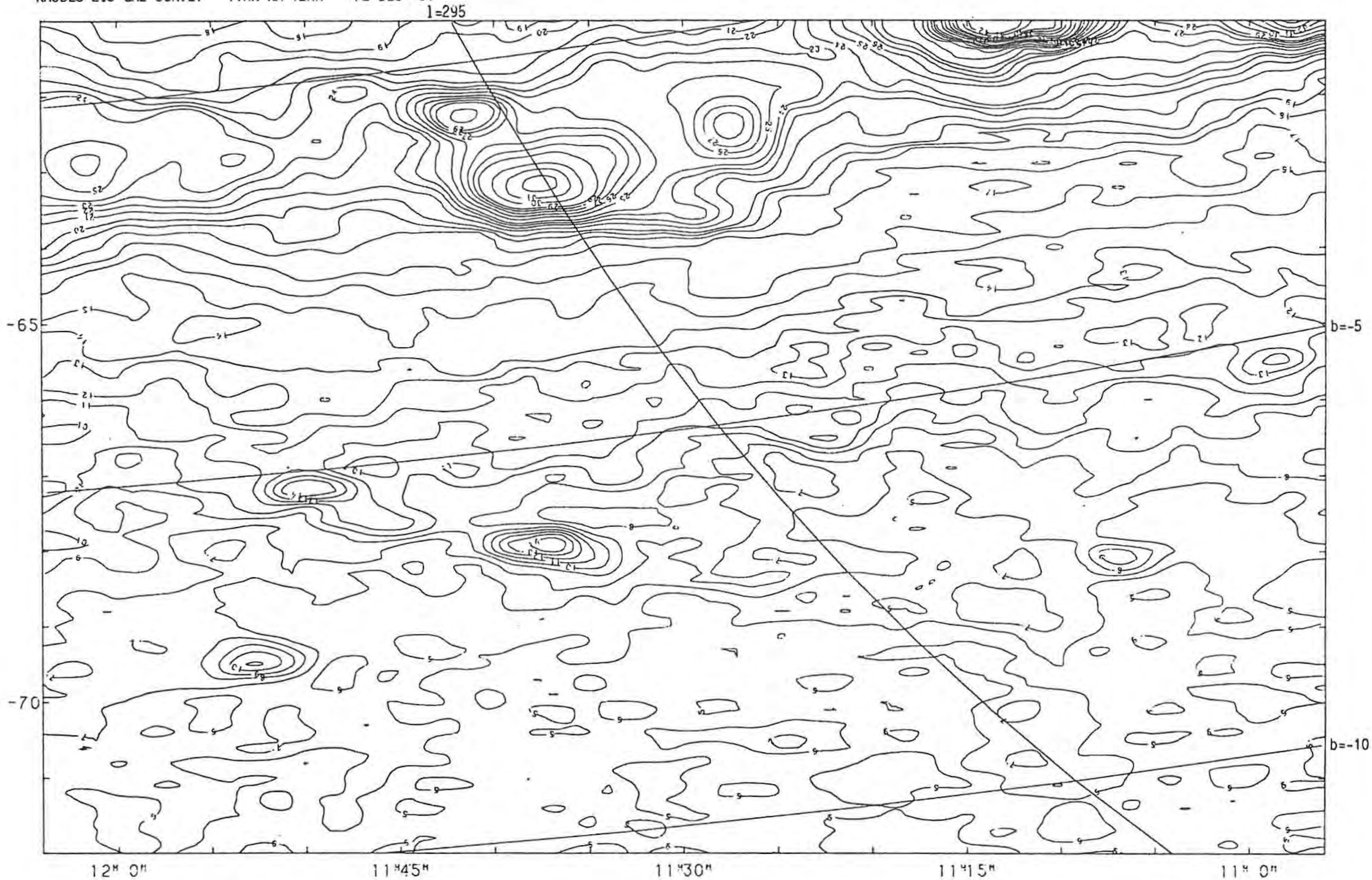

RHODES 2.3 GHZ SURVEY   12HR PA 13HR   -80 DEC -69

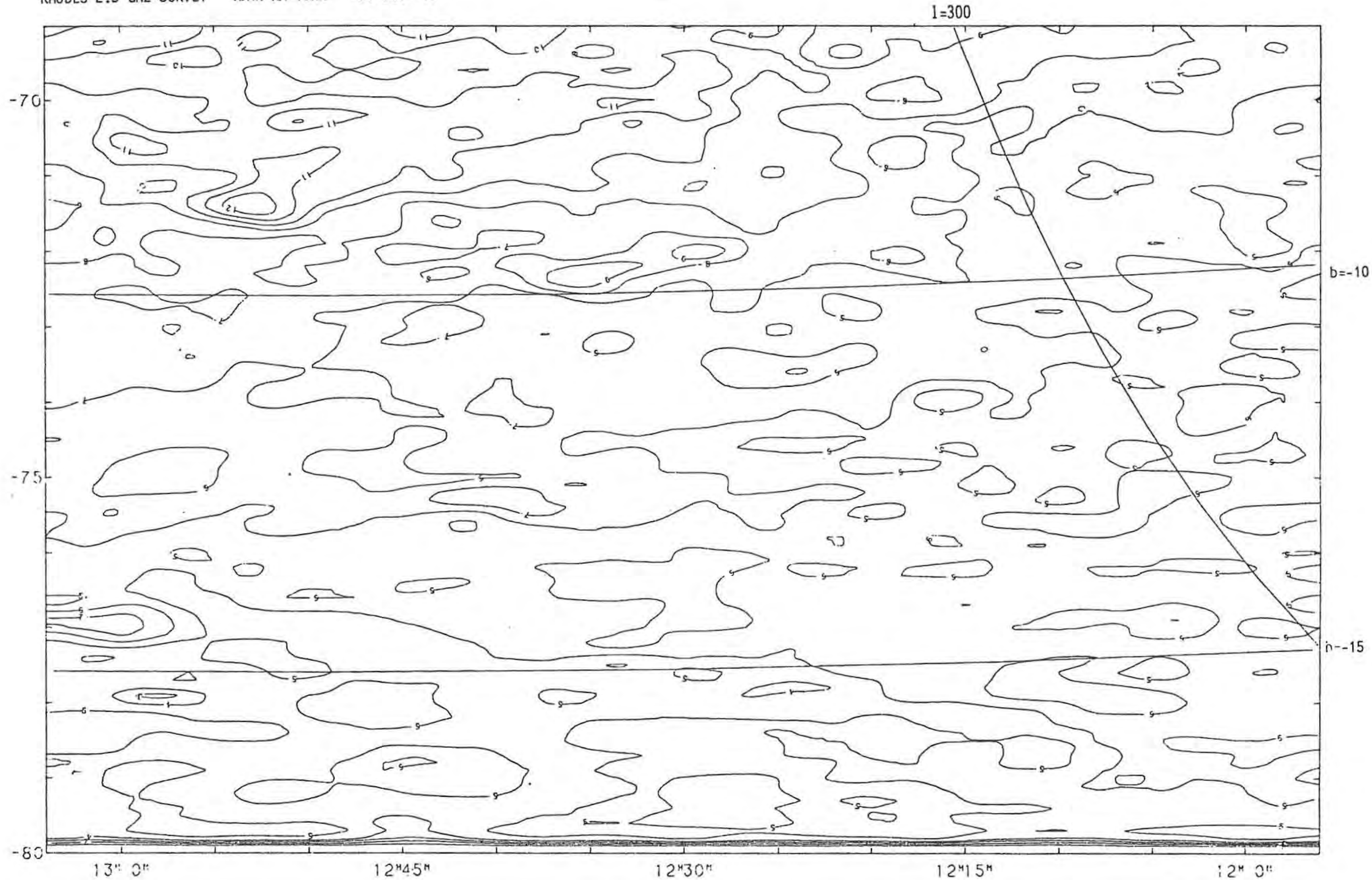

RHODES 2.3 GHZ SURVEY   12HR RA 13HR   -72 DEC -61

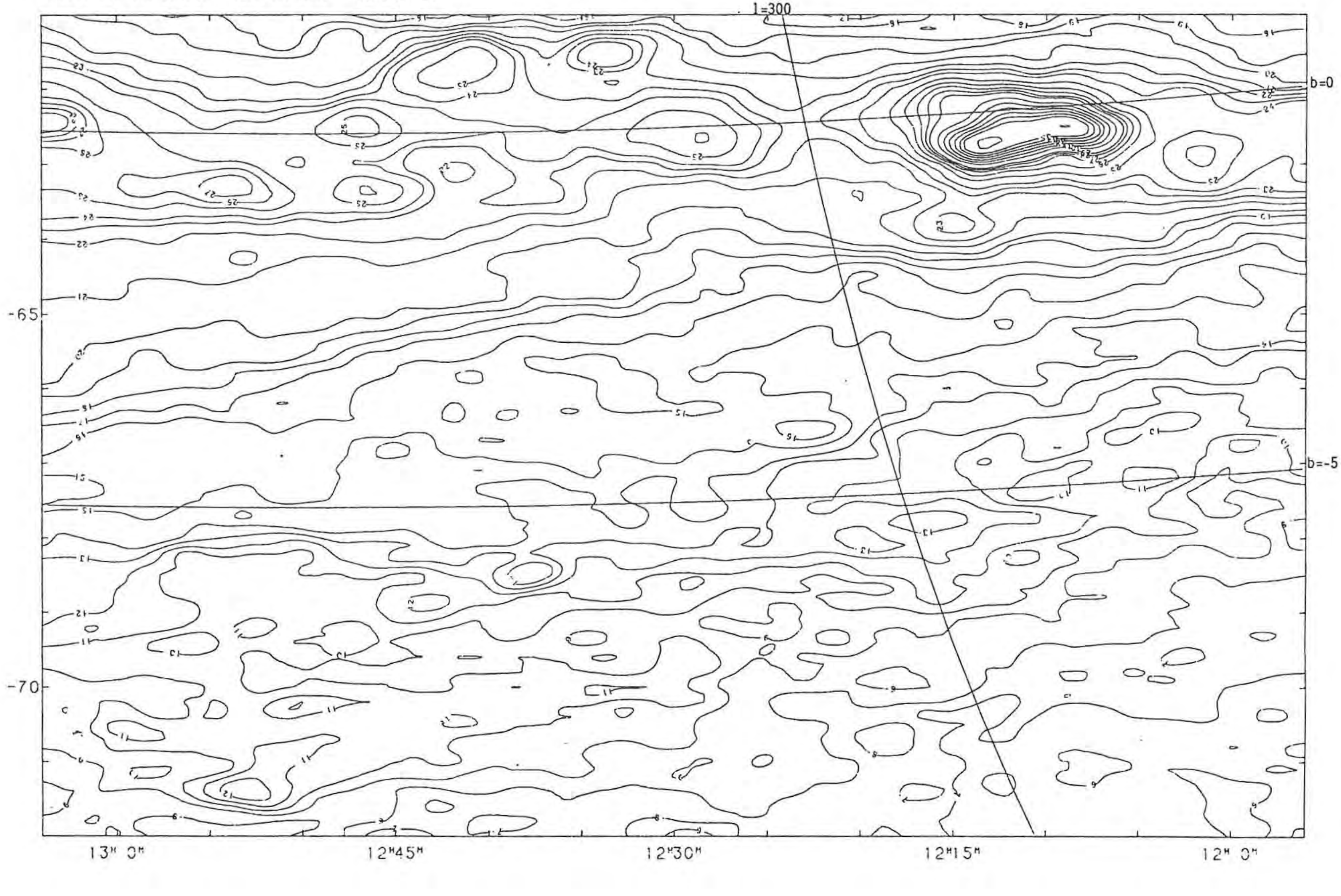

RHODES 2.3 GHZ SURVEY 13HR RA 14HR -80 DEC -69

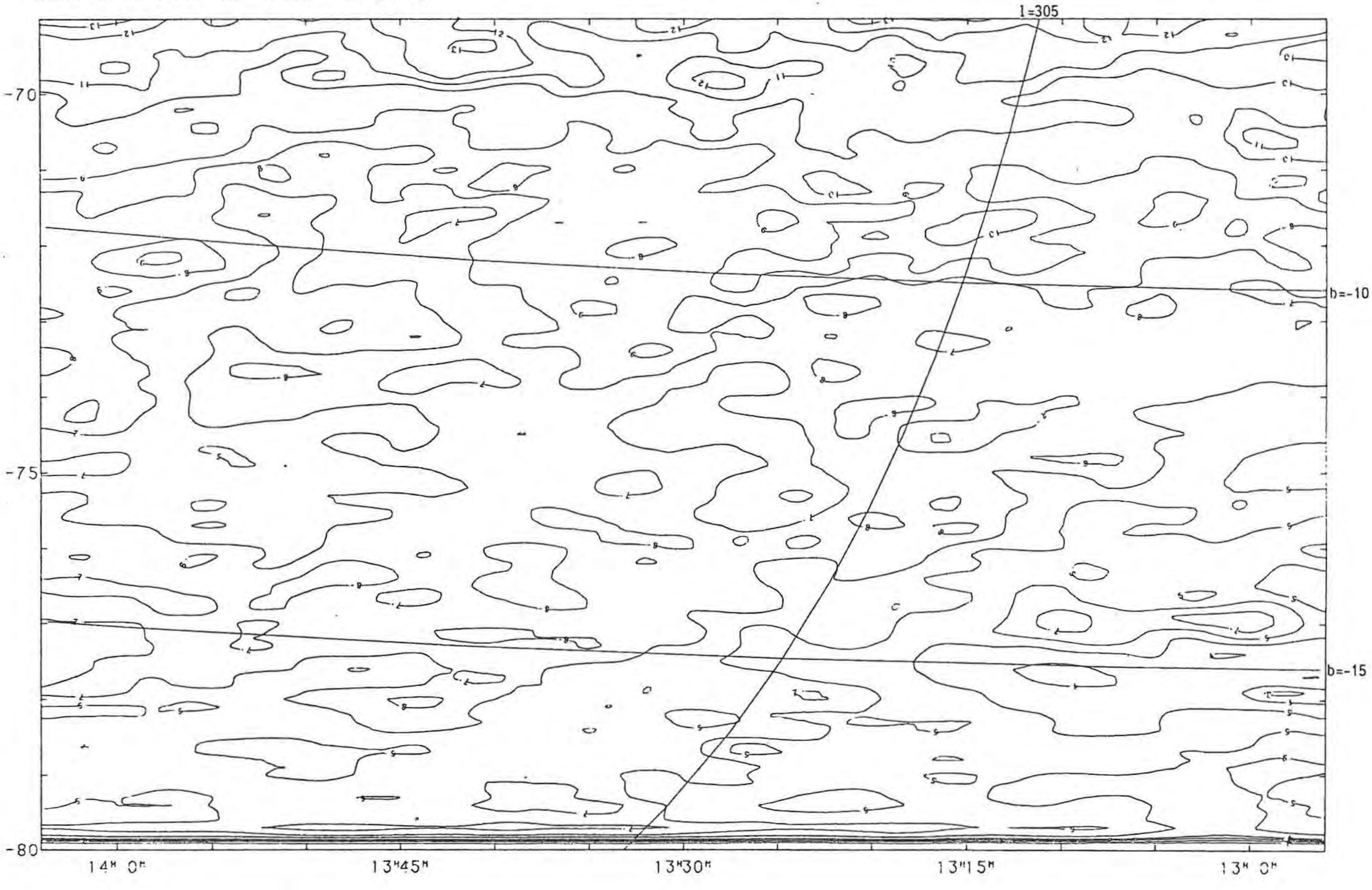

RHODES 2.3 GHZ SURVEY 13HR RA 14HR -72 DEC -61

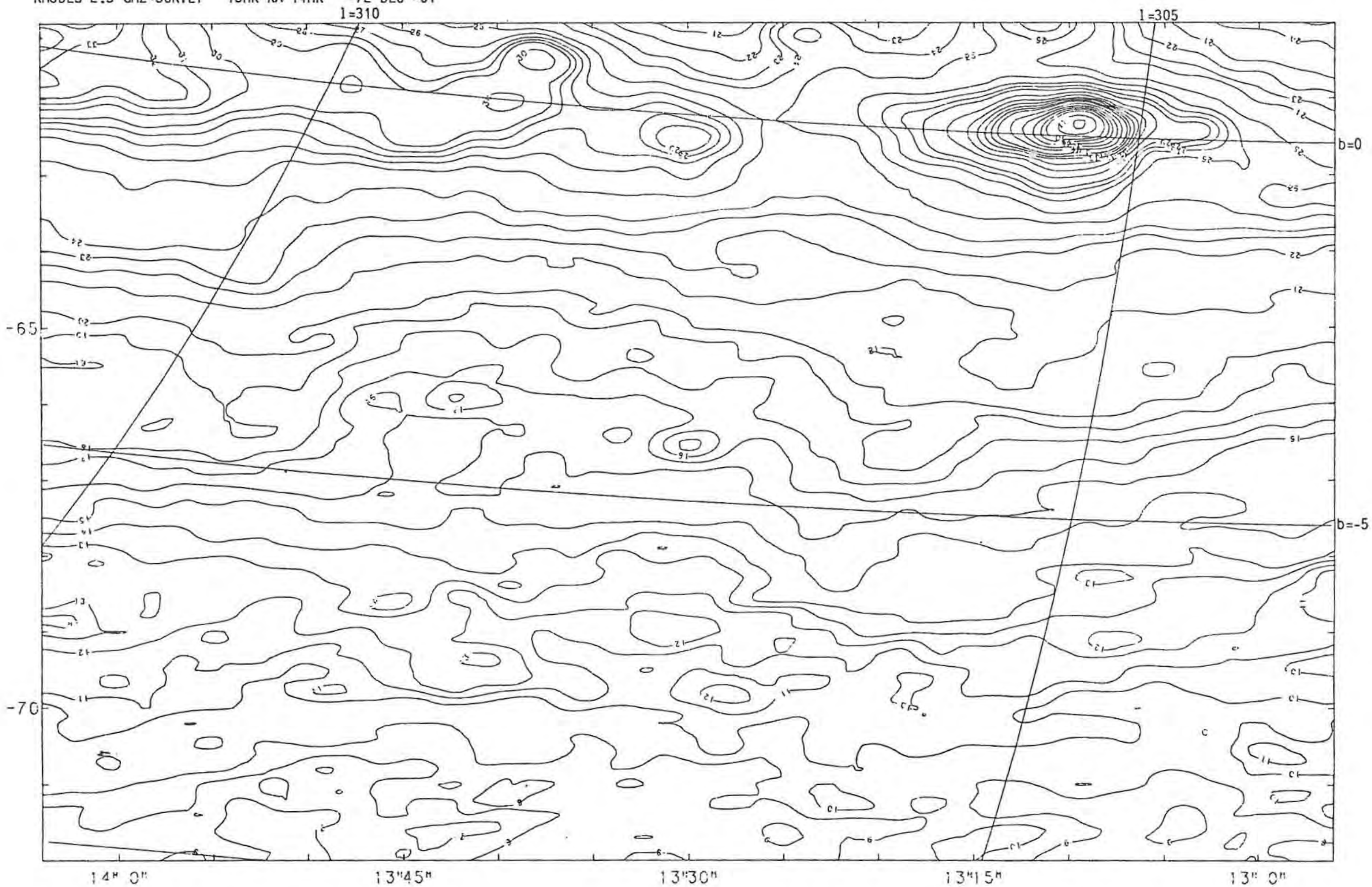

RHODES 2.3 GHZ SURVEY   14HR RA 14HR45M   -80 DEC -69

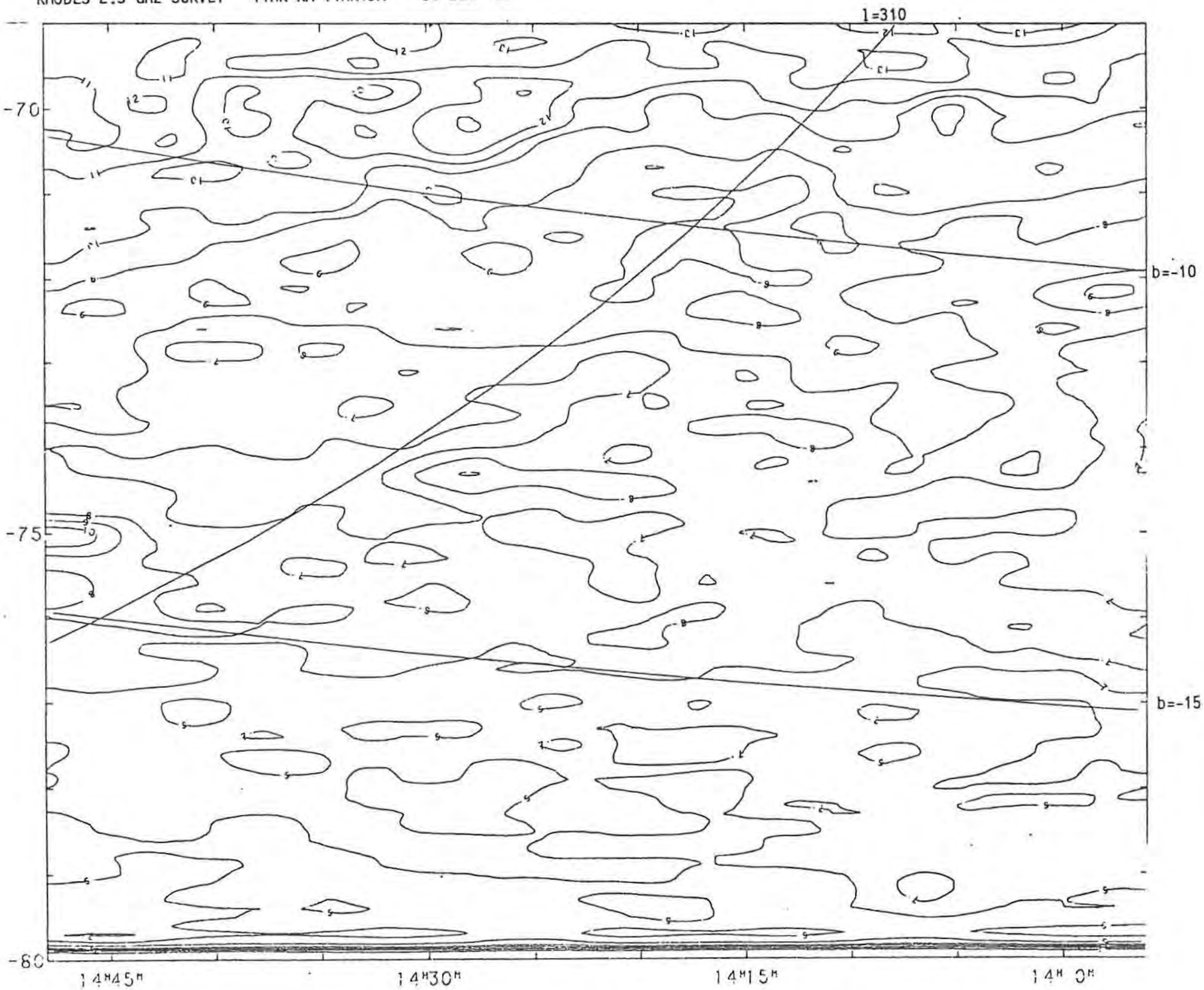

RHODES 2.3 GHZ SURVEY 14HR RA 14HR45M -72 DEC -61

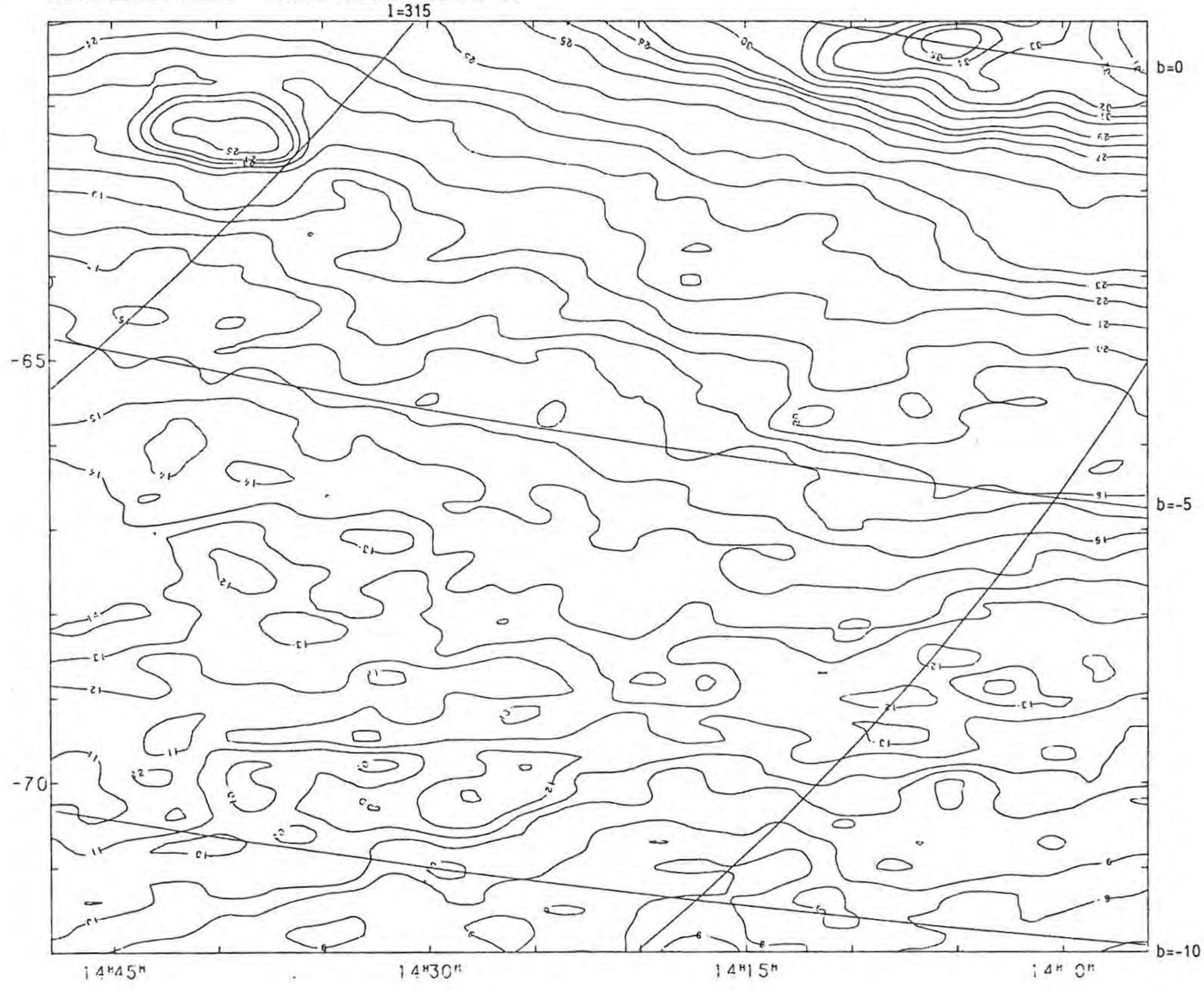

RHODES 2.3 GHZ SURVEY 13HR RA 14HR -25 DEC -15

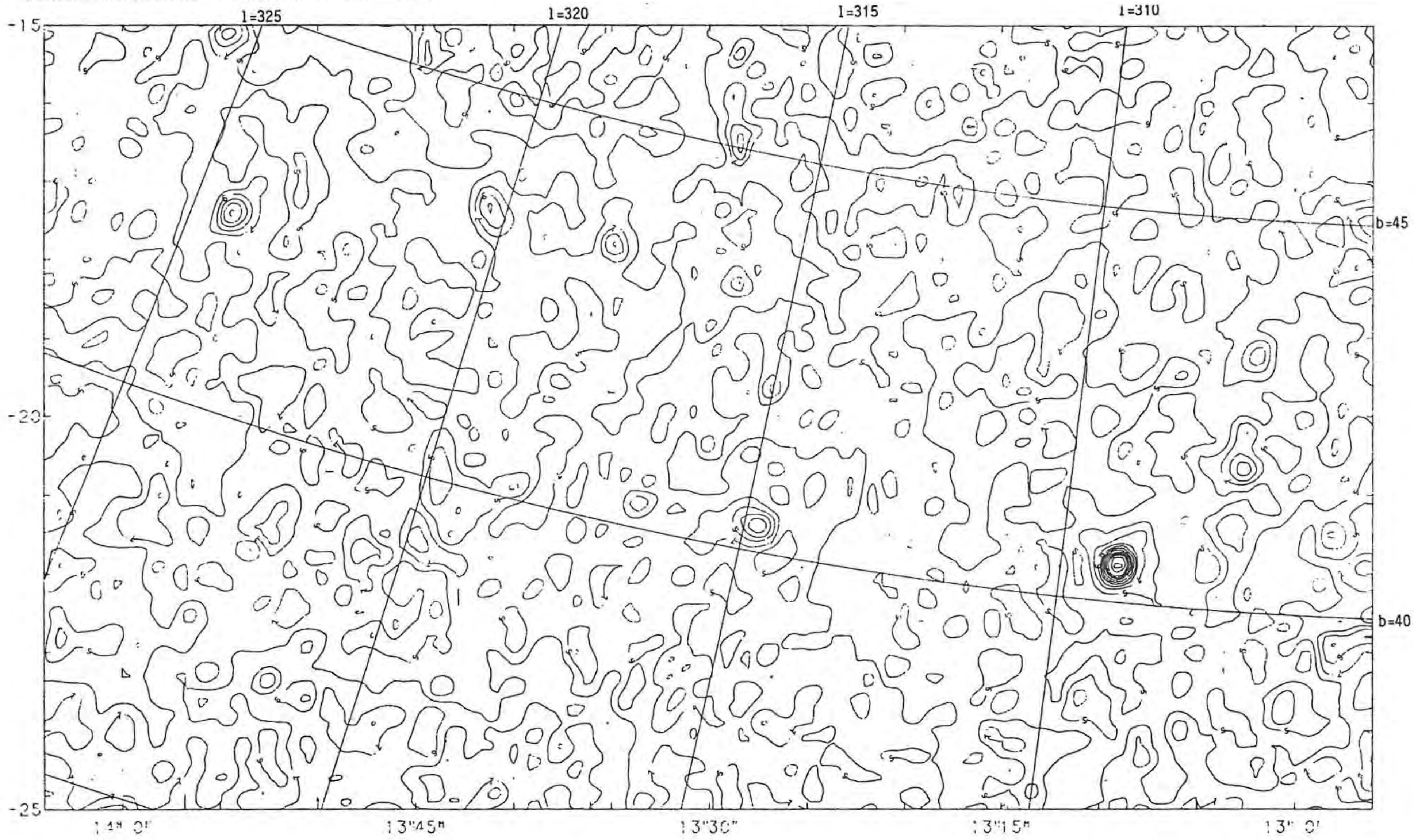

RHODES 2.3 GHZ SURVEY 13HR RA 14HR -18 DEC -7

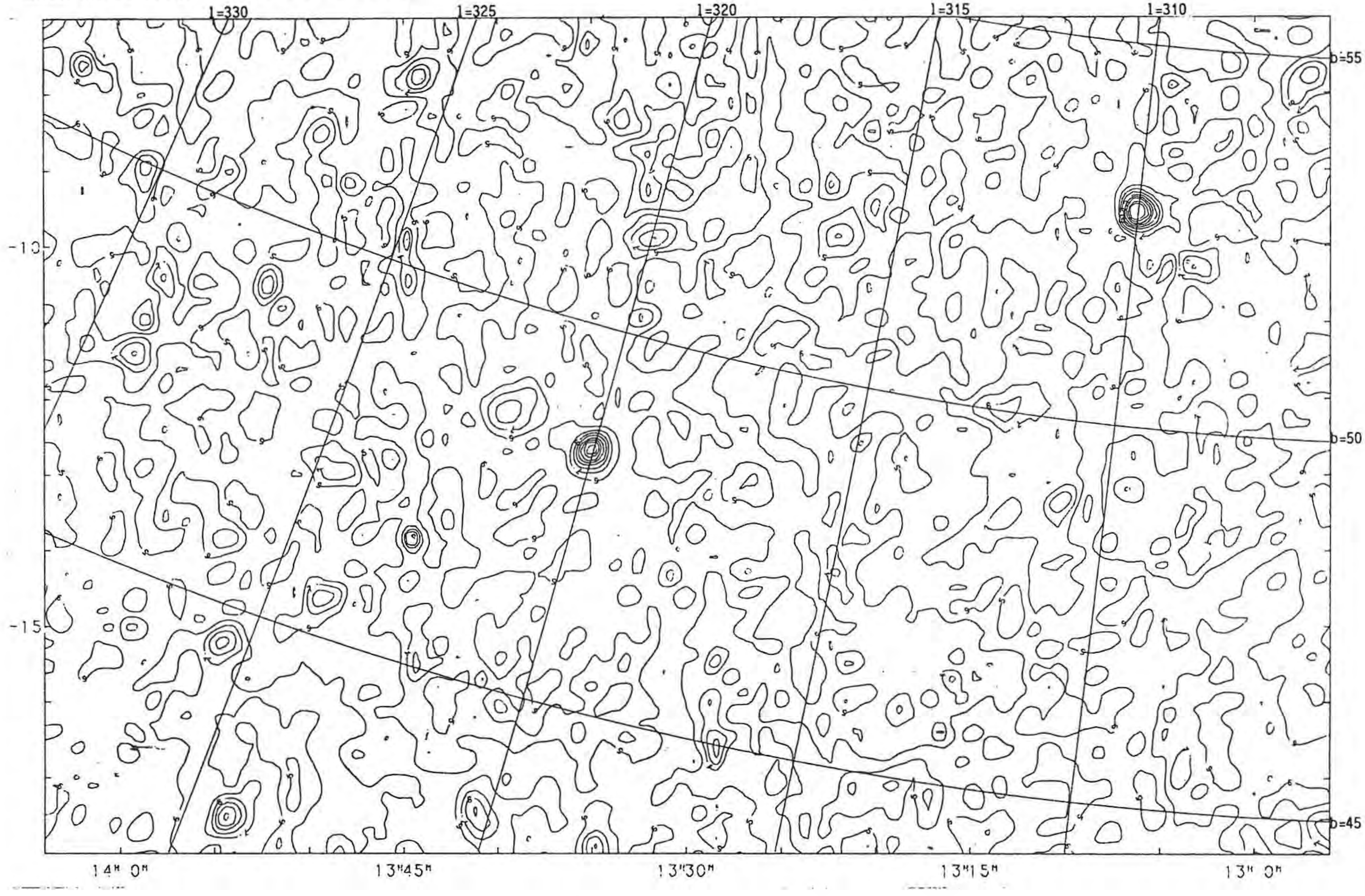

RHODES 2.3 GHZ SURVEY 14HR RA 15HR -25 DEC -15

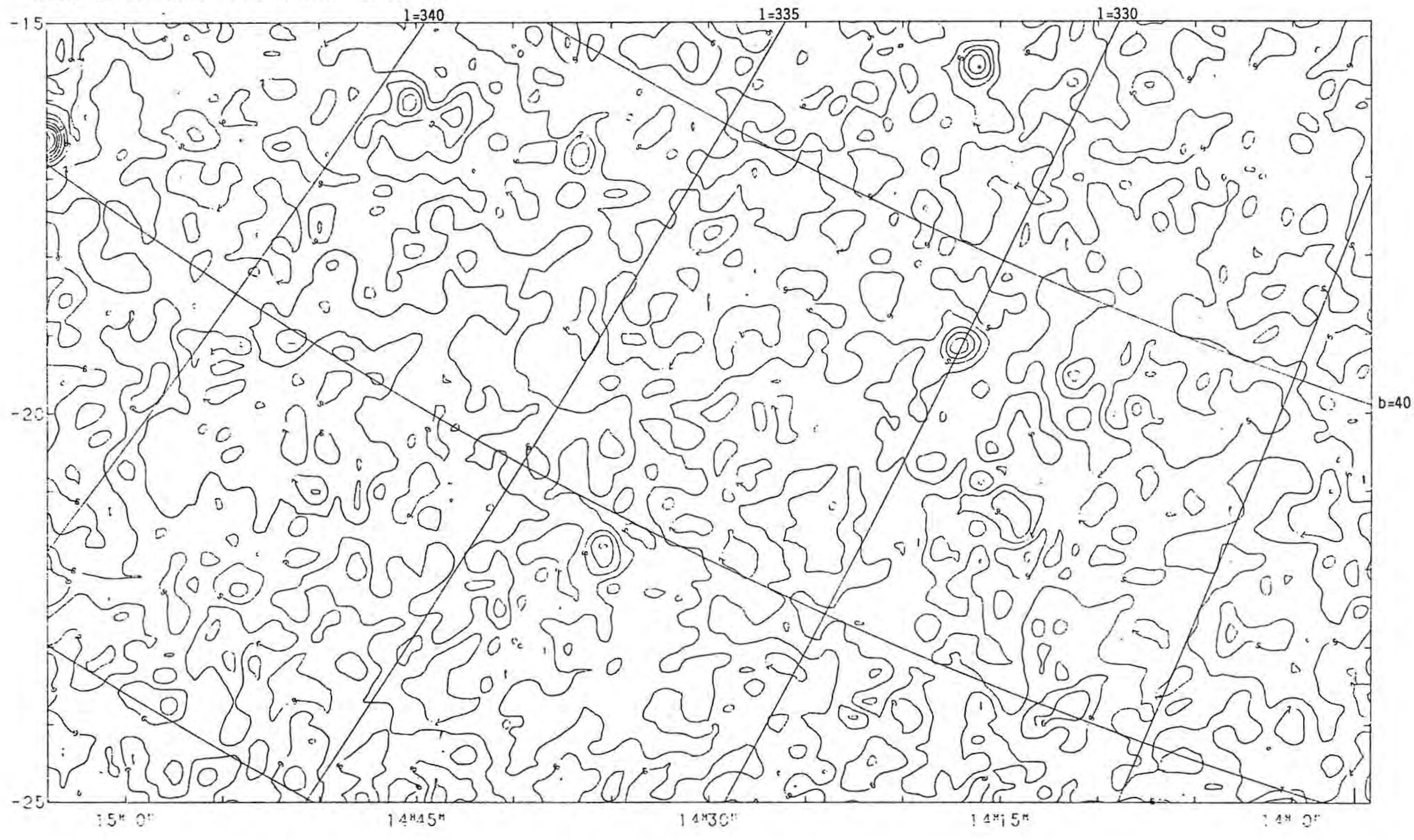

RHODES 2.3 GHZ SURVEY 14HR RA 15HR -18 DEC -7

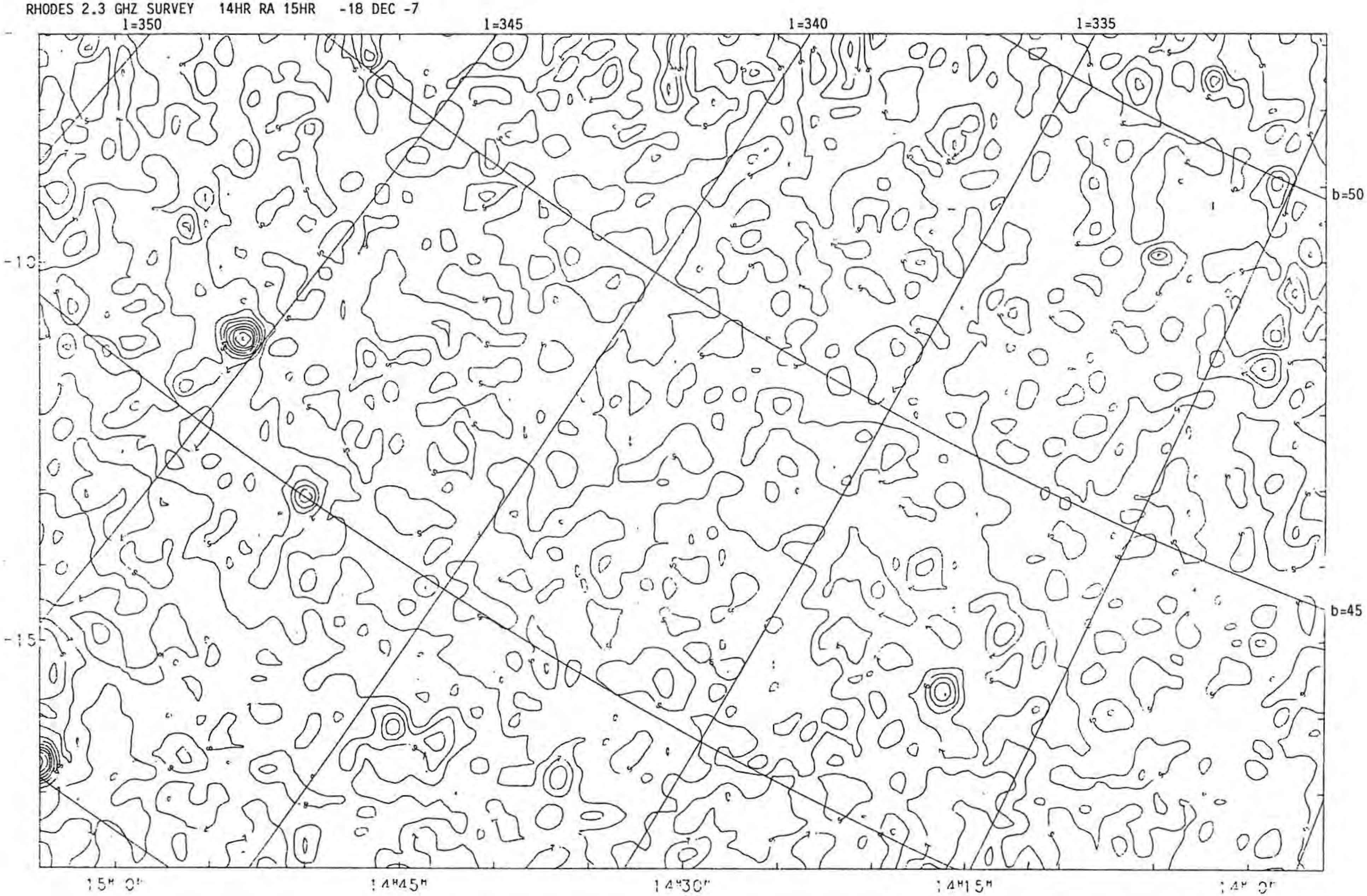

RHODES 2.3 GHZ SURVEY   15HR RA 16HR   -25 DEC -15

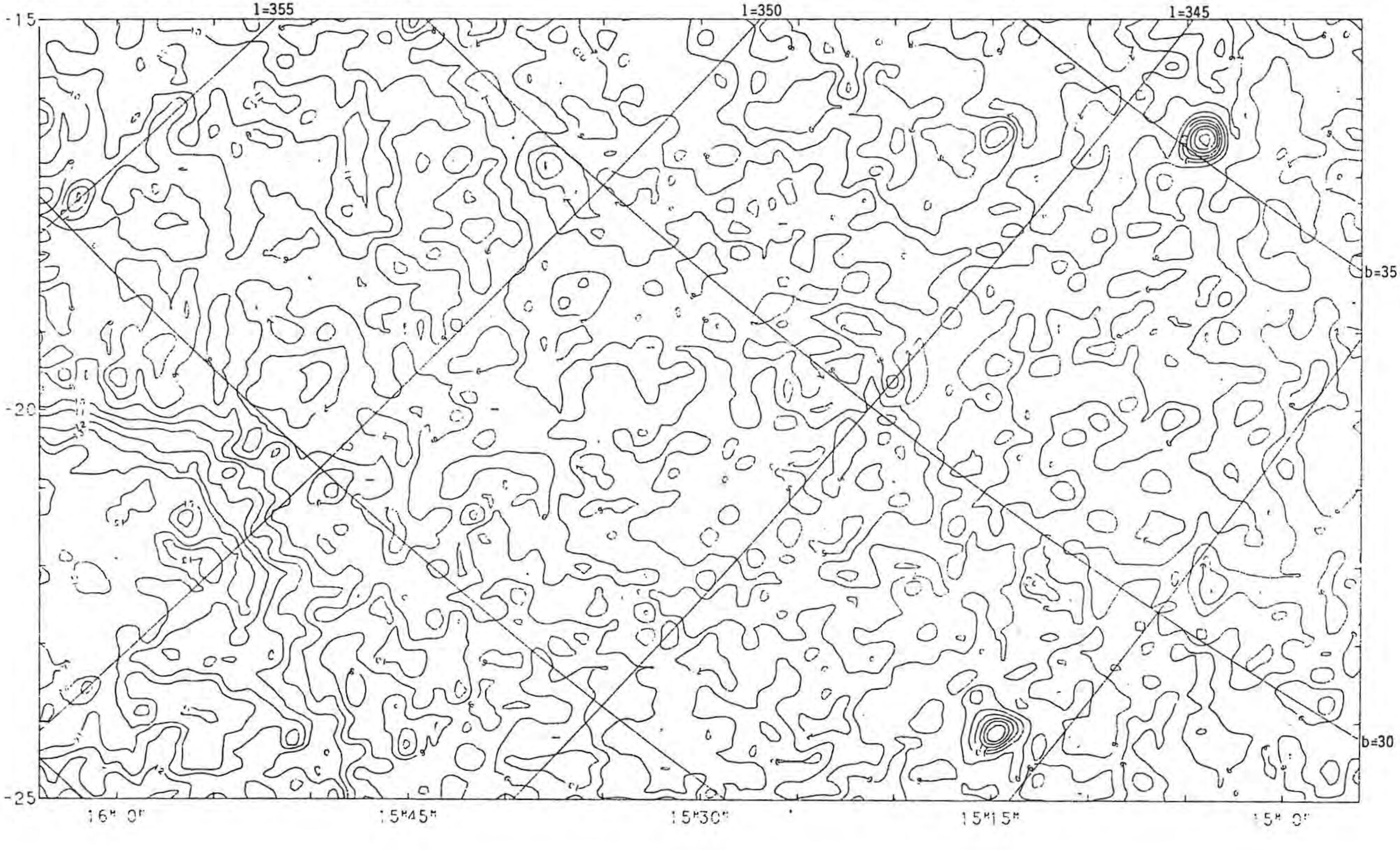

RHODES 2.3 GHZ SURVEY 15HR RA 16HR -18 DEC -7

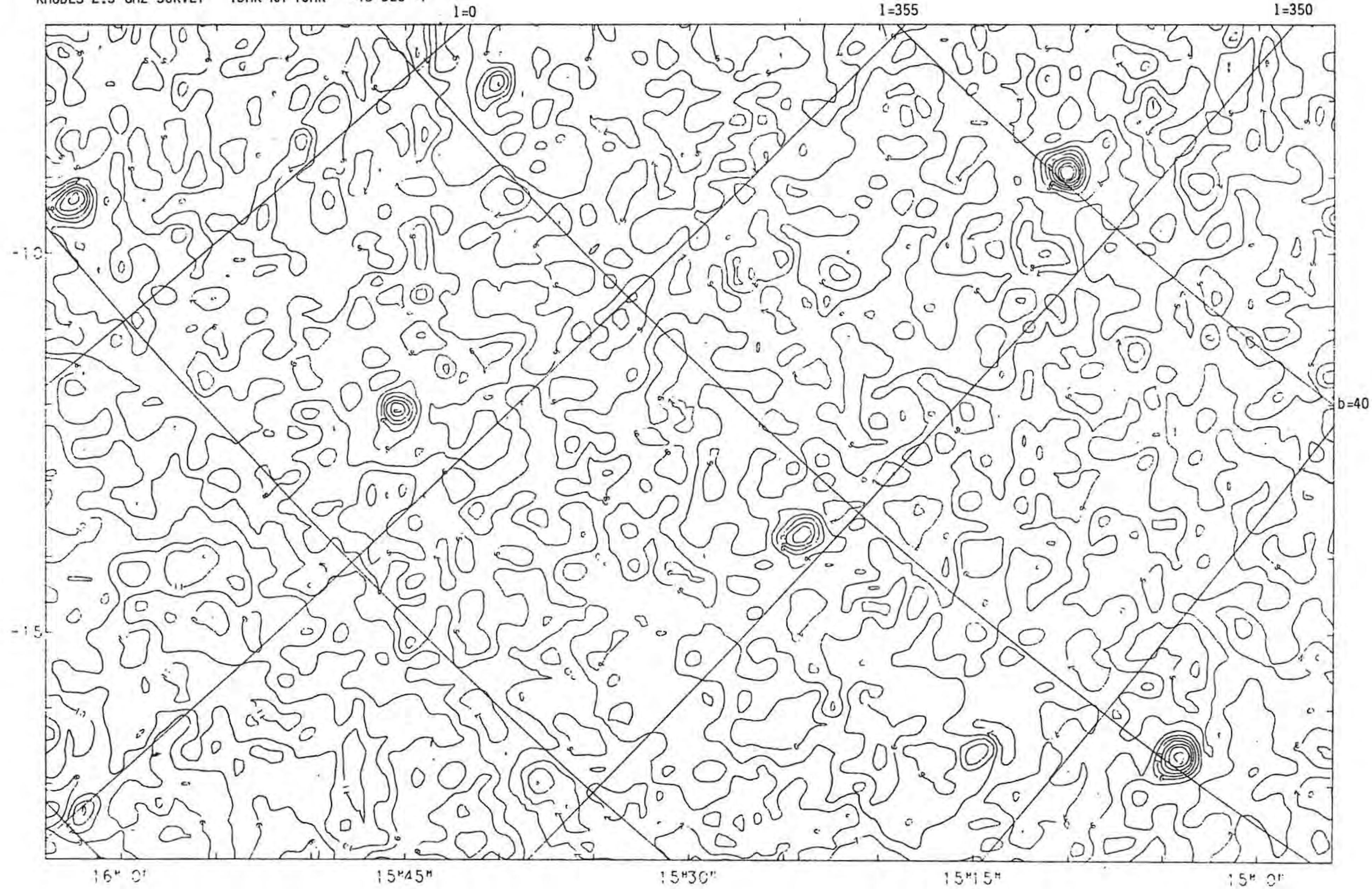

RHODES 2.3 GHZ SURVEY 16HR RA 17HR -25 DEC -15

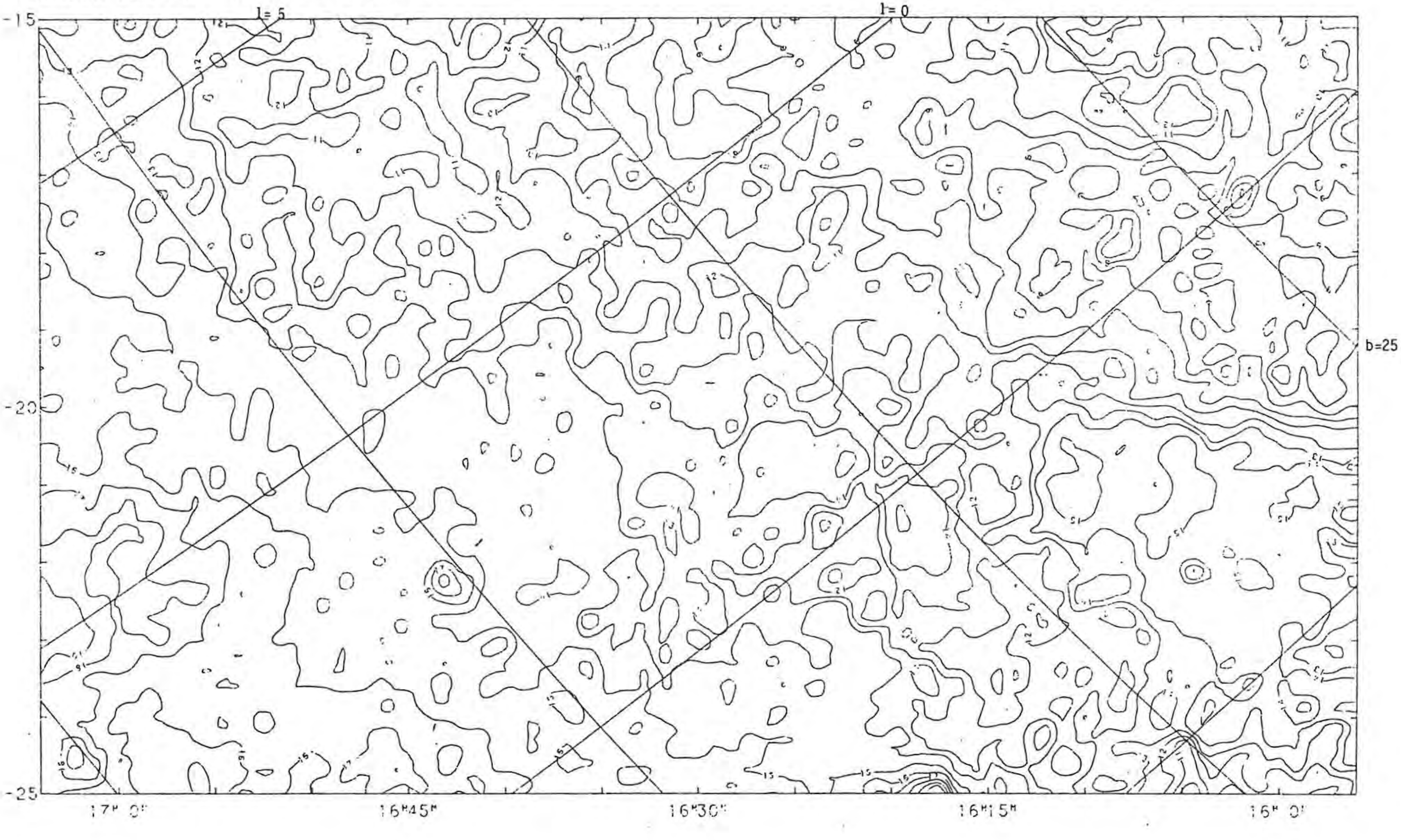

RHODES 2.3 GHZ SURVEY 16HR RA 17HR -18 DEC -7

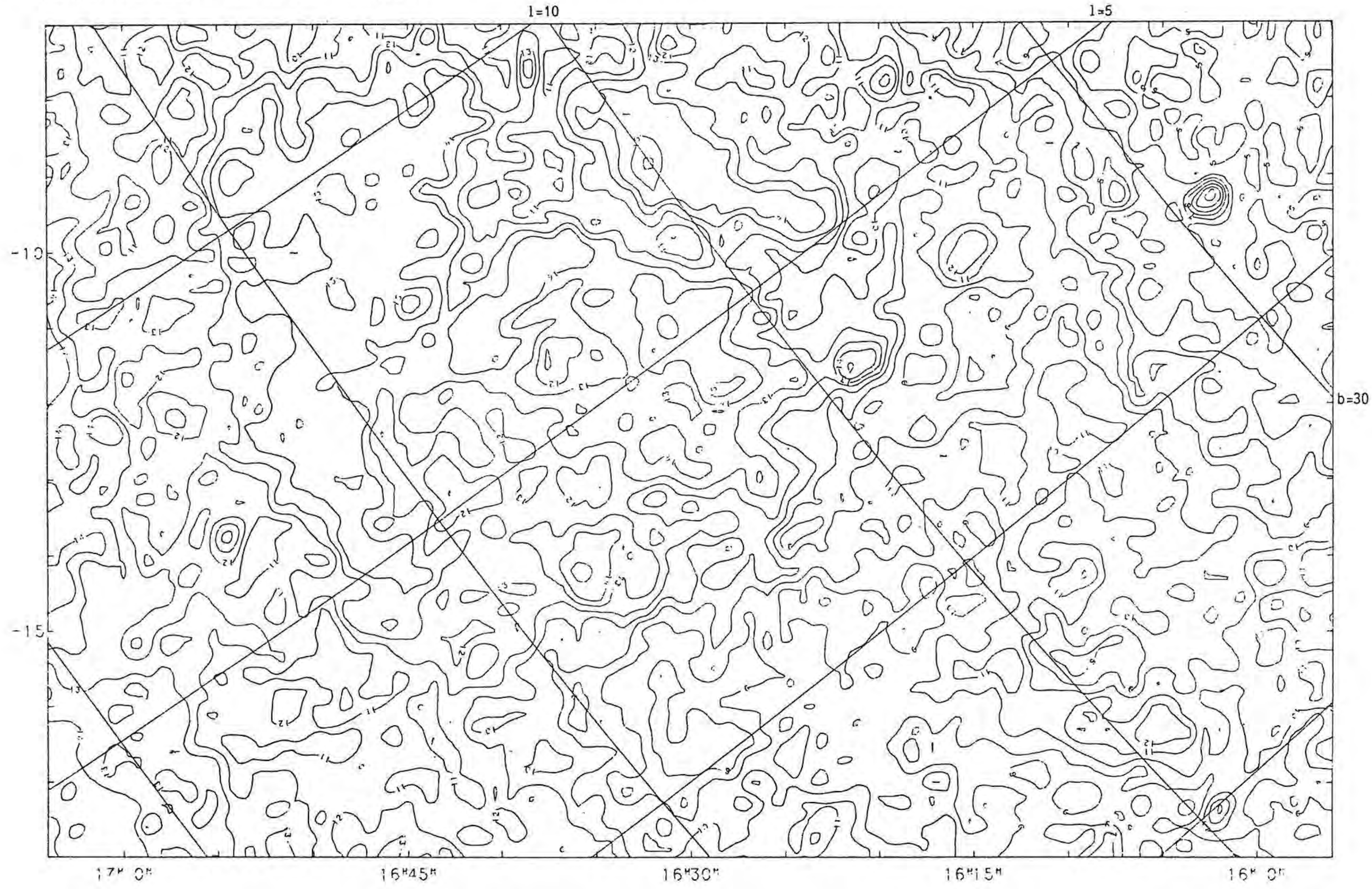

RHODES 2.3 GHZ SURVEY   17HR RA 18HR   -25 DEC -15

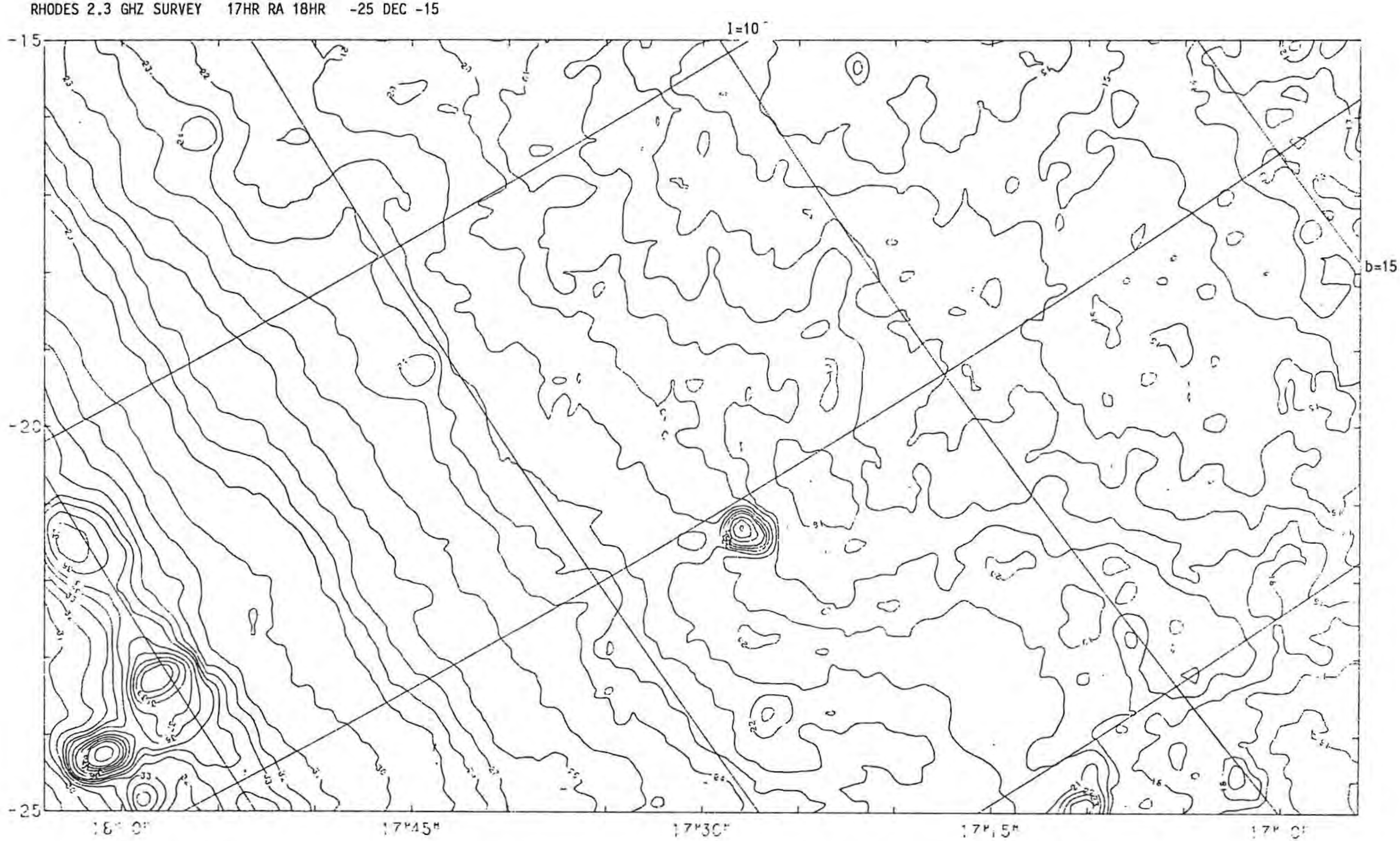

RHODES 2.3 GHZ SURVEY 17HR RA 18HR -18 DEC -7

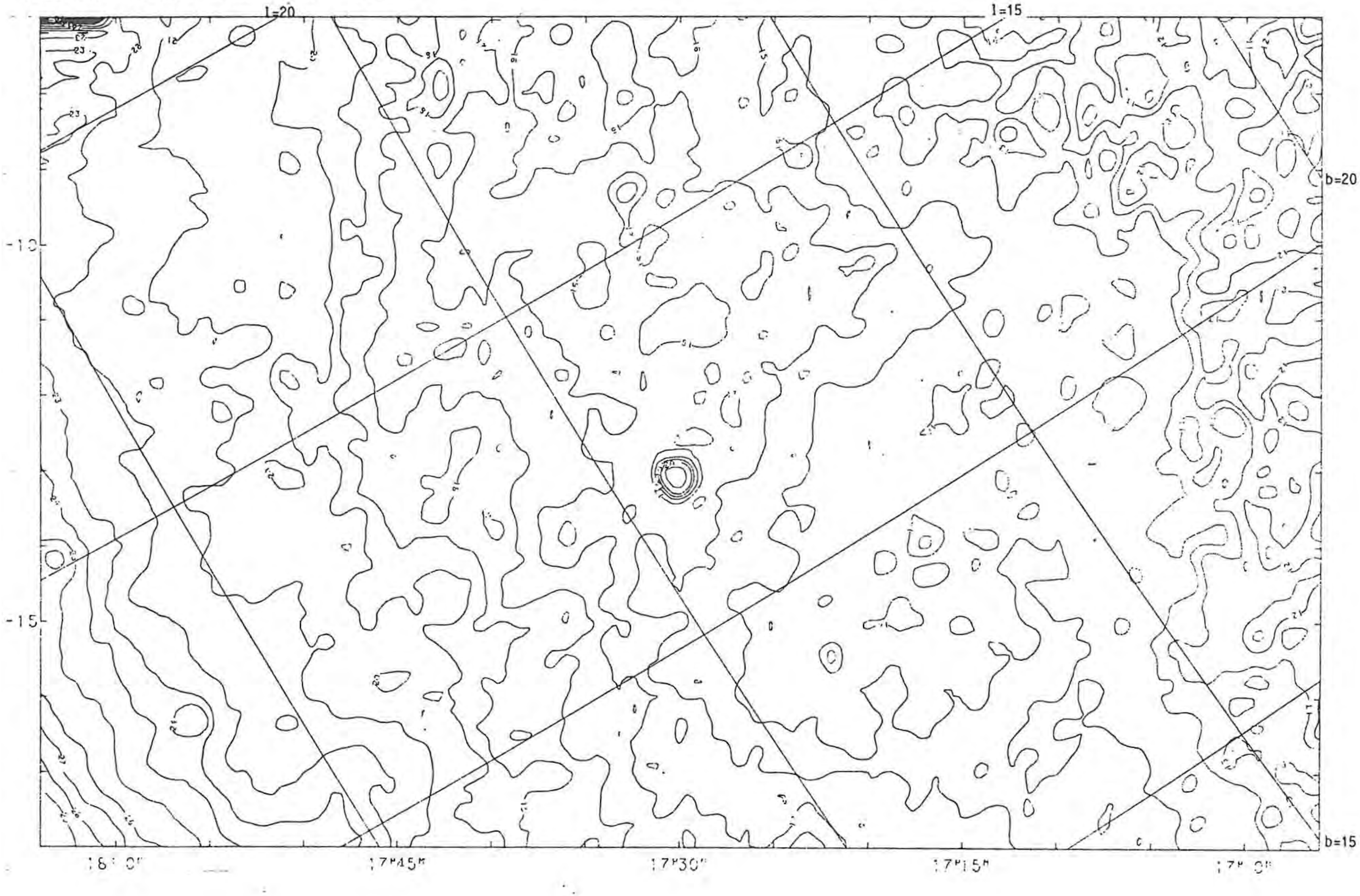

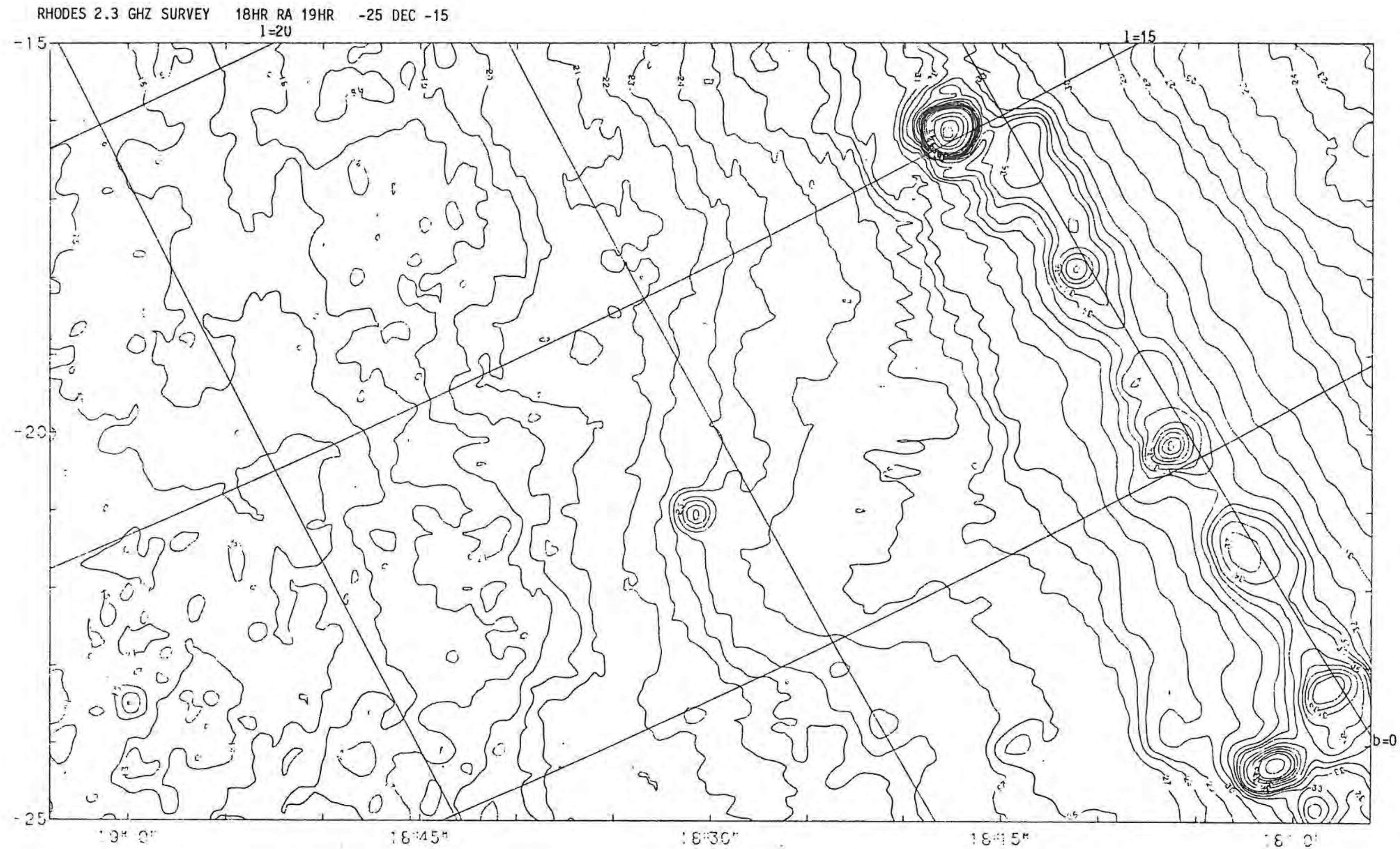

RHODES 2.3 GHZ SURVEY 18HR RA 19HR -25 DEC -15
l=20
l=15
b=0
-15
-20
-25
19h 0m
18h45m
18h30m
18h15m
18h 0m

RHODES 2.3 GHZ SURVEY 18HR RA 19HR -18 DEC -7.5

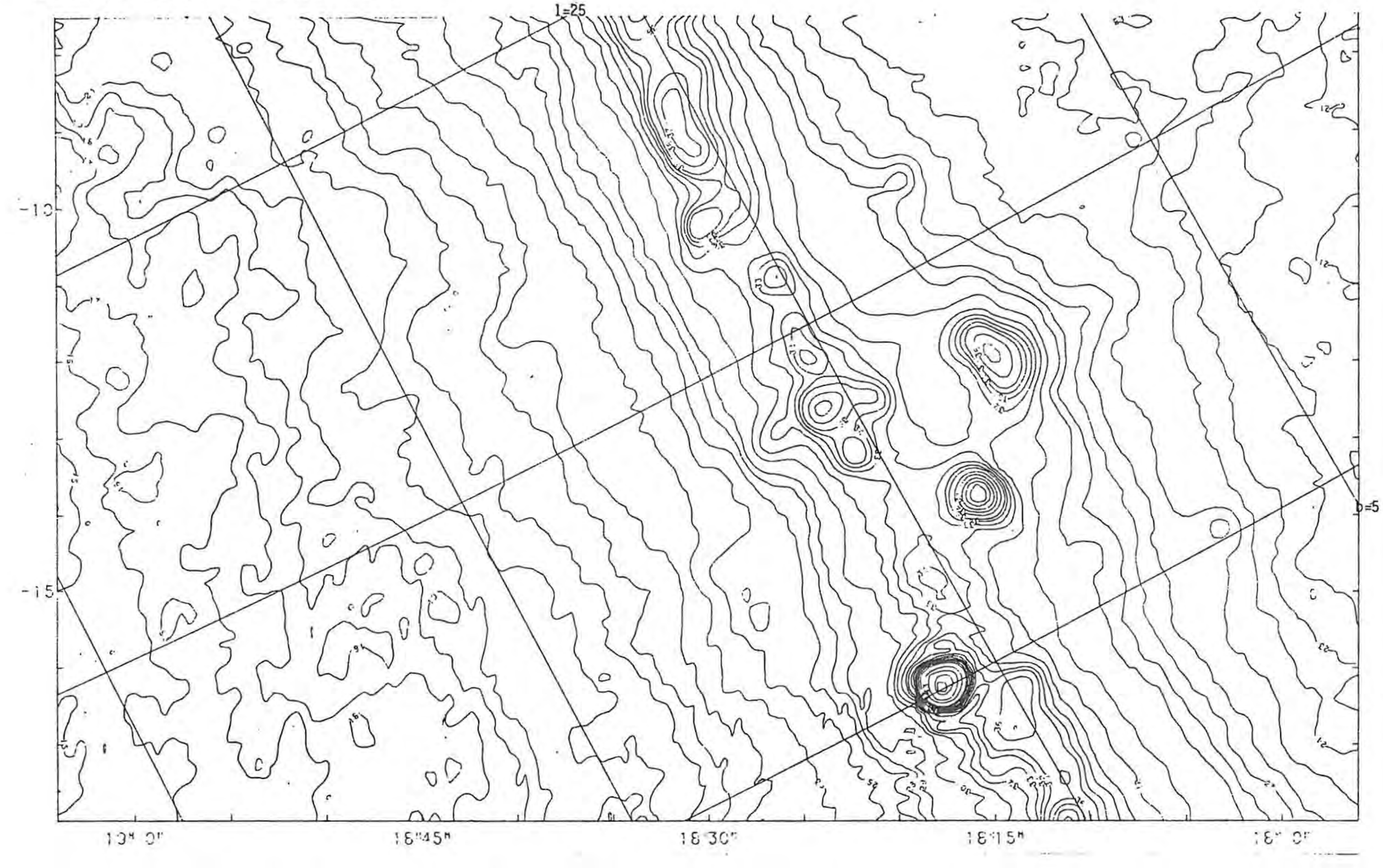

RHODES 2.3 GHZ SURVEY 19HR RA 20HR -25 DEC -15

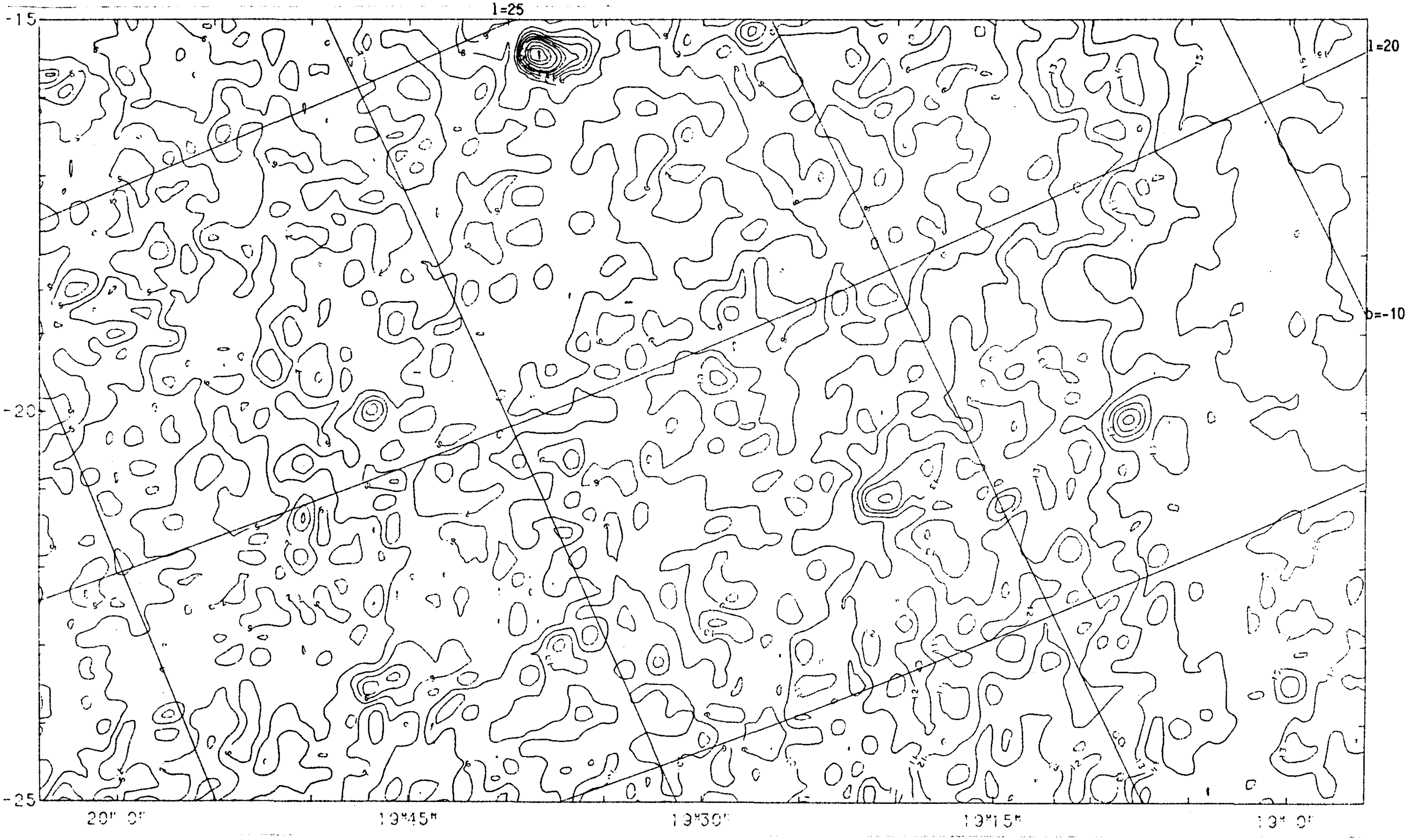

RHODES 2.3 GHZ SURVEY   19HR RA 20HR   -18 DEC -7.5

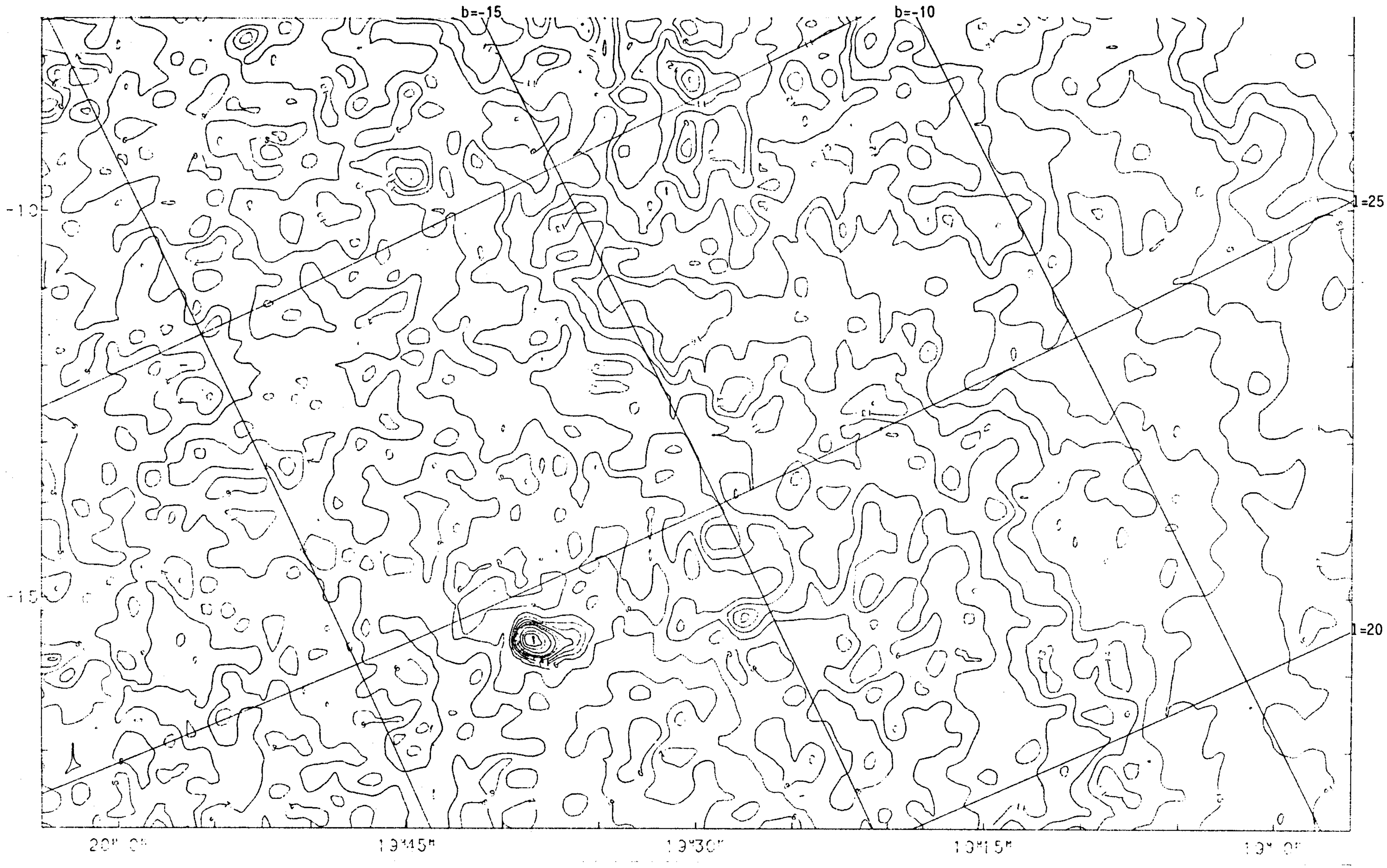

RHODES 2.3 GHZ SURVEY   20HR RA 21HR   -25 DEC -15

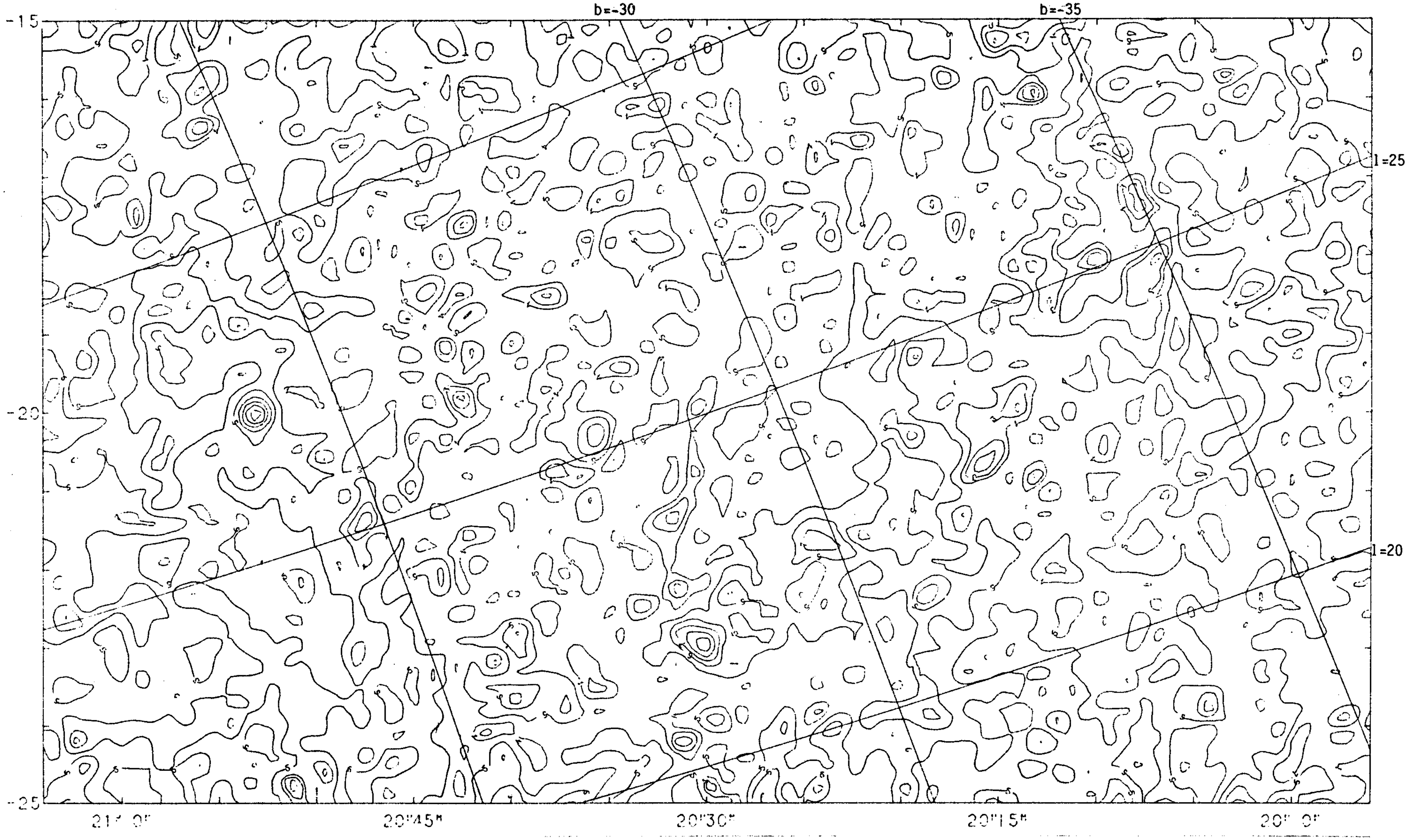

RHODES 2.3 GHZ SURVEY 20HR RA 21HR -18 DEC -7

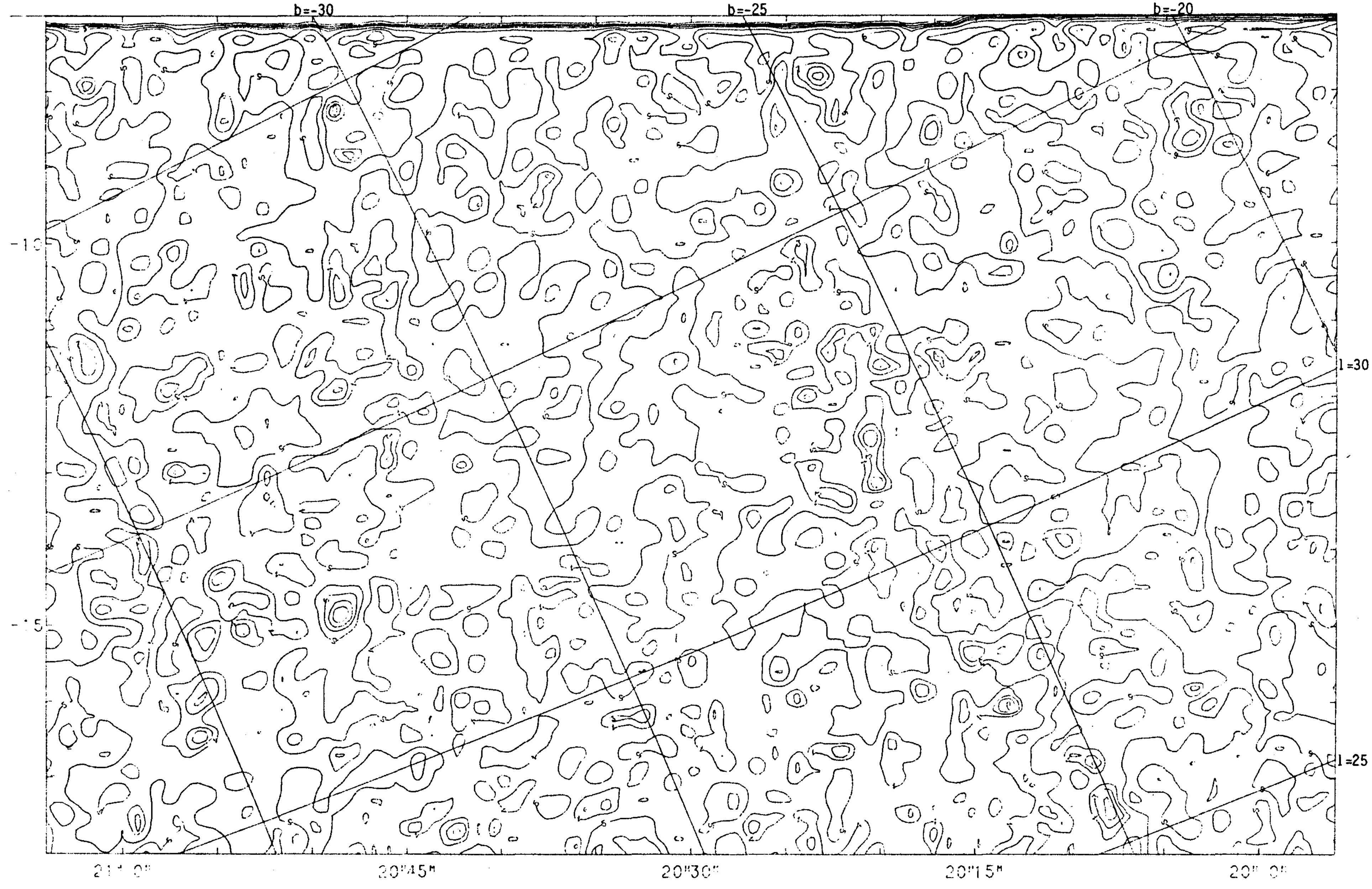

RHODES 2.3 GHZ SURVEY   21HR RA 22HR   -25 DEC -15

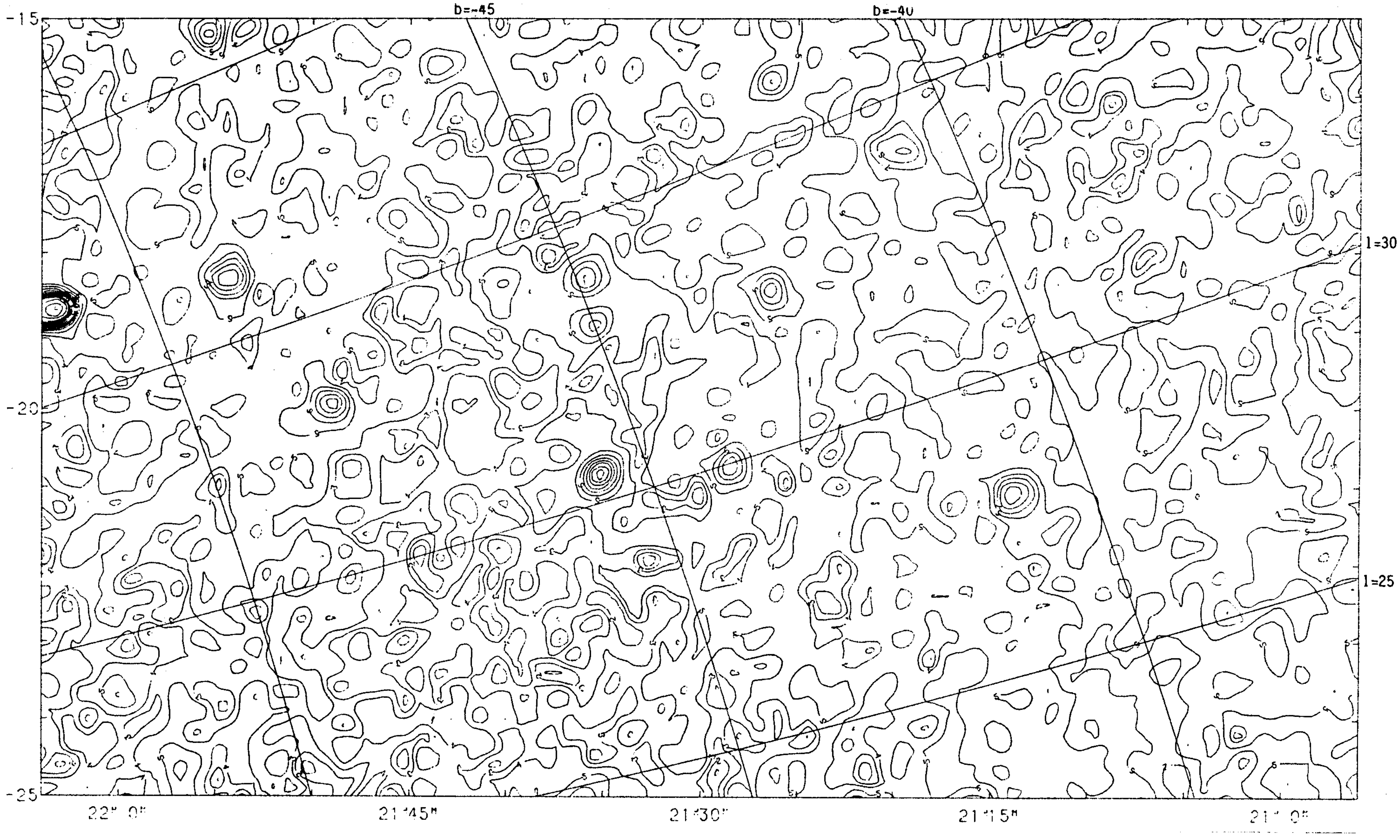

RHODES 2.3 GHZ SURVEY   21HR RA 22HR   -18 DEC -7

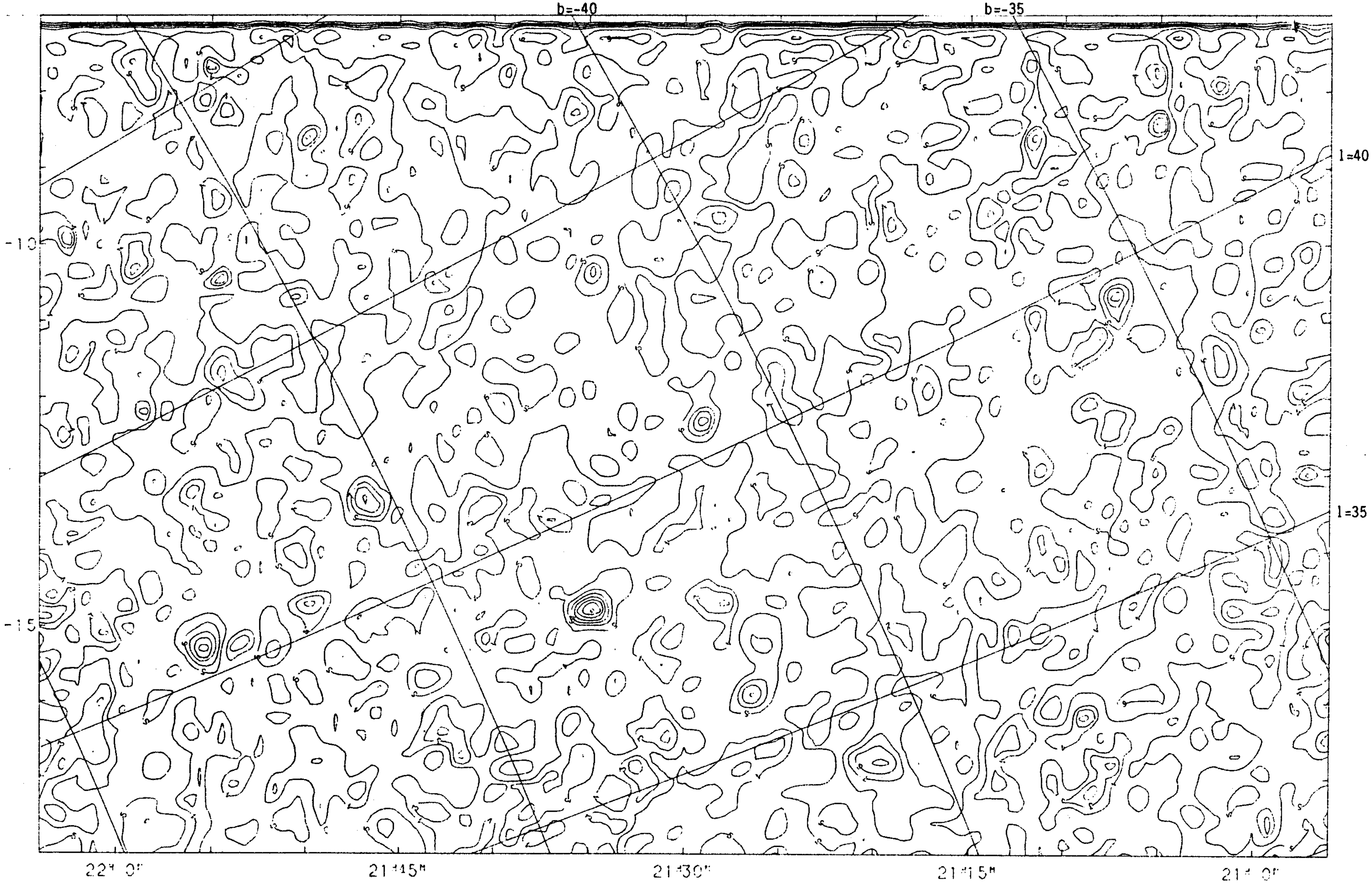

RHODES 2.3 GHZ SURVEY 22HR RA 23HR -25 DEC -15

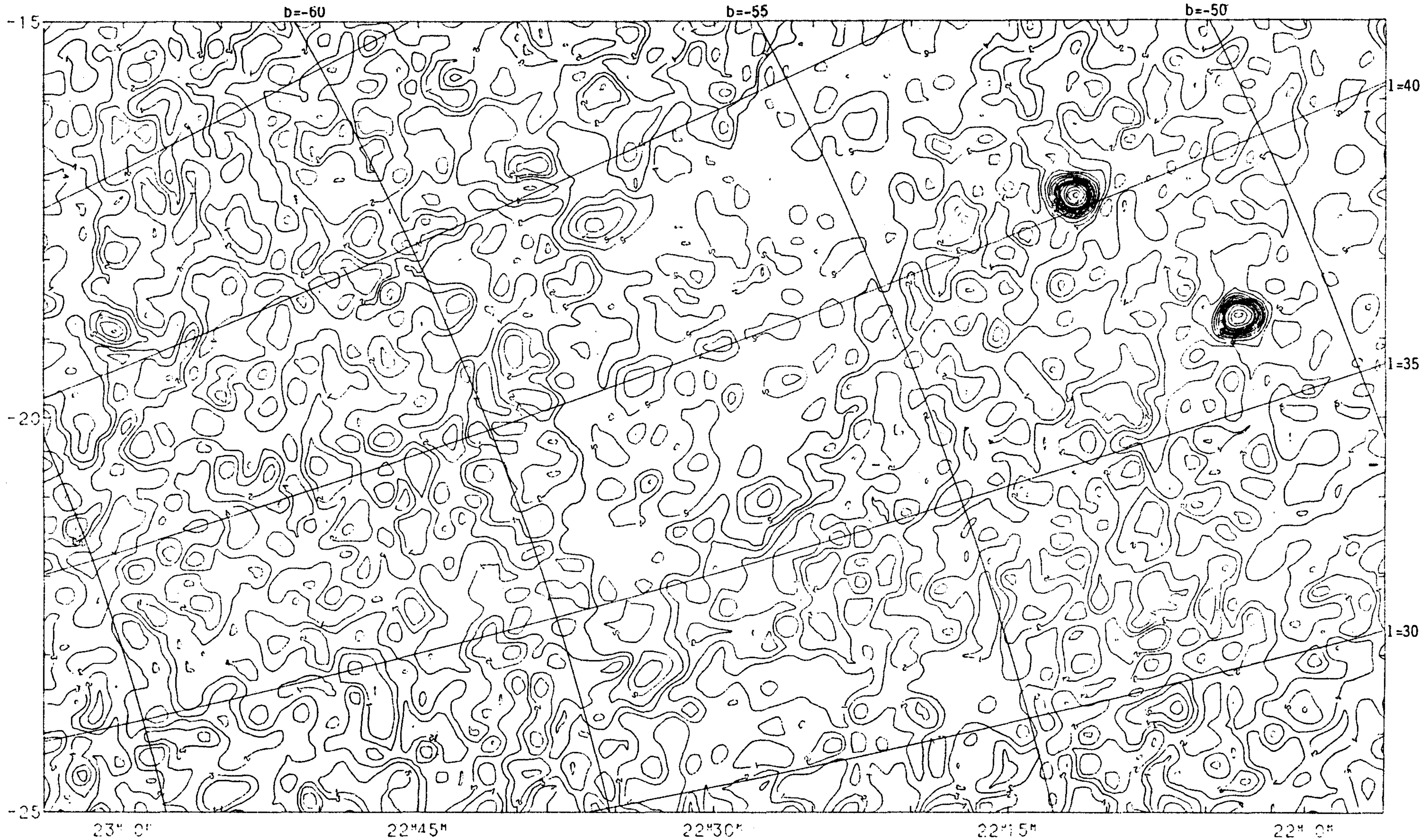

RHODES 2.3 GHZ SURVEY   22HR RA 23HR   -18 DEC -7

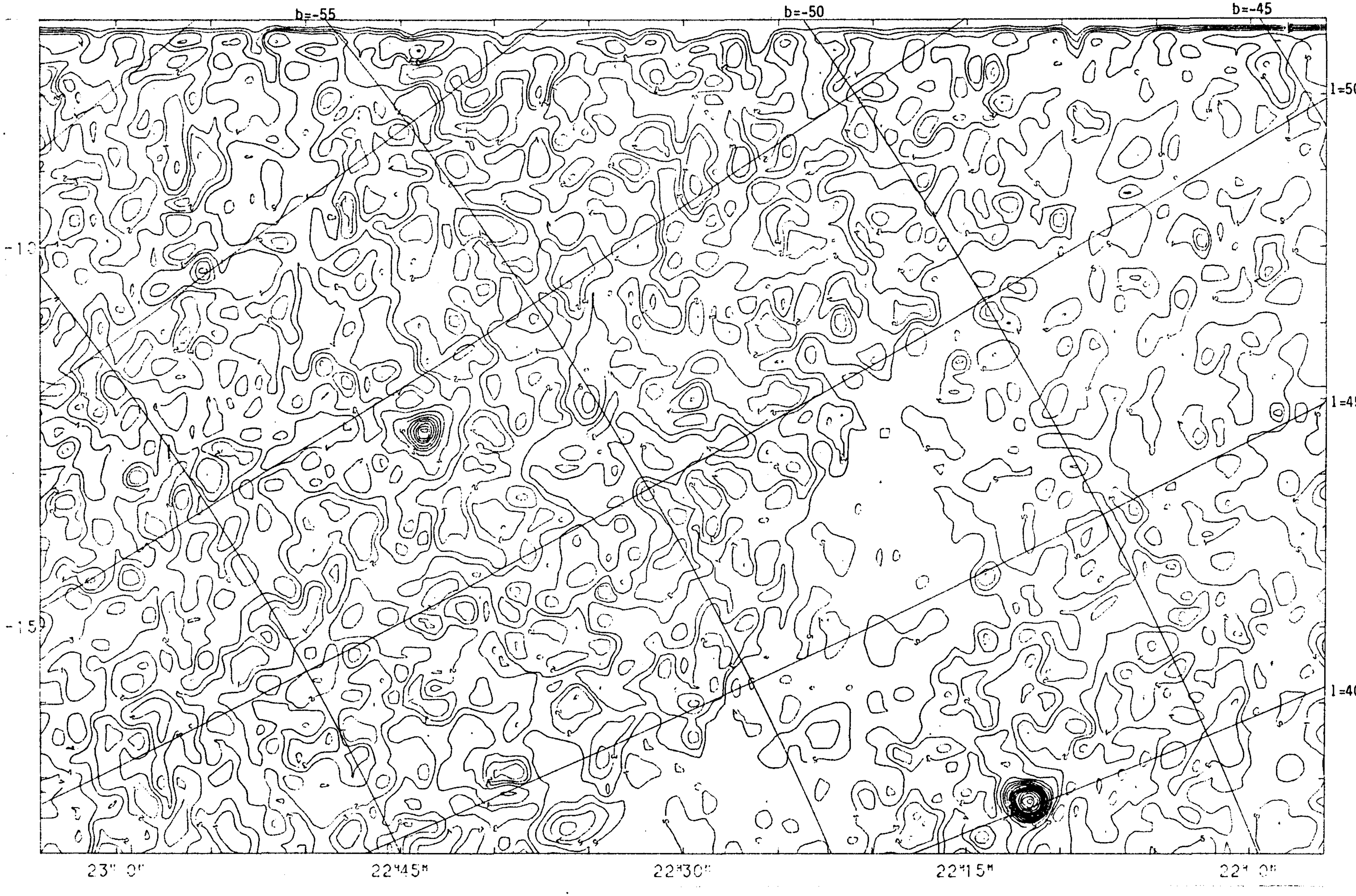

RHODES 2.3 GHZ SURVEY 23HR RA 24HR -25 DEC -15

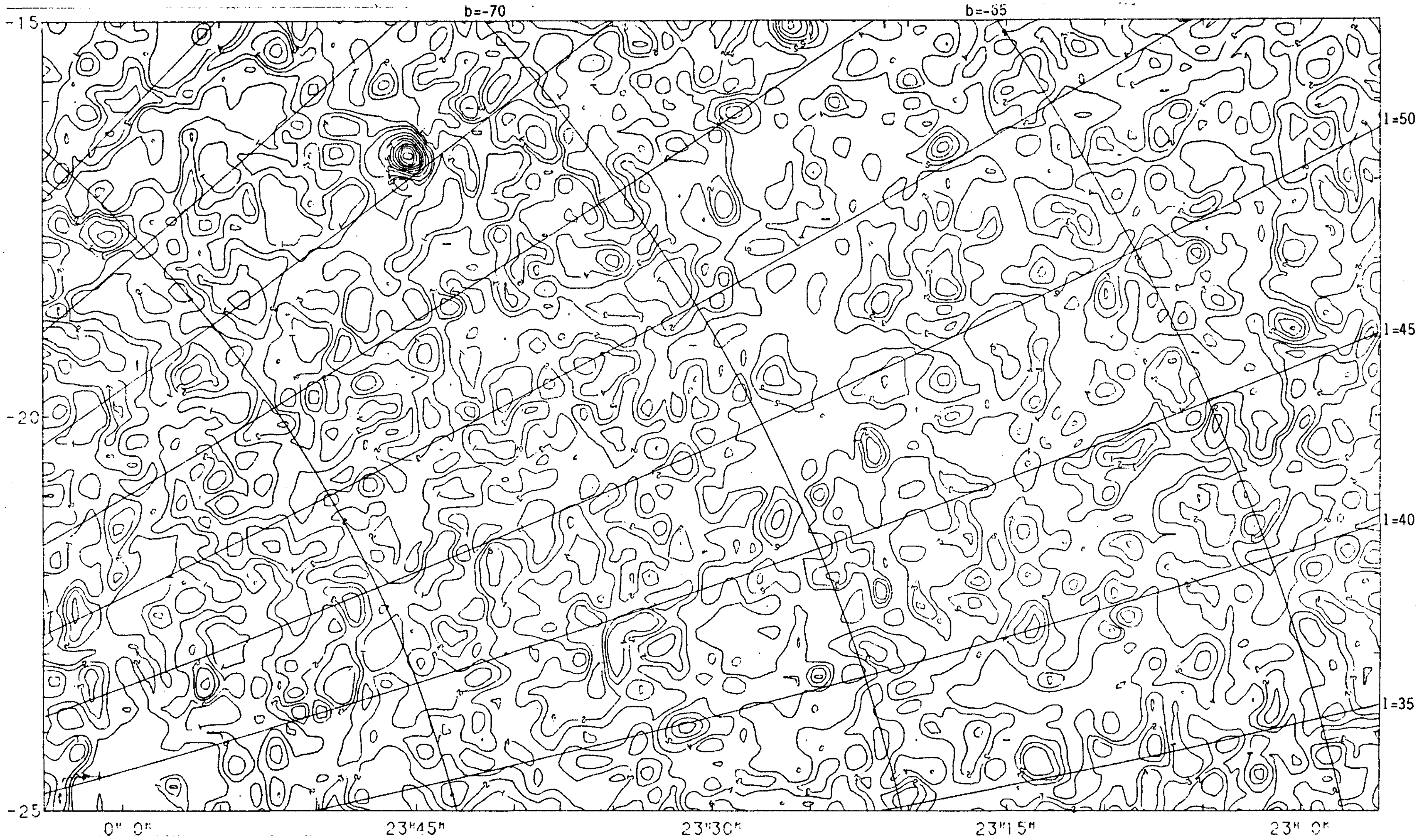

RHODES 2.3 GHZ SURVEY 23HR RA 24HR -18 DEC -7

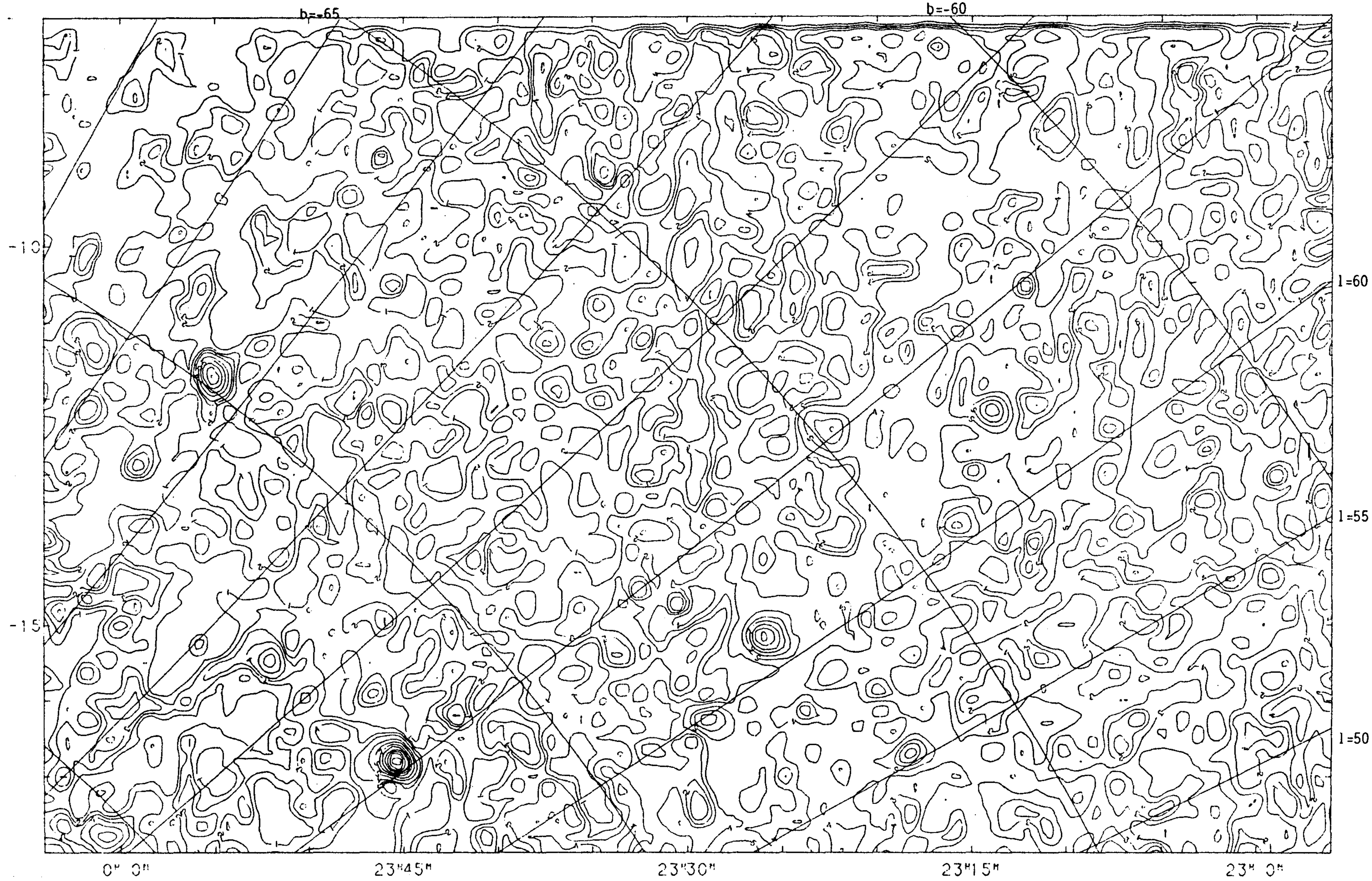

RHODES 2.3 GHZ SURVEY   OHR RA 45m   -25 DEC -15

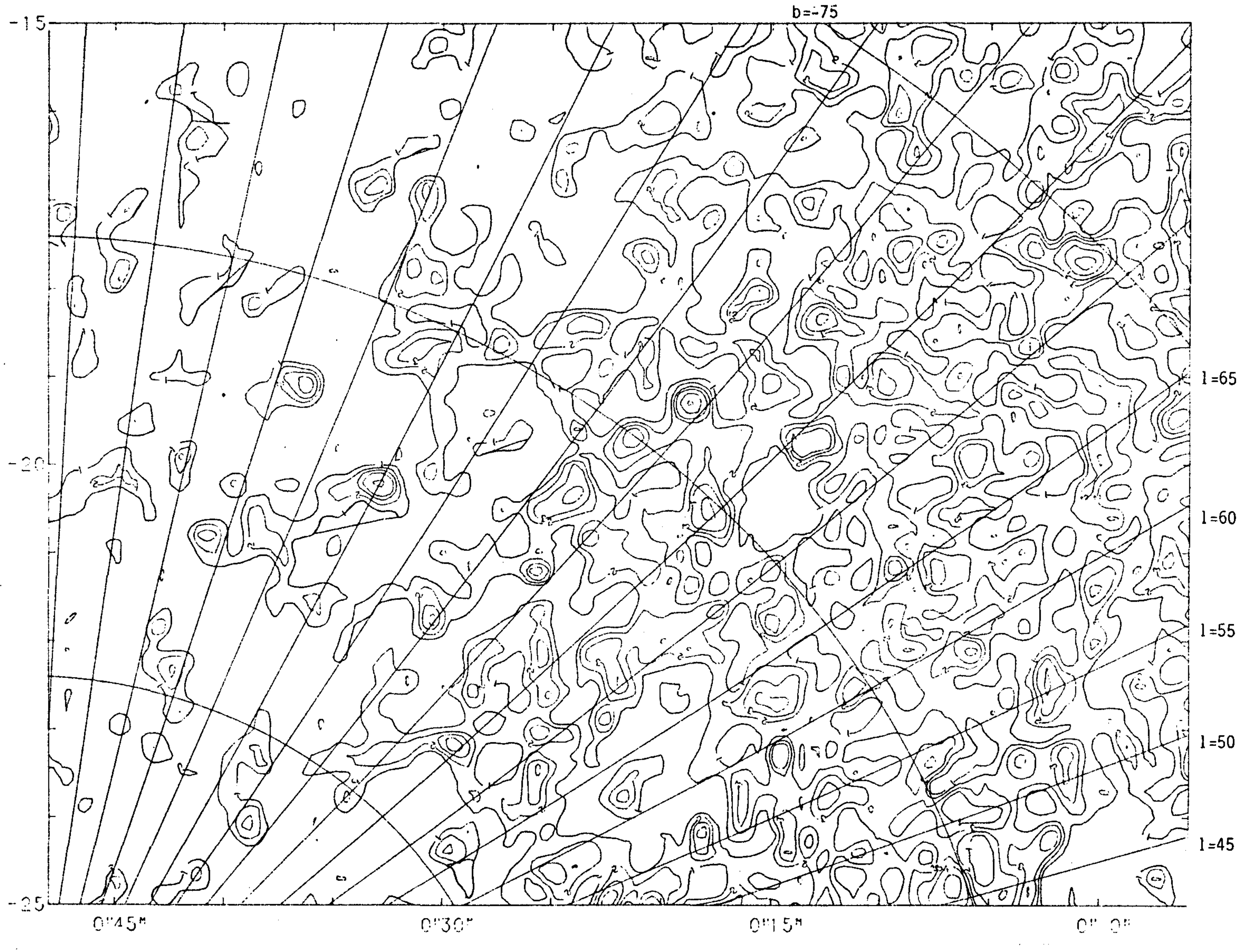

RHODES 2.3 GHZ SURVEY   OHR RA 45m   -18 DEC -7

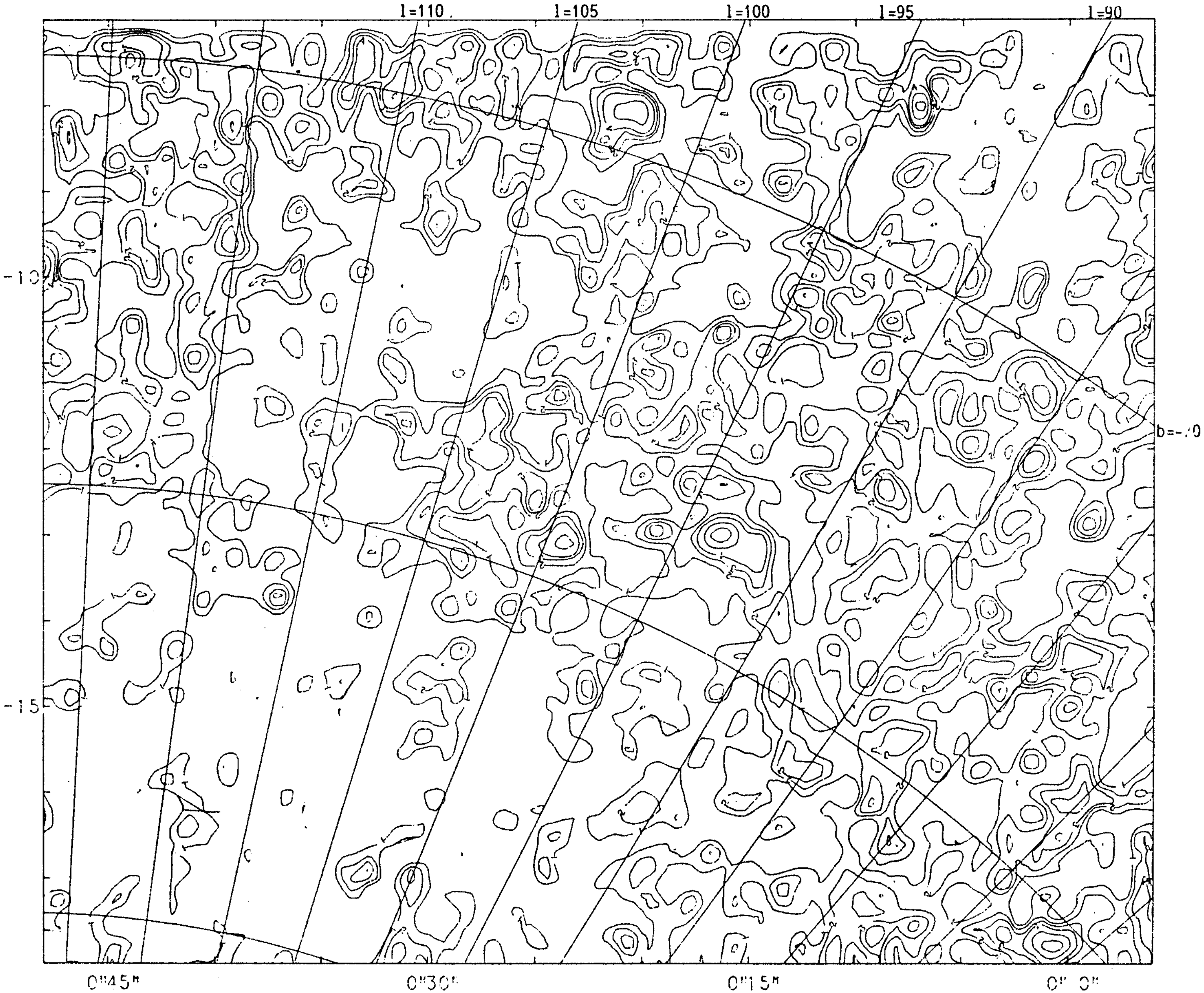

# APPENDIX 2

Key to galactic plane contour maps

Resolution (HPBW) : $0.333^{o}$

Beam sensitivity : 11.38 Jy/K

rms noise level : 16 mK

Contour label table

| contour label | $T_a$ mK | contour label | $T_a$ mK |
|---|---|---|---|
| 1 | 300 | 18 | 3000 |
| 2 | 350 | 19 | 3500 |
| 3 | 400 | 20 | 4000 |
| 4 | 450 | 21 | 4500 |
| 5 | 500 | 22 | 5000 |
| 6 | 550 | 23 | 6000 |
| 7 | 600 | 24 | 7000 |
| 8 | 700 | 25 | 8000 |
| 9 | 800 | 26 | 9000 |
| 10 | 900 | 27 | 10000 |
| 11 | 1000 | 28 | 12000 |
| 12 | 1200 | 29 | 14000 |
| 13 | 1400 | 30 | 20000 |
| 14 | 1600 | 31 | 25000 |
| 15 | 1800 | 32 | 30000 |
| 16 | 2000 | 33 | 35000 |
| 17 | 2500 | | |

1 K full beam antenna temperature corresponds to 1.41 K full beam brightness temperature.The grid lines on the maps represent right ascension and declination at $5^{o}$ spacing.

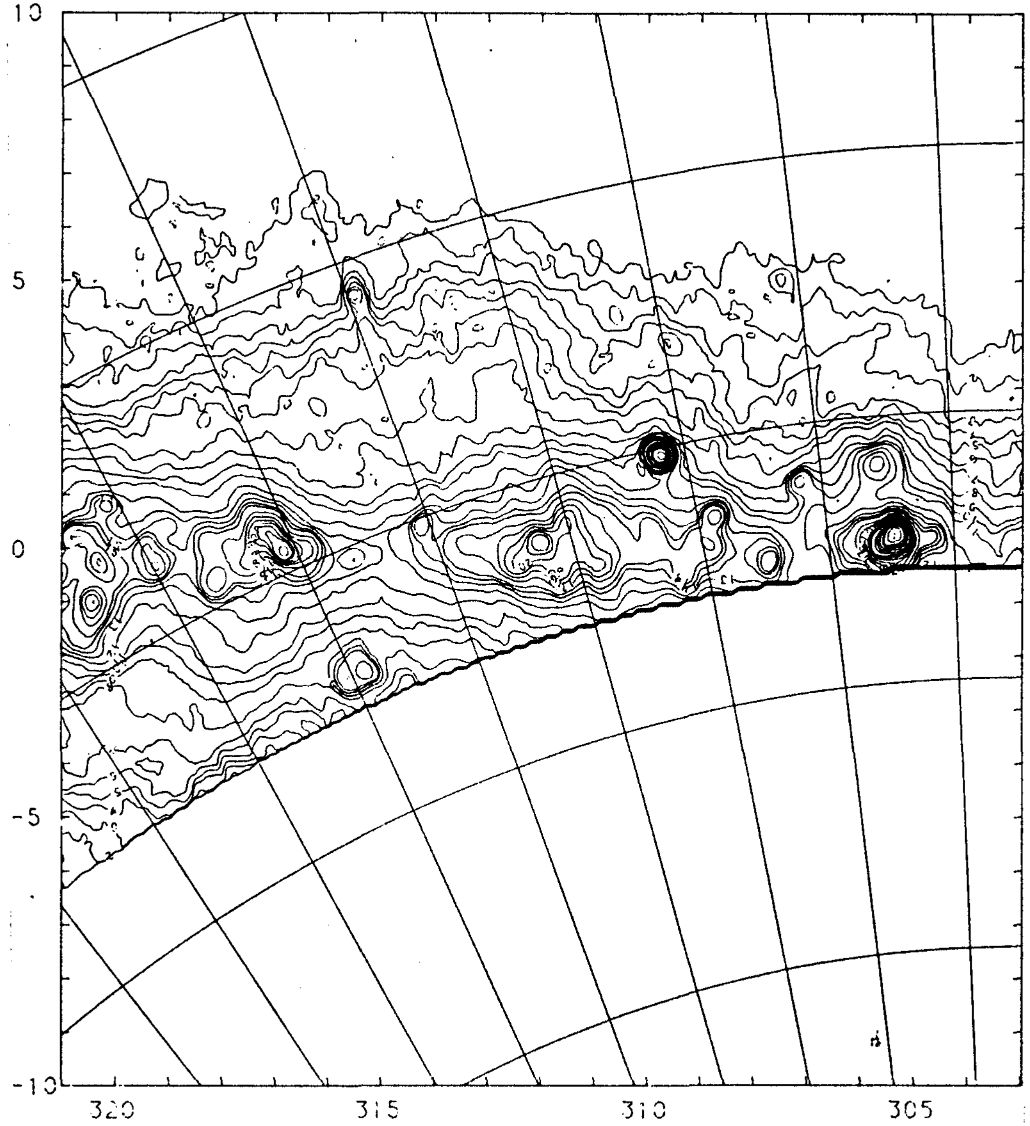

10
5
0
-5
-10
320
315
310
305

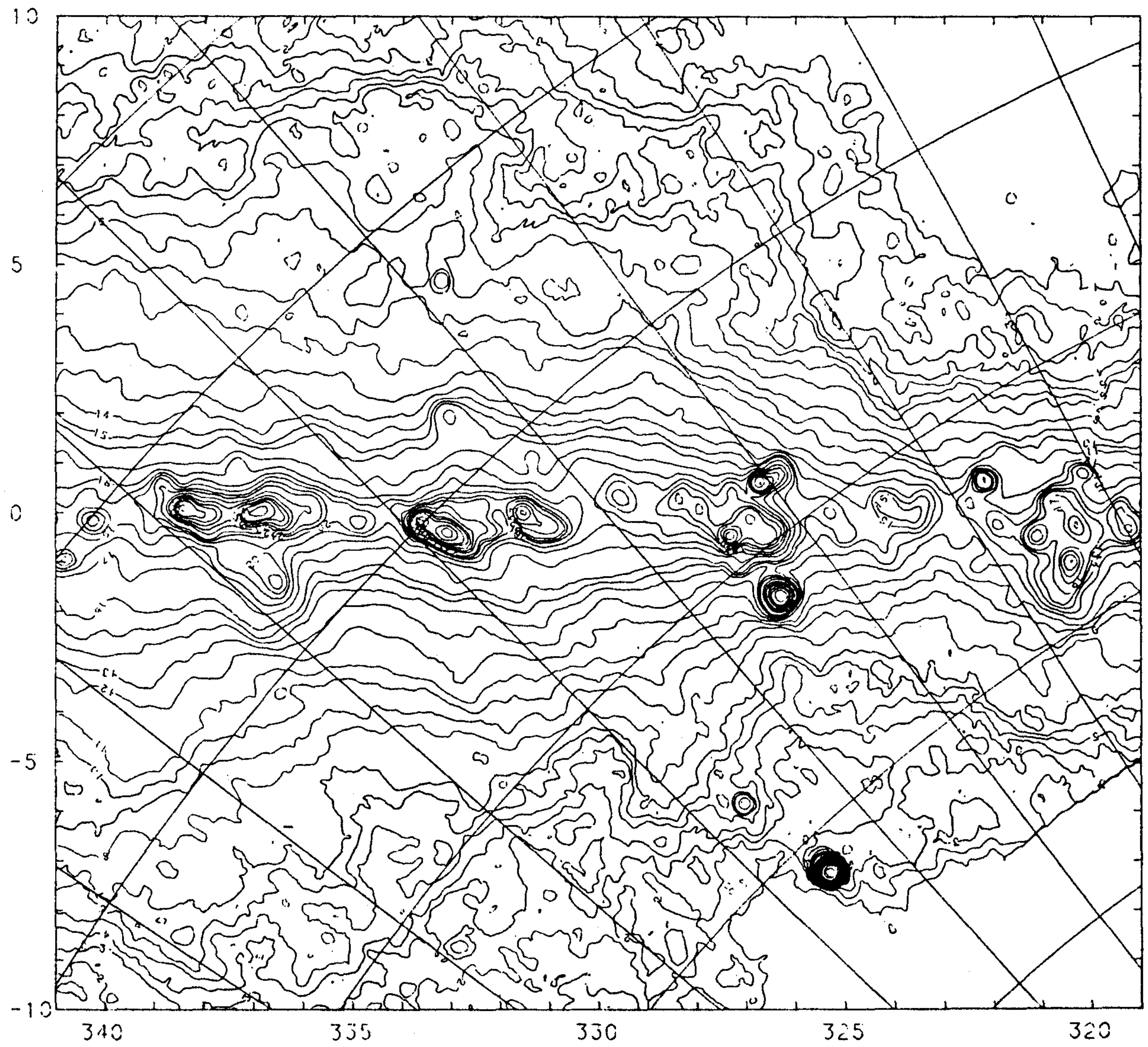

10
5
0
-5
-10
340
335
330
325
320

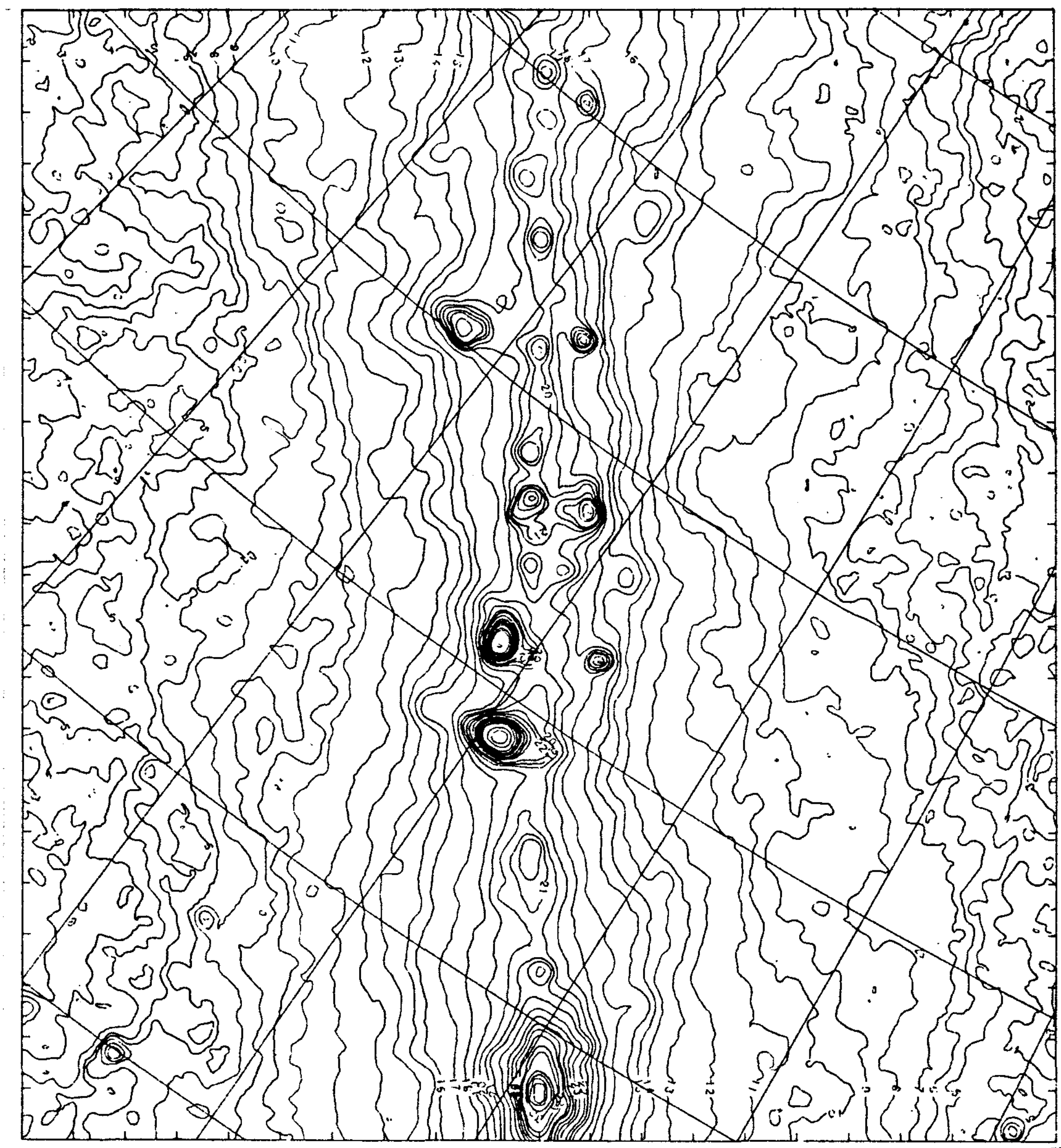
10
5
0
-5
-10
340
345
350
355
0

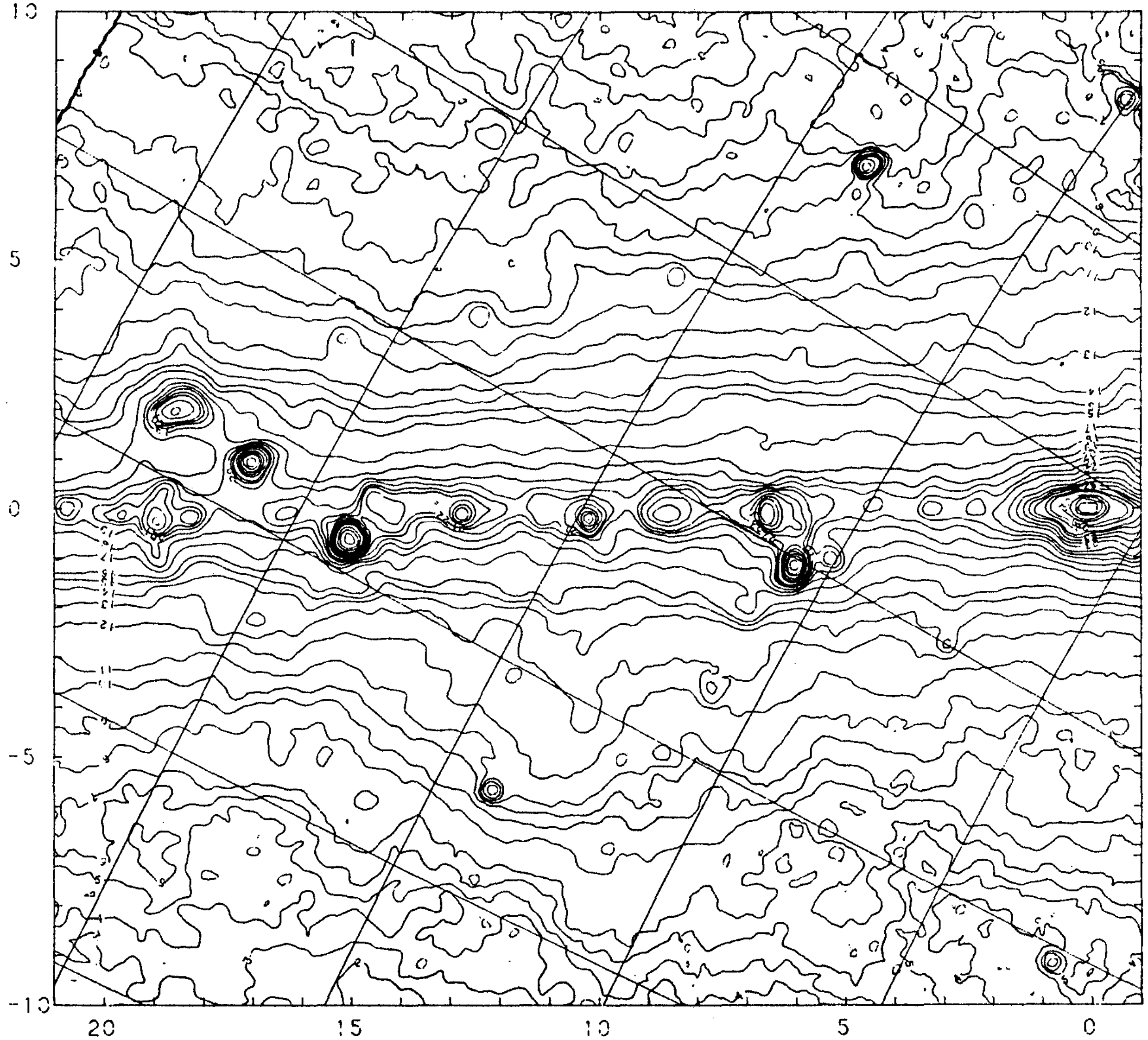
10
5
0
-5
-10
20
15
10
5
0

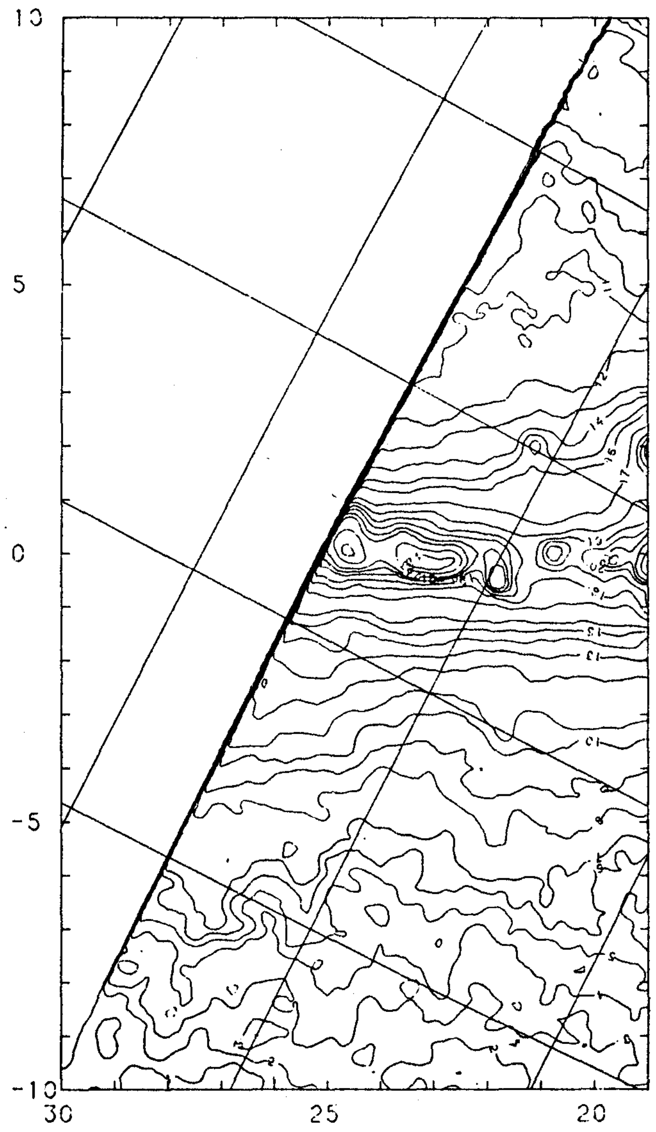
10
5
0
-5
-10
30
25
20

# APPENDIX 3

Contour label table for beam pattern plots

| contour label | $T_a$ mK |
|---|---|
| 1 | 0 |
| 2 | 50 |
| 3 | 100 |
| 4 | 150 |
| 5 | 200 |
| 6 | 250 |
| 7 | 300 |
| 8 | 350 |
| 9 | 400 |
| 10 | 450 |
| 11 | 500 |
| 12 | 550 |
| 13 | 600 |
| 14 | 650 |
| 15 | 700 |
| 16 | 750 |
| 17 | 800 |
| 18 | 850 |
| 19 | 900 |
| 20 | 950 |
| 21 | 1000 |
| 22 | 2000 |
| 23 | 3000 |
| 24 | 4000 |
| 25 | 5000 |
| 26 | 6000 |
| 27 | 7000 |
| 28 | 8000 |
| 29 | 9000 |
| 30 | 10000 |
| 31 | 20000 |
| 32 | 30000 |
| 33 | 40000 |
| 34 | 50000 |
| 35 | 60000 |
| 36 | 70000 |
| 37 | 80000 |
| 38 | 90000 |
| 39 | 100000 |